Theoretical Studies on the Molecular Basis of Free Radical Scavenging Mechanism and Photoprotective Potential of Avenanthramides

Thesis submitted to the University of Calicut
in partial fulfillment of the requirements for
the award of the degree of

DOCTOR OF PHILOSOPHY IN CHEMISTRY

by

SUMAYYA P.C.

DEPARTMENT OF CHEMISTRY
UNIVERSITY OF CALICUT
KERALA-673635
JANUARY 2024

CERTIFICATE

This is to certify that the thesis entitled "**Theoretical Studies on the Molecular Basis of Free Radical Scavenging Mechanism and Photoprotective Potential of Avenanthramides**", submitted to the University of Calicut, in partial fulfillment of the requirements for the award of **Degree of Doctor of Philosophy in Chemistry** is a bonafied record of research work done by **Ms. Sumayya P.C**, during the period 2018-2024 in the Department of Chemistry at University of Calicut, under my supervision and guidance and the thesis has not formed the basis for the award of any Degree/Diploma/Associateship/Fellowship or other similar title to any candidate of any University. The contents of this thesis have been checked for plagiarism using the software "iThenticate" and the similarity index falls under permissible limit. The corrections recommended by the adjudicators have been incorporated in the thesis and the contents in the thesis and the soft copy are the same.

University of Calicut

Dr. K. Muraleedharan
Professor
Department of Chemistry
University of Calicut
Kerala

DECLARATION

I hereby declare that the research work embodied in the thesis entitled "**Theoretical Studies on the Molecular Basis of Free Radical Scavenging Mechanism and Photoprotective Potential of Avenanthramides**", submitted to the University of Calicut is a bonafide record of research work done by me during the period 2018-2024 under the supervision and guidance of Dr. K. Muraleedharan, Professor (retd), Department of Chemistry, University of Calicut. The same has not been submitted elsewhere for any degree or diploma. I also declare that I am solely responsible for the genuineness of the findings/observations pertaining to these studies to complete this thesis.

University of Calicut **Sumayya P.C.**

ACKNOWLEDGMENTS

First and foremost, I want to express my gratitude to the universe for all of my blessings! Looking back, I see that I could not have finished my PhD without the help of many kind people in my life, such as family and my friends. I would like to use this occasion to express my gratitude to each of them.

Firstly, I would like to express my sincere gratitude to my advisor Prof. K. Muraleedharan, Department of Chemistry, University of Calicut, for his patience, motivation, and constructive criticism throughout my research work. I feel myself lucky since without his attention and assistance, I could not have accomplished this goal.

With immense appreciation, I sincerely thank Prof (Dr.) Rajeev S Menon, Head of the Department and former Heads, Prof. (Dr.) P. Raveendran and Dr. A. I. Yahya for providing me adequate facilities to carry out this research work.

I would also like to thank the faculties of the Department, Prof (Dr.) Abraham Joseph, Prof (Dr.) N. K. Renuka, Prof (Dr.) M. T. Ramesan, Prof (Dr.) Binitha N. N., Dr. Susmita De, Dr. Roymon Joseph, Dr. Fazalurahman K., Dr. Suja T. D., Dr. Derry Holaday M. G., Dr. P. Pradeepan (former Associate professor), Dr. Suresh Babu (former Assistant Professor (UGC FRP)), for their kind support for fostering a competing science environment in the Department. I like to thank Prof. V. M. Abdul Mujeeb (Retd) in particular for his support and keen interest throughout the study.

I thank the Department's technical and ministerial staff for their assistance during this course, Mr. Satheesan K, Haridasan K. K, Jinson Antony, Ms. Shaini E, Beena K. Raghavan, Rajani E. P., Sangeetha T. G., Premarajan etc.

I extend my sincere thanks to Maulana Azad National Fellowship (UGC-MANF) for the award of Research Fellowship. Also, I would like to express my sincere thanks to the University of Calicut and Central Sophisticated Instrumentation Facility (CSIF) for providing the computational facility.

I am extremely thankful to Ankit Mittal, Research scholar, Delhi university for useful discussions regarding free radical calculations also to Eric Henon-one of developer of KiSThelP program for helping me for transition state calculations.

I am also indebted to all past and current researcher sholars from the computational chemistry group, Dr.Shameera Ahamed, Dr.Vijisha K. Rajan, Dr. Sindhu N.V., Dr. Sarada K., Dr. Nusrath K., Dr. Ajmala Shireen P., Dr. Sabira K., Ms. Jaseela M.A. Mr. Shivanandan, Ms. Jalala V.K., Ms. Vinduja P., Ms. Neenu Krishna P.U., Ms.Ragi C., Ms. Gopika Krisna G.S. and Research scholars from other groups especially Deepak Joshy, Ligin Rajan for their immense support.

I am extremely grateful to all MSc project students who worked in our lab especially Ms. Arifa K.V. Ms. Aiswarya Royan, Ms. Godsa Merin Babu, and Ms. Jishma who have always been around helping me out on my work in the lab.

I feel fortunate enough to have been blessed with constantly encouraging and supporting parents Khalid P.C and Zainaba C.P. I am deeply indebted to them for this. Also I thank to my sisters (Khalisa Raihana P.C., Lubna Shahanas P.C., & Fathima Hiba mol M.), brothers (Irshad P.C. & Mohammed Arshad P.C.), and in-laws and babies in our home (Fathima Risva, Hayra, Zaya Hezlin, and Aizam) for bearing me through all the hardships. And most of all, I owe my deepest gratitude to my husband, Mr. Abdul Gafoor A., for his affection, encouragement, understanding, and patience. He supported me without any complaint or regret that enabled me to complete my Ph. D thesis. Also deep thanks to my child Afshin A., for his kind cooperation, patience and support. Also express sincere thanks to the support from Umma (Mother–in-Law), may your heart and soul find peace and comfort and also extend my sincere gratitude to whole family members of my husband home. I also thanks to Rajesh, Bina Photostat, Calicut University for making a beautiful thesis.

Aside from those listed above, I would like to express my sincere gratitude to everyone who has assisted me, either directly or indirectly, in the completion of this thesis.

Sumayya P.C.

Dedicated To

My Beloved Family

With affection and everlasting gratitude

ABSTRACT

The research work presented in this thesis comprises a theoretical study of the structural, electronic, and antioxidant properties of the Avenanthramides derived from oats. Avenanthramides are open-chain compounds containing two aromatic rings of an anthranilic acid derivative and cinnamic acid derivative and both these rings are connected through an α,β-unsaturated amide linkage. For this purpose, eight Avenanthramides of interest are selected and the geometry-optimized structures of these compounds are utilized for all the reactivity investigations using density functional theory methods. The major aim of the work comprises the comparative investigation of the radical scavenging activity of the selected compound by its structural and electronic features. The potential ability of these compounds to quench different radicals was studied both by thermodynamic as well as kinetic aspects. For this purpose, the work explored several pathways within the mechanism proposed in the literature. The possibilities of various radical stabilization pathways are also studied using electronic parameters. Utilizing the thermodynamic cycle of the radical quenching process we expanded the ability of these compounds towards a pool of radical species. Moreover, the UV absorbance and UV filtering activity of the selected compounds were analyzed. The obtained UV filtering activity and radical quenching ability of these compounds especially caffeic acid-based compounds are found to exhibit excellent photoprotective ability.

Keywords: Avenanthramides; Antioxidant activity; Hydrogen atom transfer mechanism; Free radical quenching.

സംഗ്രഹം

ഈ പ്രബന്ധത്തിൽ അവതരിപ്പിച്ച ഗവേഷണ പ്രവർത്തനങ്ങൾ ഓട് സിൽ നിന്ന് ഉരുത്തിരിഞ്ഞ അവെനൻത്രൈഡുകളുടെ ഘടനാപരവും, ഇലക് ട്രോണിക്, ആന്റിഓക്സിഡന്റ് ഗുണങ്ങളെക്കുറിച്ചുള്ള സൈദ്ധാന്തിക പഠനം ഉൾക്കൊള്ളുന്നു. ആന്ത്രാനിലിക് ആസിഡ് ഡെറിവേറ്റീവിന്റെയും സിനാമിക് ആസിഡ് ഡെറിവേറ്റീവിന്റെയും രണ്ട് ആരോമാറ്റിക് വളയങ്ങൾ അടങ്ങിയ ഓപ്പൺ-ചെയിൻ സംയുക്തങ്ങളാണ് അവെനൻത്രൈഡുകൾ, ഈ രണ്ട് വളയങ്ങളും α,β-അപൂരിത അമൈഡ് ലിങ്കേജ് വഴി ബന്ധിപ്പിച്ചിരിക്കുന്നു. ഈ ആവശ്യത്തിനായി, താൽപ്പര്യമുള്ള എട്ട് അവെനൻത്രൈഡുകൾ തിരഞ്ഞെ ടുത്തു, ഈ സംയുക്തങ്ങളുടെ ജ്യാമിതി-ഒപ്റ്റിമൈസ് ചെയ്ത ഘടനകൾ സാന്ദ്രത ഫങ്ഷണൽ തിയറി രീതികൾ ഉപയോഗിച്ച് എല്ലാ പ്രതിപ്രവർത്തന അന്വേഷണങ്ങൾക്കും ഉപയോഗിക്കുന്നു. തിരഞ്ഞെടുത്ത സംയുക്തത്തിന്റെ ഘടനാപരവും ഇലക്ട്രോണിക് സവിശേഷതകളും ഉപയോഗിച്ച് സ്വതന്ത്ര റാഡിക്കൽ നിർജ്ജീവമാക്കൽ പ്രവർത്തനത്തിന്റെ താരതമ്യ അന്വേഷണമാണ് സൃഷ്ടിയുടെ പ്രധാന ലക്ഷ്യം. വ്യത്യസ്ത റാഡിക്കലുകളെ ശമിപ്പിക്കാനുള്ള ഈ സംയുക്തങ്ങളുടെ കഴിവ് തെർമോഡൈനാമിക്, ചലനാത്മക വശങ്ങൾ എന്നിവയിലൂടെ പഠിച്ചു. ഈ ആവശ്യത്തിനായി, ലേഖനങ്ങളിൽ നിർദ്ദേശിച്ചിട്ടുള്ള മെക്കാനിസത്തിനു ള്ളിലെ നിരവധി പാതകൾ കൃതി പര്യവേക്ഷണം ചെയ്തു. ഇലക്ട്രോണിക് പാരാമീറ്ററുകൾ ഉപയോഗിച്ച് വിവിധ റാഡിക്കൽ സ്റ്റബിലൈസേഷൻ പാതകളുടെ സാധ്യതകളും പഠിക്കുന്നു. റാഡിക്കൽ ശമിപ്പിക്കൽ പ്രക്രിയയുടെ തെർമോഡൈനാമിക് സൈക്കിൾ ഉപയോഗിച്ച് ഞങ്ങൾ ഈ സംയുക്തങ്ങളുടെ കഴിവ് റാഡിക്കൽ സ്പീഷിസുകളുടെ ഒരു കൂട്ടത്തിലേക്ക് വികസിപ്പിച്ചു. കൂടാതെ, തിരഞ്ഞെടുത്ത സംയുക്തങ്ങളുടെ അൾട്രാവയലറ്റ് ആഗിരണം, യുവി ഫിൽട്ടറിംഗ് പ്രവർത്തനം എന്നിവ വിശകലനം ചെയ്തു. ലഭിച്ച അൾട്രാവയലറ്റ് ഫിൽട്ടറിംഗ് പ്രവർത്തനവും ഈ സംയുക്തങ്ങളുടെ സമൂലമായ ശമിപ്പിക്കാനുള്ള കഴിവും പ്രത്യേകിച്ച് കഫീക് ആസിഡ് അടിസ്ഥാനമാക്കിയുള്ള സംയുക്തങ്ങൾ മികച്ച ഫോട്ടോപ്രൊട്ടക്റ്റീവ് കഴിവ് പ്രകടിപ്പിക്കുന്നതായി കണ്ടെത്തി.

സൂചകപദങ്ങൾ: അവെനൻത്രൈഡുകൾ; ആന്റിഓക്സിഡന്റ് പ്രവർത്തനം; ഹൈഡ്രജൻ ആറ്റം കൈമാറ്റ സംവിധാനം; ഫ്രീ റാഡിക്കൽ ശമിപ്പിക്കൽ.

PREFACE

Opinions today on the cause of chronic illnesses including cancer, heart disease, and neurological diseases are still debatable. Although there are many contributing factors, one of the most important ones in the emergence of many chronic diseases is oxidative stress, which is brought on by an imbalance between reactive species (free radicals) and antioxidants. In fact, there is evidence from both clinical and experimental studies that oxidative stress and a number of chronic illnesses are casually related. Therefore, a lot of research is being done to see if lowering oxidative stress will help these chronic illnesses. Based on clinical and epidemiological research, natural products may be able to lower the morbidity and mortality linked to chronic illnesses by preventing oxidative stress.

Numerous naturally occurring substances have the potential to function as antioxidants. They can guard against damage caused by reactive oxygen species (ROS) or reactive nitrogen species (RNS) and improve oxidative stress-related illnesses like cancer, heart disease, neurological disorders, and inflammatory conditions. While plenty of natural products have demonstrated potential preventive effects against chronic diseases, many natural compounds' bioactivities are still unknown. Thus, a strong scientific basis for the use of natural compounds for the prevention and treatment of diseases associated with oxidative stress would come from comprehending and validating the bioactivities of the compounds and the underlying molecular pathways.

Avenanthramides are low molecular weight phenolic amides made up of an amide bond connecting an anthranilic acid to a hydroxycinnamic acid. Oats contain a unique group of approximately 40 different types of Avenanthramides, which are present in both oat grains and leaves. The research work presented in the thesis entitled with "***Theoretical Studies on the Molecular Basis of Free Radical Scavenging Mechanism and Photoprotective Potential of Avenanthramides***" comprised of theoretical investigation of structural, electronic, radical scavenging activity, TDDFT studies of the compounds called Avenanthramides isolated from *Avena sativa L*.

Chapter 1 introduces the compound Avenanthramide and detailed discussions of the structure, nomenclature, chemical stability, etc. are discussed and also the maximum possible biological applications of Avenanthramide cited so far in the literature have been reviewed. The insights from this review will further advance the role and need of Avenanthramides in the field of medicinal chemistry. ***Chapter 2*** describes the various computational techniques used in this thesis. Density functional methods, the choice of basis sets, functionals and other details are described in detail. It also introduces the several softwares used and the computer power. ***Chapter 3*** introduces the Avenanthramide molecules studied in this thesis namely, **2p**, **2f, 2c**, **2s, 1p**, **1f**, **1c**, and **1s**. Structures of these molecules are optimized and geometric parameters were correlated with the experimental data and ^{13}C NMR and ^{1}H NMR spectra are discussed. Also using QTAIM theory the non-covalent interaction in each molecules were analysed and hydrogen bonds was quantified. Moreover the conceptual density

functional theory based chemical reactivity descriptor and Fukui functions, frontier molecular orbital analysis and molecular electrostatic potential analysis also were examined. ***Chapter 4*** examines the theoretical background of the electronic transition in UV-Vis and ECD spectra of E and Z isomers of **2p** and also the physical mechanism of the electron transfer process during light excitation is more intuitively described along with two-dimensional and three-dimensional visualization methods. ***Chapter 5*** explains the antioxidant potentiality of the selected compound and importance of structural parameters towards radical activity in thermodynamic point of view. The UV filtering activities of all the studied compounds are also included in the chapter. ***Chapter 6*** includes the extended mechanism on the radical scavenging activity of the selected compounds. The study also included the quenching of five reactive species of biological importance by the eight compounds and the selectivity was identified. ***Chapter 7*** discusses the kinetic investigation of quenching of hydroperoxyl radical by the eight Avenanthramide molecules using the transition state theory. From the entire chapters till now revealed the higher reactivity potential of the **c** series compound towards radical quenching process. So in this regard as an extension ***Chapter 8*** studied the quenching of the most abundant and reactive Avenanthramide, **2c** in a pool of selected radicals and the their reactivity compared. Also the chapter enclosed the thermodynamic and kinetic aspects of methanol induced oxidative degradation pathway. ***Chapter 9*** summarizes the results of investigations done and suggests lists of possible areas of future work.

CONTENTS

LIST OF TABLES

LIST OF FIGURES

LIST OF ABBREVIATIONS

AV	:	Avenanthramides
DPPH	:	2,2-Diphenyl-1-Picryl Hydrazyl
ROS	:	Reactive Oxygen Species
RNS	:	Reactive Nitrogen Species
ORAC	:	Oxygen Radical Absorbance Capacity
DFT	:	Density Functional Theory
LDA	:	Local Density approximation
LSDA	:	Local Spin Density Approximation
GGA	:	Generalized Gradient Approximation
meta-GGA	:	meta-Generalized Gradient Approximation
HGGA	:	Hybrid Generalized Gradient Approximation
ACM	:	Adiabatic Correction Method
HMGGA	:	Hybrid Meta- Generalized Gradient Approximation
LCAO	:	Linear Combination of Atomic Orbitals
STO	:	Slater-Type Orbitals
GTO	:	Gaussian-Type Orbitals
CGTOs	:	Contracted GTOs
PGTOs	:	Primitive GTOs
DZ	:	Double Zeta
TZ	:	Triple Zeta
QZ	:	Quadruple Zeta
5Z	:	Quintuple Zeta
PES	:	Potential Energy Surface
NMR	:	Nuclear Magnetic Resonance
TMS	:	Tetramethylsilane
IGLO	:	Individual Gauge Localized Orbital
LORG	:	localized or Loacaorbital Origin
GIAO	:	Gauge Independent Atomic Orbital
TD-DFT	:	Time-dependent Density Functional Theory
RG	:	Runge-Gross

HOMO	:	Highest Occupied Molecular Orbital
LUMO	:	Lowest Unoccupied Molecular Orbital
NTO	:	Natural Transition Orbital
LE	:	Local Excitation
CT	:	Charge Transfer
R	:	Rydberg
MO	:	Molecular Orbital
Ecoul	:	Coulomb Attractive Energy
ECD	:	Electronic Circular Dichroism
QTAIM	:	Quantum Theory of Atoms in Molecules
CP	:	Critical Point
NCP	:	Nuclear Critical Point
BCP	:	Bond Critical Point
RCP	:	Ring Critical Point
CCP	:	Cage Critical Point
HOMA	:	Harmonic Oscillator Measure of Aromaticity
FLU	:	Aromatic Fluctuation Index
PDI	:	Para-Delocalization Index
TST	:	Transition State Theory
VMD	:	Visual Molecular Dynamics
PA	:	Phenylalkenoic Acid
AA	:	Anthranilic Acid
ESP	:	Electrostatic Potential
CDFT	:	Conceptual Density Functional Theory
NCI	:	Non-Covalent Interaction
IEFPCM	:	Integral Equation Formalism Polarizable Continuum Model
RDG	:	Reduced Density Gradient
vdW	:	van der Waals
GPB	:	Gas-Phase Basicity
FWHM	:	Full Width at Half Maximum
NTO	:	Natural Transition Orbital
CDD	:	Charge Difference Density
TDM	:	Transition Density Matrix
BDE	:	Bond Dissociation Enthalpy

IP	:	Ionization Potential
PDE	:	Proton Dissociation Enthalpy
PA	:	Proton Affinity
ETE	:	Electron Transfer Enthalpy
HAT	:	Hydrogen Atom Transfer
SET-PT	:	Single-Electron Transfer followed by Proton Transfer
SPLET	:	Sequential Proton Loss Electron Transfer
dHAT	:	double HAT
SPLHAT	:	Sequential Proton Loss Hydrogen Atom Transfer
StPLdET	:	Sequential triple Proton Loss double Electron Transfer
HAA	:	Hydrogen Atom Affinity
EA	:	Electron Affinity
IE	:	Ionization Energy
TST	:	Transition State Theory
FHAT	:	Formal Hydrogen Atom Transfer
RAF	:	Radical adduct Formation

Chapter 1

Introduction and Review of Literature

- ✓ *Introduce the compound Avenanthramide; structure, nomenclature, stability, and bioactivities, etc.*
- ✓ *Free radicals, role of free radical scavengers and relevance of antioxidants are includes.*
- ✓ *Review on the recent advances on the bioactivities especially antioxidant activity of the Avenanthramides*

1. Introduction

For thousands of years, the staple of the human diet has been cereal-based foods, which account for around 50% of the daily recommended consumption of fiber. The likelihood of developing some dietary-related diseases such as type 2 diabetes, obesity, cancer, and cardiovascular disease is adversely correlated with greater whole grain consumption[1, 2]. Oats (*Avena Sativa L.),* a functional cereal grain that is extensively consumed around the world, have recently attracted more attention because of their many health advantages[3–5]. These are cultivated throughout temperate zones[6, 7]. It is a versatile crop that is regarded as having higher nutritional value than many other unfortified cereals. The consumption of foods made from oats can lower serum cholesterol levels, decrease glucose uptake, and diminish the plasma insulin response, according to numerous laboratory and clinical research[7, 8]. Both the general public and scientists are interested in the nutritional advantages of oats. As a result, the food industry is using more oats as an ingredient in a variety of meals, such as breads, biscuits, beverages, breakfast cereals, and baby foods. It contains bioactive compounds such as proteins, peptides, amino acids, β-glucans, resistant starch, dietary fibers, polyunsaturated fatty acids, vitamins, minerals, polyphenols, Avenanthramides, oat saponins, and β-sitosterol [9, 10]. Avenanthramides (AVs) and steroidal saponins are two distinct classes of phytochemicals that are only produced by oats. According to recent studies, AVs are crucial in mediating the health advantages of oats[3, 11, 12].

1.1.Avenanthramides (AVs)

AVs are a group of N-containing secondary metabolites that have been found in oats (*Avena sativa. L*) groats and hulls. They were initially recognized as phytoalexins, which the plant produces in reaction to diseases like fungi[1, 13]. The commonly consumed whole-grain cereal, oats is the unique source of AVs. The first, who characterized, detected, and named the AVs by Collin[13]. These are considered one of the important groups of molecules from the group of phenolic alkaloids and display a variety of biological activities antioxidant, anti-inflammatory, anti-itch, anti-irritant, and antiatherogenic activities of AVs [1, 3].

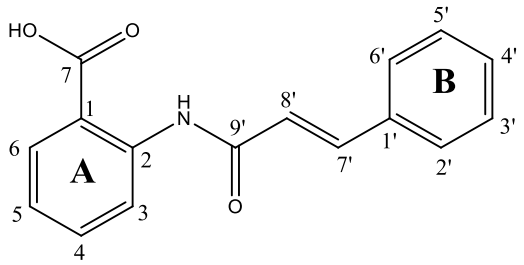

Fig. 1.1. Structure of AVs framework with atomic labelling.

From a biological perspective, it has been demonstrated that phenolic compounds have a variety of biological activities, the most significant of which is the antioxidant activity, which guards against lipid peroxidation and cellular oxidative damage caused by dangerous free radicals [4, 5]. Structure-activity relationship analyses have shown that this property is related to the capacity of phenolic compounds to donate hydrogen atoms or electrons, chelate metal cations, or scavenge free radicals. These abilities are primarily determined by the number

and position of the hydroxyl groups and the type of substitutions on the aromatic rings.

1.2.Structure and nomenclature

Structurally, AVs are open-chain compounds of substituted cinnamic acid amides of anthranilic acids (Fig.1.1). The framework containing two phenyl rings is named A and B respectively for anthranilic acid and cinnamic acid moieties. The general formula of AVs is represented by (Fig 1). Collin demonstrated AVs using alphabetic descriptors like A, B, C, D, etc., while Dimberg assigned upper case letters to the anthranilate derivate and lower case to the accompanying phenylpropanoid, such as "**c**" for caffeic acid, "**f**" for ferulic acid, or "**p**" for p-coumaric acid, and "**s**" for sinapic acid[2, 11]. Dimberg's modified the representation[14, 15], the anthranilic derivatives were assigned a number and the accompanying cinnamate derivatives were classified by a letter. Pointedly, the letters **a**, **c**, **f**, **p**, and **s** were used for cinnamic acid, caffeic acid, ferulic acid, p-coumaric acid, and sinapic acid respectively, whereas, anthranilic acid moiety with one anthranilic acid as **1**, 5-hydroxy anthranilic acid as **2**, 5- hydroxy-4-methoxy anthranilic acid as **3**, 4-hydroxy anthranilic acid as **4**, or 4,5-dihydroxy anthranilic acid as **5**. According to IUPAC naming system, Avenanthramides-A (**2p**) (N-(4′-hydroxycinnamoyl)-5-hydroxy anthranilic acid), Avenanthramides-B (N-(4′-hydroxy-3′-methoxycinnamoyl)-5- hydroxy anthranilic acid) (**2f**), and Avenanthramides-C (N-(3′-4′-dihydroxy cinnamoyl)-5-hydroxy anthranilic acid) (**2c**). Table 1.1 summarises the representative examples of both notations.

Table 1.1 The representative examples of structures and names of common AVs (These are also presented in a recently published article [3]). Both Collins's method and Dimberg's method are given. Collins's method used alphabetical names for assigning molecules. In Dimberg's method, cinnamic acid units were represented by letters **a**, **c**, **f**, **p**, and **s** (**a** for cinnamic acid, **c** for caffeic acid, **f** for ferulic acid, **p** for p-coumaric acid, and **s** for sinapic acid) and anthranilic acid by a number.

Avenanthramides	Dimberg's modified system		Collin's system	
	n=1	n=2	n=1	n=2
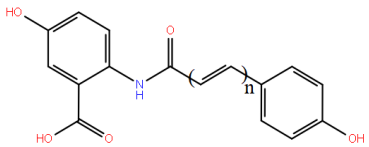	2p	2pd	A	O
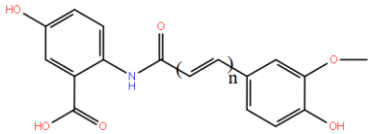	2f	2fd	B	P
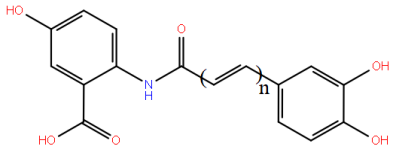	2c	2cd	C	Q

1.3.Chemical stability

It has been reported that Avennathramide can exist either cis or trans (Z or E). As per Collins's report AVs isomerize when exposed to sunlight or ultraviolet radiation, while after being exposed to UV radiation for 18 hours at a wavelength of 254 nm, Dimberg discovered that the three AVs (A, B, and C) remained in the trans conformation. Kakegawa also supports the ready isomerization of E form to z form on photo-irradiation as Collins's observation. The Z-isomer of N-(3', 4'-dimethoxy cinnamoyl)anthranilic acid has been found to possess 10 times more antiallergic properties than the Z-isomer and the photo

irradiated product of E-isomer, the Z-isomer was found to inhibit hyaluronidase more effectively than E-isomer [16].

1.4.Physicochemical and Biological Properties

Numerous studies show that these natural products have potent antioxidant activity in vitro and in vivo, as well as anti-inflammatory, anti-itching, anti-irritant, antiatherogenic, and antiproliferative properties (Fig.1.2). These properties may prevent or limit cellular oxidative dysfunctions and the development of oxidative stress-related diseases, such as neurodegenerative and cardiovascular diseases, and they may also offer additional defense against skin irritation, aging, a variety of skin conditions, cancer, etc. [17–24]. Strong anti-oxidant, anti-inflammatory, and antiproliferative properties have been found in natural, synthetic, and recombinant AVs. These properties may protect against a variety of cellular dysfunctions and human pathologies, including illnesses linked to aging.

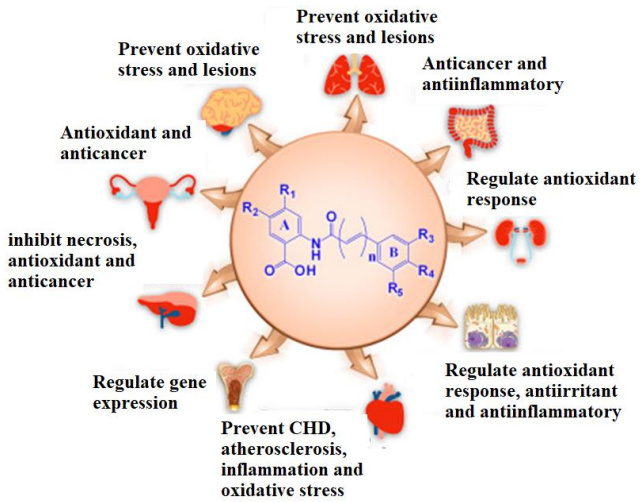

Fig. 1.2. The bioactivities of AVs and prospective health advantages.

a) Anti-oxidant activity

The studies on the antioxidant activity of the AVs from oats sources are not new. The evidence that oat flour might be employed as a food preservative against oxidative degradation due to its ability to delay the initial peroxide generation and rancidity initially showed the antioxidant activity of oat components[25, 26] (Fig.1.3). The antioxidative capacity of N-(4'-hydroxy-3'-methoxy-(E)-cynnamoil)-5-hydroxyanthranilic acid and N-(4'-hydroxy-3-methoxy-(E)-cynnamoil)-5-hydroxy-4-methoxyanthranilic acid was first discovered by Lingnert and colleagues in oxygen consumption experiments using a linoleic acid-based system[27]. By testing isolated components from several oat cultivars, the antioxidant effects of oat extracts and their constituents, including AVs, were eventually directly demonstrated[9, 28]. For instance, three AVs isoforms (A, C, and K) were among the most significant oat metabolites endowed with antioxidant activity when Emmons and colleagues analyzed oat milling fractions to identify their potential as dietary antioxidants[28]. Hydrogen peroxide (H_2O_2) and hydroxyl radicals (OH•) were shown to be significantly reduced by the AVs analog Tranilast, suggesting potential clinical applications[29]. The three main oat Avenanthramides-A, B, and C were then created by Peterson and colleagues. They then tested their antioxidant activities using two in vitro assays, including the inhibition of beta-carotene bleaching and the reaction with the free radical 2,2-diphenyl-1-picrylhydrazyl (DPPH), which revealed that Avenanthramides -C has higher antioxidant activity than Avenanthramides -B and Avenanthramides -A[30]. In vivo models

were used to research AVs ' antioxidant abilities. For example, reactive oxygen species (ROS) levels in the soleus muscle were effectively decreased by adding Avenanthramides-C to the food of rats at a concentration of 0.1 g/kg. In addition, compared to control rats, animals administered Avenanthramides-C had increased superoxide dismutase activity in the vastus lateralis muscle (DVL), liver, and kidney, as well as higher glutathione peroxidase activity in the heart and DVL. Avenanthramide-C supplementation also reduced the elevated ROS generation in the soleus muscle and the heart's lipid peroxidation that exercise-induced[31].

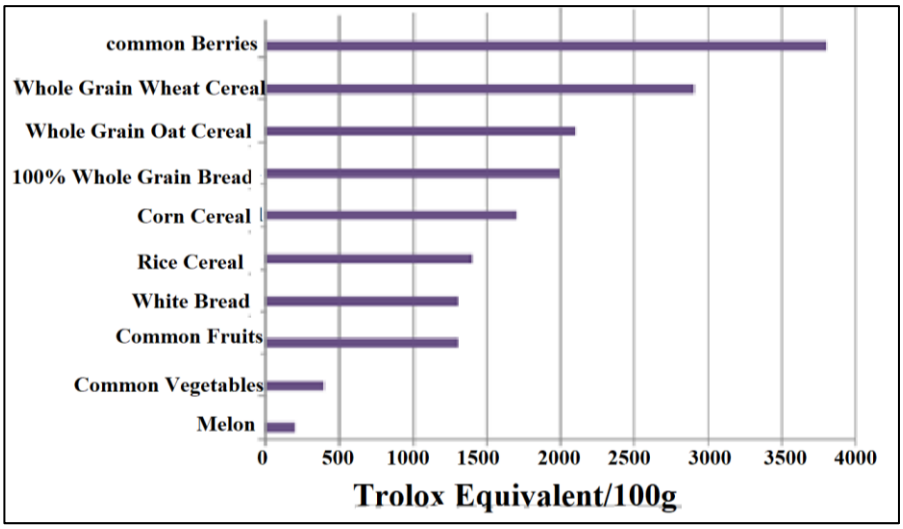

Fig.1.3. Average antioxidant activity of different foods. Data were drawn from analysis of 3 melons, 20vegitables, 12 fruits, 2 white Breads,1 rice cereal,3 corn cereals, 2 whole grain breads,3 whole grain oats cereals,3 whole wheat cereals, 2 whole grain with raisins, and 5 berries[32].

The antioxidant capacity of AVs was 10−30 times stronger than that of other phenolic compounds in oats, such as caffeic acid, vanillin,

and ferulic acid, as determined using the measuring system of linoleic acid oxidation[11]. Avenanthramides; **2c**, **2f**, and **2p** demonstrated antioxidant capacities by β-carotene bleaching and DPPH and ORAC methods, with Avenanthramides 2c exhibiting the highest activity[2, 11]. The potential mechanism stating the strong antioxidant activity of AVs might be related to the conjugation across amide bonds in AVs. Furthermore, the positions and number of hydroxyl groups were also important. For example, ortho-hydroxyl was a key group to particularly improve the antioxidant activity of Avenanthramides 2c.

b) Anti-Inflammatory Activity

The anti-inflammatory and anti-itching qualities of oat extracts were already mentioned in ancient literature. In reality, oatmeal has been used as a topical treatment for several dermatological diseases in Greek and Latin literature. Since 1945, numerous studies have demonstrated the advantages of colloidal oatmeal baths as a calming remedy and a mild, cleansing recipe for itchy, irritated skin caused by diverse xerotic dermatitis[17, 23]. Despite being used frequently to treat skin irritation, the phytochemicals in oats that are in charge of the anti-inflammatory effect weren't discovered until 2004. Liu and colleagues first reported the potential anti-inflammatory and antiatherogenic properties of Avenanthramides-enriched extracts of oats, which inhibited the IL-1βstimulated endothelial cell secretion of proinflammatory cytokines (IL-6) and chemokines (IL-8 and MCP-1), as well as expression of adhesion molecules (ICAM-1, VCAM-1, and E-selectin) and adhesion of monocytes to endothelial cell monolayer[23]. In addition, Sur and coworkers discovered that

keratinocytes treated with AVs showed a considerable suppression of TNF-induced NF-B activity and a consequent reduction in IL-8 production, indicating that oat AVs may have a potential anti-itching effect[17]. Furthermore, AVs supplementation was able to attenuate exercise-induced inflammation in postmenopausal women by reducing neutrophil respiratory burst activity, plasma C-reactive protein and IL-1β levels, and NF-κB activation in peripheral blood mononuclear cells[33, 34].

c) Antiproliferative activity

Clear evidence demonstrates that AVs inhibit the proliferation of distinct cell lines, such as human colon and breast cancer cells, and vascular smooth muscle cells (VSMC)[21, 35, 36]. In particular, it was found that Avenanthramides -enriched oat extracts, Avenanthramides-C, and the methyl-ester derivative of Avenanthramides-C were more effective on colon cancer cell lines, including CaCo-2, HT29, LS174T, and HCT116 cells than on prostate or breast cancer cell lines. This was determined by testing the antiproliferative effect of AVs on various cancer cell lines[21]. Subsequent studies also showed that AVs could inhibit cell proliferation and promote the apoptosis of MDA-MB-231 breast cancer cells, Caco-2 colon cancer cells, HepG2 liver cancer cells, and A549 and H1299 lung cancer cells[12, 35, 37, 38].

d) Potential Therapeutics for Cerebral Cavernous Malformation (CCM) Disease

Cerebral Cavernous Malformation Disease also known as cavernous angioma or cavernoma, is a major cerebrovascular disease characterized by clusters of abnormally dilated and leaky capillaries occurring in the brain, spinal cord, and retina, with a prevalence of 0.3–0.5% in the general population[1]. These vascular anomalies, also known as CCM lesions, can be single or multiple (up to hundreds), as determined by magnetic resonance imaging, and they may cause severe clinical symptoms at any age, such as recurrent headaches, focal neurological deficits, seizures, stroke, and intracerebral hemorrhage (ICH). CCM disease has proven genetic origin (OMIM 116860), being caused by loss-of-function mutations in three genes, KRIT1 (CCM1), CCM2, and PDCD10 (CCM3). there is emerging evidence that AVs and Y AVs can enhance cellular defenses against oxidative stress by inhibiting the activity of prooxidant and proinflammatory proteins, such as NADPH oxidase and NF-Kb, and stimulating the upregulation of antioxidant molecules, such as GSH and SOD2[39, 40]. Indeed, treatment of KRIT1- knockout and KRIT1-silenced cellular models with YAvns was effective in reverting molecular phenotypes caused by KRIT1 loss-of-function, including the downregulation of FOXO1 and SOD2 and the upregulation of cyclin D1[40].

e) Muscle Health

AVs, a kind of polyphenolic molecule, may be carried into muscle tissue after intake and has potent anti-inflammatory properties.

According to a study, AVs are bioavailable through blood circulation, enabling them to enter surrounding tissues and be absorbed by several organs. After gavaged administration of three kinds of AVs in rats, these AVs could be detected in skeletal muscle, which provided a theoretical basis for the potential function of AVs in regulating muscle atrophy[3, 41].

AVs may be natural functional elements that, when added to a long-term diet, specifically protect muscle and have the potential to have an impact on sustaining healthy muscle. Previous literature also indicated that many inducers, such as the ubiquitin-proteasome system, induced protein degradation, cell apoptosis, cell autophagy, and even miRNA profile alterations and were all involved in regulating muscle health. Reduced inflammatory responses have been the primary focus of the mechanism through which AVs preserve muscle health up to this point.

f) Obesity

AVs may help people lose weight because they are naturally active ingredients. Mice given AVs containing fodder showed the phenomena of weight loss in high-fat-induced obese mice. AVs (100 or 300 mg/kg per day for 8 weeks) consumption resulted in decreased weight gain, decreased glucose and insulin levels, and downregulated adipokine gene expression in diet-induced obese mice, suggesting that AVs may promote body weight loss by reducing inflammation[42].

g) Atherosclerosis

The studies found that poor NO generation, elevated expression of adhesion molecules, and proliferation of vascular smooth muscle cells (SMCs) occur often during the onset and progression of atherosclerosis[3]. In human aortic endothelial cells (HAECs), Avenanthramides treatment could significantly lower IL-1-stimulated expression of intracellular adhesion molecule-1 (ICAM-1), vascular cell adhesion molecule-1 (VCAM-1), and E-selectin and the secretion of proinflammatory IL-6, IL-8, and MCP-1, which may prevent atherosclerosis[23]. Avenanthramides-C (120 μM) administration was found to significantly reduce serum-induced SMC proliferation and boost NO generation in SMCs and HAECs in a dose-dependent way, consequently reducing atherosclerosis, according to a subsequent investigation[39].

h) Osteoporosis

Reduced bone density and increased bone fragility are the hallmarks of osteoporosis, a widespread systemic skeletal condition that significantly raises the risk of fragility fracture[43]. The main cause of osteoporosis is calcium deficiency, and calcium supplementation is one of the most significant ways to avoid it. Elevating the activity and survival of osteoblasts helps prevent and treat osteoporosis. Additionally, the imbalance of osteoblasts (which make new bone) and osteoclasts (which destroy it) is another important reason for the development of osteoporosis. AVs (1, 10, or 100 μM) administration may boost the expression of osteoprotegerin and lessen

the etoposide-induced apoptosis of OB-6 osteoblastic cells, according to an in vitro investigation[44]. AVs were found to suppress the expression of the osteoclast differentiation factor RANKL (receptor activator of nuclear factor-B ligand) in MLO-Y4 osteocytic cells, prevent osteoblast/osteocyte apoptosis, and promote osteoclast apoptosis, according to further research[3].

1.5.Role of antioxidants in living system

The release of free radicals (A molecular species with an unpaired electron in an atomic orbital that is capable of independent existence) is crucial to our metabolic system. The removal of free radicals from the biological system is critical for the long-term viability of cellular functioning due to their damaging effects. The free radicals such as reactive oxygen species and reactive nitrogen species (ROS/RNS) in increased concentration are very dangerous to the living system leading to inflammation, metabolic disorders, cellular aging, reperfusion damage, atherosclerosis, carcinogenesis, etc. Radicals originating from oxygen, or ROS, are the most significant free radicals created during metabolic reactions. Both ROS and RNS can be classified as radicals and non-radicals [45] and the classification is given in Fig.1.4 The overproduction of ROS/RNS derived from both endogenous sources (mitochondria, peroxisomes, endoplasmic reticulum, phagocytic cells, etc.) and exogenous sources (pollution, alcohol, tobacco smoke, heavy metals, transition metals, industrial solvents, and pesticides, certain drugs like halothane, paracetamol, and radiation).

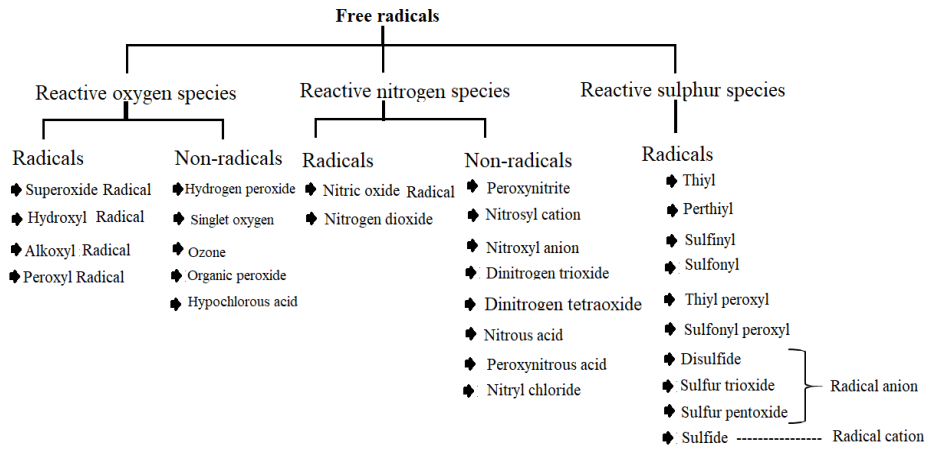

Fig. 1.4. Classification of Free radicals

Although these non-radical species are not free radicals, they can easily cause free radical reactions in living organisms[46]. Free radicals are natural byproducts produced by normal metabolism and they are involved in various physiological and pathological conditions (i.e. Cell signaling, tissue homeostasis, redox regulation, immunity, defense against infectious diseases, etc[47, 48]. An imbalance between the antioxidants and free radicals and nonradicals leads to the accumulation of vigorous damage of nucleic acids, proteins lipids, etc., and leads to oxidative stress [49](Fig.1.5). The phenomenon of oxidative stress is caused by an imbalance between the production and accumulation of oxygen-reactive species (ROS) in cells and tissues and the ability of a biological system to detoxify these reactive products. The oxidative stress caused by free radicals has been implicated in the development of cataracts, rheumatoid arthritis, diabetes mellitus, neurodegenerative disorders (Parkinson's disease, Alzheimer's disease, and Multiple Sclerosis), cardiovascular diseases (atherosclerosis and

hypertension), respiratory diseases (asthma), and various cancers (colorectal, prostate, breast, lung, bladder cancers)[50]. It is known that living organisms (at all levels of complexity) evolved antioxidant molecules and proteins to prevent or repair oxidative damage.

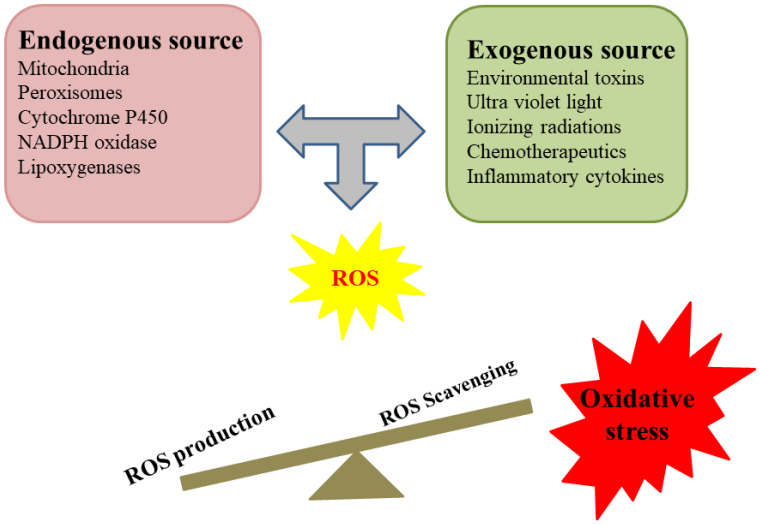

Fig. 1.5. Generation of the different classes of ROS, viz. free radicals and non-radicals, from endogenous and exogenous sources

The reactive species harming the biological system include reactive oxygen and nitrogen species (ROS/RNS). Biologically important ROS include radicals such as hydroxyl, hydroperoxyl, peroxyl, alkoxyl, and radical anions like carbonate and superoxide, whereas RNS includes radicals like nitrogen dioxide, nitric oxide, azide, and many others[51–54]. Moreover, reactive sulfur species include radicals like thiyl ($RS^{\cdot}$), perthiyl ($RSS^{\cdot}$), sulfinyl ($RSO^{\cdot}$), sulfonyl ($RS(O)_2^{\cdot}$), thiyl peroxyl ($RSOO^{\cdot}$),sulfonyl peroxyl ($RS(O)_2OO^{\cdot}$), and radical anions like disulfide ($RSSR^{\cdot-}$), sulfur trioxide

($SO_3^{\cdot-}$), sulfur pentoxide ($SO_5^{\cdot-}$), and radical cation like sulfide ($RSR^{\cdot+}$)[55].

Hydroxy radicals are the most reactive species among other radicals since they volgeruosly react with DNA, proteins, lipids, and carbohydrates and cause severe damage to the cells. It reacts immediately with the organic and inorganic molecules in its vicinity. Moreover, the hydroperoxyl radical, generated by the protonation of superoxide radical anion, and the peroxyl radicals can cause lipid peroxidation. Furthermore, protein oxidation can be appropriately stimulated by alkoxyl and peroxyl radicals, both of which are capable of oxidizing specific amino acids. This can result in the formation of protein-protein connections and, eventually, the loss of protein activity[56, 57].

Nitric Oxide or Nitrogen Monoxide ($NO^{\bullet}$) is a very low reactive species among RNS. However the reaction of Superoxide anion radical with $NO^{\bullet}$ forms Peroxynitrite. The peroxynitrite is the highly toxic nitrogen-containing reactive species that reacts directly with CO_2 to form other highly reactive nitroso peroxo carboxylate ($ONOOCO_2^-$) or peroxynitrous acid (ONOOH). The formed peroxynitrous acid upon hemolysis produces OH• and NO_2 (or sometimes rearranges to form NO_3). The deprotonated $OONO^-$ oxidizes methionine and tyrosine residues in proteins, The presence of nitrotyrosine residues is seen as a sign of cellular damage caused by peroxynitrite[57].

Following that, reactive sulfur species (RSS) are molecules with sulfur in a high oxidation state. These are sulfur-containing redox-active compounds that can either oxidize or reduce biomolecules under physiological conditions. Reactive sulfur species include various forms of cysteine and methionine, as well as several low molecular mass compounds such as glutathione, trypanothione, and mycothiol. H_2S, a completely reduced form of sulfur, is classified as an RSS because it interacts with proteins in redox processes and changes their activities. Thiols and disulfides oxidize rapidly to sulfur species with sulfur in higher oxidation states. Thiyl radicals, disulfides, sulfenic acids, and disulfide-S-oxides are examples of such agents. They rapidly oxidize and then block thiol-proteins and enzymes, thus they can be considered a distinct class of oxidative stressors that provide new antioxidant therapeutic targets.

Antioxidants are therefore needed to remove the surplus reactive species that have been produced. Thus, the hunt for molecules with strong antioxidant properties and their mechanisms of action will always be a fascinating field of study. To be a good antioxidant, the species formed after the scavenging process must be more stable than the prior one. Here the work intended to identify the mechanism of action and pathways of radical scavenging mechanism along with other properties of AVs molecule.

1.6. Scope of the present study

Theoretical works on Avenanthramides are scarce compared to other polyphenolic components. There are too many research papers

on both theoretical and experimental research into the reactivity and especially biological activities of phytochemicals found in fruits and vegetables and are still underway. Nevertheless, cereals are largely ignored as a key contributor to dietary antioxidants. Avenanthramides as a unique component found in cereals, detailed investigation of the reactivity, bioactivity, radical mechanism, and absorption characteristics are important. Hence in the presented study, eight Avenanthramides are selected. We have attempted a theoretical study on the structure and many plausible applications of these molecules.

1.7. Objectives of the present study

Oats, a grain of the Poaceae family, are one of the staple food crops that human beings can consume directly. The cereals are rich in polyphenols and Avenanthramides. Avenanthramides are the unique component found exclusively in oats among cereals. Numerous researches showed that Avenanthramides had antioxidant, anti-inflammatory, anti-itch, anti-irritant, and antiatherogenic properties [1, 3, 12]. Hence for the purpose eight Avenanthramides namely **2p**, **2f**, **2c**, **2s**, **1p**, **1f**, **1c**, and **1s** are selected. The detailed structural features of the compounds are included in Chapter 3.

Considering the success of the density functional theory (DFT) method in elucidating the antioxidant property of phenolic compounds, we aimed to perform a systematic DFT study to clarify the relationship between the molecular/electronic structure and free radical scavenging activity and the possible mechanisms of Avenanthramides. Eight

representative Avenanthramides with different substitution patterns in both aromatic rings (A and B) were chosen for the investigation.

Our knowledge of the antioxidant property of Avenanthramides has been substantially enhanced by earlier investigations, but the understanding of the structure–activity link and the underlying mechanisms is still lacking[58, 59]. The possibilities of the compound's ability to scavenge radicals from various reactive species are also not investigated. To the best of our knowledge, theoretical knowledge about these molecules is very limited in the literature. In this context, we attempt:

- Theoretical investigation of the structure and reactivity of selected Avenanthramides
- Optical signature of the E and Z isomers of the Avenanthramides
- Theoretical study of antioxidant potential and antioxidant mechanism operating in these compounds
- Investigations on the structure-activity relationship and the role of the catechol, guaiacyl, and carboxyl groups in activity and the mechanism were paid special attention.
- Theoretical study of UV absorbance of all selected compounds and their potential application as UV filters.
- To investigate the thermodynamic aspects of the radical quenching process involved different radicals from different

sources involving reactive oxygen, nitrogen, sulfur, and carbon species.

- To investigate the kinetics and rate constant calculations of radical quenching activity of the selected Avenanthramides with peroxyl radical species.
- To investigate the pathways of methanol-induced oxidative degradation of reactive Avenanthramides among selected compounds.

References

1. Perrelli A, Goitre L, Salzano AM, et al (2018) Biological Activities, Health Benefits, and Therapeutic Properties of Avenanthramides: From Skin Protection to Prevention and Treatment of Cerebrovascular Diseases. Oxid Med Cell Longev 2018:6015351. https://doi.org/10.1155/2018/6015351

2. Fagerlund A, Sunnerheim K, Dimberg LH (2009) Radical-scavenging and antioxidant activity of avenanthramides. Food Chem 113:550–556. https://doi.org/https://doi.org/10.1016/j.foodchem.2008.07.101

3. Yu Y, Zhou L, Li X, et al (2022) The Progress of Nomenclature, Structure, Metabolism, and Bioactivities of Oat Novel Phytochemical: Avenanthramides. J Agric Food Chem 70:446–457. https://doi.org/10.1021/acs.jafc.1c05704

4. Tang Y, Li S, Yan J, et al (2022) Bioactive Components and Health Functions of Oat. Food Rev Int 1–20. https://doi.org/10.1080/87559129.2022.2029477

5. Sang S, Chu Y (2017) Whole grain oats, more than just a fiber: Role of unique phytochemicals. Mol Nutr Food Res 61:1600715. https://doi.org/https://doi.org/10.1002/mnfr.201600715

6. Jágr M, Dvořáček V, Čepková PH, Doležalová J (2020) Comprehensive analysis of oat avenanthramides using hybrid quadrupole-Orbitrap mass spectrometry: Possible detection of new compounds. Rapid Commun Mass Spectrom 34:e8718. https://doi.org/https://doi.org/10.1002/rcm.8718

7. Rasane P, Jha A, Sabikhi L, et al (2015) Nutritional advantages of oats and opportunities for its processing as value added foods - a review. J Food Sci Technol 52:662–675. https://doi.org/10.1007/s13197-013-1072-1

8. Reiners S, Hebestreit S, Wedekind L, et al (2023) Effect of a regular consumption of traditional and roasted oat and barley flakes on blood lipids and glucose metabolism–A randomized crossover trial . Front. Nutr. 10

9. Dimberg LH, Theander O, Lingnert H (1993) Avenanthramides--a group of phenolic antioxidants in oats. Cereal Chem 70:637–641

10. Shi Y, Johnson J, O'Shea M, Chu Y (2014) The Bioavailability and

Metabolism of Phenolics, a Class of Antioxidants Found in Grains. Cereal Foods World 59:52–58. https://doi.org/10.1094/CFW-59-2-0052

11. Bratt K, Sunnerheim K, Bryngelsson S, et al (2003) Avenanthramides in Oats (Avena sativa L.) and Structure−Antioxidant Activity Relationships. J Agric Food Chem 51:594–600. https://doi.org/10.1021/jf020544f

12. Li X, Zhou L, Yu Y, et al (2022) The Potential Functions and Mechanisms of Oat on Cancer Prevention: A Review. J Agric Food Chem 70:14588–14599. https://doi.org/10.1021/acs.jafc.2c06518

13. Collins FW (1989) Oat phenolics: avenanthramides, novel substituted N-cinnamoylanthranilate alkaloids from oat groats and hulls. J Agric Food Chem 37:60–66. https://doi.org/10.1021/jf00085a015

14. Ishihara A, Kojima K, Fujita T, et al (2014) New series of avenanthramides in oat seed. Biosci Biotechnol Biochem 78:1975–1983. https://doi.org/10.1080/09168451.2014.946390

15. de Bruijn WJC, van Dinteren S, Gruppen H, Vincken J-P (2019) Mass spectrometric characterisation of avenanthramides and enhancing their production by germination of oat (Avena sativa). Food Chem 277:682–690. https://doi.org/https://doi.org/10.1016/j.foodchem.2018.11.013

16. Kakegawa H, Mitsuo N, Matsumoto H, Satoh T, Akagi M TK (1985) Hyaluronidase-inhibitory and anti-allergic activities of the photo-irradiated products of tranilast. Chem Pharm Bull 33:3738–44. https://doi.org/10.1248/cpb.33.3738

17. Sur R, Nigam A, Grote D, et al (2008) Avenanthramides, polyphenols from oats, exhibit anti-inflammatory and anti-itch activity. Arch Dermatol Res 300:569–574. https://doi.org/10.1007/s00403-008-0858-x

18. Rao S, Santhakumar AB, Chinkwo KA, Blanchard CL (2019) Characterization of phenolic compound antioxidant activity in oat varieties using UHPLC–online ABTS and LC Q-TOF. Cereal Chem 96:958–966. https://doi.org/https://doi.org/10.1002/cche.10200

19. Chen C-Y, Milbury PE, Kwak H-K, et al (2004) Avenanthramides and Phenolic Acids from Oats Are Bioavailable and Act Synergistically with Vitamin C to Enhance Hamster and Human LDL

Resistance to Oxidation12. J Nutr 134:1459–1466. https://doi.org/https://doi.org/10.1093/jn/134.6.1459

20. Chu Y-F, Wise ML, Gulvady AA, et al (2013) In vitro antioxidant capacity and anti-inflammatory activity of seven common oats. Food Chem 139:426–431. https://doi.org/https://doi.org/10.1016/j.foodchem.2013.01.104

21. Guo W, Nie L, Wu D, et al (2010) Avenanthramides Inhibit Proliferation of Human Colon Cancer Cell Lines In Vitro. Nutr Cancer 62:1007–1016. https://doi.org/10.1080/01635581.2010.492090

22. Kurtz E, Wallo W (2007) Colloidal Oatmeal: History, Chemistry and Clinical Properties. J Drugs Dermatol 6:167–170

23. Liu L, Zubik L, Collins FW, et al (2004) The antiatherogenic potential of oat phenolic compounds. Atherosclerosis 175:39–49. https://doi.org/https://doi.org/10.1016/j.atherosclerosis.2004.01.044

24. Wang C, Eskiw CH (2019) Cytoprotective effects of Avenathramide C against oxidative and inflammatory stress in normal human dermal fibroblasts. Sci Rep 9:2932. https://doi.org/10.1038/s41598-019-39244-9

25. Lowen L, Anderson L, Harrison RW (1937) Cereal Flours as Antioxidants for Fishery Products. Ind Eng Chem 29:151–156. https://doi.org/10.1021/ie50326a006

26. Peters FN (1937) Oat Flour as an Antioxidant. Ind Eng Chem 29:146–151. https://doi.org/10.1021/ie50326a005

27. LINGNERT H, VALLENTIN K, ERIKSSON C (2007) Measurement of antioxidative effect in model system. J Food Process Preserv 3:87–103. https://doi.org/10.1111/j.1745-4549.1979.tb00574.x

28. Emmons CL, Peterson DM, Paul GL (1999) Antioxidant Capacity of Oat (Avena sativa L.) Extracts. 2. In Vitro Antioxidant Activity and Contents of Phenolic and Tocol Antioxidants. J Agric Food Chem 47:4894–4898. https://doi.org/10.1021/jf990530i

29. Miyachi Y, Imamura S, Niwa Y (1987) The effect of tranilast of the generation of reactive oxygen species. J Pharmacobiodyn 10:255–259. https://doi.org/10.1248/bpb1978.10.255

30. Peterson DM, Hahn MJ, Emmons CL (2002) Oat avenanthramides

exhibit antioxidant activities in vitro. Food Chem 79:473–478. https://doi.org/https://doi.org/10.1016/S0308-8146(02)00219-4

31. Li Ji L, Lay D, Chung E, et al (2003) Effects of avenanthramides on oxidant generation and antioxidant enzyme activity in exercised rats. Nutr Res 23:1579–1590. https://doi.org/https://doi.org/10.1016/S0271-5317(03)00165-9

32. Miller HE, Rigelhof F, Marquart L, et al (2000) Antioxidant Content of Whole Grain Breakfast Cereals, Fruits and Vegetables. J Am Coll Nutr 19:312S-319S. https://doi.org/10.1080/07315724.2000.10718966

33. Zhang T, Zhao T, Zhang Y, et al (2020) Avenanthramide supplementation reduces eccentric exercise-induced inflammation in young men and women. J Int Soc Sports Nutr 17:. https://doi.org/10.1186/s12970-020-00368-3

34. Koenig R, Dickman JR, Kang C, et al (2014) Avenanthramide supplementation attenuates exercise-induced inflammation in postmenopausal women. Nutr J 13:21. https://doi.org/10.1186/1475-2891-13-21

35. Hastings J, Kenealey J (2017) Avenanthramide-C reduces the viability of MDA-MB-231 breast cancer cells through an apoptotic mechanism. Cancer Cell Int 17:93. https://doi.org/10.1186/s12935-017-0464-0

36. Nie L, Wise ML, Peterson DM, Meydani M (2006) Avenanthramide, a polyphenol from oats, inhibits vascular smooth muscle cell proliferation and enhances nitric oxide production. Atherosclerosis 186:260–266. https://doi.org/https://doi.org/10.1016/j.atherosclerosis.2005.07.027

37. Scarpa ES, Antonini E, Palma F, et al (2018) Antiproliferative activity of vitexin-2-O-xyloside and avenanthramides on CaCo-2 and HepG2 cancer cells occurs through apoptosis induction and reduction of pro-survival mechanisms. Eur J Nutr 57:1381–1395. https://doi.org/10.1007/s00394-017-1418-y

38. Yonghui YU, Keshan LIU, Jing W Research Progress on Physiological Function of Oat Avenanthramides. J Food Sci Technol 38:21–28

39. Chen C-YO, Milbury PE, Collins FW, Blumberg JB (2007) Avenanthramides Are Bioavailable and Have Antioxidant Activity in Humans after Acute Consumption of an Enriched Mixture from Oats12. J Nutr 137:1375–1382. https://doi.org/https://doi.org/10.1093/jn/137.6.1375

40. Moglia A, Goitre L, Gianoglio S, et al (2015) Evaluation of the bioactive properties of avenanthramide analogs produced in recombinant yeast. BioFactors 41:15–27. https://doi.org/https://doi.org/10.1002/biof.1197

41. Koenig RT, Dickman JR, Wise ML, Ji LL (2011) Avenanthramides Are Bioavailable and Accumulate in Hepatic, Cardiac, and Skeletal Muscle Tissue Following Oral Gavage in Rats. J Agric Food Chem 59:6438–6443. https://doi.org/10.1021/jf2002427

42. Zhang Y, Ni T, Zhang D, et al (2020) Consumption of avenanthramides extracted from oats reduces weight gain, oxidative stress, inflammation and regulates intestinal microflora in high fat diet-induced mice. J Funct Foods 65:103774. https://doi.org/https://doi.org/10.1016/j.jff.2019.103774

43. Xu X, Yang J, Ye Y, et al (2021) SPTBN1 Prevents Primary Osteoporosis by Modulating Osteoblasts Proliferation and Differentiation and Blood Vessels Formation in Bone . Front. Cell Dev. Biol. 9

44. Pellegrini GG, Morales CC, Wallace TC, et al (2016) Avenanthramides Prevent Osteoblast and Osteocyte Apoptosis and Induce Osteoclast Apoptosis in Vitro in an Nrf2-Independent Manner. Nutrients 8:423. https://doi.org/10.3390/nu8070423

45. Çalişkan B, Çalişkan AC (2021) Antioxidant and Oxidative Stress. In: Waisundara V (ed). IntechOpen, Rijeka, p Ch. 6

46. Genestra M (2007) Oxyl radicals, redox-sensitive signalling cascades and antioxidants. Cell Signal 19:1807–1819. https://doi.org/https://doi.org/10.1016/j.cellsig.2007.04.009

47. Nordberg J, Arnér ESJ (2001) Reactive oxygen species, antioxidants, and the mammalian thioredoxin system1 1This review is based on the licentiate thesis “Thioredoxin reductase—interactions with the redox active compounds 1-chloro-2,4-dinitrobenzene and lipoic acid” by Jonas Nordberg,. Free Radic Biol Med 31:1287–1312. https://doi.org/https://doi.org/10.1016/S0891-5849(01)00724-9

48. Valko M, Leibfritz D, Moncol J, et al (2007) Free radicals and antioxidants in normal physiological functions and human disease. Int J Biochem Cell Biol 39:44–84. https://doi.org/https://doi.org/10.1016/j.biocel.2006.07.001

49. Pizzino G, Irrera N, Cucinotta M, et al (2017) Oxidative Stress: Harms and Benefits for Human Health. Oxid Med Cell Longev

2017:8416763. https://doi.org/10.1155/2017/8416763

50. Phaniendra A, Jestadi DB, Periyasamy L (2015) Free Radicals: Properties, Sources, Targets, and Their Implication in Various Diseases. Indian J Clin Biochem 30:11–26. https://doi.org/10.1007/s12291-014-0446-0

51. Kapoor D, Singh S, Kumar V, et al (2019) Antioxidant enzymes regulation in plants in reference to reactive oxygen species (ROS) and reactive nitrogen species (RNS). Plant Gene 19:100182. https://doi.org/https://doi.org/10.1016/j.plgene.2019.100182

52. Turkan I (2018) ROS and RNS: Key signalling molecules in plants. J Exp Bot 69:3313–3315. https://doi.org/10.1093/jxb/ery198

53. Shlapakova T, Kostin R, Tyagunova E (2020) Reactive Oxygen Species: Participation in Cellular Processes and Progression of Pathology. Russ J Bioorganic Chem 46:657–674. https://doi.org/10.1134/S1068162020050222

54. Obeagu E (2018) A Review on Free Radicals and Antioxidants. 4:123–133. https://doi.org/10.22192/ijcrms.2018.04.02.019

55. Giles G, Jacob C (2002) Reactive Sulfur Species: An Emerging Concept in Oxidative Stress. Biol Chem 383:375–388. https://doi.org/10.1515/BC.2002.042

56. Galano A, Raúl Alvarez-Idaboy J (2019) Computational strategies for predicting free radical scavengers' protection against oxidative stress: Where are we and what might follow? Int J Quantum Chem 119:e25665. https://doi.org/https://doi.org/10.1002/qua.25665

57. Ferreira CA, Ni D, Rosenkrans ZT, Cai W (2018) Scavenging of reactive oxygen and nitrogen species with nanomaterials. Nano Res 11:4955–4984. https://doi.org/10.1007/s12274-018-2092-y

58. Xue Y, Teng Y, Chen M, et al (2021) Antioxidant Activity and Mechanism of Avenanthramides: Double H+/e– Processes and Role of the Catechol, Guaiacyl, and Carboxyl Groups. J Agric Food Chem 69:7178–7189. https://doi.org/10.1021/acs.jafc.1c01591

59. Purushothaman A, Jishnu Gopal P, Janardanan D (2022) Mechanistic insights on the radical scavenging activity of oat avenanthramides. J Phys Org Chem 35:e4391. https://doi.org/https://doi.org/10.1002/poc.4391

Chapter 2

Computational Methodology

- ✓ *Describes the various computational methodologies and strategies adopted in this research work.*
- ✓ *Details of various software, computational tools and computer power used for this work.*

2. Computational techniques

2.1. General

The last chapter provided a quick overview of the advancements made thus far in the biological uses of AVs. The specific theoretical techniques used in this thesis to examine the structural, electronic, and antioxidant characteristics of AVs isolated from oats (*Avena Sativa L.*) are described in depth in this chapter.

2.2. Density functional theory (DFT)

For the past 30 years density functional theory has been the dominant method for the quantum mechanical simulation of periodic systems[1]. This is justified based on the pragmatic observation that it is less computationally intensive than other methods with similar accuracy. The premise behind DFT is that the energy of a molecule can be determined from the electron density instead of a wave function[1, 2].

2.2.1. Wave functions versus electron density

Density functional theory is based on electron density function rather than wave function. It is designated as ρ (x, y, z). Herein the electron density is expressed as a linear combination of basis functions. A determinant is formed from these functions and is called as Kohn-Sham orbitals and electron density obtained from the determinant is used to calculate the energy. A density functional is used to calculate energy from this electron density and here the functional (function of a function) is the electron density.

The relationship between wave function and electron density is given as:

$$\rho = \sum_{i=1}^{n} n_i \mid \psi_i \mid^2 \tag{2.1}$$

All properties are computed from the electron density, which becomes more difficult for a multi-electron system. This electron density ρ is the "density" in density functional theory, and it is the foundation not only of DFT but of a complete array of methods for considering and investigating atoms and molecules; unlike the wave function, it is observable, for example, by X-ray or electron diffraction. The benefit of employing electron density is that it is only a function of position and hence can be represented by three variables (x, y, z). The wave function of a 'n' electron system, on the other hand, is a function of 4n variables, three spatial coordinates, and one spin coordinate. Thus, as the complexity of the molecule grows, so does the complexity of the wave function, although electron density remains a function of three electrons. Thus, electron density is observable, intuitively understandable, and mathematically tractable.

2.2.2. Current DFT Methods: The Kohn–Sham Approach

2.2.2.1. The Hohenberg–Kohn Theorems

Currently, DFT calculations on molecules are based on the Kohn-Sham method, which was put in motion by two theorems published by Hohenberg and Kohn in 1964 [3]. The first Hohenberg-Kohn theorem indicates that the ground state electron density function

$\rho_0(x, y, z)$ determines all properties of a molecule in a ground electronic state[4].

$$\rho_o(x, y, z) \rightarrow E_o \tag{2.2}$$

Any ground state attribute of a molecule is a functional of ground state electron density, according to the first Hohenberg-Kohn theorem.

$$E_o = F(\rho_o) = E(\rho_o) \tag{2.3}$$

The second Hohenberg–Kohn theorem asserts that any trial electron density function will produce an energy greater than or equal to true ground state energy[4]. It is given mathematically by

$$E_v[\rho_t] \geq E_o[\rho_o] \tag{2.4}$$

Where ρ_t is a trial electronic density, and $E_0[\rho_0]$ is the true ground state energy, corresponding to the true electronic density ρ_0. The trial density must meet the requirements $\int \rho_t(r)dr = n$, where n is the number of electrons in the molecule and $\rho_t(r) \geq 0$ for all values of r.

2.2.2.2. The Kohn–Sham Energy and the KS Equations

The first Kohn-Sham theorem states that it is worthwhile to seek a method to calculate molecular characteristics from electron density. The second theorem implies that a variational approach may offer a method for calculating energy and electron density[5]. Kohn Sham's approach is based on the two Hohenberg- Kohn theorems. The

two fundamental concepts behind the KS method are 1) molecular energy is expressed as a sum of terms in which a relatively small term involves the unknown functional. Thus, moderately large errors in this term will not introduce large errors in the total energy. 2) An initial guess of the electron density in the KS equation is used to calculate the initial guess of KS orbitals and energy levels[1]. The initial guess is further used to calculate the KS orbitals and energy levels which are used to calculate the electron density and further energy.

1) The Kohn–Sham Energy

The ground state energy of a real molecule can be expressed as a summation of electron kinetic energies, the nucleus-electron attraction potential energies, and the electron-electron repulsion potential energies[1]

$$E_0 = \langle T[\rho_0] \rangle + \langle V_{Ne}[\rho_0] \rangle + \langle V_{ee}[\rho_0] \rangle \quad (2.5)$$

Incorporating the Nucleus-electron potential energy ($\langle V_{Ne}[\rho_0] \rangle$), kinetic energy ($\Delta\langle T[\rho_0] \rangle$) (the deviation of electronic kinetic energy from the reference system, $\Delta\langle T[\rho_0] \rangle \equiv \langle T[\rho_0] \rangle_{rea} - \langle T[\rho_0] \rangle_{ref}$), electronic potential energy ($\Delta\langle V_{ee} \rangle$) as a difference of real electron-electron repulsion energy from the classical charge cloud repulsion energy ($\Delta\langle V_{ee}[\rho_0] \rangle = \langle V_{ee}[\rho_0] \rangle_{rea} - \frac{1}{2\iint \frac{\rho_0(r_1)\rho_0(r_2)}{r_{12}} dr_1 dr_2}$), the KS equation can be expressed as

$$E_0 = \int \rho_0(r) v(r) dr + \langle T[\rho_0] \rangle_{ref} + \frac{1}{2} \iint \frac{\rho_0(r_1)\rho_0(r_2)}{r_{12}} dr_1 dr_2 + \Delta\langle T[\rho_0] \rangle + \Delta\langle V_{ee}[\rho_0] \rangle \quad (2.6)$$

Or (for detailed conversion refer [6])

$$E_0 = -\sum_{\text{nuclei A}} Z_A \int \frac{\rho_0(r_1)}{r1_A} dr_1 - \frac{1}{2} \sum_{i=1}^{2n} \left\langle \psi_1^{KS}(1) \middle| \nabla_1^2 \middle| \psi_1^{KS}(1) \right\rangle + \frac{1}{2} \int \int \frac{\rho_0(r_1)\rho_0(r_2)}{r_{12}} dr_1 dr_2 + E_{XC}[\rho_0]$$

(2.7)

The last two terms of Equation 2.6 are collectively called exchange-correlation energy (E_{XC}), which is the deviation of kinetic energy from a reference system and the deviation of electron-electron repulsion energy from the classical system. This exchange-correlation energy is a functional of the electron density function

$$E_{XC}[\rho_0] \equiv \Delta\langle T[\rho_0] \rangle + \Delta\langle V_{ee}[\rho_0] \rangle \quad (2.8)$$

Developing good exchange-correlation functionals for determining energy from electron density has become the primary focus of DFT research. For this purpose, several methods are used, such as the local density approximation (LDA), the local spin density approximation (LSDA), the generalized gradient approximation (GGA), the meta GGA (MGGA), the hybrid GGA, and so on.

2) The Kohn–Sham Equations

Differentiating the energy about the KS molecular orbitals yields the KS equations. Mathematical representation of Kohn–Sham Equations are given as below

$$\left[-\frac{1}{2}\nabla_i^2 - \sum_{\text{nucei A}} \frac{Z_A}{r_{1A}} + \int \frac{\rho(r_2)}{r_{12}} dr_2 + \nu_{XC}(1) \right] \Psi_i^{KS}(1) = \varepsilon_i^{KS} \psi_i^{KS}(1) \tag{2.9}$$

where ε_i^{KS} are the Kohn–Sham energy levels and $\nu_{XC}(1)$ the exchange-correlation potential, which is a functional derivative of the exchange-correlation energy $E_{XC}(\rho(r))$. The expression in brackets is the Kohn–Sham operator, $\hat{h}^{KS}$

The Kohn–Sham energy Equation 2.9 is exact, only if we know the density function $(\rho_0(r))$ and the functional for the exchange-correlation energy $E_{XC}(\rho(r))$, then it gives exact energy solutions for problems.

a) The local density approximation (LDA)

This method is based on the assumption that at every point in the molecule, energy density has a value equal to that of homogeneous electron gas of the same electron density at that point[6].

b) The Local Spin Density Approximation (LSDA)

The "spin" here means that electrons of opposite spin (α and β) are placed in different Kohn–Sham orbitals (ψ_α^{KS} and ψ_β^{KS}). The LSDA approach extends the LDA method by assigning electrons of α and β spin to different spatial KS orbitals from which different electron density functions ρ^α and ρ^β follow. All the electrons are securely paired; the LSDA is equivalent to the LDA. LSDA has the advantage of being able to handle systems with one or more unpaired electrons.

The geometries, frequencies, and electron-distribution properties tend to be reasonably good under LSDA and poor for the dissociation energies, including atomization energies. A popular LSDA functional was the SVWN (Slater exchange plus Vosko, Wilk, Nusair)[7, 8].

c) Gradient-Corrected Functionals: The Generalized Gradient Approximation (GGA)

Nowadays, most DFT computations use exchange-correlation energy functionals EXC, which use both the electron density and its gradient, the first derivative of ρ concerning location. Then the E_{XC} will be the sum of exchange - energy functional and correlation - energy functional as; $\mathbf{E_{XC} = E_X + E_C}$ Both these values are negative, $|E_X|$ being greater than $|E_C|$. For exchange energy functionals, gradient corrections are therefore more useful. One of the much better functionals for exchange energy is the B88 functionals (Becke 1988)[9]. The known gradient-corrected correlation energy functionals are the P86 (Perdew 1986) and the LYP (Lee-Yang-Parr). All these functionals are used in Gaussian functions to represent KS orbitals.

d) Meta-Generalized Gradient Approximation Functionals (meta-GGA, MGGA)

Functionals that use the second derivative of electron density are called meta-gradient corrected whereas GGA functionals use the first derivative of electron density[10]. This is the Laplacian of the electron density function. While functionals that rely on Laplacian functions provide certain improvements, there are several issues with

them. Some examples are τHCTH (Hamprecht, Cohen, Tozer, Handy) and B98 (Becke 1998).

e) Hybrid GGA (HGGA) Functionals: The Adiabatic Correction Method (ACM)

Hartree-Fock exchange has been added to these functionals. The adiabatic connection method (ACM) provides a rationale for the method and the exchange-correlation energy EXC(r) can be taken as a weighted sum of the DFT exchange-correlation energy and HF exchange energy[11]. The Hybrid functionals are functionals that contain HF exchange, the correction energy to the classical coulomb repulsion. B3LYP was the first hybrid method which is the Exchange energy functional developed by Becke in 1993 and includes LYP correlation energy functional is one of the common functionals used in DFT[12].

f) Hybrid Meta-GGA (HMGGA) Functionals

These are the highest-level functionals in routine use which include the first derivative of electron density and its second derivative, or the kinetic energy density, and Hartree–Fock exchange[13].

g) Fully Nonlocal Theory

Non-local functionals have been in research for many years[13]. Fully non-local theories are those in which all properties are considered non-locally.

2.3. Basis sets

The basis set is a collection of wavefunctions that characterize the properties of atomic orbitals. Then molecular orbitals are computed using a theoretical model by linear combination of atomic orbitals (LCAO). Although not all theoretical models require the specification of a basis set, ab initio and density functional theory do. The level of approximation employed in a particular computation is determined by the type of the specified basis set. The choice of which also influences the correctness of the outcome and the CPU execution time[14, 15].

Mathematical expression for atomic orbitals is given by the expression

$$\psi_i = \Sigma_i C_{\mu i} \phi_\mu \qquad (2.10)$$

where ψ_i are the i^{th} molecular orbital, $C_{\mu i}$ the coefficients of linear combination, and ϕ_μ μ^{th} the atomic orbital.

Both Slater-type orbitals (STOs)[16] and Gaussian-type orbitals (GTOs) [17] are used to represent atomic orbitals. Even though STOs describe the atomic orbital more accurately, GTOs are more typically utilized because they are considerably easier and faster to compute. It takes less time to compute a large number of GTOs and combine them to represent an atomic orbital than it does to compute a single STO. As a result, GTO combinations are used to define STOs, which in turn characterize atomic orbitals. Semi-empirical calculations use Slater type orbitals and ab initio calculations use Gaussian type

orbitals. The mathematical function used to represent Slater-type orbitals and Gaussian-type orbitals respectively are given in Equations 2.11 & 2.12

$$S^{\zeta}_{nlm}(r,\theta,\phi) = Nr^{n-1}e^{-\zeta r}Y^{m}_{l}(\theta,\phi) \tag{2.11}$$

$$G^{\zeta}{}_{nlm}(r,\theta,\phi) = Nr^{n-1}e^{-\zeta r^{2}}Y^{m}_{l}(\theta,\phi) \tag{2.12}$$

where Y^{m}_{l} are the spherical harmonic functions where the subscript indicates the orbital angular momentum and magnetic quantum number dependence, N is the normalization constant, ζ is the orbital exponent, and r, θ, and Φ represent the polar coordinates. Herein, Gaussian-type functions differ from Slater functions in the exponential part where the former involves the square of the radius (r^2). STOs, represent 'real' atomic functions better than GTOs and can represent electron density in valence regions and beyond almost well but are not good for core electron density. Single GTO gives a poor representation of the approximation of the basis set, thereby providing less accurate results. This issue is solved by combining GTOs to approximate an STO function. This combined function is referred to as contracted GTOs (CGTOs), while the individual GTOs in the combination are referred to as primitive GTOs (PGTOs). Such basis sets are commonly referred to as STO-nG type basis sets, where n is the number of Gaussian primitives used to describe a certain STO. Based on the size and complexity, basis sets can be classed as minimal or extended basis sets. The simplest basis sets are minimal basis sets, i.e. the minimum number of functions used to describe the electrons of

a neutral atom determines the contents of the minimum basis set. The same number of PGTOs are used for both core and valence orbitals with a single basis function. In the extended basis set, a detailed analysis of each atomic orbitals can be obtained as they consist of more than one basis function characterized by its coefficient, which allows a better description of the electron distribution. The split valence, polarized, diffuse, correlation consistent sets, etc. are the several types of extended basis sets.

A basic description of the many types of extended basis sets is as follows; two basis functions per atomic orbital are applied for a double zeta (DZ) basis set (zeta (ζ) derived from the exponent of the STO basis function). The double zeta basis includes two s-functions for hydrogen (1s and 1s') and four for helium (1s, 1s', 2s and 2s'). Triple Zeta (TZ) basis functions are the next improvement to DZ, in which the basis set contains three basis functions to define an orbital i.e., six s-functions and three p- 11 functions for the first row elements. Quadruple Zeta (QZ) and Quintuple zeta (5Z) are the further extensions of the DZ and DunningHuzinaga (D95), cc-pVDZ, and cc-pVTZ are examples of such a basis set. Split valence basis sets allow specifying the number of GTOs to be used to describe the core and valence electrons separately[18]. These are either double Zeta or triple Zeta. These are represented as K-LMG, where, K = number of sp-type inner shell GTOs, L = number of inner valence s- and p-type GTOs, M = number of outer valence s- and p-type GTOs G = indicates that GTOs are used. For example 3-21G: 3 GTOs for inner shell, 2 GTOs for inner valence, and 1 GTO for outer valence. Other examples of

split valence basis sets are 6-31G[19] and 6-311G[20], which correspond to the double and triplet zeta basis sets. The basis set can be further improved by adding polarisation functions and diffuse functions. In the case of molecules containing heavier atoms, the presence of more atoms alters the environment around each atom, causing an electronic cloud deformation known as polarization. Because polarisation removes the spherical symmetry of the atomic orbitals larger angular momentum functions are required to allow this. With the addition of the polarisation function, molecular orbitals can be more asymmetric about the nucleus, allowing for greater flexibility within the basis set. Polarisation can be induced by adding a p-function to H. Similarly, adding a d-function to a basis set containing p-valence orbitals and f-functions for d-valence orbitals causes polarization. In the 6-31G (p) or 6-31G* basis set, the asterisk indicates polarization of the non-hydrogen atoms introducing p-orbital to the heavier atoms. For a hydrogen atom with a 6-31G basis set, both p and d polarisation functions can be added for more exact results, denoted by two asterisks (**) and denoted as 6-31G(p d) or 6-31g**. When studying systems involving heteroatoms, anions, lone pairs, and weak bonds where the electrons are relatively loosely held, to simulate well the behavior of these "expanded" electron clouds, diffuse functions are used. They are represented with a plus '+' sign. A single ‘+’ denotes diffuse functions added on to atoms other than Hydrogens and ‘++’ denotes diffuse functions added on to all atoms.

More recent surveys oriented toward the quality of molecular properties from DFT especially in the field of natural products. DFT

advancements have progressed to the point where they can be used to supplement experimental results and, in some cases, anticipate experimentally unknown terrain. DFT appears to be highly dependable in terms of geometry and quite good in terms of predicting a variety of molecular and spectroscopic properties[6]. Hence we used density functional theory to explore reactivity of AVs. In the process of computational investigation of AVs molecules attempted in this thesis, we have adopted several methodologies. These methodologies and the different software employed to carry out different works are briefly outlined in the below sections.

2.4. Theoretical and methodological overview

2.4.1. Potential Energy Surface

The potential energy surface (PES) provides a relationship between the energy of a molecule and its geometry. A PES can provide a complete description of different conformers, isomers, and energetically accessible motions of a molecule. The minima on the surface provide the optimized geometries and the lowest-energy minimum is called the global minimum. The local minima in the plot correspond to the higher-energy conformers or isomers of the molecule. A saddle point on this surface represents the transition structure between the reactants and products of a reaction. Computing a complete PES for a molecule with N atoms requires computing energies for geometries on a grid of points in 3N-6 dimensional space. Gradient is a vector constituted by 3N-6 first partial derivatives of energy concerning the variables on which energy is dependent and

stationary points are points on the PES where the gradient is zero. The saddle point, local minima, and global minima are three types of stationary points in the PES as discussed above.

The potential energy scan of a molecule starts with an initial structure at a given level of theory. Then, it proceeds through structures created by altering the specified variables like dihedral angle, bond length, etc. After the process, a plot of potential energy versus variable was obtained. From the obtained two-dimensional or three-dimensional graph, the structure corresponding to global minima can be nominated for further geometrical optimization [1, 2].

2.4.2. Geometry optimization

Geometry optimization is the name of the procedure that attempts to find the minimum energy configuration of a molecule or it is the energy minimization of the systems by changing the geometry[1, 2]. This is accomplished by characterizing a stationary point on a PES which might be a minimum energy point, a transition state, or, occasionally, a higher-order saddle point. The energy minimization is done by starting with the guess of the molecular geometry which is close to the desired stationary point to the computer algorithm which then systematically changes the geometry to achieve the best-minimized geometry by varying the positions of the atoms in such a way that the energy decreases[11]. Once the chosen stationary point has been optimized, it is necessary to determine if the resulting geometry is a minimum or a saddle point. This is accomplished by computing the normal mode of vibrations, which are the most basic

vibrations that a molecule can exhibit. All of the normal mode force constants in a structure that is a real minimum should be positive. For a transition state vibration force constant will be negative and the vibrational frequency (square root of force constant) will be imaginary and for an *n*-th order saddle point will have 'n' negative force constant or imaginary frequencies.

2.4.3. Nuclear magnetic resonance (NMR) spectra

The NMR spectroscopic techniques are outstanding tools for the structural elucidation of organic molecules, and they arise when an atomic nucleus in a magnetic field transitions from a low-energy to a high-energy state. The quantum-mechanical calculation of NMR spectra has two aspects; calculation of shielding (chemical shifts) and calculation of splitting (coupling constants) and most of the calculations focussed on shielding of a nucleus. The magnetic shielding of the nuclei of the molecule is usually referenced with a standard reference molecule, normally tetramethylsilane (TMS). These shielding tensors are then converted to chemical shifts using the equation 2.13,

$$\delta_i = \sigma_{TMS} - \sigma_i \tag{2.13}$$

Theoretically, there are several methods to calculate the chemical shift of magnetically active nuclei; IGLO (individual gauge localized orbital), LORG (localized or Loacaorbital origin)[21], and GIAO (gauge independent or invariant or including atomic orbital)[22]. The GIAO method was combined with DFT by Friedrich et al.[23] and DFT/GIAO is known to satisfactorily calculate the NMR

spectra of organic molecules[22]. Here both the ^{1}HNMR and ^{13}CNMR were recorded using DFT/GIAO formalism and recorded the chemical shift values of each about TMS.

2.4.4. Time-dependent density functional theory (TD-DFT)

DFT is useful for studying the ground state properties of the electrons, while it is inadequate for excited state properties. TDDFT is a modified version of DFT incorporating the time-dependent external potentials and can be used to study the excited states as the processes describing photon-electron interactions are time-dependent[24, 25]. As the basic theory of DFT is the Hohenberg-Korn theorem, the fundamental theory of TDDFT is the Runge-Gross (RG) theorem[25]. In circumstances of one-to-one correspondence of time-dependent density n(r, t) and time-dependent potential υ_{ext} (r, t) for a given initial state on a system of non-interacting electrons, a time-dependent Kohn-Sham scheme is created which obeys time-dependent Schrödinger equation. Like DFT, the time-dependent Hamiltonian includes the kinetic and time-dependent potential operators T and $\hat{V}(t)$, respectively. Time-dependent Kohn-Sham equations were constructed to calculate the system's kinetic energy and electron density accurately. Here the non-interacting electrons occupy Kohn-Sham orbitals φi and the fictitious Kohn-Sham system provided electron density equivalent to that of a "real" system of interacting electrons

$$n(r,t) = \sum_{i}^{occ} \left|\Phi_i(r,t)\right|^2 \tag{2.14}$$

The electrons in the fictitious time-dependent system move in an external Kohn-Sham potential, ν_{KS} and it will be the sum of external, the electrostatic Hartree (Equation 2.16), and exchange potentials (Equation2.17) as given in equations 2.15,

$$\nu_{KS}(r,t) = \nu_{ext}(r,t) + \nu_{HARTEE}(r,t) + \nu_{XC}(r,t) \tag{2.15}$$

$$\nu_{HARTEE}(r,t) = \int d^3r' \frac{n(r,t)}{r - r'} \tag{2.16}$$

$$\nu_{XC}(r,t) = \left.\frac{\delta \tilde{A}_{XC}}{\delta(r,\tau)}\right|_{n(r,t)} \tag{2.17}$$

The ν_{XC} is obtained by using the exchange-correlation component of the action potential Axc and the pseudo time τ, functional must be used to approximate vxc, whose value is unknown Like the time-independent Kohn-Sham equations.

2.4.4.1. Analysis of one electron excitation characteristics using electron-hole concepts

The electronic properties of the molecules including excitation and de-excitation can be done theoretically through the TD-DFT method. The process of single-electron excitation can be described as "an electron leaves a hole and goes to an electron", it is a very powerful and practical set of methods to explore the characteristics of electron excitation. It describes the electron excitation as "hole to electron" so that it examines the distribution of "holes" as to where the electron goes from and the distribution of "electrons" as to where the

electron being excited goes [26, 27]. If an excitation can be properly described as a HOMO to LUMO transition, then the hole and electron can be represented by HOMO and LUMO, respectively. This method will be helpful in situations where the absence of dominant MO pairs is suitable to represent a transition even in NTOs.

The electron excitation can be local excitation (LE) a charge transfer excitation (CT) or a Rydberg excitation (R). The hole and electron occupy similar spatial regions in Local excitation (LE) and in Charge-transfer excitation (CT), the spatial separation of hole and electron is large, leading to the evident displacement of charge density. Whereas, in Rydberg excitation, the electron mainly consists of very diffuse MOs, therefore the overlap between electron and hole must be small. In general Rydberg type of excitation does not lead to prominent long-range displacement of charge density. In support of the program Multiwfn, a detailed hole-electron analysis was carried out in TDDFT calculation. For this purpose, the distance between the centroid of the hole and electron or charge transfer length (D), the overlapping extent of hole and electron (Sr), the average degree of the spatial extension of the hole and electron distribution (H), separation degree of hole and electron (t), and the coulomb attractive energy (Ecoul) are fetched from hole electron analysis and included in the discussions electron transfer processes.

The excited state wave function for TD-DFT calculations is [28],

$$\Psi^{exc} = \sum_{i\to a} w_i^a \Phi_i^a + \sum_{i\leftarrow a} w_i^{'a} \Phi_i^a \qquad (2.18)$$

Where w and w' are the configuration coefficients for excitation and de-excitation, respectively. The first term in equation 2.18 is for excitation and the second term is for de-excitation. Φ_i^a is the configuration state wave function when moving an electron from originally occupied MOi to virtual MO a.

The density distribution of hole and electron can be represented as

$$\rho^{hole}(r) = \rho_{loc}^{hole}(r) + \rho_{cross}^{hole}(r) = \sum_{i\to a}(w_i^a)^2\varphi_i(r)\varphi_i(r) + \sum_{i\to a}\sum_{j\neq i\to a} w_i^a w_j^a \varphi_i(r)\varphi_j(r)$$

(2.19)

$$\rho^{ele}(r) = \rho_{loc}^{ele}(r) + \rho_{cross}^{ele}(r) = \sum_{i\to a}(w_i^a)^2\varphi_a(r)\varphi_a(r) + \sum_{i\to a}\sum_{i\to b\neq a} w_i^a w_j^b \varphi_a(r)\varphi_b(r)$$

(2.20)

Where φ denote MO wavefunction and loc and cross are the contributions of local and cross terms to hole and electron distribution. All functions of electron excitations are calculated based on equation 2.19 & 2.20.

Sr index is used to define the overlapping extent of hole and electron

$$S_r index = \int \sqrt{\rho^{hole}(r)\rho^{ele}(r)}dr \qquad (2.21)$$

D index reveals the distance between the centroid of the hole and the electron or charge transfer length can be represented as

$$D_{index} = |D| = \sqrt{(D_x)^2 + (D_y)^2 + (D_z)^2} \qquad (2.22)$$

Where X, Y, Z are coordinates and Dx=$|X_{ele} - X_{hole}|$ and for X coordinate of the centroid, $X_{ele}=\int x.\rho^{ele}(r))dr$ where x is the X component of position vector r.

$$H_{index} = \frac{|\sigma_{ele}| + |\sigma_{hole}|}{2} \tag{2.23}$$

where, $\sigma_{hole,X} = \sqrt{\int (x - X_{hole})^2 \rho^{hole}(r)dr}$ for X component. The $|\sigma_{hole}|$ are referred to as σ_{hole} measures overall RMSD of the hole. Same for electron representation.

The measure of separation of the degree of hole and electron in the CT direction is called the t index. When t<0 the hole and electron separation are not adequate.

$$t_{index} = D_{index} - H_{CT} \tag{2.24}$$

Coulomb attraction between hole and electron (exciton binding energy) considers the electron as negative charge and the hole as a positive charge, the attractive interaction between them is the coulomb attractive energy between hole and electron and its negative values is called exciton binding energy (positive). This can be calculated by using the formula[29],

$$E_c = \iint \frac{\rho^{hole}(r_1)\rho^{ele}(r_2)}{|r_1 - r_2|} dr_1 dr_2 \tag{2.25}$$

2.4.4.2. Transition density matrix and transition density T(r)

The Transition density matrix and transition density T(r) is a real space function that provides underlying characteristics of electron excitation. The transition density matrix between excited state and ground state of an N-electron system in real space

$$T(r;r') = T(r_1;r'_1) = \int \Phi^0(X_1, X_2, X_3 \ldots\ldots\ldots X_N)\psi^{exc}(X_1', X_2', X_3' \ldots\ldots\ldots X_N')d\sigma_1 dX_2 dX_3 \ldots\ldots dX_N \quad (2.26)$$

where Φ^0 is the Slater-determinant of the ground state wave function, x is the spin-space coordinate, and σ stands for spin coordinate. Equation 2.26 can be modified as equation 2.27 by applying ψ^{exc} and Slater-Condon rule.

$$T(r;r') = \sum_i \sum_a w_i^a \phi_i(r)\phi_a(r') \quad (2.27)$$

$T(r;r')$ is changed to $T(r)$, when diagonal terms of the transition density matrix are considered. In a region with a large magnitude of transition density T(r), the hole and electron must be strongly coupled in this region; while if a region has a small distribution of T(r), then overlap between hole and electron in this area are irrelevant. The characteristics of T(r) are closely related to the Sr(r) function. Hence the characteristics of one electron transitions of relevant excited state were analyzed with the parameters of electron–hole concept and correlated with TDDFT studies.

2.4.4.3. Transition electric/magnetic dipole moment density

The decomposition of electromagnetic response in interaction with light and the compound of the investigation was analyzed based on chiral analysis theory by separating the electric and magnetic dipole moments during the electromagnetic interactions. The ECD spectrum, which represents the chiral of molecules, is the asymmetric response of the transition magnetic and electric dipole moments[30]. Besides, the strength of ECD can be expressed by a formula[31]

$$I \propto \langle \varphi_j | \mu_e | \varphi_i \rangle \langle \varphi_j | \mu_m | \varphi_i B \rangle \tag{2.28}$$

where μe is the transition electric dipole moment and μm is the transition magnetic dipole moment. In equation 2.28, the first term in the absolute value is light absorption, and the second term characterizes circular dichroism. The second largest element in this equation is the tensor product of the transition magnetic and electric dipole moments.

The transition electric dipole moment density in X, Y, and Z components can be represented as negative of the product of X, Y, and Z coordinate variables and transition density, respectively (Equation 2.29).

$$T_x(r) = -xT(r) \quad T_y(r) = -yT(r) \quad T_z(r) = -zT(r) \tag{2.29}$$

The transition electric dipole moment density and transition dipole moment D are related (Equation 2.30),

$$D_x = \int T_x(r)dr \quad D_y = \int T_y(r)dr \quad D_z = \int T_z(r)dr \tag{2.30}$$

The study of the contribution to the transition electric dipole moment of various molecular regions will be possible by plotting the transition electric dipole moment density. The X component of transition magnetic dipole moment density can be explicitly defined as

$$m_x(r) = \sum_{i\to a} w_i^a \varphi_i(r)\left[y\frac{\partial \varphi_a}{\partial z}(r) - z\frac{\partial \varphi_a}{\partial y}(r)\right] - \sum_{j\leftarrow b} w_j^b \varphi_j(r)\left[y\frac{\partial \varphi_b}{\partial z}(r) - z\frac{\partial \varphi_b}{\partial y}(r)\right] \tag{2.31}$$

2.4.5. Quantum Theory of Atoms in Molecules (QTAIM)

Bader's Quantum Theory of Atoms in Molecules (QTAIM) is used to study the nature of bonding in molecular systems by exploiting the charge density or electron density of molecules ρ(r; X) (Equation 2.32)[32]. This theory has been widely applied to unravel atom-atom interactions in covalent and non-covalent interactions in molecules, molecular clusters, small molecular crystals, proteins, DNA base pairing, and stacking.

$$\rho(r;X) = N\int d\tau' \psi^*(x;X)\psi(x;X) \tag{2.32}$$

where N is the no. of electrons, x is the electronic coordinates, X is the nuclear coordinates and dτ' represents the volume element of the system under consideration

In topology analysis language, the point where the first derivatives of $\rho(r_c)$ vanish, i.e., $\nabla\rho(r_c) = 0$ is called the critical point (CP). Where $\nabla\rho(r_c)$ is given in Equation 2.33 and r_c is the critical point

$$\nabla\rho(r_c) = i\frac{\partial\rho}{\partial x} + j\frac{\partial\rho}{\partial y} + k\frac{\partial\rho}{\partial z} \tag{2.33}$$

The CPs can be classified into four types; (3, −3), (3, −1), (3, +1), and (3, +3), according to how many eigenvalues of the Hessian matrix of real space function are negative. The first number in the bracket of CP notation is designated as the number of non-zero eigenvalues (non-zero curvatures of $\rho(r_c)$ at the CPs) and the second is the algebraic sum of the signs of eigenvalues (signs of curvatures of $\rho(r_c)$ at the CPs), i.e. first one rank and second is the signature of CP. For (3,-3), all three eigenvalues of the Hessian matrix of function are negative, and electron density ρ is the local maximum at r_c and these are called nuclear critical points (NCP). A hessian matrix is the nine second-order derivatives of electron density represented in the form of a real and symmetric matrix. For (3, −1), Two eigenvalues of the Hessian matrix of function are negative, namely the second-order saddle point, and generally appear between attractive atomic pairs in electron density analysis. This is called a bond critical point (BCP) and its value of real space functions at BCP have great significance. The value of ρ and the sign of $\nabla^2\rho$ at BCP is closely related to bonding strength and bonding type. It is used to define the hydrogen bond binding energies. In the case of (3, +1), only one eigenvalue of the Hessian matrix of function is negative. It is the first-order saddle point-like transition state in the potential energy surface. It appears in the center of the ring system and displays a steric effect in the electron density analysis. Hence it is called ring critical point (RCP). None of the eigenvalues of the Hessian matrix of function are negative (local

minima) in (3, +3), and appear in the center of the cage system, hence the cage critical point (CCP).

2.4.5.1. Laplacian of electron density ($\nabla^2\rho$)

It is very useful for the characterization of chemical bonding. The $\nabla^2\rho(r_c) < 0$, the negative value of second-order electron density indicates the concentration of charge towards the interaction line leads to contraction of $\rho(r_c)$ perpendicular to the interaction line and lowers the potential energy. An attractive interaction due to the lowering of the potential energy is greater than the kinetic energy from the same region by magnitude. The $\nabla^2\rho(r_c) > 0$, the interaction is dominated by the contraction of ρ(rc) towards each nucleus, then the parallel gradient and the curvature of $\rho(r_c)$ are large, and net forces of repulsion act on the nuclei.

The high value of the electron density at BCP of order $>10^{-1}$ a.u. and negative value of $\nabla^2\rho(r_c)$ and critical for the covalent interactions. The negative value of $\nabla^2\rho(r_c)$ implies that there is a concentration of electrical charge at the BCP, indicating that the bond is covalent.

Herein, we used the QTAIM investigation to identify the intramolecular hydrogen bond and other non-covalent interactions in the molecules by analyzing electron density $\rho(r)$ and its Laplacian $\nabla^2\rho(r)$ at the bond critical points (BCP). For this purpose, we utilized the 'AIM All' program in the multiwfn 3.8 suite[33]. In addition to the ρ and $\nabla^2\rho$, the Lagrangian kinetic electron density (g) and the potential electron density (v) were analyzed. From these, the total energy

density (H) was estimated as the sum of the kinetic electron density (g) and potential energy density (v). The $g(r)$ is the kinetic energy density at the BCP (always positive), while v(r) is the potential energy density at the BCP (always negative). The hydrogen bond energy (E_{HB}) is half of V_{BCP} as suggested by Espinosa et al[34]. The Nature of hydrogen bond were explored according to literature, i) values of $\nabla^2\rho(r) < 0$, and $g(r)+v(r) > 0$ are associated with strong hydrogen bond (ii) values of $\nabla^2\rho(r) > 0$, and $g(r)+v(r) < 0$ signify intermediate type hydrogen bonds (iii) values of $\nabla^2\rho(r) > 0$, and $g(r)+v(r) > 0$ are associated weak hydrogen bond interactions[35].

The visual inspections of non-covalent interactions (NCI) were carried out using the reduced density gradient (RDG) obtained from the quantum-mechanical electron density[36]. The regions of van der Waals interactions, hydrogen bonds, and steric clashes, regions were identified.

2.4.6. Aromaticity index

The aromaticity of each benzene ring in the AVs was calculated using three models; harmonic oscillator measure of aromaticity (HOMA), Aromatic fluctuation index (FLU), and Para-delocalization index (PDI). The major piece of the work deals with the antiradical property of the molecules, hence analyzing the aromaticity, especially for para-substituted polyphenolic compounds produces crucial information as also reported in the literature. The bridging of the phenolic group in para-position due to better overlapping of the

substituent orbital with the aromatic system can increase the reactivity of phenol.

The harmonic oscillator measure of aromaticity (HOMA) is the popular geometry-based index for the calculation of aromaticity, which was originally proposed by J. Kruszewski et.al [37] and the generalized representation was given by Tadeusz Marek Krygowski [38]

$$HOMA = 1 - \sum_i \frac{\alpha_{i,j}}{N} (R_{ref} - R_{i,j})^2 \tag{2.34}$$

where N is the total number of the atoms considered, j is the atom next to atom i, and α (Equation 2.36) and R_{Ref} (Equation 2.35) are pre-calculated constants for each type of atomic pair.

$$R_{ref} = (R_s + wR_d) / (1 + w) \tag{2.35}$$

$$\alpha = \frac{2}{(R_s - R_{ref})^2 + (R_d - R_{ref})^2} \tag{2.36}$$

where Rs and Rd, respectively are experimental bond lengths of a single bond and double bond. The $w=k_d/k_s$, where k_s and k_d are force constants of single and double bonds, respectively. If the system is fully aromatic then the value of HOMA is equal to 1 and nonaromatic if it is zero.

The aromatic fluctuation index (FLU) calculates the aromaticity index based on the delocalization index[39] and it can be used to study rings with any number of atoms. The FLU index was

constructed by measuring divergences (DI differences for each single pair bonded) from aromatic molecules chosen as a reference and it can be represented as

$$FLU = \frac{1}{n}\sum_{A-B}^{ring}\left[\left(\frac{V(B)}{V(A)}\right)^{\alpha}\left(\frac{\delta(A,B)-\delta_{ref}(A,B)}{\delta_{ref}(A,B)}\right)\right]^{2} \tag{2.37}$$

Here the summation runs over all adjacent pairs of atoms around the ring. The n is equal to the number of atoms in the ring; δref is the reference DI value (precalculated parameter). The parameter α is used to ensure the ratio of atomic valences is greater than one. The first factor in Equation 2.37 penalizes those with highly localized electrons, while the second factor measures the relative divergence concerning a typical aromatic system. The lower value of r FLU corresponds to the stronger aromaticity of the ring.

The aromaticity of six-membered rings is measured using the Para-delocalization index (PDI)[40, 41]. It is the averaged para-delocalization index (para-DI) in six-membered rings and can be represented as

$$PDI = \frac{\delta(1,4)+\delta(2,5)+\delta(3,6)}{3} \tag{2.38}$$

The underlying notion behind PDI is that Bader and colleagues discovered that DI in benzene is higher for para-related carbon atoms than for meta-related carbon atoms. So, the larger the PDI, the larger the delocalization, and the stronger the aromaticity. The major limitations regarding the method are 1) it can only be used to study the

aromaticity of six-membered rings, and 2) inappropriate for the cases when the ring plane has an out-plane distortion.

2.4.7. Solvent effects

Significant scientific efforts have been committed in recent years to developing models for researching the solvation effects and it can be incorporated in two different methods: explicit and implicit models[42]. The explicit solvent model treats solvents explicitly where the solute is surrounded by several discrete solvent molecules and it considers the molecular details of each solvent molecule [42]. This method can provide solute-solvent interactions in great depth and accuracy; however, it is computationally expensive. The easiest technique to include solvent effects in chemical processes is to explicitly enter all of the solvent molecules and then conduct molecular dynamics or Monte Carlo calculations to obtain a time-averaged ensemble average of the property of interest[43]. Implicit (continuum) solvation is a technique for representing a solvent as a continuous medium (solvent molecules are replaced by a homogeneously polarizable medium) rather than as separate "explicit" solvent molecules.

2.4.7.1. Implicit Solvent Models

Several implicit or solvation models are already available to incorporate the influence of solvents and this is the simplified solvent model[44]. The solvent is viewed as a structureless continuum with certain dielectric and interfacial properties in the majority of implicit solvent models[42]. Continuum solvation places the solute molecule in

a cavity in a continuous medium which simulates the sea of solvent molecules with the cost of cavitation energy, ΔG_{cav}, due to removed solvent–solvent interactions[45]. Through both electrostatic and non-electrostatic interactions, the solute inside the cavity interacts with the polarizable medium. The total solvation energy can be taken as

$$\Delta G_{solvation} = \Delta G_{Elec} + \Delta G_{cav} + \Delta G_{Nonelec} \tag{2.39}$$

ΔG_{Elec} is the electrostatic contribution which includes attractive terms and the energetic cost of polarizing the solute and solvent, $\Delta G_{Nonelec}$ is the non-electrostatic contribution to the solvation energy like dispersion, and ΔG_{cav} is the cavitation energy. Among various solvation models, the current study included the Integral equation formalism polarizable continuum model (IEF-PCM).

2.4.8. Rate constant calculation

In the thermodynamic formulation of the Transition State Theory (TST), the rate constants (k) were calculated with the following equation (Equation 2.40) as implemented in the KiSThelP 2019 program[46].

$$k^{TST}(T) = \sigma \frac{k_B T}{h} \left(\frac{RT}{P^0} \right)^{\Delta n} e^{-\frac{\Delta G^{\neq}(T)}{k_B(T)}} \tag{2.40}$$

where σ and k_B are the reaction path degeneracy and Boltzmann's constant respectively, h is Planck's constant, and T and P^0 are the temperature (298.15 K) and pressure (1 atm) respectively. The

$\Delta G^{\neq}(T)$ y speak for the standard Gibbs free energy of activation for the considered reaction and Δn = 1 or 0 respectively, for bimolecular or unimolecular reactions. Additionally, the intrinsic reaction coordinate (IRC) computations were performed to verify the transition state's relationship to the right minima.

2.5. Softwares

2.5.1. Computational software

a) Gaussian 16

In the current study, the version of Gaussian software used is Gaussian 16[47]. The Gaussian software helps us to do electronic-structure calculations and quantum chemical calculations. The spectra calculations, thermodynamics, and kinetics of the free radical scavenging mechanism and reactive species screening have been carried out using the software. Also utilized to study the ground state and excited state properties of the molecules.

b) Multiwfn – A Multifunctional Wavefunction Analyzer - Version 3.8

Multiwfn is a multifunctional program for wave function-based analysis[33]. The analyses such as Electrostatic Potential, Fukui functions, spin density, hole-electron analysis, aromaticity index calculation, QTAIM investigations, conceptual density functional theory-based reactivity parameters, Transition electric/magnetic dipole

moment density, Transition density matrix and transition density, etc, were finished by the software.

c) KiSThelP- Kinetic and Statistical Thermodynamical Package

It is a cross-platform free open-source program used to calculate the molecular thermodynamic properties and transition state theory rate coefficient[46].

d) Open Babel

Open Babel is an open software that helps with file type conversion, which allows one to search, analyze, or convert data for research[48].

2.5.2. Visualization software

a) GaussView 6.1

GaussView is a graphical user interface designed to prepare input structures for submission to Gaussian software and helped to examine the results of Gaussian calculations using a variety of graphical techniques[49]. The current work has a heavy dependence on GaussView for preparing input files to analyze output structures.

b) Chemcraft

Chemcraft is a graphical program for working with quantum chemistry computations and is a convenient tool for visualizing computed results and preparing new jobs for calculation[50]. In the

current work, the software is utilised for creating some publication-ready images of molecules in customizable display modes.

c) Visual Molecular Dynamics (VMD) Program-Version 1.9.1

VMD is a molecular visualization program for displaying, animating, and analyzing molecular structures using 3-D graphics[51]. In the work, the program was utilized to visualize the isosurface diagrams of spin density, Fukui functions, and transition dipole moment density matrix.

d) Gnuplot-Version 5. 4

The gnuplot is a command-line and graphical user interface program that can generate two- and three-dimensional plots of functions, data, and data fits[52]. The program was utilized to get the colored 2-D images of the reduced density gradient versus the electron density multiplied by the sign of the second Hessian eigenvalue of studied compounds.

2.6. Computer Power

All the calculations included in this thesis are performed using 1) Lenovo Thinkstation with processor Intel®Xeon®CPU E5-2660 v3 @2.60 GHz and 32.0 GB RAM, 2)FUJITSU with processor Intel®Xeon®CPU E5-2640 v4 @2.40 GHz and 32.0 GB RAM.

References

1. Lewars EG (2007) Computational Chemistry, Introduction to the Theory and Applications of Molecular and Quantum Mechanics, 3rd ed. Springer Dordrecht Heidelberg London New York

2. Young DC (2001) Computational Chemistry: A Practical Guide for Applying Techniques to Real World Problems. John Wiley & Sons, Inc

3. Hinde RJ (2000) Quantum Chemistry, 5th Edition (by Ira N. Levine). J Chem Educ 77:1564. https://doi.org/10.1021/ed077p1564

4. Hohenberg P, Kohn W (1964) Inhomogeneous Electron Gas. Phys Rev 136:B864–B871. https://doi.org/10.1103/PhysRev.136.B864

5. Kohn W, Sham LJ (1965) Self-Consistent Equations Including Exchange and Correlation Effects. Phys Rev 140:A1133–A1138. https://doi.org/10.1103/PhysRev.140.A1133

6. Lewars EG (2011) Computational Chemistry: Introduction to the Theory and Applications of Molecular and Quantum Mechanics, 2nd Editio. Springer, New York

7. Perdew JP, Burke K, Ernzerhof M (1997) Generalized Gradient Approximation Made Simple [Phys. Rev. Lett. 77, 3865 (1996)]. Phys Rev Lett 78:1396. https://doi.org/10.1103/PhysRevLett.78.1396

8. Perdew JP, Burke K, Ernzerhof M (1996) Generalized Gradient Approximation Made Simple. Phys Rev Lett 77:3865–3868. https://doi.org/10.1103/PhysRevLett.77.3865

9. Perdew JP, Schmidt K (2001) Jacob's ladder of density functional approximations for the exchange-correlation energy. In: Density Functional Theory and its Application to Materials. AA(Tulane University, Louisiana), AB(Tulane University, Louisiana), pp 1–20

10. Kurth S, Perdew JP, Blaha P (1999) Molecular and solid-state tests of density functional approximations: LSD, GGAs, and meta-GGAs. Int J Quantum Chem 75:889–909. https://doi.org/https://doi.org/10.1002/(SICI)1097-461X(1999)75:4/5<889::AID-QUA54>3.0.CO;2-8

11. Cramer C (2004) Essentials of Computational Chemistry

12. Becke AD (1993) Density-functional thermochemistry. III. The role of exact exchange. J Chem Phys 98:5648–5652. https://doi.org/10.1063/1.464913

13. Sousa SF, Fernandes PA, Ramos MJ (2007) General Performance of Density Functionals. J Phys Chem A 111:10439–10452. https://doi.org/10.1021/jp0734474

14. scholar (2)

15. Wiberg KB (1986) Ab Initio Molecular Orbital Theory by W. J. Hehre, L. Radom, P. v. R. Schleyer, and J. A. Pople, John Wiley, New York, 548pp. Price: $79.95 (1986). J Comput Chem 7:379. https://doi.org/https://doi.org/10.1002/jcc.540070314

16. Slater JC (1930) Atomic Shielding Constants. Phys Rev 36:57–64. https://doi.org/10.1103/PhysRev.36.57

17. Boys SF, Egerton AC (1997) Electronic wave functions - I. A general method of calculation for the stationary states of any molecular system. Proc R Soc London Ser A Math Phys Sci 200:542–554. https://doi.org/10.1098/rspa.1950.0036

18. Binkley JS, Pople JA, Hehre WJ (1980) Self-consistent molecular orbital methods. 21. Small split-valence basis sets for first-row elements. J Am Chem Soc 102:939–947. https://doi.org/10.1021/ja00523a008

19. Ditchfield R, Hehre WJ, Pople JA (2003) Self- Consistent Molecular- Orbital Methods. IX. An Extended Gaussian- Type Basis for Molecular- Orbital Studies of Organic Molecules. J Chem Phys 54:724–728. https://doi.org/10.1063/1.1674902

20. McLean AD, Chandler GS (2008) Contracted Gaussian basis sets for molecular calculations. I. Second row atoms, Z=11–18.

J Chem Phys 72:5639–5648. https://doi.org/10.1063/1.438980

21. Malkin VG, Malkina OL, Salahub DR (1993) Calculations of NMR shielding constants by uncoupled density functional theory. Chem Phys Lett 204:80–86. https://doi.org/https://doi.org/10.1016/0009-2614(93)85608-Q

22. Ditchfield R (1974) Self-consistent perturbation theory of diamagnetism. Mol Phys 27:789–807. https://doi.org/10.1080/00268977400100711

23. Thomas Frauenheim, Gotthard Seifert, Marcus Elstner, et al (2002) Atomistic simulations of complex materials: ground-state and excited-state properties. J Phys Condens Matter 14:3015. https://doi.org/10.1088/0953-8984/14/11/313

24. (1995) Recent Advances in Density Functional Methods. Recent Adv. Comput. Chem. Volume 1:428

25. Runge E, Gross EKU (1984) Density-Functional Theory for Time-Dependent Systems. Phys Rev Lett 52:997–1000. https://doi.org/10.1103/PhysRevLett.52.997

26. Zeng X, Xiao X, Chen J, Wang H (2019) Electron-hole interactions in choline-phosphotungstic acid boosting molecular oxygen activation for fuel desulfurization. Appl Catal B Environ 248:573–586. https://doi.org/https://doi.org/10.1016/j.apcatb.2018.09.038

27. B. FR, Prasana JC, Muthu S, Abraham CS (2019) Molecular docking studies, charge transfer excitation and wave function analyses (ESP, ELF, LOL) on valacyclovir : A potential antiviral drug. Comput Biol Chem 78:9–17. https://doi.org/https://doi.org/10.1016/j.compbiolchem.2018.11.014

28. Le Bahers T, Adamo C, Ciofini I (2011) A Qualitative Index of Spatial Extent in Charge-Transfer Excitations. J Chem Theory Comput 7:2498–2506. https://doi.org/10.1021/ct200308m

29. Chen X, Zheng S (2021) On the study of influence of molecular arrangements and dipole moment on exciton binding energy in

solid state. Int J Quantum Chem 121:e26511. https://doi.org/https://doi.org/10.1002/qua.26511

30. Mu X, Sun M (2020) The linear and non-linear optical absorption and asymmetrical electromagnetic interaction in chiral twisted bilayer graphene with hybrid edges. Mater Today Phys 14:100222. https://doi.org/https://doi.org/10.1016/j.mtphys.2020.100222

31. Warnke I, Furche F (2012) Circular dichroism: electronic. WIREs Comput Mol Sci 2:150–166. https://doi.org/https://doi.org/10.1002/wcms.55

32. Escudero F, Yáñez M (1982) Atoms in molecules. Mol Phys 45:617–628. https://doi.org/10.1080/00268978200100471

33. Analyzer AMW, Lu T (2019) Multiwfn. 7:

34. Espinosa E, Molins E, Lecomte C (1998) Hydrogen bond strengths revealed by topological analyses of experimentally observed electron densities. Chem Phys Lett 285:170–173. https://doi.org/https://doi.org/10.1016/S0009-2614(98)00036-0

35. Rozas, I., Alkorta, I., Elguero J (2000) Behavior of ylides containing N, O, and C atoms as hydrogen bond acceptors. J Am Chem Soc 122:11154–11161. https://doi.org/https://doi.org/10.1021/ja0017864

36. Johnson ER, Keinan S, Mori-Sánchez P, et al (2010) Revealing Noncovalent Interactions. J Am Chem Soc 132:6498–6506. https://doi.org/10.1021/ja100936w

37. Kruszewski J, Krygowski TM (1972) Definition of aromaticity basing on the harmonic oscillator model. Tetrahedron Lett 13:3839–3842. https://doi.org/https://doi.org/10.1016/S0040-4039(01)94175-9

38. Krygowski TM (1993) Crystallographic studies of inter- and intramolecular interactions reflected in aromatic character of .pi.-electron systems. J Chem Inf Comput Sci 33:70–78. https://doi.org/10.1021/ci00011a011

39. Matito E, Duran M, Solà M (2004) The aromatic fluctuation

index (FLU): A new aromaticity index based on electron delocalization. J Chem Phys 122:14109. https://doi.org/10.1063/1.1824895

40. Poater J, Duran M, Solà M, Silvi B (2005) Theoretical Evaluation of Electron Delocalization in Aromatic Molecules by Means of Atoms in Molecules (AIM) and Electron Localization Function (ELF) Topological Approaches. Chem Rev 105:3911–3947. https://doi.org/10.1021/cr030085x

41. Poater J, Fradera X, Duran M, Solà M (2003) The Delocalization Index as an Electronic Aromaticity Criterion: Application to a Series of Planar Polycyclic Aromatic Hydrocarbons. Chem – A Eur J 9:400–406. https://doi.org/10.1002/chem.200390041

42. Zhang J, Zhang H, Wu T, et al (2017) Comparison of Implicit and Explicit Solvent Models for the Calculation of Solvation Free Energy in Organic Solvents. J Chem Theory Comput 13:1034–1043. https://doi.org/10.1021/acs.jctc.7b00169

43. Skyner RE, McDonagh JL, Groom CR, et al (2015) A review of methods for the calculation of solution free energies and the modelling of systems in solution. Phys Chem Chem Phys 17:6174–6191. https://doi.org/10.1039/C5CP00288E

44. Roux B, Simonson T (1999) Implicit solvent models. Biophys Chem 78:1–20. https://doi.org/https://doi.org/10.1016/S0301-4622(98)00226-9

45. Cossi M, Barone V, Cammi R, Tomasi J (1996) Ab initio study of solvated molecules: a new implementation of the polarizable continuum model. Chem Phys Lett 255:327–335. https://doi.org/https://doi.org/10.1016/0009-2614(96)00349-1

46. S. Canneaux, F. Bohr and EH (2014) KiSThelP: a program to predict thermodynamic properties and rate constants from quantum chemistry results. J Comp Chem 35:82–93. https://doi.org/http://dx.doi.org/10.1002/jcc.23470.

47. M. J. Frisch, G. W. Trucks, H. B. Schlegel, G. E. Scuseria, M. A. Robb, J. R. Cheeseman, G. Scalmani, V. Barone, G. A.

Petersson, H. Nakatsuji, X. Li, M. Caricato, A. V. Marenich, J. Bloino, B. G. Janesko, R. Gomperts, B. Mennucci, H. P. Hratchian, J. V. and DJF (2016) Gaussian 16, Revision C.01

48. O'Boyle NM, Banck M, James CA, et al (2011) Open Babel: An open chemical toolbox. J Cheminform 3:33. https://doi.org/10.1186/1758-2946-3-33

49. Dennington R, Keith TA, Millam JM (2008) GaussView {V}ersion {5.0.8}

50. G.A. Zhurko DAZ (2009) Chemcraft 1.6, Chemcraft Graphical Program for Working with Quantum Chemistry Results

51. Humphrey W, Dalke A, Schulten K (1996) VMD: Visual molecular dynamics. J Mol Graph 14:33–38. https://doi.org/https://doi.org/10.1016/0263-7855(96)00018-5

52. Others} TW and CK and {many (2010) Gnuplot 5.4: an interactive plotting program

Chapter 3

Theoretical assessment of the conformational, structural, electronic, and reactivity features of selected Avenanthramides including QTAIM and CDFT theories

- ✓ *Conformational analysis and geometry optimization of selected eight Avenanthramide molecules.*
- ✓ *Spectral Characterization, Aromaticity indices, and QTAIM &NCI analysis to investigate the structural properties of the molecules.*
- ✓ *Reactivity studies –ESP, Fukui, CDFT based chemical reactivity descriptors, Frontier molecular orbital analysis*
- ✓ *Gas-phase basicity (GPB) and acidity constant (pKa) determination in order to understand the order of deprotonation of each hydroxyl group.*

3.1. Introduction

Avenanthramides (AVs) are secondary metabolites found in oats (*Avena Sativa. L*). These metabolites consist of a phenylalkenoic acid (PA) subunit linked to an anthranilic acid (AA) subunit via an amide bond. The PA subunits generally belong to hydroxycinnamic acid derivatives of p-coumaric acid (**p**), caffeic acid (**c**), ferulic (**f**), and sinapic acid (**s**). So collectively AVs are derivatives of different cinnamoyl anthranilic acids and around 40 different derivatives of hydroxyl and methoxy-substituted compounds are isolated from oats. The first characterized AVs from oats are described to exhibit inhibition of fungal germination and to play a role in disease resistance of oats. The early research indicates wide application in biological activity including antioxidants, protection against the development of chronic diseases such as cardiovascular diseases, cancers, and diabetes etc.

The eight AVs (as per relevance and availability), derived from anthranilic acid or 5-hydroxy anthranilic acids and p-coumaric, ferulic, sinapic or caffeic acids were selected and are N-(4'- hydroxy-(E) -cinnamoyl)-5-hydroxyanthranilic acid (**2p**), N-(4' -hydroxy-3' -methoxy-(E)-cinnamoyl)-5-hydroxyanthranilic acid (**2f**), N-(3', 4' -dihydroxy-(E)- cinnamoyl)-5- hydroxyanthranilic acid (**2c**), N-(4' -hydroxy-3',5' -dimethoxy-(E)-cinnamoyl)-5-hydroxyanthranilic acid (**2s**), N-(4' - hydroxy-(E)- cinnamoyl)- anthranilic acid (**1p**), N-(3', 4' -dihydroxy-(E)-cinnamoyl)-anthranilic acid (**1c**), N-(4' -hydroxy-3' -methoxy-(E)-cinnamoyl)-anthranilic acid (**1f**), and N-(4' - hydroxy-3',5' -dimethoxy-(E)-cinnamoyl)-anthranilic acid (**1s**). The structures of

the compounds are shown in Fig 3.1. The compounds are grouped into 1 and 2 categories where 1 stands for anthranilic acid derivative and 2 for 5-hydroxy anthranilic acid derivative. These are structurally related, in which the **2p** is 5-hydroxy-4' hydroxy Avanenthramide whereas **2f**, **2c**, and **2s** are the 3' -O- methyl, 4' –O- hydroxy, and 3', 5' -di-O-methyl derivative of **2p**. Similarly, the **1p** is 4' hydroxy Avanenthramide whereas the **1f**, **1c**, and **1s** are the 3' -O- methyl, 4' –O- hydroxy, and 3', 5' -di-O-methyl derivative of **1p**.

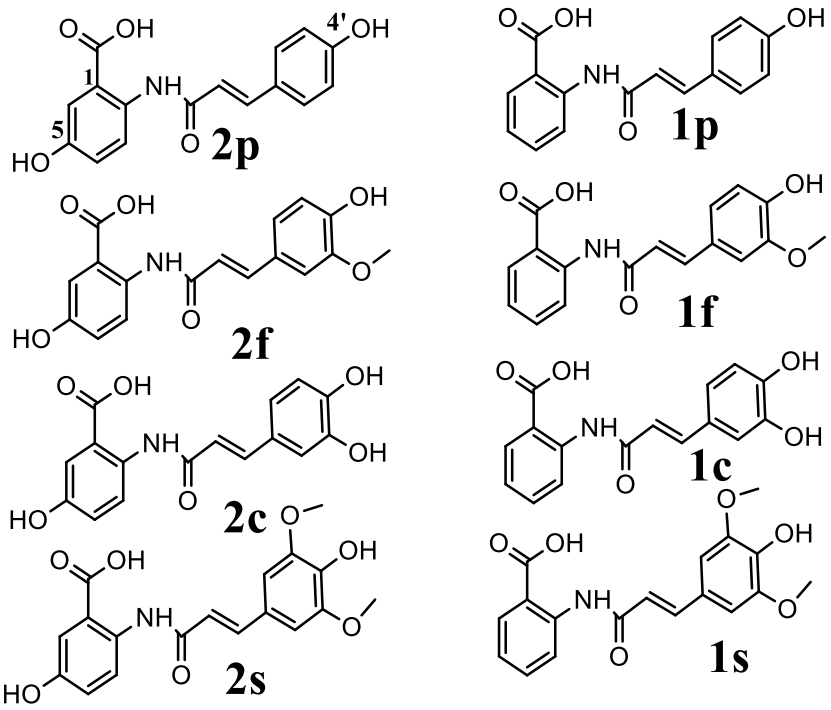

Fig. 3.1. Structures of AVs selected for the study (Anthranilic acid moiety containing aromatic system –Ring A and Cinnamic acid moiety containing aromatic system-Ring B)

Structurally, the AV molecule contains two aromatic rings; the acid-containing moiety is named as A ring and the other as B ring. The

two rings are connected through α, β unsaturated amide linkage. The selected molecules are varied according to the substitution pattern among the two aromatic rings. The presence of several single bonds in the compounds makes it a flexible molecule, and rotation about these bonds can produce a variety of conformations.

AVs can occur in two isomeric forms, s-cis if synperiplanar and s-trans if antiperiplanar, depending on the spatial configuration of the C=O and C=C bonds about the intervening single bond. Among these, the s-cis form (Fig.3.5) is more stable than the s-trans form (Fig.3.5). According to the chalcones conformational search the s-cis form is more stable than the s-trans form[1].

However, AVs can have one more geometric isomer in which both hydrogens of the α,β-double bond are on the same side, as seen in Fig.3.5. The non-planar structure and thus instability of this isomer can be attributed to the steric contact between the carbonyl group and the ring B.

Hence a detailed investigation of the stability of the conformers and geometric isomers is carried out to analyse the lowest energy structure of the molecule. Electrostatic potential (ESP) maps and conceptual density functional theory parameters were used to forecast the various reactive sites. Furthermore, an in-depth examination of the effect of pH on the deprotonation sites and corresponding pKa values was investigated. The vibrational and NMR spectra are then calculated. Furthermore, a thorough surface analysis of molecules is used to explore weak interactions within the molecule. Theoretical studies

using computational methods constantly aid us in understanding the characteristics and reactivity of molecules, providing us with many options for fine-tuning and utilizing their properties.

3.2. Computational Methodology

All calculations described in this work were performed with the Gaussian 16 computational programming package [2]. The molecular structures of AVs are downloaded from the PubChem database [3] in SDF file format and converted to a GJF file using the OpenBabel application [4]. Density functional theory (DFT) has been adopted for calculation among various computational calculation tools because it is a convenient method for predicting the physical and chemical properties with great accuracy. The effect of different solvents was evaluated using an implicit solvation model, the Polarizable Continuum *Model* (PCM) using the integral equation formalism variant (*IEF-PCM*) as the default SCRF method. The aromaticity index, "Quantum Theory of Atoms in Molecules (QTAIM), Non-covalent interaction (NCI) analysis, has been carried out using Multifunctional Wave function Analyzer, Multiwfn 3.3.8 suite [5] using M06-2X/6–31+G (d, p) level of theory. To visualize the obtained isosurfaces of NCI analysis, the visual molecular dynamics (VMD) molecular graphics program [6] was used.

3.3. Results and Discussion

3.3.1. Conformational Analysis

To elucidate the relationship between the molecular structure and reactivity, an analysis of the conformation and geometric

characteristics of the compounds considered is significant. Each molecule's conformational analysis was checked using a dihedral scan at key locations, as this appears to be important in forward search. The dihedral angles in 12 steps of 30° from 0 to 360° were carried out at the B3LYP/3-21G level of theory. The dihedral scan of **2p** at Φ (C6', C1', C7', C8') and Φ (C7', C8', C9', O9') reveals that trans-s-cis conformers of the molecule are lowest in energy and the 3D plot of potential energy scan is given Fig. 3.2. The C7'-C8' double bond is in trans and the C=C double bond is in cis conformation with the carbonyl functional group. The lowest energy conformer thus obtained is subjected to a scan of dihedral Φ (C9', N, C2, C3). The lowest energy conformer provides N-H functionality in hydrogen bonding with the carbonyl functionality of A-ring and it is given in Fig. 3.2. So the basis skeleton of all the selected compounds is similar, this conformation is applied to all other forms too. Further, the dihedral Φ(H, C4'O, C4', C3') was selected to check the orientation of the OH substituent and followed the procedure from the lowest energy conformer obtained earlier. Two orientations with very slight energy differences are obtained. The one with the very lowest energy is selected and the conformer is given in Fig. 3.2. After all these conformational quests, the molecule was subjected to energy minimization.

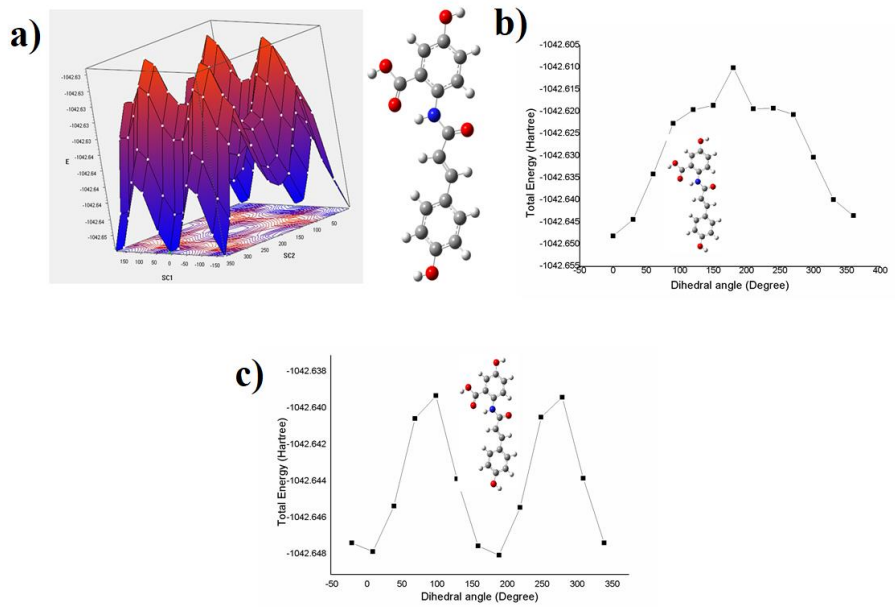

Fig. 3.2. PES of **2p** on dihedrals **a)** Φ (C6', C1', C7', C8') and Φ (C7', C8', C9', O9'), **b)** Φ(C9', N, C2, C3), and **c)** Φ (H, C4'O, C4', C3')

Except for the C3' carbon of aromatic ring B, the structures of compounds **2f** and **2c** were remarkably similar. In **2f**, the C3' carbon was occupied with an OMe substituent as in **2c** with an OH substituent. The PES on dihedral Φ (C4', C5', O5', CH_3) of **2f** and Φ (C3', C4', O4', H) of **2c** where performed and the lowest energy conformer thus obtained are given in Fig. 3.3 & 3.3 respectively. This shows that the OH and OMe groups were oriented in such a way that they formed an intramolecular hydrogen bonding interaction with nearby OH functionality. The resultant structure was improved further using a higher basis set to achieve the final structure.

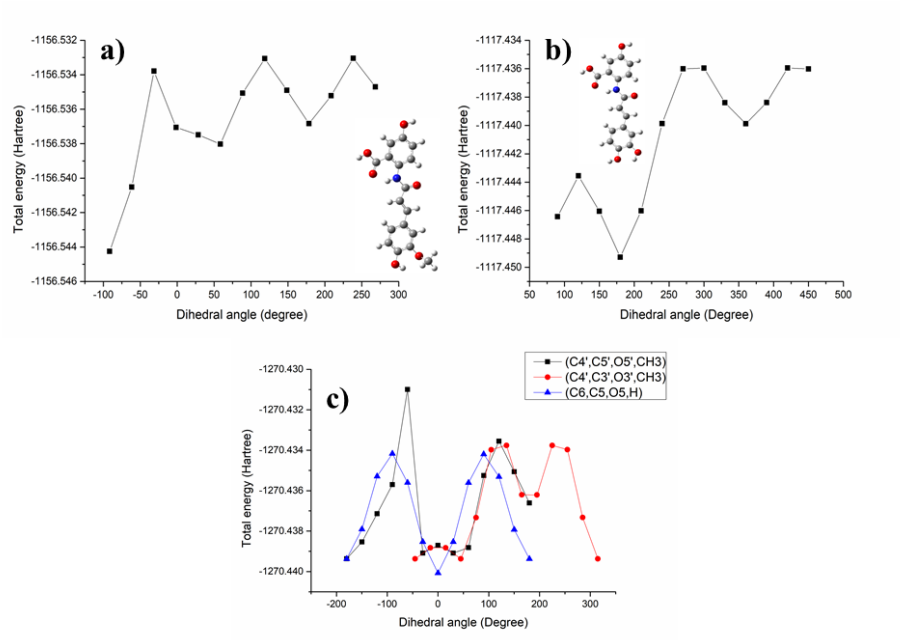

Fig.3.3. PES of **a) 2f** on dihedral Φ(C4',C5',O5',CH3), **b) 2c** on dihedral Φ(C3',C4',O4',H), and **c) 2s** for dihedral (C4',C5',O5',CH3), (C4',C3',O3',CH3), & (C6,C5,O5,H)

The compound **2s** has a very close structural relationship with **2f**. Here next ortho position of OH was occupied by one more OMe. Hence step by step potential energy scanning on dihedral (C4',C5',O5',CH3), (C4',C3',O3',CH3), & (C6,C5,O5,H) was conducted with 12 steps of interval 30°. The lowest energy conformation obtained (Fig. 3.3) was further moved into energy minimization. The lowest conformer thus obtained preferred a less sterically crowded environment in a bulky environment of two -OMe functional groups. Then, the next set of molecules **1p**, **1c**,**1f**, and **1s** shows a very close relationship in structure with **2p**, **2c**, **2f**, and **2s**, except that C5-OH. Thus, the structural framework obtained after

energy minimization of **2p**, **2c**, **2f**, and **2s** was taken as the starting geometry for **1p**, **1c**, **1f**, and **1s**. The lowest energy conformers thus obtained are further subjected to geometry optimization by higher order level of theory namely, B3LYP/6-31G(d), B3LYP/6-31+G(d,p), B3LYP/6-311+G(d,p), B3LYP/6-311++G(d,p), M06-2X/6-311+G(d,p), M06-2X/6-31+G(d,p), M06-2X/6-31++G(d,p), and M06-2X/6-31+G(2d,2p). The crystal structure data available for Tranilast (a synthetic compound with an AV skeleton) was used to correlate with the theoretical data involving the above basis sets and functional[7] (Table 3.1). The correlation coefficient was calculated for structures optimized with different basis sets. It could be seen that the correlation coefficient (R) was around 0.97 for all the sets. Previous research has documented that Functionals, M05-2X and M06-2X [22] functional from the family of Minnesota Functionals, M05-2X [21] and seem to give good results for main group thermochemistry, kinetics, and non-covalent interactions over B3LYP functional, the M06-2X suite of DFT are selected for the study with 6–31 + G (d, p) basis set with correlation coefficient (R) = 0.978 and R^2 = 0.954.

Table 3.1. Bond lengths of Tranilast optimized in different basis sets are compared to experimental bond length (Å)

Bond	Expt[7]	B3LYP/6-31g(d)	B3LYP/6-31+g(d,p)	B3LYP/6-311+g(d,p)	B3LYP/6-311++g(d,p)	M062X/6-311+g(d,p)	M062X/6-31+g(d,p)	M062X/6-31++g(d,p)	M062X/6-31+g(2d,2p)
C1-C2	1.412	1.428	1.429	1.427	1.427	1.418	1.420	1.420	1.418
C2-C3	1.399	1.409	1.410	1.407	1.407	1.404	1.406	1.406	1.403
C3-C4	1.381	1.390	1.391	1.387	1.387	1.385	1.388	1.388	1.385
C4-C5	1.380	1.399	1.400	1.397	1.397	1.393	1.396	1.396	1.393
C5-C6	1.382	1.386	1.388	1.384	1.384	1.382	1.385	1.385	1.382
C6-C1	1.397	1.407	1.409	1.406	1.406	1.400	1.403	1.403	1.400
C1-C7	1.486	1.475	1.475	1.474	1.474	1.478	1.479	1.479	1.477
C1'-C2'	1.404	1.406	1.408	1.404	1.404	1.397	1.401	1.400	1.397
C2'-C3'	1.371	1.392	1.394	1.391	1.394	1.389	1.392	1.392	1.389
C3'-C4'	1.405	1.395	1.396	1.392	1.392	1.388	1.391	1.391	1.388
C4'-C5'	1.378	1.412	1.413	1.410	1.410	1.406	1.408	1.408	1.406
C5'-C6'	1.387	1.389	1.390	1.387	1.387	1.384	1.386	1.386	1.384
C6'-C1'	1.383	1.408	1.409	1.406	1.406	1.401	1.403	1.403	1.401
C1'-C7'	1.456	1.461	1.463	1.461	1.461	1.465	1.466	1.466	1.464
C7'-C8'	1.328	1.346	1.348	1.343	1.343	1.336	1.340	1.340	1.337
C8'-C9'	1.468	1.484	1.484	1.484	1.484	1.488	1.488	1.488	1.487
C9'=O	1.242	1.228	1.230	1.222	1.222	1.214	1.221	1.221	1.215
C7=O	1.220	1.229	1.230	1.223	1.223	1.214	1.221	1.221	1.215
C7-O	1.320	1.354	1.355	1.354	1.354	1.344	1.345	1.345	1.343
C4'-O	1.363	1.374	1.374	1.372	1.372	1.366	1.368	1.368	1.366
C3'-O	1.370	1.378	1.378	1.376	1.376	1.369	1.371	1.371	1.367
C4'O-CH3	1.436	1.434	1.438	1.437	1.437	1.428	1.428	1.428	1.426
C3'O-CH3	1.430	1.433	1.437	1.436	1.376	1.428	1.428	1.428	1.369
C9'-N	1.358	1.388	1.388	1.388	1.388	1.381	1.380	1.380	1.379
C2-N	1.403	1.392	1.393	1.392	1.392	1.392	1.392	1.392	1.389
Correlation coefficient (R)		0.974	0.975	0.974	0.952	0.977	0.978	0.978	0.954
R^2		0.947	0.948	0.946	0.902	0.952	0.954	0.954	0.905

3.3.2. Geometry Optimization and Structural parameters

Optimized structures of eight AVs are given in Fig. 3.4. Vibrational frequency calculations were performed at the same level to confirm the absence of imaginary frequencies. The structural parameters of compounds are tabulated in Table 3.2.

Table 3.2. The selected geometric parameters of the studied AVs in the gas phase at M06-2X/6-31+g(d,p) level of theory, Bond length(Å), Bond Angle (^{o}), and Dihedral Angle (^{o}).

Bond								
	Bond length(Å)							
	2p	**2f**	**2c**	**2s**	**1p**	**1f**	**1c**	**1s**
1C-7C	1.481	1.481	1.481	1.479	1.478	1.478	1.478	1.479
2C- N	1.396	1.395	1.396	1.395	1.392	1.392	1.392	1.392
N -9'C	1.376	1.377	1.376	1.378	1.381	1.381	1.381	1.380
9'C-8'C	1.486	1.486	1.487	1.487	1.486	1.486	1.487	1.486
8'C-7'C	1.340	1.340	1.339	1.340	1.341	1.341	1.340	1.340
7'C-1'C	1.463	1.464	1.466	1.465	1.464	1.464	1.466	1.464
5C-5O	1.364	1.364	1.364	1.364	-	-	-	-
7C-7OH	1.343	1.343	1.343	1.346	1.345	1.345	1.345	1.345
7C-7O	1.219	1.219	1.219	1.219	1.221	1.221	1.221	1.220
9'C-9'O	1.223	1.223	1.222	1.223	1.221	1.222	1.221	1.222
4'C-4'O	1.359	1.353	1.368	1.355	1.359	1.353	1.369	1.355
3'C-3'O	-	1.367	1.356	1.366		1.367	1.357	1.367
10'C-3'O	-	1.415	-	1.416	-	1.415	-	1.416
5'C-5'O	-	-	-	1.367	-	-	-	1.366
11'C-5'O	-	-	--	1.426	-	-	-	1.426
5-O-H	0.963	0.964	0.964	0.964	-	-	-	-
4'-O-H	0.964	0.968	0.963	0.968	0.964	0.968	0.963	0.968
3'-O-H	-		0.967	-	-	-	0.967	-
	Bond Angle (^{o})							
H5-O5-C5	110.170	110.172	110.171	110.231	-	-	-	-
H4'-O4'-C4'	110.302	108.441	110.952	108.012	110.351	108.441	110.961	108.031
H3'-O3'-C3'	-	-	108.913	-	-	-	108.910	-
10'C-3'O-C3’	-	117.540	-	117.543	-	117.533	-	117.540
	Dihedral Angle (^{o})							
11'C-5'O-C5’	-	-	-	114.76	-	-	-	114.772
(C4, C3, C2, N)	180.000	179.861	179.860	179.871	180.000	179.971	180.000	179.783
(C3', C2',C1', C7')	18.000	179.672	180.000	179.694	180.000	179.742	180.000	179.712

In final the molecules are found to be in trans-s-cis conformation throughout the analysis. An intramolecular hydrogen bonding (IHB) between the carbonyl oxygen of carboxylic acid and the NH group was seen in all optimized structures of AVs. These intramolecular interactions will be detailed in the latter. The data of dihedral angles given in Table 3.2 at Φ (C4, C3, C2, N) and Φ (C3',

C2', C1', C7'), it can be seen that the compounds **2p**, **2c**, **1p**, **1c**, and **1f** are completely planar and **2f**, **1s**, and **2s** are very slightly deviating from planarity. The IHB may be the reason for preferring coplanarity between the A- ring, bridging chain, and the B ring. The deviation of planarity in some cases will be due to steric crowding at the B-ring.

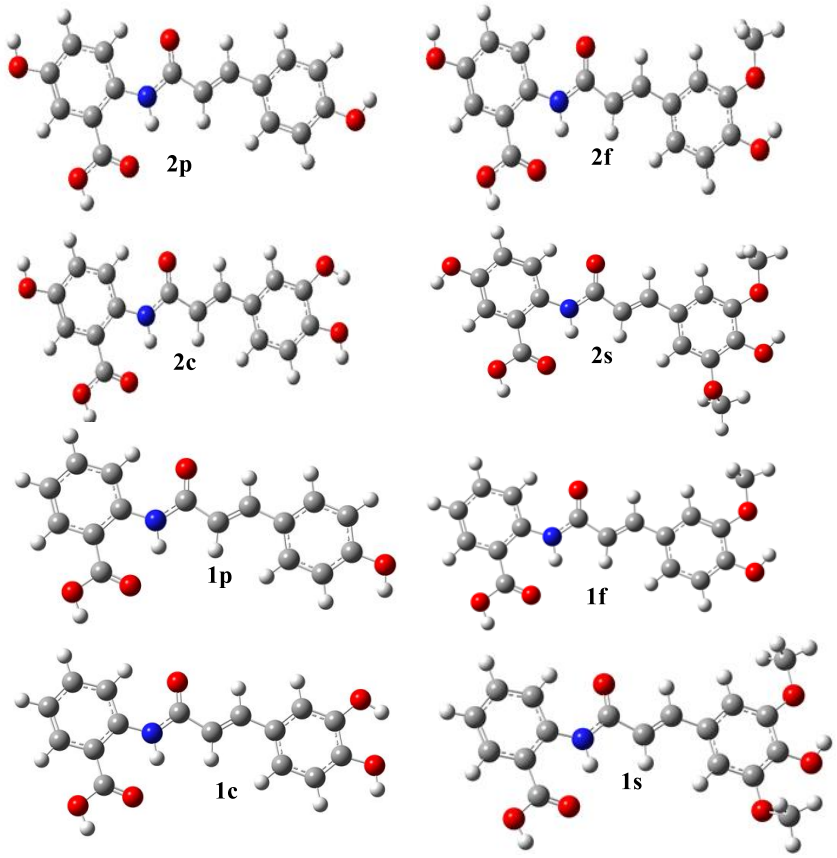

Fig. 3.4. Optimized geometries of the AVs selected in the gas phase

3.3.3. Relative Gibbs energies of the different conformers

The detailed conformer searches of the compounds of the selected AVs are discussed earlier and now the relative Gibbs energies

of the conformers formed during E-Z rearrangements are involved. The main concept of this study is to analyze how much the barrier between different conformers especially the structures in Fig.3.5 For this purpose the **2p** are considered. The conformational search on the molecules revealed a total of 51 conformers. During the analysis, 31 conformers of the E form and 20 conformers of the Z form are obtained. The geometry optimization of all the conformers is carried out using the M06-2X/6-31+G (d,p) level of theory. The optimized structures of the E and Z forms are given in Fig.A3.1 & Fig.A.3.2, respectively. The relative Gibbs energies of all the conformers are also calculated in the gas phase and tabulated in Table 3.3.

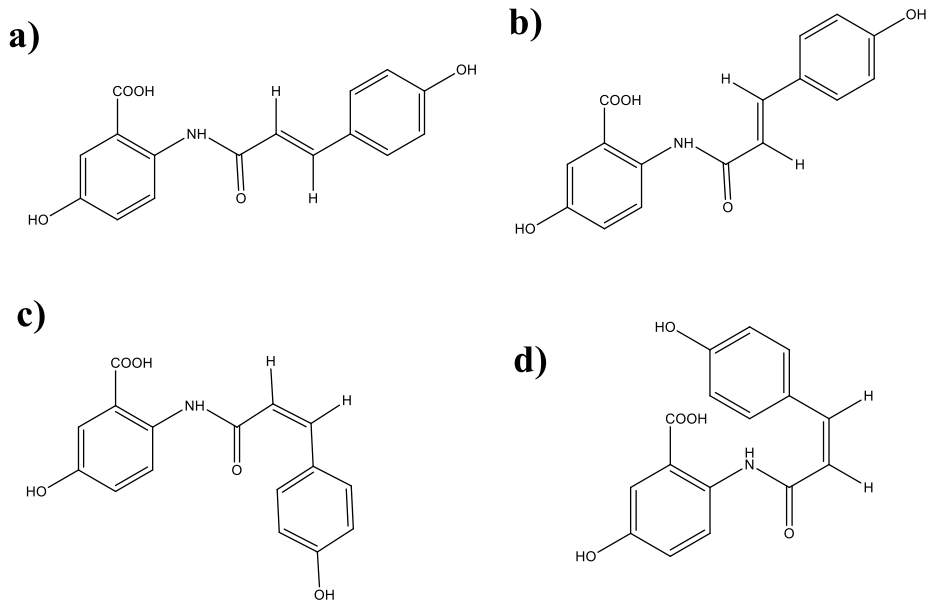

Fig. 3.5: (a) s-cis and (b) s-trans conformers of the E form, and (c) s-cis and (d) s-trans of Z form of **2p.**

Among the E forms, E0-E16 and E21-E27 are in-plane conformers of the molecule, whereas E17 is out of out-of-plane

conformers. The E28-E31 is the s-trans conformes. The conformers of relatively slight differences in their relative Gibbs energies, it appears that isolating these conformers will be challenging, and higher-energy conforms are very difficult to form. The Energy difference between s-cis and s-trans conformers is found to be 3.44 kcal/ mol. *i.e.*, the s-cis conformer is 3.44 kcal/mol lower in energy than the s-trans conformer. The relative Gibbs energies of Z isomer show that the lowest energy conformer is 5.47 kcal/ mol higher in energy than the lowest energy E conformer. Hence, none of the Z conformers exists in the gas phase at room temperature. The trans-s-cis conformer of **2p** was found to be less energy-demanding. The **2f**, **2c**, **2s**, **1p**, **1f**, **1c**, and **1s** structures were also selected in the same geometry as **2p**.

Table 3.3 Relative Gibbs energies of the conformers of the E form and Z form of AVs in the gas phase. Gibbs energies in the gas phase are relative to the gas phase Gibbs energy of the E0 conformer (i.e. -1047.851962 Ha in 1M standard state). The Gibbs energy of the Z0 conformer is -1047.843245 Ha.

Conformer	Relative Gibbs energy (kcal mol^{-1})	Conformer	Relative Gibbs energy (kcal mol^{-1})
E form		Z form	
E0	0.000	Z0	0.000
E1	1.960	Z1	5.287
E2	1.958	Z2	2.615
E3	1.959	Z3	2.614
E4	0.564	Z4	2.612
E5	0.004	Z5	7.445
E6	0.008	Z6	5.981
E7	0.001	Z7	5.983
E8	0.004	Z8	7.048

E9	0.002	Z9	7.355
E10	0.003	Z10	0.268
E11	0.041	Z11	0.267
E12	1.958	Z12	0.497
E13	0.024	Z13	0.499
E14	0.028	Z14	0.499
E15	0.008	Z15	0.498
E16	0.041	Z16	0.269
E17	7.906	Z17	0.269
E18	7.908	Z18	0.267
E19	8.176	Z19	0.008
E20	8.166	Z20	0.501
E21	5.136		
E22	5.134		
E23	2.613		
E24	5.134		
E25	0.006		
E26	0.004		
E27	0.004		
E28	2.027		
E29	2.025		
E30	2.024		
E31	2.962		

3.3.4. Vibrational spectra

The vibrational assessment for the compounds is carried out by using the M06-2X/6-31+G(d,p) level of theory. The selected stretching frequencies of the compounds are tabulated in Table 3.4. All the vibrational wavenumbers are scaled by a factor of 0.952 to account for anharmonicity and other factors.

Table 3.4 Selected stretching frequencies (cm^{-1}) of the selected compound in the gas phase

Stretching frequency	**2p**	**2f**	**2c**	**2s**	**1p**	**1f**	**1c**	**1s**
5 OH	3712	3712	3712	3710	-	-	-	-
4'OH	3705	3657	3719	3650	3706	3655	3719	3649
3'OH	-	-	3670	-	-	-	3670	-
OH(carboxylic)	3649	3653	3650	3652	3650	3653	3652	3552
NH	3383	3384	3384	3386	3370	3371	3372	3371
CH (aromatic)	3138, 3108, 3088, 3069, 3064	3133, 3108, 3087, 3079, 3073	3139, 3108, 3084, 3047, 3048	3140, 3086, 3085, 3080, 3079	3143, 3101, 3088, 3083, 3074, 3066	3139, 3102, 3087, 3085, 3073, 3064	3140, 3102, 3084, 3083, 3073, 3060	3142, 3102, 3087, 3086, 3083, 3063
CH (α-β unsaturated)	3047, 3035	3053, 3032	3053, 3038	3054, 3035	3053, 3035	3054, 3034	3053, 3037	3055, 3034
C=O(carboxylic)	1729	1728	1727	1729	1724	1724	1725	1725
C=O(carbonyl)	1711	1709	1712	1712	1717	1716	1718	1716
C=C (α-β unsaturated)	1646	1645	1648	1647	1646	1646	1648	1646
C=C (aromatic)	1626, 1614, 1591, 1585	1627, 1590, 1609, 1596	1627, 1618, 1602, 1590	1622, 1604, 1599 1592	1612 1605 1585 1581	1609 1605 1596 1581	1618 1606 1602 1581	1606 1604 1599 1581
C-N	1513	1515	1514	1519	1512	1513	1513	1513

The most intense peak corresponds to the carbon-nitrogen asymmetric stretching vibration. The stretching vibrations of phenolic O-H are observed to be higher than $3700cm^{-1}$ which is higher than acid OH and accounts for the lower bond strength and tendency to form its carboxylate anion. Moreover, the stretching vibrations of phenolic OH are observed to be higher than the free O-H stretch in a vacuum, indicating the strengthening of the O–H bond in AVs. Likewise, because of conjugation with the α-β unsaturation and lone pair of electrons from nitrogen, the carbonyl group stretches with a decreased

frequency. Furthermore, on comparing the 4'OH stretching vibrations of **2c** and **2f** with **2p**, it is observed that the OH (4') is decreased in **2f** and increased in **2c**. So in **2f**, the OH acts as a hydrogen atom donor in the hydrogen bond while in **2c** it acts as an acceptor. Similar is also for **1c** and **1f** on comparing with **1p**. From Table 3.4, upon varying substitution, appreciable changes in stretching frequencies of the skeletal atoms are not observed.

3.3.5. NMR spectra

The NMR spectra were calculated using the Gauge-independent atomic orbital (GIAO) method which provides a magnetic shielding constant (σ). The chemical shifts were obtained on the δ-scale relative to TMS using the equation 3.1,

$$\delta_i = \sigma^{TMS} - \sigma_i \qquad (3.1)$$

where the value of σ^{TMS} for ^{13}CNMR in DMSO solvent 197.65, was obtained at the same level of theory. The calculated experimental and theoretical ^{13}CNMR values are given in Table 3.5. A good correlation between the calculated and experimental δ-values for ^{13}C-NMR was obtained, thereby confirming the structure[8]. Likewise, the calculated ^{1}HNMR spectra of AVs were also determined using the same level of theory (Table 3.6). The chemical shifts were obtained on the δ-scale relative to TMS with σ^{TMS} = 31.7561 and 31.7630, respectively using DMSO and acetone as solvents. Both the ^{1}HNMR and ^{13}C-NMR values showed a close correlation, thereby confirming the structures of AVs [8]. A Linear regression analysis of ^{1}H NMR and

^{13}C NMR spectra of the compounds in comparison to the experimental findings are involved in Fig.A.3.3.

Table 3.5 Comparison of ^{13}C NMR chemical shifts (ppm) of **2p**, **2f**, **1p**, and **1f** with the experimental results[8].

	2p		**2f**		**1p**		**1f**	
	Expt.	Calc.	Expt.	Calc.	Expt.	Calc.	Expt.	Calc.
C1	118.5	125.2	118.6	125.7	116.6	123.9	116.6	124.2
C2	133.1	149.8	133.3	149.3	141.5	157.0	141.3	156.4
C3	122.5	133.5	122.8	133.7	120.4	131.6	120.4	132.2
C4	121.0	134.8	121.0	134.6	134.2	151.7	134.1	151.4
C5	152.6	161.2	152.8	161.4	122.7	134.9	122.9	134.6
C6	116.6	129.7	116.8	130.1	131.4	146.5	131.2	146.9
C7	163.9	178.9	164.1	179.8	164.5	179.6	164.5	179.9
C1'	125.7	140.4	126.4	139.1	125.7	140.1	126.1	138.9
C2'	129.9	149.0	111.5	127.3	130.2	149.6	111.5	127.3
C3'	115.8	125.5	149.1	156.5	116.0	127.2	149.1	156.4
C4'	159.4	170.2	148.1	159.5	159.8	170.3	148.1	159.6
C5'	115.8	128.4	115.9	127.3	116.0	127.0	115.8	127.3
C6'	129.9	140.6	122.8	130.7	130.2	140.5	122.7	131.0
C7'	140.8	159.1	141.4	159.9	141.8	159.7	142.1	160.9
C8'	119.1	129.4	119.5	130.1	118.9	129.4	119.0	130.1
C9'	169.3	174.1	169.5	174.1	169.9	174.6	169.7	174.9
OCH3			55.9	55.6			55.8	55.8
Correlation coefficient (R)		0.98		0.99		0.98		0.99

Table 3.6 Comparison of ^{1}H NMR chemical shifts (ppm) of **2p**, **2f**, **2c**, **1p**, and **1f** with the experimental results [8]. For **2p** acetone and the remaining DMSO are used as solvents.

	2p		**2f**		**2c**		**1p**		**1f**	
Proton	Expt.	Calc.	Expt.	Calc.	Expt.	Calc.	Expt.	Calc.	Expt.	Calc.
H-2'	7.52(d)	8.59	7.29(d)	7.46	7.05(d)	7.7	7.53(dt)	8.2	7.33(d)	7.53
H-6'	7.52(d)	7.90	7.10(dd)	8.45	6.96(dd)	8.26	7.53(dt)	8.81	7.13(dd)	8.49
H-3'	6.85(d)	7.71	-	-	-	-	6.82(dt)	7.88	-	-
H-5'	6.85(d)	8.22	6.81(d)	7.79	6.75(d)	7.56	6.82(dt)	7.53	6.81(d)	7.83
H-7'	7.55(d)	8.57	7.50(d)	8.53	7.37(d)	8.52	7.57(d)	8.63	7.53(d)	8.6
H-8'	6.56(d)	7.42	6.67(d)	7.29	6.46(d)	7.29	6.61(d)	7.33	6.70(d)	7.34
H-3	8.58(d)	9.83	8.40(d)	10.01	8.31(d)	10.08	8.67(dd)	10.19	8.63(dd)	10.08
H-4	7.07(dd)	7.68	7.04(dd)	7.63	6.99(dd)	7.71	7.56(ddd)	8.54	7.60(ddd)	8.47
H-5	-	-	-	-	-	-	7.11(ddd)	7.92	7.15(ddd)	8.07
H-6	7.49(d)	8.61	7.41(d)	8.73	7.36(d)	8.68	8.01(dd)	9.25	8.00(dd)	9.23
Correlation coefficient (R)		0.91		0.90		0.97		0.98		0.92

3.3.6. Aromaticity indices

The aromaticity of each benzene ring was calculated using three methods to identify the reactivity of the molecules. The three methods; harmonic aromatic oscillator model (HOMA)[9], aromatic fluctuation index (FLU)[10], and para-delocalization index (PDI) [9]are used and the result was compared. If the HOMA value is equal to 1, then the ring is fully aromatic. The higher the value of PDI, the delocalization will be higher, and the stronger the aromaticity. Lower FLU corresponds to stronger aromaticity. The aromatic indices of rings A and B correspond to each AVs are given in Table 3.7. Analyzing all these aromatic indexes, it is found that ring B is more aromatic than

ring A due to the more efficient overlap of the substituent orbitals within the aromatic system. It is consistent with the report that the para-substituted polyphenol compounds were exciting candidates for the evaluation of antioxidant potentials[11].

Table 3.7 Aromaticity Indices AVs studied

		HOMA	PDI	FLU
2p	Ring A	0.942	0.083	0.007
	Ring B	0.973	0.087	0.004
2f	Ring A	0.942	0.084	0.007
	Ring B	0.966	0.081	0.006
2c	Ring A	0.942	0.084	0.007
	Ring B	0.977	0.083	0.006
2s	Ring A	0.934	0.083	0.007
	Ring B	0.969	0.077	0.008
1p	Ring A	0.929	0.086	0.005
	Ring B	0.975	0.088	0.004
1f	Ring A	0.929	0.086	0.005
	Ring B	0.965	0.081	0.006
1c	Ring A	0.929	0.086	0.005
	Ring B	0.977	0.083	0.006
1s	Ring A	0.929	0.087	0.005
	Ring B	0.969	0.077	0.008

3.3.7. Quantum Theory of Atoms in Molecules (QTAIM) & Non-covalent interaction (NCI) analysis

The "Quantum Theory of Atoms in Molecules (QTAIM)" proposed by Bader [12] discloses the covalent and non-covalent interactions between atoms in light of electron density ρ(r) and its Laplacian $\nabla^2\rho(r)$ at the bond critical points (BCP), a region between a pair of nuclei where $\nabla\rho(r)=0$. From the BCP parameters obtained from the QTAIM study, such as the Lagrangian kinetic electron density (g) and the potential electron density (v), total energy density (H), the existence of stabilizing interactions between nuclei can be studied, which are quite significant in dealing with the radical scavenging behavior of substances. The nature of stabilizing interaction, type of bond, bond strength, and energy of hydrogen bond ($E_{HB;}$ equation 3.2) [13] between nuclei of interest can also be examined. Since the entire work concerns the antiradical properties of polyphenol, AVs obtained from oats, BCP parameter evaluation is critical. The Poincaré-Hopf relationship of all critical points is evaluated and found to be valid in all topological analyses of AVs instances.

$$E_{HB}=1/2(V_{BCP}) \tag{3.2}$$

Using quantum-mechanical electron density and its derivatives, qualitative and quantitative analyses of non-covalent molecular interactions in real space can be explored using the approach of reduced gradient density (RDG)[14]. It is a fundamental dimensionless quantity used in DFT to define the deviation from the homogeneous distribution of electrons and gives a rich description of van der Waals interactions, hydrogen bonds, and steric repulsions in molecules. The definition of the RDG function is shown in equation 3.3 below.

$$RDG(r) = \frac{1}{2(3\pi^2)^{1/3}} \frac{|\nabla\rho(r)|}{\rho(r)^{\frac{4}{3}}} \quad (3.3)$$

To visualize the obtained isosurfaces of NCI analysis, the visual molecular dynamics (VMD) molecular graphics program was used. Plots of reduced density gradient (RDG) versus the electron density multiplied by the sign of the second Hessian eigenvalue, as in Fig. 3.6, reveal the basic pattern of intramolecular interactions. In three-dimensional space, the weak interactions are the reduced density gradient (RDG) at low densities appears as colored regions (isosurfaces). These regions are defined as strong attractive interactions, weak interactions, and strong repulsive interactions.

Table 3.8 BCP parameters of intermolecular hydrogen bonds: electron density, Laplacian of the electron density, and hydrogen bond strength (kcal/mol) (calculated from M06-2X/6-31+G(d,p) wave function in the gas phase) for AVs.

	BCP parameters					
	ρ(r)	g(r)	v(r)	g(r)+v(r)	$\Delta^2\rho$(r)	E_{HB} (kcal/mol)
NH----CO						
2p	0.03290	0.02840	-0.02830	0.00002	0.11353	-8.87926
2f	0.03310	0.02850	-0.02840	0.00001	0.11394	-8.91064
2c	0.03289	0.02829	-0.02827	0.00002	0.11328	-8.86985
1p	0.03363	0.02890	-0.02888	0.00002	0.11564	-9.06124
1c	0.03378	0.02903	-0.02901	0.00002	0.11618	-9.10203
1f	0.03388	0.02911	-0.02909	0.00002	0.11653	-9.12399
1s	0.03361	0.02887	-0.02885	0.00002	0.11556	-9.05183
2s	0.03267	0.02811	-0.02809	0.00002	0.11257	-8.81337
OH---OCH3						
2f	0.01976	0.02014	-0.01838	0.00176	0.08760	-5.76681
1f	0.01973	0.02013	-0.01836	0.00177	0.08759	-5.76054
1s	0.02014	0.02047	-0.01876	0.00171	0.08873	-5.89859
2s	0.02011	0.02045	-0.01873	0.00172	0.08865	-5.87977

Table 3.8, clearly explains quantitatively the nature of hydrogen bonding interaction between the stabilizing groups, which are essential for dealing with the antiradical properties of polyphenols, using the parameters of QTAIM theory. The parameters, electron density (ρ(r)), its second derivative or Laplacian of electron density ($\Delta^2\rho$(r)), lagrangian kinetic electron density (g(r)), potential electron density (v(r)), total energy density (g(r) + v(r)), hydrogen bond energy (E_{HB}), at BCP, were analyzed. From Table 3.8, the nature of hydrogen bonding can be examined as follows, 1) For strong hydrogen bond, the parameters should be $\nabla^2\rho(r) < 0$, and $g(r)+v(r) > 0$, 2) for intermediate type of hydrogen bond, it should be $\nabla^2\rho(r) > 0$, and $g(r)+v(r) < 0$, and for weak hydrogen bonds, $\nabla^2\rho(r) > 0$, and $g(r)+v(r) > 0$. The positive values of $\nabla^2\rho(r)$ and $g(r)+v(r)$, as per Table 3.8, indicate the existence of weak interaction between NH----CO and OH--- OCH3. Moreover, the negative value of E_{HB} for all cases, indicates the formation of these weak hydrogen bonding interactions is thermodynamically feasible. Because the magnitude of the E_{HB} is about the strength of the hydrogen bond, the NH --- CO bonds are relatively stronger than the OH --- OCH3.

The NCI isosurfaces of all the compounds are represented in Fig. 3.6. Based on the second derivative of the hessian matrix a continuous color-coding scheme is used, where strong attractive interactions are represented in blue, weak interactions in green, and strong repulsive interactions in red. Visual inspection of AVs clearly illustrates the hydrogen bonding interaction between the C=O of carboxylic acid and the NH group in all cases. Here, isosurfaces between the C=O of carboxylic acid and NH are a mixture of blue and

yellow The presence of critical points is still clearly marked by a distinct blue region centered at the BCP corresponding to a moderate hydrogen bond and a distinct yellow region centered at the ring critical point.

However, because of the absence of a bond critical point between the catechol moiety in the **2c** and **1c** compound, the hydrogen bonding interaction cannot be quantified quantitatively. Since experimental reports reveal the existence of hydrogen bonding interactions between nuclei, the absence of BCP cannot be concluded as a lack of hydrogen bonding interactions which may be due to the collapse of two critical points, BCP and RCP (ring critical point; a second-order saddle point found at the center of the ring) in intramolecular bonding [15]. The absence of BCP doesn't mean evidence against hydrogen bonding, but only the absence of a single piece of evidence of hydrogen bonding using this theory [15]. Hence the strength of hydrogen bonding was estimated by calculating the difference in energy between the optimum geometry and the geometry with the O3'-H3'….O4' bond rotated 180° away from the optimum position. The difference in energy obtained is -4.4634 kcal/mol and -4.4630 kcal/mol respectively for **2c** and **1c** and is the hydrogen bonding interaction strength.

In the RDG Vs sign $(\lambda 2)\rho$ curve (Fig.3.7), the hydrogen bonds are represented by the Low-density, low-gradient spikes at negative values (blue) and the low-density, low-gradient spike at very near zero, with slightly negative values, indicates the weak van der Waals attraction (Light green).

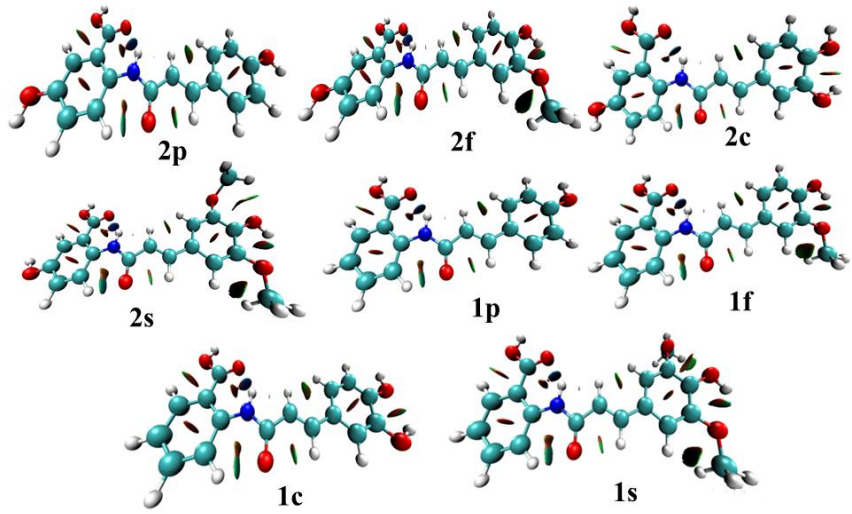

Fig.3.6. The color-filled RDG map showing non-covalent interactions, the hydrogen bonds are displayed in blue, van der Waals is presented in light green, and steric repulsions are shown in red.

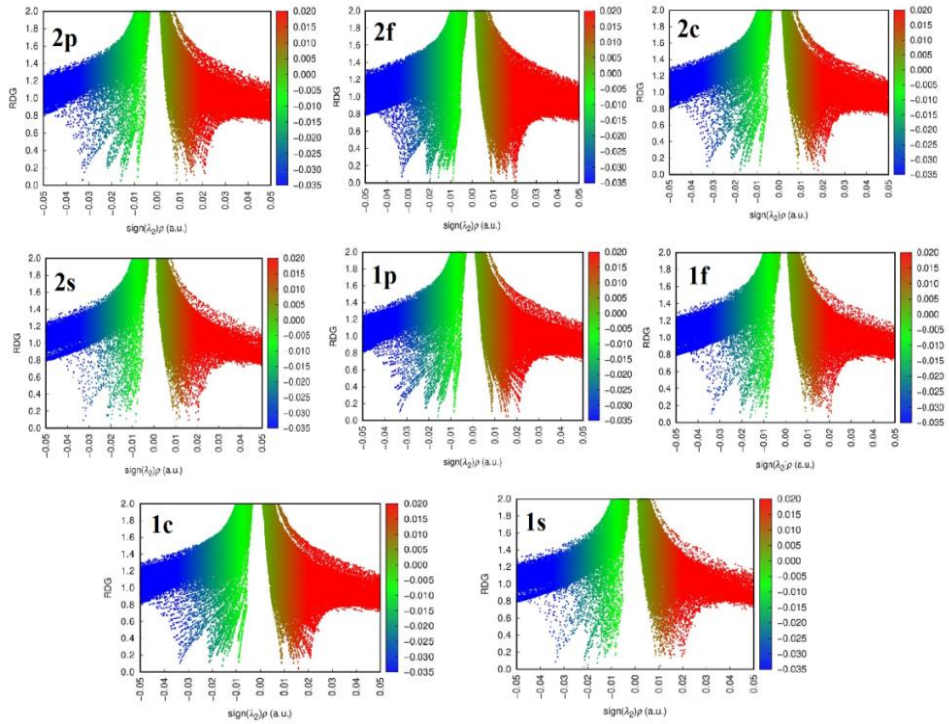

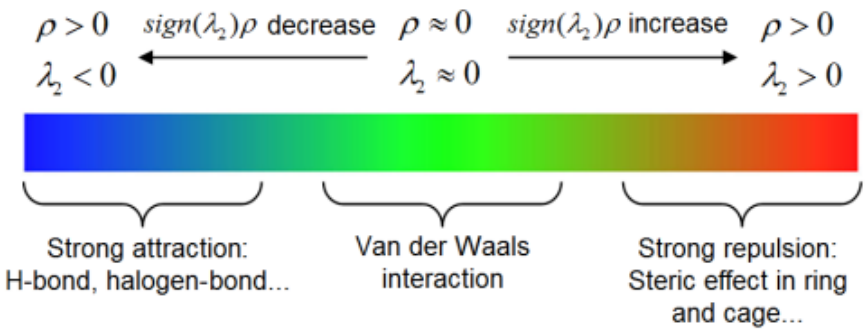

Fig.3.7. Plots of the reduced density gradient versus the electron density multiplied by the sign of the second Hessian eigenvalue of **2p**, **2f**, **2c**, **2s**, **1p**, **1f**, **1c**, and **1s.** A labelled color bar is given for easily understanding the nature of Non-covalent interactions.

3.3.8. Frontier molecular orbital analysis

The energy and distribution of the highest occupied molecular orbital (HOMO) and lowest unoccupied molecular orbital (LUMO) are also important parameters for explaining the radical scavenging activity of the molecule. In a comparative study compounds with a higher value of HOMO and lower value of LUMO are the criterion for a good radical scavenging molecule. Moreover, the distribution of HOMO-LUMO orbitals and the energy gap or band gap (ΔE) explain the reactivity of the molecule. Lowering the band gap easier the electron movement from HOMO-LUMO easier, hence higher the reactivity. The region where HOMO orbital contributions are absent and are found is an electrophilic center and electrons are like to come at these sites. The HOMO–LUMO distribution and the energies of HOMO, LUMO, and band gap are respectively provided in Fig.3.8. The HOMO distribution in all molecules are almost similar means, the

electron distribution equally contributed in all atoms except carbonyl carbon and hydroxyl group of the carboxylic functional group. Also, the LUMO distribution is throughout the molecule except at C3' and C5' atoms and the -OCH3 functional group.

For the molecules studied here, the calculated values of E_{HOMO} and E_{LUMO} in the gas phase are E_{HOMO} (2p) = -7.11 eV and E_{LUMO} (2p) = -1.15, E_{HOMO} (2f) = -7.00 eV and E_{LUMO} (2f) = -1.15 eV, E_{HOMO} (2c) = -7.10 eV E_{LUMO} (2c) = -1.16 eV, E_{HOMO} (2s) = -7.02 eV and E_{LUMO} (2s) = -1.18 eV, E_{HOMO} (1p) = -7.32 eV and E_{LUMO} (1p) =-1.17 eV, E_{HOMO} (1f) =-7.10 eV and E_{LUMO} (1f) = -1.18 eV, E_{HOMO} (1c) = -7.26 eV and E_{LUMO} (1c) =-1.19 eV, and E_{HOMO} (1s) = -7.11 eV and E_{LUMO} (1s) = -1.18 eV, respectively. These are comparable to the E_{HOMO} and E_{LUMO} values of quercetin, -5.69 eV and -2.3 eV respectively. The computed values of energy gap are ΔE for **2p**, **2f**, **2c**, **2s**, **1p**, **1f**, **1c**, and **1s** respectively are 5.96 eV, 5.85 eV, 5.94 eV, 5.84 eV, 6.15 eV, 5.92 eV, 6.06 eV, and 5.94 eV. The compounds **2s** and **2f** present the highest HOMO energy and the lowest energy difference between HOMO and LUMO, among the studied AVs, while the lowest HOMO energy and higher energy gap are found for **1p**, indicating that **2s** or **2f** would be the strongest electron donor and **1p** will be the weakest electron donor. By comparison, the order of the electron-donating ability predicted by the HOMO energies follows **2f** = **2s** > **1f** > **2c** > **2p** > **1s** > **1c** > **1p**.

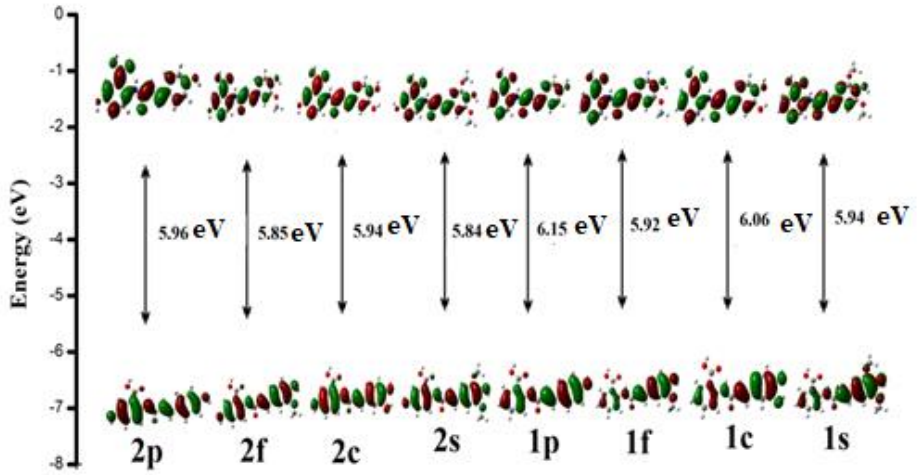

Fig.3.8. Energy diagram of the frontier molecular orbitals of the compounds studied along with their energy gaps (eV) in gas

3.3.9. ESP

Electrostatic potential (ESP) is a popular way of visualizing the electrostatic nature of molecules on three-dimensional surfaces. It is a useful descriptor related to chemical reactivity, especially for identifying the sites of electrophilic and nucleophilic attack[16]. The molecular electrostatic potential V(r) in the space around a molecule is given by the equation 3.4

$$V(r) = \sum_A \frac{Z_A}{R_A - r} - \int \frac{\rho(r')}{(r' - r)dr} \qquad (3.4)$$

Where Z_A is the charge of nucleus A, located at R_A, $\rho(r')$ is the electronic density function for the molecule, r' is the dummy integration variable, and V(r) at any point gives the interaction between the electric charge generated by the molecule and a proton

kept at a distance r. The electrostatic potential on a van der Waals (vdW) surface of compounds is shown in Fig.3.9. The blue regions indicate positive potential, i.e., the sites for nucleophilic attack, while the red regions are prone to electrophilic attack. The interpretation of ESP can be done by using the color spectrum, where, the red color indicates the negative extreme and blue indicates the positive extreme. These color spectrums containing red and blue regions represent the electrostatic nature of the compounds. The red color region indicates the minimum electrostatic potential site where electrons are loosely bound or have excess electrons and acts as a site for electrophilic attack. The blue region indicates maximum electrostatic potential and acts as a site for the nucleophilic attack. That means, the electrophile attack at the site where the electrostatic potential is most negative, and nucleophiles attack where it is most positive. The green regions are neutral.

It can be seen that the blue regions in all the compounds are located on the hydroxyl proton, whereas the red regions lie at the oxygen atoms. Apart from the surface color the diagrams also represented the quantitative nature of surface local minima (small blue spheres) and maxima (small orange spheres). The largest negative value was found to be at O9' (carbonyl) in all the compounds and it lies around 35-37 kcal/mol, which corresponds to the global minimum on the surface. The highest negative potential at the O9' reveals the high delocalizing nature of the carbonyl bond. Moreover, for **2c** and **1c**, the highest positive potential or global maximum was found to be arising from the 4 hydroxyl proton. This gives information regarding the

intramolecular interactions which are likely to be displayed by the molecule. For all the other compounds (except **2c** and **1c**) the highest global maximum lies on the hydroxyl proton of the carboxylic group. For **2f** and **2p,** the next highest positive potential was exhibited by the proton of 5 hydroxyl proton. Also found that substitution of the ortho position of 4'OH decreases the positive potential value of upon methoxy group (**2s** and **1s**), whereas increases with the hydroxyl group (**2c** and **1c**).

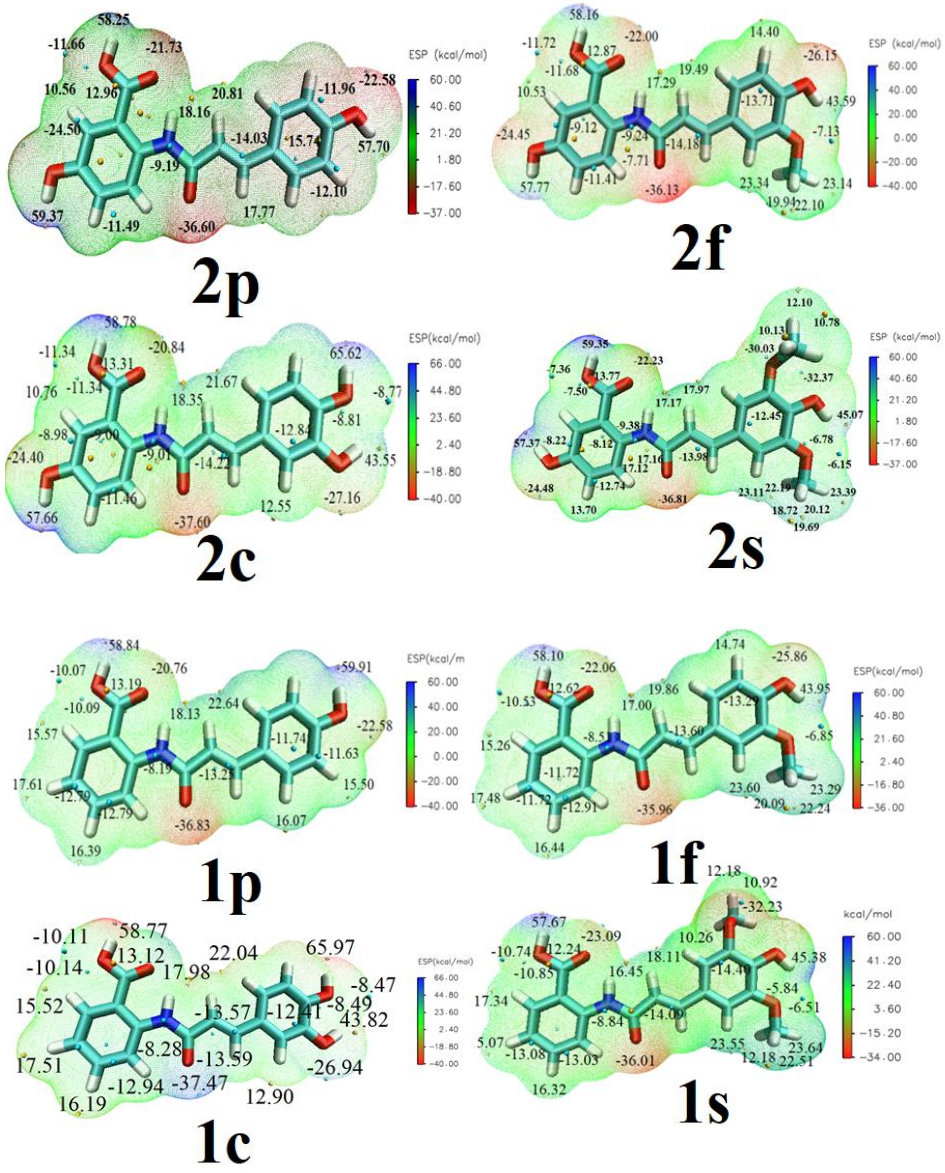

Fig.3.9. ESP-mapped molecular vdW surface of the compound studied. All values are given in kcal/mol.

3.3.10. Conceptual density functional theory (CDFT) - Reactivity site analysis

The conceptual density functional theory (CDFT) originally developed by Robert Parr is a theory framework aiming to unravel the reactivity of the chemical system. CDFT contains numerous concepts and quantities, some of them can be used to predict favorable reactive sites and reactive character, and some of them can compare reactivity among different chemical species. Here under conceptual density functional theory the chemical descriptors such as electronegativity (χ), chemical hardness (η), chemical softness (S), electrophilicity index (ω), and chemical potential (μ), and Fukui functions are involved[17–20].

3.3.10.1. Chemical descriptors

The conceptual density functional theory based chemical reactivity descriptors such as electronegativity (χ), chemical hardness (η), chemical softness (S), electrophilicity index (ω) and chemical potential (μ) were defined to get a deeper understanding of the chemical reactivity of the compound. The reactivity descriptors are tabulated in Table 3.9. The capability of the compound to accept precisely one electron from a donor is measured by its electron affinity (EA) and the measure of the compound to give away an electron is given by its ionization potential (IP) (equation3.5-3.12). The ionization potential obtained is in the range of 7.55 -7.87 eV and electron affinity is around 0.55-0.60 eV. These values are comparable to the values of Quercetin which is a well-known antioxidant molecule, where IP and EA respectively, are 7.86 and 1.03 eV.

$$Vertical\ ionization\ potential\ (VIP) = E_{cation} - E_{neutral} \tag{3.5}$$

$$Vertical\ electron\ affinity\ (VEA) = E_{neutral} - E_{anion} \tag{3.6}$$

$$Mulliken\ electronegativity(\chi) = \frac{1}{2}(VIP + VEA) \tag{3.7}$$

$$Chemical\ potential(\mu) = -\chi \tag{3.8}$$

$$Hardness(\eta) = \frac{1}{2}(VIP - VEA) \tag{3.9}$$

$$Softness(s) = \frac{1}{2\eta} \tag{3.10}$$

$$Electrophilicity\ index(\omega) = \frac{\mu^2}{2\eta} \tag{3.11}$$

$$Nucleophilicity\ index(N_{Avenanthramide}) = E_{HOMO(Avenanthramide)} - E_{HOMO(Tetracyanoethylene)} \tag{3.12}$$

The chemical hardness of the molecule is the rigidity of the molecule, i.e., the resistance of a molecule to undergo polarization of the atom according to the external environment[18]. It reveals the overall charge cloud and the stability of the molecule. Chemical softness is the reverse of hardness, i.e., it explains the easiness of the electron cloud to undergo polarization[18]. The chemical potential of the molecule is generally the tendency of the electron to move from the region of higher potential to lower potential until it becomes equilibrated. In DFT, chemical potential measures the escaping tendency of an electron from equilibrium and is the negative of

electronegativity[21]. Electronegativity is the tendency to attract electrons towards it. The electrophilicity index is the strength of the electrophilicity of the species which is an indication of chemical reactivity and a useful tool in accessing chemical and toxicological potentials of the molecule[20]. The values of these descriptors are comparable to the values of quercetin, then; these can be considered potential antioxidant compounds.

Table 3.9 The chemical reactivity descriptors of the selected AVs obtained at the M06-2X/6-31+G (d, p) level of theory in the gas phase (Unit eV and for softness eV^{-1}). All the descriptors are calculated for Quercetin and taken as a reference for comparing results

	2p	**2f**	**2c**	**2s**	**1p**	**1f**	**1c**	**1s**	**Quer***
IP	7.67	7.55	7.66	7.55	7.93	7.71	7.87	7.68	7.86
EA	0.54	0.55	0.55	0.59	0.59	0.58	0.59	0.60	1.03
Electronegativity	4.11	4.05	4.10	4.07	4.26	4.14	4.23	4.14	4.44
Chemical potential	-4.11	-4.05	-4.10	-4.07	-4.26	-4.14	-4.23	-4.14	-4.44
Hardness	3.57	3.50	3.56	3.48	3.67	3.56	3.64	3.54	3.41
Softness	0.14	0.14	0.14	0.14	0.14	0.14	0.14	0.14	0.15
Electrophilicity index	1.18	1.17	1.18	1.19	1.24	1.21	1.23	1.21	2.89
Nucleophilicity index	2.04	2.16	2.06	2.14	1.82	2.05	1.90	2.03	-

***** The nucleophilicity index was calculated about Tetracyanoethylene.

*Quer is Quercetin used as a reference to compare results

3.3.10.2. Fukui function and dual descriptor

The electron density-based local reactivity descriptors, such as the Fukui functions (equation 3.13), were proposed in addition to the

chemical descriptors to offer a deeper understanding of the chemical selectivity or reactivity at a specific region of a chemical system[22].

$$f(r) = \left[\frac{\partial \rho(r)}{\partial N} \right]_v \tag{3.13}$$

where N is the number of electrons in the present system, electronic density is denoted by ρ, and the constant term ν in the partial derivative is external potential. The reactive locations often have a higher Fukui function value than the other areas. With the aid of Fukui indices, it is possible to pinpoint the atomic locations vulnerable to nucleophilic and electrophilic attack. The dual descriptor ((Δf(r))) is an additional tool for identifying reactive areas[23]. To characterize the reactive sites of a chemical, it is defined as the distinction between nucleophilic and electrophilic Fukui functions (equation 3.14).

$$\Delta f(r) = f^{+}(r) - f^{-}(r) \tag{3.14}$$

The condensed version of the Fukui function and dual descriptor are reported to be more appropriate for quantifying electrophilic and nucleophilic sites. The condensed version of Fukui functions atomic population number is used to represent the amount of electron density distribution around an atom. The condensed Fukui function and dual descriptor for atom A can be represented as

$$\textit{nucelophilic attack} \qquad f_A^{+} = q_N^A - q_{N+1}^A$$

$$\textit{electrophilic attack} \qquad f_A^{-} = q_{N-1}^A - q_N^A$$

radical attack $f_A^0 = \frac{q_{N-1}^A - q_{N+1}^A}{2}$

$$\Delta f_A = f_A^+ - f_A^- = (q_N^A - q_{N+1}^A) - (q_{N-1}^A - q_N^A) = 2q_N^A - q_{N+1}^A - q_{N-1}^A$$

With the aid of Fukui indices, it is possible to pinpoint the atomic locations vulnerable to nucleophilic and electrophilic attack. Table 3.10 lists the Fukui functions and dual descriptors for each of the compound's atomic sites. A pictorial representation of Fukui dual descriptors is shown in Fig.3.10. The isovalue of 0.004 was used in representations of Fukui functions and dual descriptors. The blue regions correspond to negative regions prone to electrophilic attack and the green regions are positive areas prone to nucleophilic attack. The Fig.3.10 depicts the nucleophilic and electrophilic sites in each compound. The central bridging atoms between two aromatic rings are found to be incredibly contributing towards electrophilic or nucleophilic attack in each compound along with the oxygen atoms in the hydroxyl group. The quantitative nature of reactive sites is estimated by the condensed Fukui function utilizing the Hirshfeld charge, which is one of the most recommended methods for population analyses.

For 2p, the electrophilic attack or atomic sites with nucleophilic character are in the order of 2N > 5(O)> 5(C) >3(C) >6(C)> 4'(O)> 4'(C) >2(C) and the electrophilic character of atomic sites are in the order of 7'(C) > 9'(O) > 7(C) > 7(O) of C=O > 9'(C) > 4(C) as respectively from f- and f+ values given in the Table 3.10. As discussed earlier the Δf also provides a simultaneous description of

both electrophilic and nucleophilic sites in the molecules. if $\Delta f > 0$, then the site is favorable for a nucleophilic attack, or the atom acts as an electrophile, whereas if $\Delta f < 0$ then the site is favorable for an electrophilic attack. The order of Δf ($\Delta f > 0$) are in the order of 7(C)> 9'(C)> 7'(C)> 9'(O)> 7(O) of C=O>4(C)> 7(O) of OH>7'(H)> 8'(H)> 7(H)> 8'(C)> 6'(C)> 4(H)> 6'(H)> 1(C). The series from 7(C) to 1(C) are in the decreasing order of positive value of Δf. That means it is the order of $\Delta f > 0$ or the atomic position according to nucleophilic attack. 7C is highly electrophilic, i.e. more positive can be revealed as a more favorable site for nucleophilic attack [23]. Since the electronegativity of the carbon, oxygen, and nitrogen atoms is greater than the hydrogen atoms, the hydrogen atoms are electron-deficient and prone to nucleophilic attack. The order of Δf ($\Delta f < 0$) are in the order of 3'(H)< 5'(H)< 4'(C)<2'(H)<2'(C)< 6(H)< 4'(H)<5'(C)< 3'(C)< 6(C)< 3(H)< 5(H)< N(H) < 4'(O) < 2(C) < 1'(C) < 3(C) < 5(C) < 5(O) < 2N. The highest negative value of 2N revealed it as the most nucleophilic position in the molecule or it is the most favorable site for electrophilic attack. The electron rich hydrogen are in the order of 3'(H)< 5'(H) <2'(H)< 6(H)< 4'(H)< 3(H)< 5(H)< N(H). The high nucleophilic character of NH hydrogen was due to the hydrogen bonding interaction with the carbonyl oxygen of the carboxylic functional group. The hydrogen bonding interaction and its quantified results are published in our previous work[24]. Among phenolic hydrogen atoms, the 5(H) are found to be electron-rich and the results obtained are consistent with the ESP value given in Fig.3.9. The higher electron-rich character of the 5(H) position is also

consistent with the reactivity of the molecule towards radicals in the studies of the antioxidant activity[24–26].

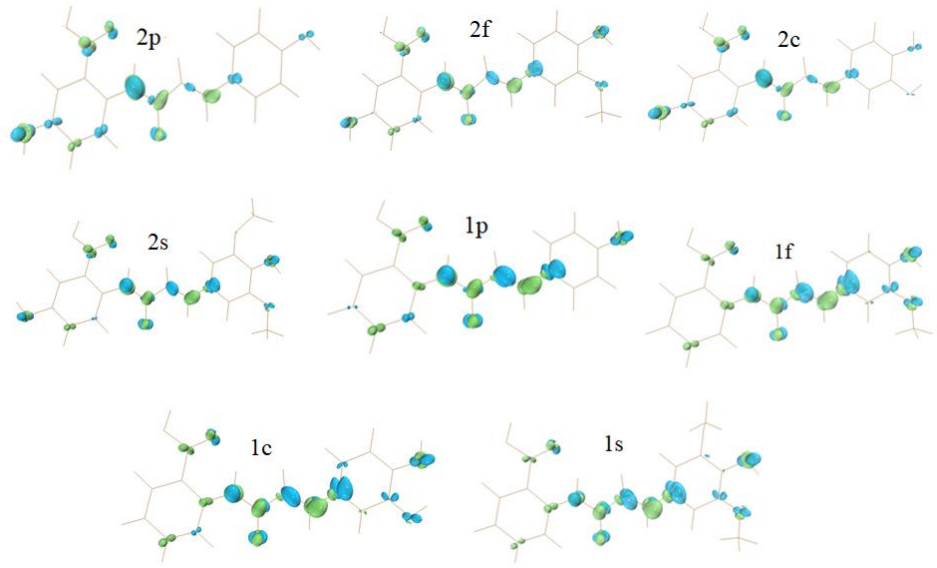

Fig.3.10. The contour graph of the dual descriptor of AVs studies in the gas phase.

Table 3.10 The Fukui descriptors of **2p** in the gas phase

Atom	**q(N)**	**q(N+1)**	**q(N-1)**	**f^-**	**f^+**	**f^0**	**Δf**
5(O)	-0.191	-0.217	-0.127	0.065	0.026	0.045	-0.039
7(O) of OH	-0.159	-0.192	-0.141	0.018	0.033	0.026	0.015
9'(O)	-0.283	-0.340	-0.254	0.028	0.057	0.043	0.029
4'(O)	-0.185	-0.213	-0.143	0.042	0.029	0.035	-0.013
7(O) of C=O	-0.265	-0.319	-0.240	0.025	0.054	0.039	0.029
2N	-0.079	-0.083	-0.014	0.065	0.004	0.035	-0.061
2(C)	0.054	0.0315	0.092	0.038	0.023	0.030	-0.015
1(C)	-0.033	-0.069	0.001	0.033	0.036	0.035	0.002
3(C)	-0.045	-0.061	0.0011	0.046	0.016	0.031	-0.030
6(C)	-0.047	-0.084	-0.0031	0.044	0.037	0.040	-0.007
5(C)	0.066	0.034	0.1281	0.062	0.032	0.047	-0.030
4(C)	-0.045	-0.093	-0.016	0.029	0.048	0.039	0.019
1'(C)	-0.017	-0.025	0.006	0.023	0.008	0.016	-0.015
9'(C)	0.165	0.115	0.175	0.010	0.050	0.030	0.040
7'(C)	-0.011	-0.081	0.026	0.037	0.070	0.054	0.033
8'(C)	-0.067	-0.105	-0.035	0.031	0.038	0.035	0.007

2'(C)	-0.028	-0.054	-0.001	0.028	0.026	0.027	-0.001
6'(C)	-0.026	-0.051	-0.006	0.020	0.026	0.023	0.006
7'(C)	0.213	0.159	0.227	0.013	0.055	0.034	0.042
3'(C)	-0.066	-0.088	-0.039	0.027	0.022	0.024	-0.004
5'(C)	-0.052	-0.073	-0.027	0.025	0.021	0.023	-0.004
4'(C)	0.081	0.042	0.121	0.040	0.040	0.040	-0.001
3(H)	0.041	0.027	0.062	0.021	0.013	0.017	-0.008
6(H)	0.048	0.024	0.073	0.026	0.024	0.025	-0.002
N(H)	0.094	0.087	0.113	0.019	0.007	0.013	-0.012
4(H)	0.047	0.017	0.072	0.025	0.030	0.028	0.005
7'(H)	0.044	0.017	0.061	0.017	0.027	0.022	0.010
8'(H)	0.039	0.019	0.051	0.012	0.021	0.016	0.009
2'(H)	0.047	0.032	0.063	0.016	0.015	0.016	-0.001
6'(H)	0.046	0.033	0.056	0.011	0.013	0.017	0.002
3'(H)	0.042	0.022	0.061	0.020	0.020	0.020	-0.000
5'(H)	0.049	0.032	0.068	0.019	0.018	0.018	-0.001
5(H)	0.169	0.150	0.198	0.029	0.019	0.024	-0.010
7(H)	0.183	0.157	0.201	0.019	0.026	0.022	0.007
4'(H)	0.171	0.153	0.191	0.020	0.017	0.019	-0.002

3.3.11. Gas-phase basicity (GPB) and acidity constant (pKa) determination

Next, the order of deprotonation tendencies of each hydroxyl group in the selected AVs compounds was analysed. The phenolic hydroxyl groups as well as the carboxylic functional group may dissociate or get ionised depending on the pH of the medium. Hence, the step-wise proton release in aqueous solution of compounds was studied by calculating the pKa values of each OH proton using the thermodynamic cycle given in Fig.3.11. The gas-phase basicity (GPB) of a base is the negative of the Gibbs energy change associated with its protonation reaction in the gas phase. Equations 3.15 &3.16 depict the calculation of Gibbs energy change associated with the deprotonation of neutral and carboxylate forms of selected AVs and equation 3.17 is used to calculate pKa values of each deprotonation.

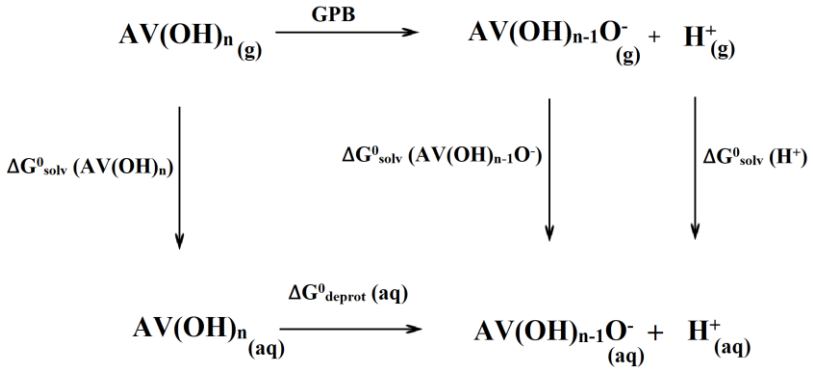

Fig.3.11. Thermodynamic cycle to calculate the GPB and first pKa values of the deprotonation sites present in AVs (AV (OH)n) (here AV are represented as AV (OH)n for including OH groups).

$$\Delta G^{0}_{deprot}(aq) = GPB + \Delta G^{0}_{solv}(AV(OH)_{n-1}O^{-}) + \Delta G^{0}_{solv}(H^{+}) - \Delta G^{0}_{solv}(AV(OH)_{n}) \quad (3.15)$$

$$\Delta G^{0}_{deprot}(aq) = GPB + \Delta G^{0}_{solv}(AV(OH)_{n-2}O_{2}^{-}) + \Delta G^{0}_{solv}(H^{+}) - \Delta G^{0}_{solv}(AV(OH)_{n-1}O^{-}) \quad (3.16)$$

$$pK_{a} = \frac{\Delta G^{0}_{deprot}(aq)}{RT\ln 10} \quad (3.17)$$

The computed gas and aqueous solution basicities for the ionization of each hydroxyl group present in the compounds, along with their sequential pKa values, are given in Table 3.11. The lower pKa value of the carboxylic hydroxyl group of all the selected compounds revealed the predominance of carboxylates of AVs in physiological pH. The second deprotonation sites in all the compounds are found to be favored from 4'OH. It refers to the enhanced charge delocalization of anionic species generated from the para-phenolic group via extended conjugation. On comparing, the pKa for second deprotonation, the lower was found to be for caffiec acid derivatives, **2c** and **1c**. The lower value of pKa of **2c** and **1c** will be due to

stabilization by intramolecular hydrogen bonding from the nearest hydroxyl group in addition to the charge delocalization. The methoxy substitution (electron donating) ortho to 4' OH decreases the tendency of proton transfer due to the formation increased charge cloud near the anionic species. For **2c** and **1c**, the pka value 5oh and 3' oh lies in the range of (16-18) meant for the higher basicity. The bulkiness and type of the substituents are two significant elements that influence the deprotonation sequence. Furthermore, the stability of the resultant anionic species is important in defining the subsequent deprotonation and pKa values of the phenolic groups.

Table 3.11 Calculated gas and aqueous solution basicities (kcal/mol) and pKa values of AVs.

Compound	Bond	GPB	ΔG^0 deprot(aq)	pKa1	pKa2
2p	COOH	317.33	3.36	**2.473**	-
	5 OH	332.25	18.08	13.31	17.17
	4' OH	323.02	15.97	11.75	**12.75**
2f	COOH	317.27	4.22	**3.10**	-
	5 OH	330.21	18.32	13.48	17.76
	4' OH	327.81	18.23	13.42	**15.63**
2c	COOH	316.16	4.18	**3.08**	-
	5 OH	331.55	18.30	13.47	17.70
	4' OH	316.18	11.70	8.61	**9.92**
	3' OH	335.98	20.08	14.78	17.16
2s	COOH	316.30	6.34	**4.66**	-
	4' OH	325.09	17.04	12.54	**13.90**
	5 OH	330.72	18.29	13.46	17.21
1p	COOH	317.20	5.82	**4.28**	-
	4' OH	322.31	15.61	11.49	**12.67**
1f	COOH	317.55	5.51	**4.06**	-
	4' OH	327.16	17.60	12.95	**14.37**
1c	COOH	316.77	4.54	**3.34**	-
	4' OH	316.09	12.23	9.00	**8.73**
	3' OH	335.87	21.05	15.49	16.08
1s	COOH	318.19	5.57	**4.10**	-
	4' OH	325.19	16.67	12.27	**13.24**

3.3.12. Influence of pH on the ionization of AVs

The pKa values show that the compounds exist as their mono-deprotonated forms carboxylate form at physiological pH. With the increase in pH, at next deprotonation occurs from the 4'OH phenolic hydroxyl group of the compounds, which results in the formation of dianion of AVs. The pH range at which each compound forms its dianion changes according to the structure. The compound **1c** and **2c** around pH 8.7 and 9.92 respectively, forms their Avenanthramide 4'-O-monoanion carboxylates.

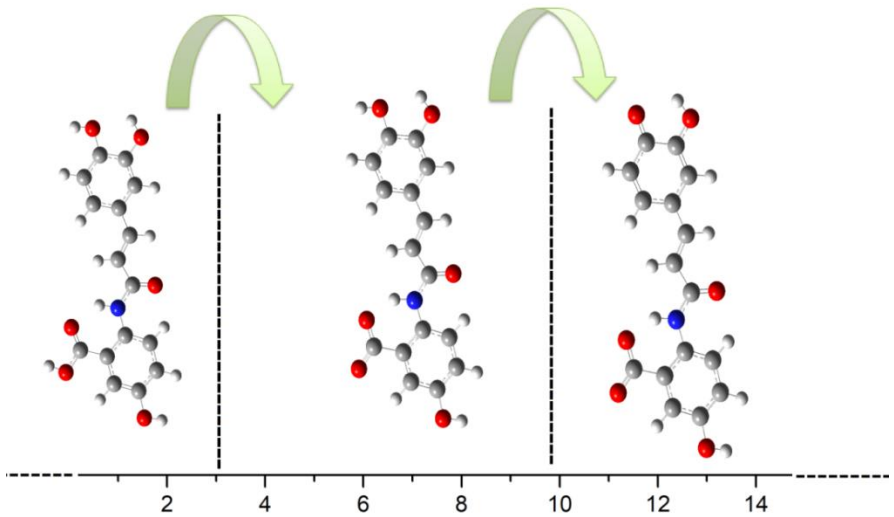

Fig. 3.12. Effect of pH on the ionization of **2c**

The pKa values of other AVs **2p**, **2f**, **2s**, **1p**, **1f**, and **1s** respectively for the formation of its dianionic form are 12.75, 15.63, 13.9, 12.67, 14.37, and 13.24. It means that these compounds form 4'O^- anion from the carboxylate forms of its corresponding AV at an

increased pH value. The Fig.3.12 represents the effect of pH on the ionization of **2c**.

3.4. Conclusions

In this work, the computational investigation of conformation, and structural properties of eight AVs namely **2p**, **2f**, **2c**, **2s**, **1p**, **1f**, **1c**, and **1s** were investigated. Structures were carefully optimized following conformational analysis and optimal basis set selection. The density functional theory with M06-2X/6-31+G (d, p) was used to explore computational investigations. The computed molecular structural parameters, and ^{1}HNMR and ^{13}CNMR exhibit satisfactory correlation with the experimental results using the same level of theory. The non-covalent interactions were studied using the QTAIM method and quantified the intramolecular hydrogen bonding interactions in all the studied compounds. Aromatic index values point out that ring B is more aromatic than ring A. The nucleophilic and electrophilic attack regions in the molecules are characterized using electrostatic potential map and fukui indices. Using the conceptual density functional theory the chemical and global reactive indices are carried out. Using the pKa calculation, the different deprotonating sites were analysed and the anionic forms according to different pH ranges were identified.

References

1. Kozlowski D, Trouillas P, Calliste C, et al (2007) Density Functional Theory Study of the Conformational, Electronic, and Antioxidant Properties of Natural Chalcones. J Phys Chem A 111:1138–1145. https://doi.org/10.1021/jp066496+
2. M. J. Frisch, G. W. Trucks, H. B. Schlegel, G. E. Scuseria, M. A. Robb, J. R. Cheeseman, G. Scalmani, V. Barone, G. A. Petersson, H. Nakatsuji, X. Li, M. Caricato, A. V. Marenich, J. Bloino, B. G. Janesko, R. Gomperts, B. Mennucci, H. P. Hratchian, J. V. and DJF (2016) Gaussian 16, Revision C.01
3. Bolton EE, Wang Y, Thiessen PA, Bryant SH (2008) Chapter 12 - PubChem: Integrated Platform of Small Molecules and Biological Activities. In: Wheeler RA, Spellmeyer DCBT-AR in CC (eds). Elsevier, pp 217–241
4. O'Boyle NM, Banck M, James CA, et al (2011) Open Babel: An open chemical toolbox. J Cheminform 3:33. https://doi.org/10.1186/1758-2946-3-33
5. Lu T, Chen F (2012) Multiwfn: A multifunctional wavefunction analyzer. J Comput Chem 33:580–592. https://doi.org/10.1002/jcc.22885
6. Humphrey W, Dalke A, Schulten K (1996) VMD: Visual molecular dynamics. J Mol Graph 14:33–38. https://doi.org/https://doi.org/10.1016/0263-7855(96)00018-5
7. Vogt FG, Cohen DE, Bowman JD, et al (2005) Structural analysis of polymorphism and solvation in tranilast. J Pharm Sci 94:651–665. https://doi.org/https://doi.org/10.1002/jps.20268
8. Collins FW (1989) Oat phenolics: avenanthramides, novel substituted N-cinnamoylanthranilate alkaloids from oat groats and hulls. J Agric Food Chem 37:60–66. https://doi.org/10.1021/jf00085a015
9. Poater J, Fradera X, Duran M, Solà M (2003) The Delocalization Index as an Electronic Aromaticity Criterion: Application to a Series of Planar Polycyclic Aromatic Hydrocarbons. Chem – A Eur J 9:400–406. https://doi.org/10.1002/chem.200390041
10. Matito E, Duran M, Solà M (2004) The aromatic fluctuation index (FLU): A new aromaticity index based on electron delocalization. J Chem Phys 122:14109. https://doi.org/10.1063/1.1824895
11. Wright JS, Johnson ER, Dilabio GA (2001) Predicting the Activity of Phenolic Antioxidants : Theoretical Method , Analysis of Substituent

Effects , and Application to Major Families of Antioxidants. J Am Chem Soc 123:1173–1183. https://doi.org/10.1021/ja002455u

12. Escudero F, Yáñez M (1982) Atoms in molecules. Mol Phys 45:617–628. https://doi.org/10.1080/00268978200100471

13. Espinosa E, Molins E, Lecomte C (1998) Hydrogen bond strengths revealed by topological analyses of experimentally observed electron densities. Chem Phys Lett 285:170–173. https://doi.org/https://doi.org/10.1016/S0009-2614(98)00036-0

14. Johnson ER, Keinan S, Mori-Sánchez P, et al (2010) Revealing Noncovalent Interactions. J Am Chem Soc 132:6498–6506. https://doi.org/10.1021/ja100936w

15. Lane JR, Contreras-García J, Piquemal J-P, et al (2013) Are Bond Critical Points Really Critical for Hydrogen Bonding? J Chem Theory Comput 9:3263–3266. https://doi.org/10.1021/ct400420r

16. Zhang J, Lu T (2021) Efficient evaluation of electrostatic potential with computerized optimized code. Phys Chem Chem Phys 23:20323–20328. https://doi.org/10.1039/D1CP02805G

17. Khlaifia D, Massuyeau F, Ewels C, et al (2017) DFT Modeling of Novel Donor- Acceptor (D- A) Molecules Incorporating 3-hexylthiophene (3HT) for Bulk Heterojunction Solar Cells. ChemistrySelect 2:10082–10090. https://doi.org/10.1002/slct.201701481

18. Zhan C-G, Nichols JA, Dixon DA (2003) Ionization Potential, Electron Affinity, Electronegativity, Hardness, and Electron Excitation Energy: Molecular Properties from Density Functional Theory Orbital Energies. J Phys Chem A 107:4184–4195. https://doi.org/10.1021/jp0225774

19. Putz M V (2013) Koopmans' Analysis of Chemical Hardness with Spectral-Like Resolution. Sci World J 2013:348415. https://doi.org/10.1155/2013/348415

20. Parr RG, Szentpály L v., Liu S (1999) Electrophilicity Index. J Am Chem Soc 121:1922–1924. https://doi.org/10.1021/ja983494x

21. Chakraborty D, Chattaraj PK (2021) Conceptual density functional theory based electronic structure principles. Chem Sci 12:6264–6279. https://doi.org/10.1039/d0sc07017c

22. Parr RG, Yang W (1984) Density functional approach to the frontier-electron theory of chemical reactivity. J Am Chem Soc 106:4049–4050. https://doi.org/10.1021/ja00326a036

23. Morell C, Grand A, Toro-Labbé A (2005) New Dual Descriptor for

Chemical Reactivity. J Phys Chem A 109:205–212. https://doi.org/10.1021/jp046577a

24. Sumayya PC, Babu G, Muraleedharan K (2021) Quantum chemical investigation of the antiradical property of avenanthramides, oat phenolics. Heliyon 7:e06125. https://doi.org/10.1016/j.heliyon.2021.e06125

25. Xue Y, Teng Y, Chen M, et al (2021) Antioxidant Activity and Mechanism of Avenanthramides: Double H+/e– Processes and Role of the Catechol, Guaiacyl, and Carboxyl Groups. J Agric Food Chem 69:7178–7189. https://doi.org/10.1021/acs.jafc.1c01591

26. Purushothaman A, Jishnu Gopal P, Janardanan D (2022) Mechanistic insights on the radical scavenging activity of oat avenanthramides. J Phys Org Chem 35:e4391. https://doi.org/https://doi.org/10.1002/poc.4391

Appendix 3

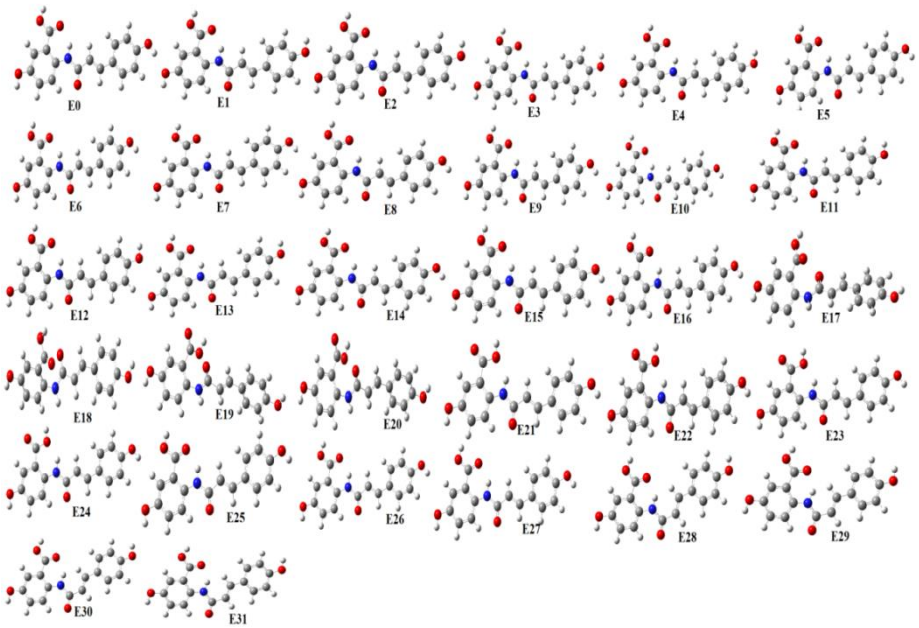

Fig.A.3.1. Optimised structures of E forms fromE0-E31

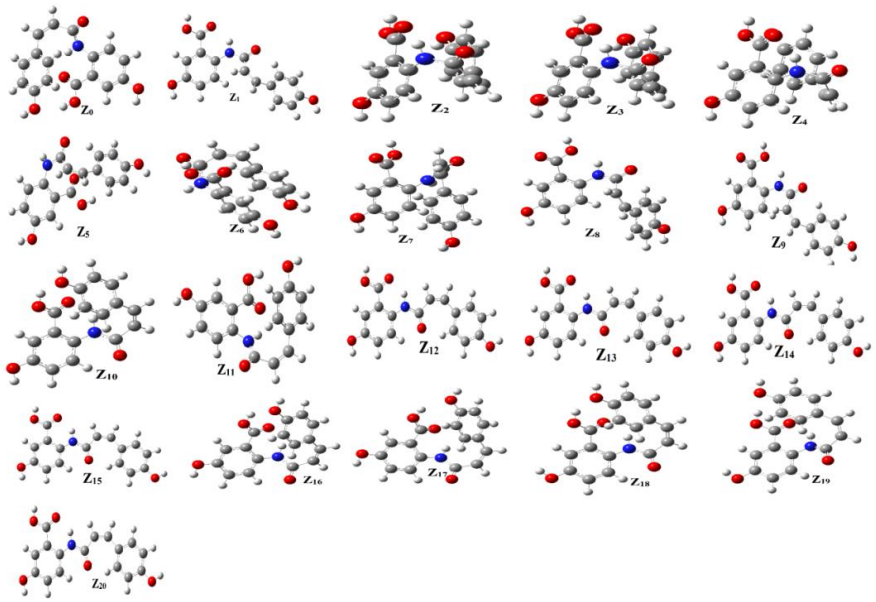

Fig.A.3.2.Optimised structures of Z forms from Z0-Z20

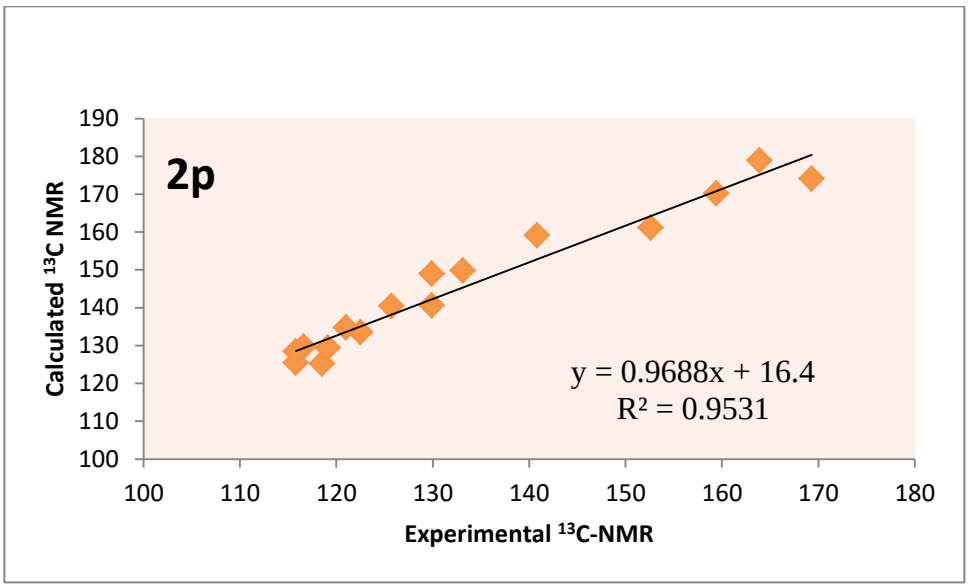
2p
Calculated ¹³C NMR
Experimental ¹³C-NMR
y = 0.9688x + 16.4
R² = 0.9531
190
180
170
160
150
140
130
120
110
100
100
110
120
130
140
150
160
170
180

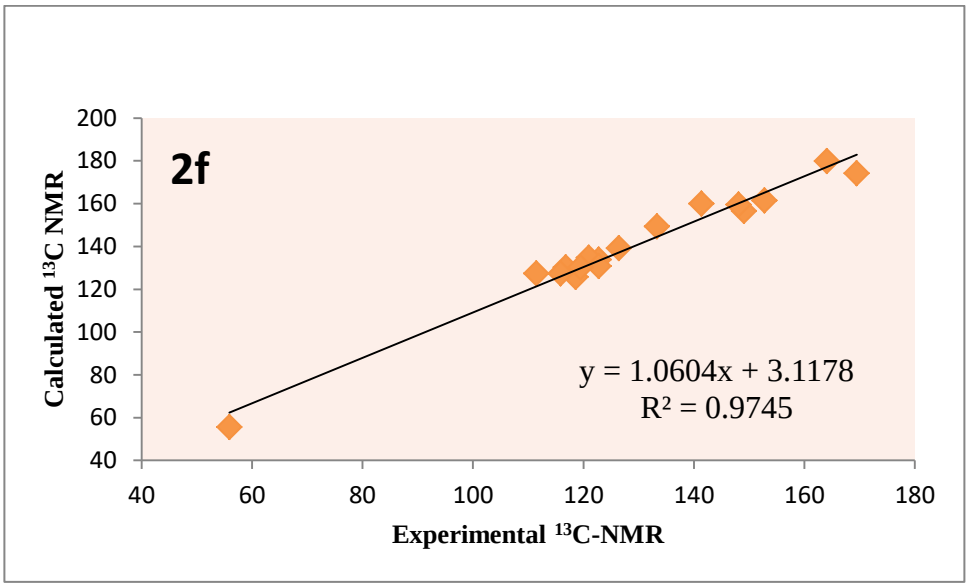
2f
Calculated ¹³C NMR
Experimental ¹³C-NMR
y = 1.0604x + 3.1178
R² = 0.9745
200
180
160
140
120
100
80
60
40
40
60
80
100
120
140
160
180

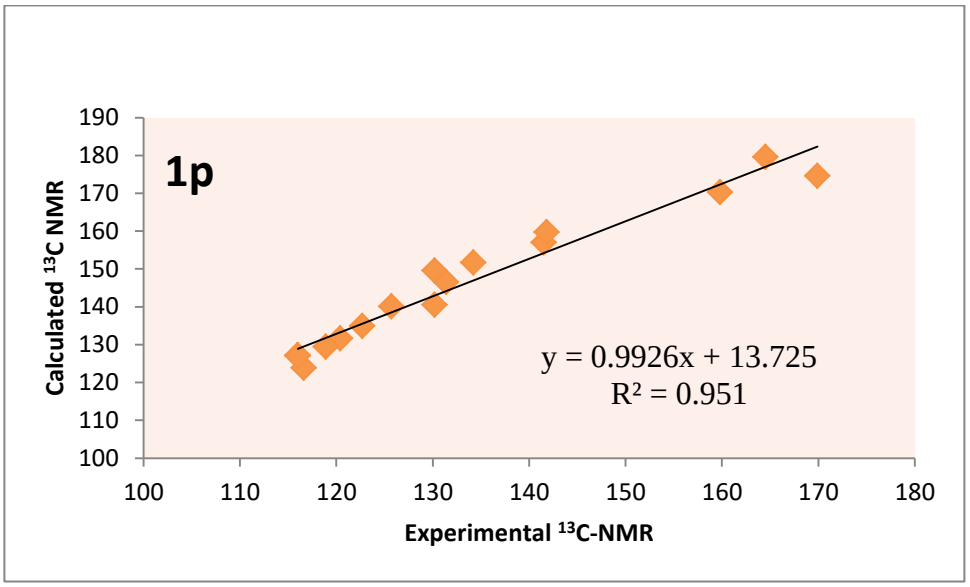
1p
Calculated ¹³C NMR
Experimental ¹³C-NMR
y = 0.9926x + 13.725
R² = 0.951
190
180
170
160
150
140
130
120
110
100
100
110
120
130
140
150
160
170
180

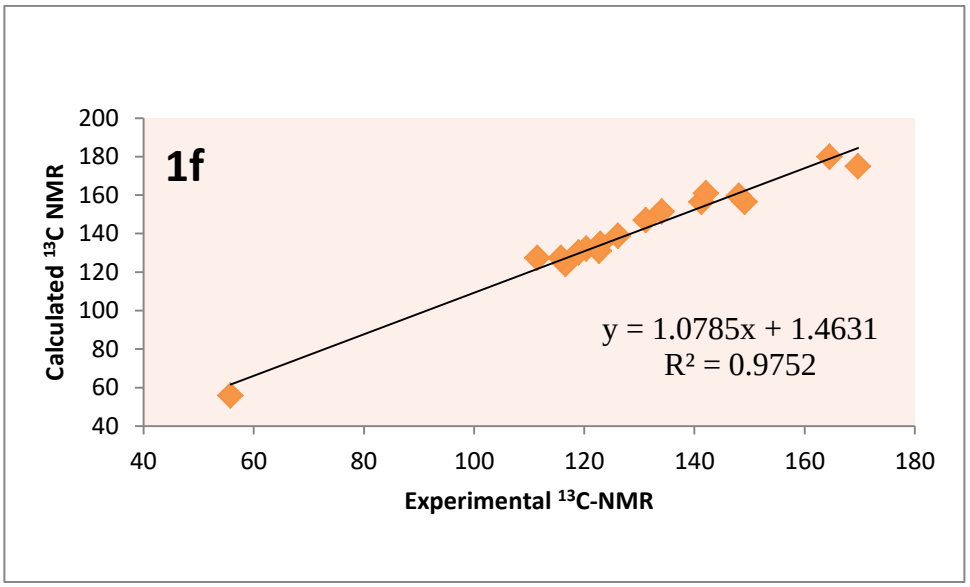
1f
Calculated ¹³C NMR
Experimental ¹³C-NMR
y = 1.0785x + 1.4631
R² = 0.9752
200
180
160
140
120
100
80
60
40
40
60
80
100
120
140
160
180

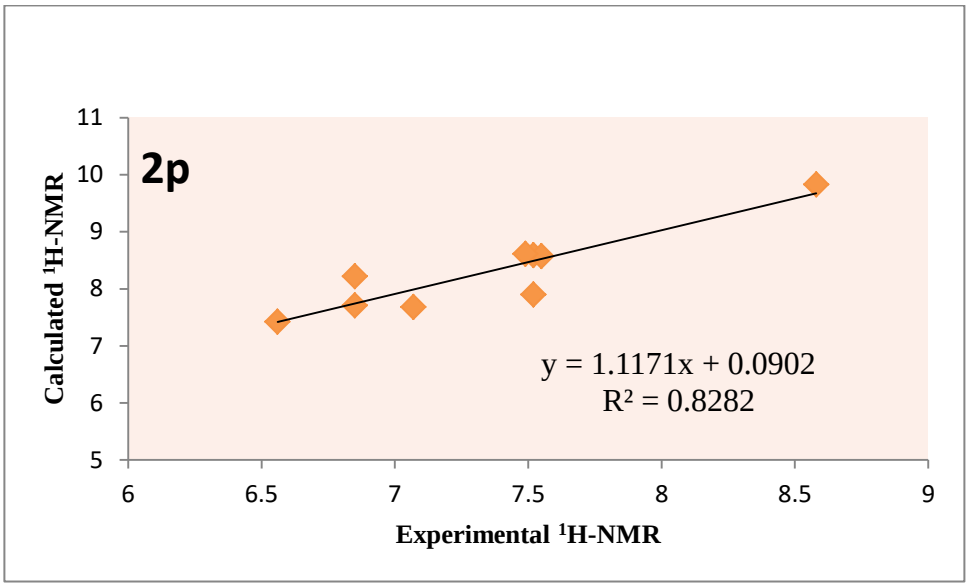
2p
Calculated ¹H-NMR
Experimental ¹H-NMR
y = 1.1171x + 0.0902
R² = 0.8282
11
10
9
8
7
6
5
6
6.5
7
7.5
8
8.5
9

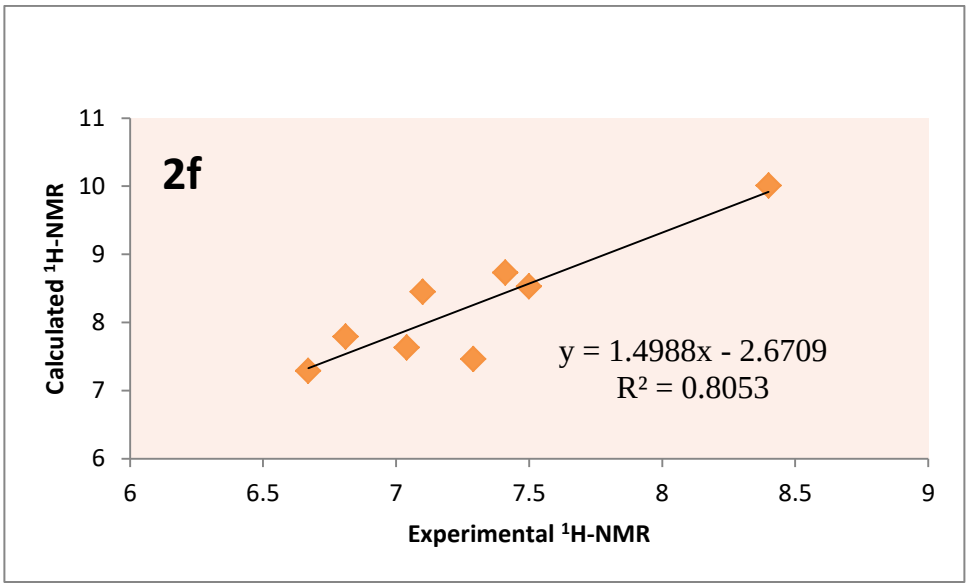
2f
Calculated ¹H-NMR
Experimental ¹H-NMR
y = 1.4988x - 2.6709
R² = 0.8053
11
10
9
8
7
6
6
6.5
7
7.5
8
8.5
9

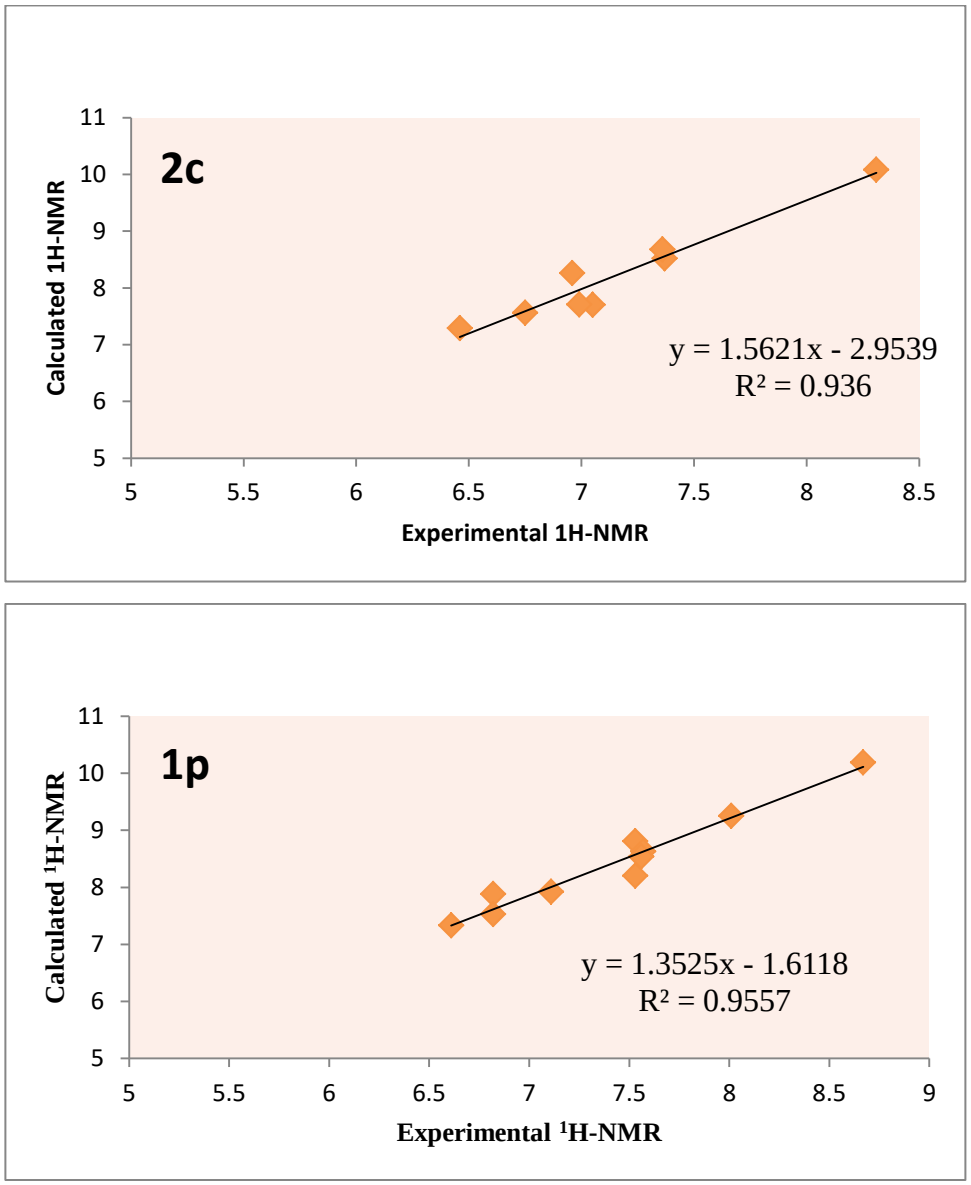

Fig.A.3.3. Linear regression analysis of ^{1}H NMR and ^{13}C NMR spectra

Chapter 4

Visualization of UV and ECD spectra of E&Z isomers of N-(4'-Hydroxy-cinnamoyl)-5- hydroxyanthranilic acid

- ✓ *The theoretical background of the electronic transition in UV-Vis and ECD spectra of E and Z isomers of Avenanthramide-2p examined*
- ✓ *The physical mechanism of the electron transfer process during light excitation is more intuitively described along with two-dimensional and three-dimensional visualization methods.*

4.1.Introduction

The AVs; N-(4'-Hydroxy-cinnamoyl)-5- hydroxyanthranilic acid (**2p**) is the nitrogen-containing polyphenolic compounds found application in radical-scavenging and antioxidant activity, anti-inflammatory activity, antiproliferative activity, potential therapeutics for cerebral cavernous malformation disease, anti-aging, and anticancer activities, etc., [1–8] and all are discussed in earlier. Here the transition characteristics and absorbance of the selected AV molecules are involved. Because of absence literatures especially theoretical investigations on the optical properties of the AVs, the discussions are somewhat indispensible.

As mentioned earlier AVs are cinnamoyl-anthranilic acids, as due to the α,β-double bond they can form two isomers, E & Z isomers. The formation of both these isomers is evidenced in the article proposed by F. William Collins[9]. AVs undergoes E&Z isomerisation in day light or UV light and E &Z forms of different AVs compounds are identified [9–11]. The Z-isomer of N-(3',4'-dimethoxycinnamoyl)anthranilic acid has found to possess 10 times antiallergic property than the Z-isomer and the photo irradiated product of E-isomer, the Z-isomer was found to inhibit hyaluronidase more effectively than E-isomer [11]. Therefore, a thorough excitation study of the compounds is of utmost importance when taking into account both isomers.

The E & Z isomers of AVs called N-(4'-Hydroxycinnamoyl)-5-hydroxyanthranilic acid (**2p**) are selected for the study (Fig. 4.1.).

Here in we've begun with defining the theoretical background of the electronic transition in UV-Vis and ECD spectra. Then the physical mechanism of the electron transfer process during light excitation is more intuitively described along with two-dimensional and three-dimensional visualization methods.

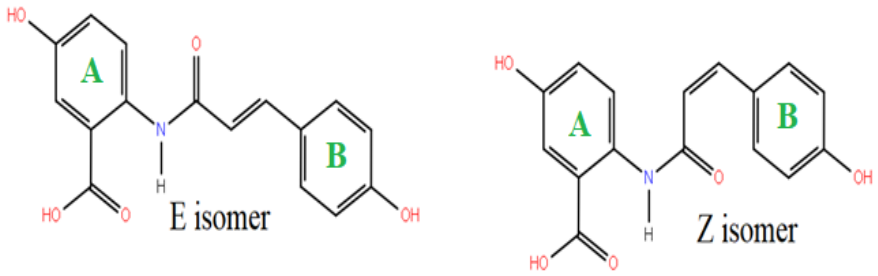

Fig.4.1. The molecular structure of E and Z isomers

4.2.Computational details

Gaussian 16 software is used for quantum calculations[12]. The geometric optimization was carried out with the 6-31+G (d, p) basis set and M06-2X functional [13]which were chosen for the high-quality theoretical approach. The optimized structures of the compounds are shown in Fig. 4.2. The calculations of excited states and UV and ECD were obtained by performing the TD-DFT calculation method; using PCM (Polarizable Continuum Model) as the solvent model [22]. The Gaussian broadening function and the FWHM (full width at half maximum) value of 0.66667 eV was used to plot UV and ECD spectra. The frontier molecular orbitals (FMO) were plotted and the energy gap was calculated. The Natural transition orbital (NTOs) [15], electron−hole pair analysis[16], the transition dipole moment density

matrix, the transition electric dipole moment, and the transition magnetic dipole moment density are performed by the Multiwfn 3.8 program[17]. The wave function files for the compounds were obtained from the Gaussian 16 W, which serves as the input file for Multiwfn 3.8, a wave function analyzer software program. The isosurface for the distribution of electron-hole coherence, NTOs, transition electric dipole moment density, and transition magnetic dipole moment density maps in three-dimensional (3D) space was rendered by using VMD software[18].

4.3. Results and discussion

4.3.2. Electronic properties

4.3.1.1. UV spectral analysis

The two isomers were optimized with M06-2X/6-31+G (d, p) using Gaussian 16 program. The optimized structure of E-**2p** and Z-**2p** are given in Fig. 4.2. The potential energy surface scanning of Z-2p is detaled in Fig.A.4.1**.** A Time-dependent DFT approach was carried out on the compounds to study the solvent effect on the compound in the aqueous phase. The solvent model IEFPCM (Integral Equation Formalism Polarizable Continuum Model) was applied to study the solution phase and SMD solvent model also checked and no major deviation in absorption intensities are observed. The UV spectra of the compounds are given in Fig.4.3. The excited state calculations and UV absorption analysis of these compounds are carried out using the vertical transition method. The molecular orbitals involved in the main transition with the largest oscillator strength have been considered and

shown in Fig.4.4. The calculated λ_{max}, energy gap (ΔE), oscillator strength (f), and the corresponding assignments are tabulated in Table 4.1.

In an electronic transition, the smallest energy gap exists between its HOMO (H) and LUMO (L) energy levels. This is the maximum wavelength at which absorption takes place in a molecule. The energy gap of near 4 eV reveals the absorption in the UV region of the electromagnetic spectrum [1, 19, 20]. For E-**2p**, the ΔE for transitions H to L, and H to L+1 are around 4 eV, and similarly the H to L+1 of Z-**2p**. Hence both these transitions span the UV region of the electromagnetic spectrum.

UV radiations can be UVA, UVB, and UVC where the long-wavelength UV A (320-400 nm), medium wavelength UV B (290-320nm), and short-wavelength UV C (200-290 nm). Exposure to both UV A and UV B rays may sometimes lead to sunburn, long-term skin damage such as wrinkles, skin cancer, such as melanoma, aging of the skin, etc[19, 21]. The absorption maxima of these compounds lie in the region of UVB (~ 320 nm) with an appreciable oscillatory strength. Since these can be a good candidate for UV absorption study more into toxicity analysis, penetration power, the efficiency of absorption, etc. We already reported the antioxidant activity of the Anvs and so photoprotection of these compounds is another area to explore and it will discuss in coming chapters.

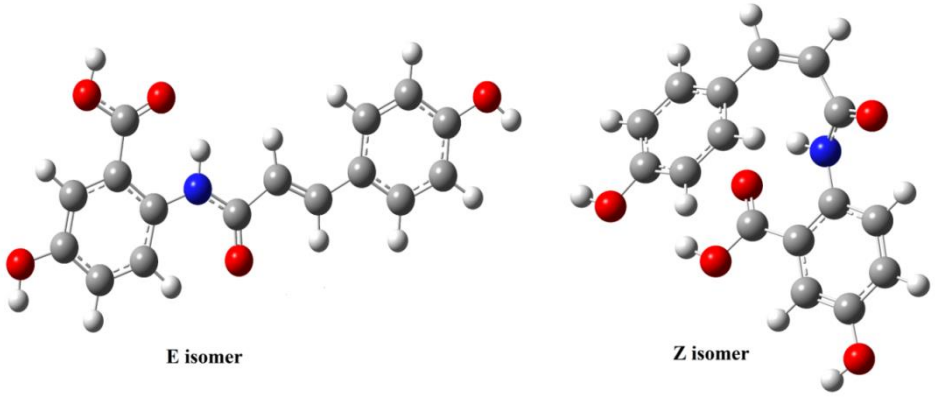

Fig.4.2. Optimized structure of E and Z isomers of **2p**

The curve of the UV-Vis spectrum together with the contributions from the transitions whose absolute value of strength is larger than 0.01 is plotted for both E-**2p** and Z-**2p** in both the gas phase and aqueous medium and is shown in Fig.4.3. The black curve is the underlying character of the total UV-Vis spectrum of compounds. So the total spectrum contains only two peaks not correspond to any transitions individually. From Fig.4.3.a, predominantly the S0 → S1 and S0 → S2 transition completely merged and correspond to the intense peak between 280-320 nm. Similarly, the S0 → S12 and S0 → S14 transitions merged and formed the shoulder band around 200 nm. So for further UV analysis the transitions S0 → S1, S0 → S2, S0 → S12, and S0 → S14 are considered for E-**2p** in the gas phase. The transitions S0 → S1, S0 → S2, S0 → S12, and S0 → S14 are respectively the transition between orbitals HOMO to LUMO, HOMO to LUMO+1, HOMO-2 to LUMO, and HOMO to LUMO+7. In water (Fig.4.3.b), S0 → S1, S0 → S2 transitions merged and correspond to the intense peak between 290-320 nm, and a shoulder peak

corresponds to S0 → S10, and S0 → S13 transitions. The major transitions in water corresponding to S0 → S1, S0 → S2, S0 → S10, and S0 → S13 are HOMO to LUMO, HOMO to LUMO+1, HOMO-2 to LUMO, and HOMO to LUMO+4. E-**2p** in water forms an additional peak on the shoulder peak out of the UV range with non-negligible oscillator strength corresponding to S0 → S 21 transition. In an aqueous medium, the intensity of S0 → S1 (f=0.80) will be more than that of S0 → S2 (f= 0.62). But the intensity of those transitions is reversed in the gas phase, where f= 0.52 for S0 → S1 and f=0.72 for S0 → S2. Hence in water, the electron movement takes place from filled molecular orbitals (HOMO) to vacant molecular orbitals (LUMO) corresponds to intense peaks, whereas HOMO to LUMO+1 in the gas phase.

a)

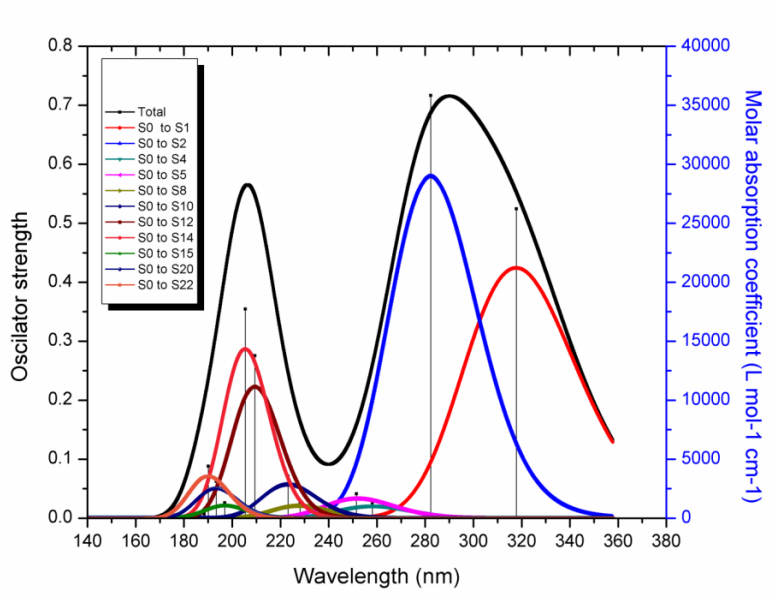

b)

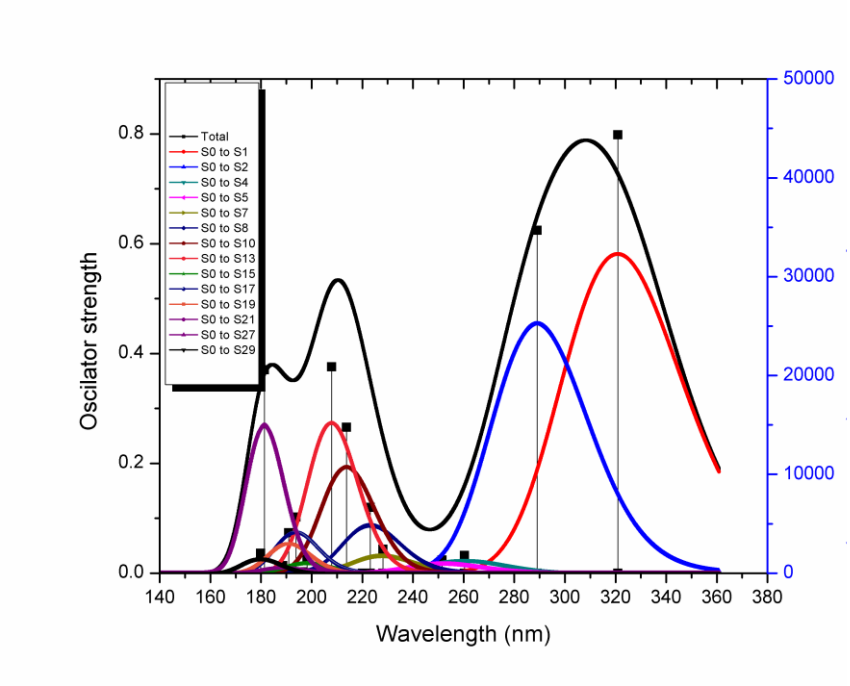
Oscilator strength
Wavelength (nm)
Total
S0 to S1
S0 to S2
S0 to S4
S0 to S5
S0 to S7
S0 to S8
S0 to S10
S0 to S13
S0 to S15
S0 to S17
S0 to S19
S0 to S21
S0 to S27
S0 to S29

c)

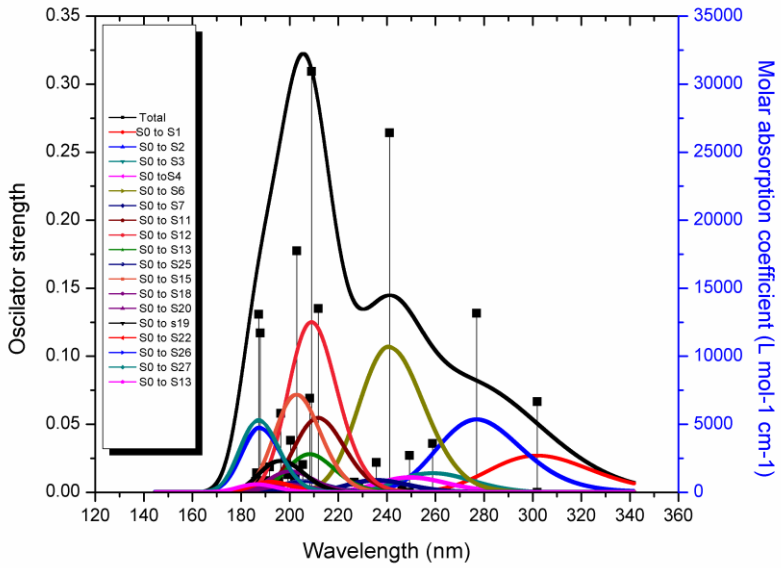
Oscilator strength
Molar absorption coefficient (L mol-1 cm-1)
Wavelength (nm)
Total
S0 to S1
S0 to S2
S0 to S3
S0 toS4
S0 to S6
S0 to S7
S0 to S11
S0 to S12
S0 to S13
S0 to S25
S0 to S15
S0 to S18
S0 to S20
S0 to s19
S0 to S22
S0 to S26
S0 to S27
S0 to S13

d)

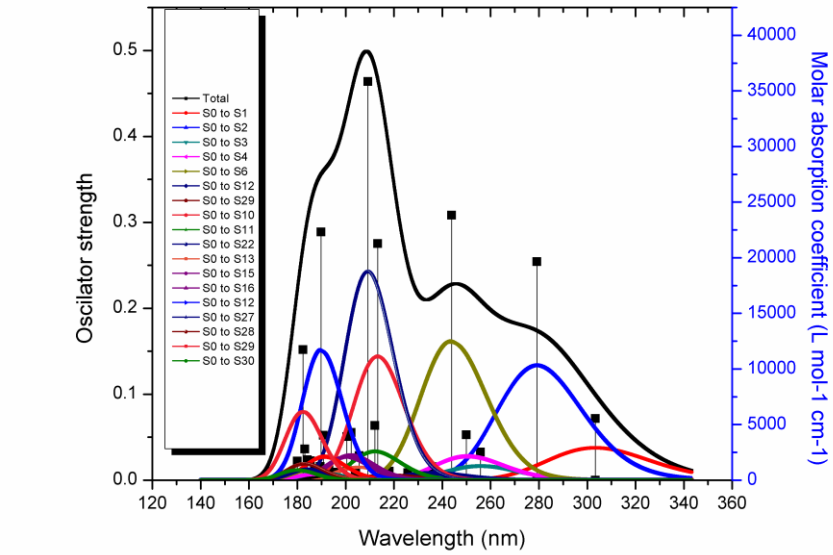

Fig. 4.3. UV–Vis spectrum of the E-**2p** a) in vacuum b) in water, and Z- **2p** c) in vacuum d) in water

The UV curve of Z- **2p** was quite different from E- **2p** (Fig.4.3.c & d). The transitions in Z isomer span in UVC region while that of E isomer majorly in UVB region of electromagnetic spectra. Exposure to all UV rays (UVA, UVB, and UVC) leads to sunburn and skin damage, fortunately, UVC radiations are completely absorbed by molecular oxygen and ozone in the earth's atmosphere. Hence these radiations do not come in contact with skin. So, a wide application of Z- **2p**, especially in the cosmetic industry as UV filters or UV blockers can be excluded, since it absorbs only in the UVC region.

For Z isomer in gas phase main transitions, S0 → S2, S0 → S6, S0 → S11, and S0 → S15 respectively corresponds to HOMO to LUMO+1, HOMO-1 to LUMO+1, HOMO to LUMO+3, and HOMO-

3 to LUMO transitions. Whereas, in water, S0 → S2, S0 → S6, S0 → S10, and S0 → S12 respectively the HOMO to LUMO+1, HOMO-1 to LUMO+1, HOMO-2 to LUMO, and HOMO-2 to LUMO+1. Table 4.1 represents detailed UV data of both the E & Z isomers of **2p**.

Table 4.1 Theoretical absorption wavelength maximum (nm), energies (ΔE), % molecular orbital contributions, and oscillator strengths (f) of E-**2p** & Z-**2p** both in a vacuum and aqueous phase (H-HOMO and L-LUMO)

	ΔE (eV)	λ_{max} (nm)	f	%	Transition	ΔE (eV)	λ_{max} (nm)	f	%	Transition
	Absorption energies									
	E-2p		-1047.925263 A.U.			**Z-2p**		-1048.06419090 A.U.		
Gas	3.90	317.54	0.52	76.88	H to L	4.48	276.92	0.13	46.08	H to L+1
	4.40	282.07	0.72	52.02	H to L+1	5.14	240.89	0.26	62.36	H-1 to L+1
	5.92	209.29	0.28	38.72	H-2 to L	5.86	211.63	0.14	57.97	H to L+3
	6.04	205.25	0.35	44.18	H to L+7	6.12	202.73	0.18	44.33	H-3 to L
	E-2p		1047.948302 A.U.			**Z-2p**		-1048.08624301 A.U.		
Water	3.87	320.66	0.80	81.97	H to L	4.44	279.20	0.25	60.50	H to L+1
	4.29	288.82	0.62	52.58	H to L+1	5.08	243.84	0.31	54.65	H-1 to L+1
	5.80	213.63	0.27	45.84	H-2 to L	5.81	213.25	0.27	50.34	H-2 to L
	5.97	207.70	0.38	51.77	H to L+4	5.92	209.24	0.46	33.84	H-2 to L+1

In the gas phase, E-**2p** shows an intense absorption band at 317.54 nm with 0.52 oscillating strength, which is from the highest molecular orbital (HOMO) to the lowest unoccupied molecular orbital (LUMO) (~ 77%). In the HOMO, the electron is delocalized through the whole molecule except the hydroxyl group of carboxylic moiety and the delocalization of electrons in LUMO orbitals is throughout the molecule as well. The second dominant transition is at 282.07 nm with a 4.40 eV energy gap. This transition is between HOMO to LUMO+1 (~ 52%), wherein LUMO+1 orbital, the electrons are delocalized throughout the molecule except the phenolic OH at the acid-containing

aromatic ring. Here, the significant transition among this set of compounds is due to HOMO - LUMO for intense transition and HOMO - LUMO+1 for second dominant transition. So this means that for an increase in the band intensity or oscillator strength there should be a good overlap between the orbitals involved in the electronic transition. Apart from these two transitions, another transition with non-negligible oscillator strength is observed corresponding to HOMO-2 to LUMO and HOMO to LUMO+7. The absorption at 209.29 nm corresponds to HOMO-2 to LUMO whereas HOMO to LUMO+7 at 205.25nm. These transitions possess a high energy gap (~ 6 eV), and low oscillator strength (f=0.28 for HOMO-2 to LUMO and f=0.35 for HOMO to LUMO+7).

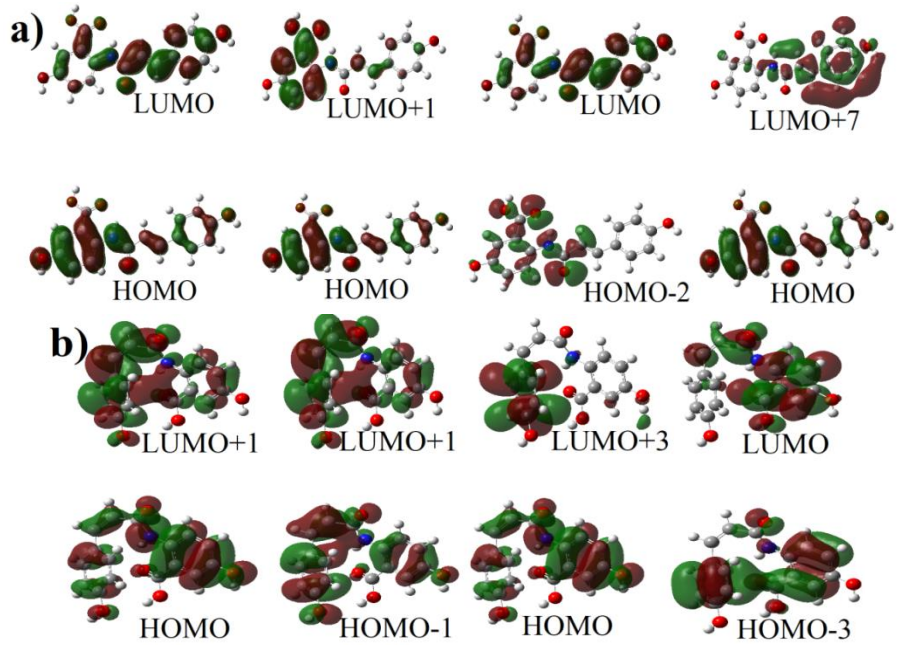

Fig.4.4. Topology of orbitals having maximum contribution towards the intense band and shoulder bands of a) E-**2p** and b) Z-**2p** in the gas phase

Compare to the E isomer, the absorption intensities of transitions of the Z isomer possess low oscillator strength. The four transitions of prominent oscillator strength are given in Table 4.1. The major absorption at 240.89 nm (f= 0.26) corresponds to HOMO-1 to LUMO+1 transition. The peaks at 202.73 nm (f=0.18), 211.63 nm (f=0.14), and 276.92 (f=0.13) are respectively due to transitions HOMO-3 to LUMO, HOMO to LUMO+3, and HOMO to LUMO+1.

The absorption characteristics of these compounds are studied in solvent water too. It is observed that the absorption maxima are red-shifted for both the intense and shoulder bands when the solution changes to a more polar one. For E-**2p**, major peaks are continues to be HOMO-LUMO and HOMO-LUMO+1. The main absorption band is observed at 320 nm with oscillator strength of 0.80, which is due to the HOMO to LUMO transition. The second major transition at 288 nm of oscillator strength 0.62 occurs between HOMO to LUMO+1. In Z-**2p**, the intense band was shifted to 209.24 nm due to HOMO-2 to LUMO+1 transition (f= 0.46) and next higher absorption at 243.84 nm due to HOMO-1 to LUMO+1 (f=0.31). The absorption characteristics of the E-**2p** were studied in methanol solvent because of the availability of the experimental UV in this solvent. The absorption peak obtained can be comparable with the experimental absorption band at 339 nm and 298 nm [9]. The details of transition in methanol are not included in this work other than in Table 4.2. The correlation between experimental and theoretical absorption reflects the reliability of the level theory selected for computational analysis.

Table 4.2 Comparison of experimental (References are given) and computational UV–Vis of E isomer

Compound	UV- Vi spectra (nm)	
	Experimental [9]*	Theoretical*
E-AVA	298	288.75
	339	320.65

*In solvent methanol

The observed bathochromic shift in polar media of two isomers was due to the increased stabilization of π* orbitals (excited state) more compared to π orbitals (ground state). It could also be observed that as the solvent becomes polar, the oscillator strengths are found to increase and it could be due to better orbital overlap. This increase in overlap is found to be evident only in main peak absorption and found to be a decrease for shoulder peaks. That means the HOMO to LUMO transition intensity increases as the solvent polarity increases and HOMO to LUMO+1 transition intensity decreases. In water, the oscillator strengths of values of HOMO to LUMO transition have changed to f= 0.7984 from gas-phase values of f= 0.5243. Thus, with an increase in polarity of the medium, the oscillator strength is found to increase.

4.3.2.1.1. Natural transition orbital (NTO) analysis

NTO analysis is found to be essential in this case because the MO of many transitions has no dominant contributions. Clearly, in the excitation of S0 → S2, the largest contribution of a single MO pair is merely 52.02 % (Table 4.1). Hence it is found difficult to conclude transition by viewing only one MO pair. So, two NTO pairs (occupied and virtual pairs) faithfully reveal the real character of electron

excitation. The NTO pairs of each transition of E-**2p** are given in Fig.4.5. The eigenvalue of each NTO pair is given in Table 4.3. For the S0→S1 transition, the occupied NTO with an index of 78 and the virtual NTO with an index of 79 constitute the NTO pair with an eigenvalue of 0.924810. Hence S0-S1 excitation can be regarded as a transition from π orbitals of the A-ring to the π* orbital of the same ring including a carboxylic functional group of at least 92.48 % confidence. For S0-S2, NTO78 → NTO79 transition pairs with a contribution of 75.63 % (eigenvalue of 0.756267) in which the transition occurs from π orbitals of B ring to the antibonding π* orbitals of atoms (C9', C8', C7', C1'). For the same the NTO pair; NTO77 → NTO80 also has a small contribution (22.26 %) to the excitation. For the S0→S12 transition, the major transition happens between NTO78 → NTO79 (59.34%) and NTO77 → NTO80 (31.57%). Both the occupied NTO in this transition occupied in B aromatic ring. Similarly, the S0-S14 transition occurs within the A aromatic system. The NTO78 → NTO79 (49.15%) and NTO77 → NTO80 (33.85%) are the NTO pair of major contributions.

Table 4.3 points out the NTO details of four transitions of Z isomer too. The isosurface map of NTO pairs of each transition is also given in Fig. 4.6. For the S0-S2 transition, the contribution of NTO78 → NTO79 was found to be 79% corresponding to MO's contribution of 46.08%. For that, the S0-S6 transition occurs from NTO78 → NTO79 with 85.24% and S0-S11with 83.46 %. For S0-S15 transition occurs from NTO78 → NTO79 (69%) and NTO77 → NTO80 with a non-negligible contribution (18%).

Table 4.3 Occupied NTO, Virtual NTO, Eigen value, and % contribution of transitions of E-**2p** and Z- **2p**

E - 2p				
Transition	Occupied NTO	Virtual NTO	Eigen value	% contribution
S0→S1	78	79	0.924810	92.48
S0→S2	78	79	0.756267	75.63
	77	80	0.222633	22.26
S0→S12	78	79	0.593451	59.35
	77	80	0.315703	31.57
S0→S14	78	79	0.491561	49.16
	77	80	0.338553	33.86
Z - 2p				
S0→S2	78	79	0.789764	78.98
	77	80	0.156980	15.70
S0→S6	78	79	0.852463	85.25
S0→S11	78	79	0.834554	83.46
S0→S15	78	79	0.690639	69.06
	77	80	0.178642	17.86

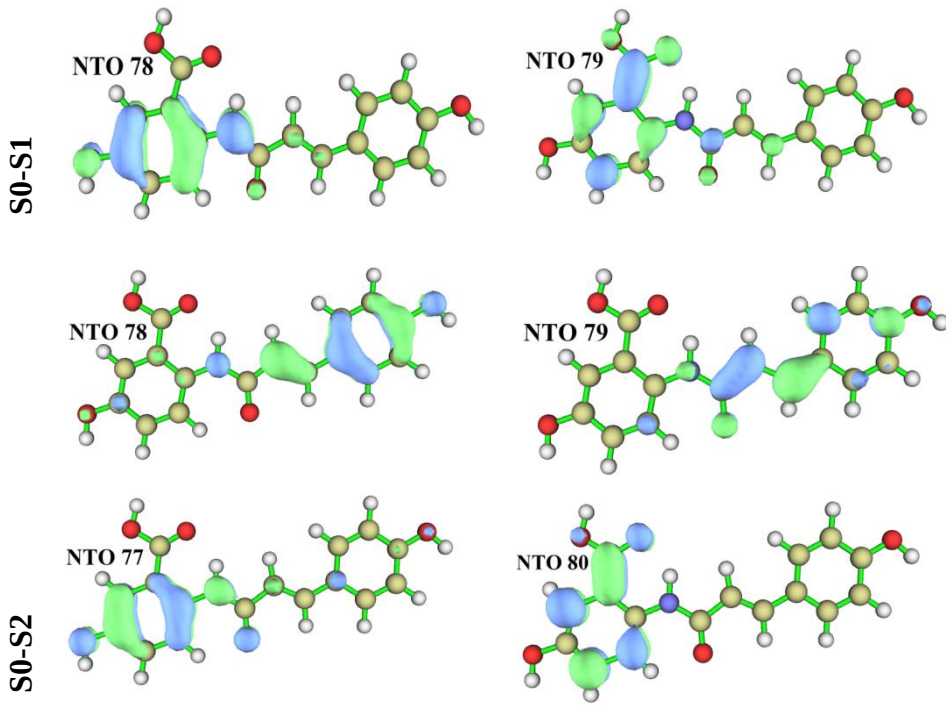

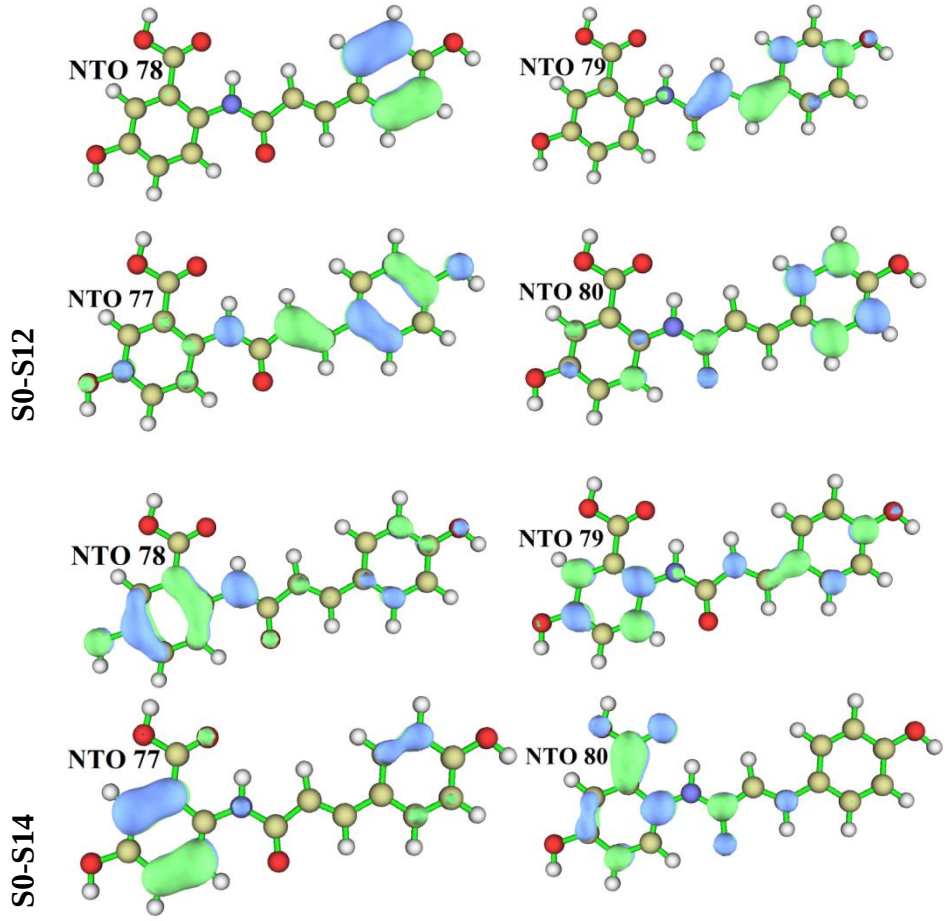

Fig.4.5. Natural transition orbital analysis of E-**2p** in each transition states

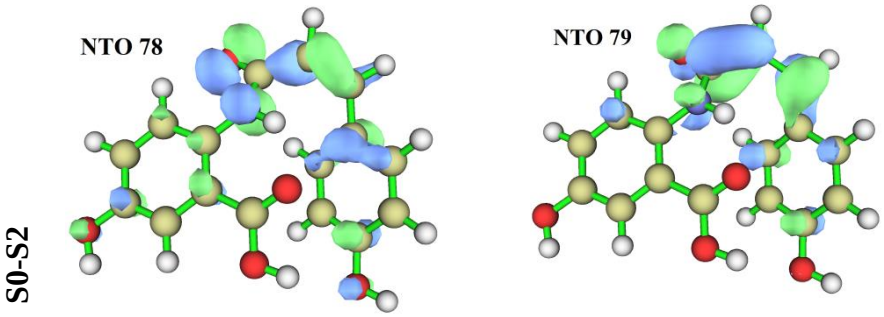

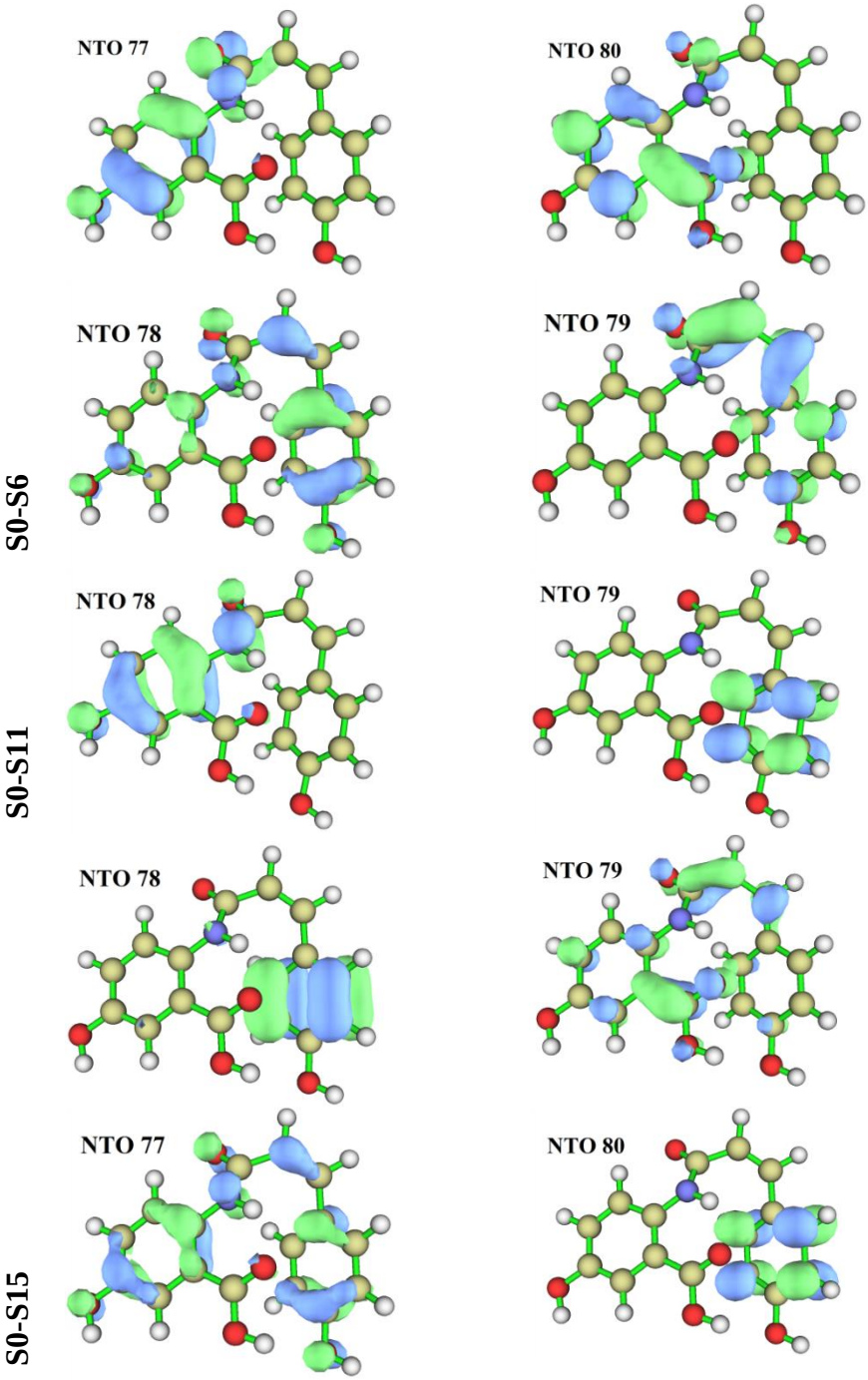

Fig.4.6. Natural transition orbital analysis of Z-**2p** in each transition states

4.3.2.1.2. Charge difference density (CDD) via electron-hole

The electron-hole analysis is a very powerful and practical set of methods to explore the characteristics of electron excitation[17, 22]. It describes the electron excitation as "hole to electron" so that it examines the distribution of "holes" as to where the electron goes from and the distribution of "electrons" as to where the electron being excited goes. The electron excitation is a local excitation (LE) or a charge transfer excitation (CT) or a Rydberg excitation (R)[17, 23]. The type of transition involved during electron transfer can be easily analyzed by the concept of electron-hole coherence. The hole and electron share the same spatial range in a LE excitation whereas the separation between hole and electron will be larger in CT so that the movement of charge density is possible from one place to another. In support of the program Multiwfn, a detailed hole-electron analysis was carried out in TDDFT calculation and only those transitions of our interest are reported here. The distance between the centroid of hole and electron or charge transfer length (D), overlapping extent of hole and electron (Sr), the average degree of the spatial extension of the hole and electron distribution (H), separation degree of hole and electron (t), and the coulomb attractive energy (E_{coul}) [17, 23–25] are fetched from hole electron analysis and included in the discussions electron transfer processes.

In the examination, hole and electron are decomposed to orbital pair contributions as well as fragment contributions and then quantitatively investigated the electron transfer distance, the degree of separation between holes and electrons, the contribution of each fragment to electron excitation, and the coulomb attractive energy.

Then for visual inspection, a heat map and isosurface representations of the excited state were also plotted.

The two-dimensional map of the transition density matrix (TDM) was also included to know electron-hole coherence in deep [26–33]. The nature of transition with help of TDM can be identified by the diagonal and off-diagonal terms. If the diagonal terms have a large magnitude implies that the corresponding atom has a large contribution to both hole and electron. So therefore the electron excitation should result in evident charge reorganization within the atom. If the off-diagonal terms have a large magnitude one atom has a large contribution to either hole/electron while meantime other atom has a large contribution to electron/hole, implying that electron excitation leads to CT from one to another. The indices of the TDM plot correspond to the atom index and the X-axis corresponds to hole position and the Y-axis for electron position. In the present instance, because all matrix elements far from the diagonal are very close to 0 (shown as dark blue), hence the long-range coupling between atoms does not contribute substantially to electronic transition as shown by TDM (Fig.4.7 & 4.8).

The fragment-based analysis of electron & hole contribution during the transition is analyzed to get a deeper insight into the involvement of fragments and atoms. For that, seven fragments are assigned namely, fragment 1(1), fragment 2 (9, 8, 10), fragment 3 (2, 3, 4, 5, 6, 7), fragment 4 (11, 12, 13), fragment 5 (14, 15), fragment 6 (16, 17, 18, 19, 20, 21), and fragment 7 (22). The number given to the fragments is atom number and the fragments selected are pictorially represented in Fig.4.9.a & Fig.4.10.a.

Table 4.4 summarizes the D, Sr, H, t, and E_{coul} of two isomers. For S0→S1 excitation of E-AVA it can be seen that the D index is very small (0.66 Å) and its value is very much less than half the length of a typical C-C bond (1.54 angstroms[34]). The Sr index value (0.72349 a.u.) is very much greater since the theoretical upper limit is 1.0, which implies that almost more than half part of the hole and electron are perfectly matched and hence can conclude that these transitions are purely a local excitation. The t index also supports this observation. Since the t index value of this transition is -0.663 Å and which is much less than 0, meaning that there is no significant separation of hole and electron distributions.

Table 4.4 Charge transfer length, overlap integral, t index, H index of E & Z isomers of **2p**.

E-AVA						
		D(Å)	Sr (a.u)	H(Å)	t(Å)	E_{coul} (eV)
Gas phase	S0→S1	0.66	0.72	3.43	-0.66	4.78
	S0→S2	0.62	0.80	4.12	-3.25	4.43
	S0→S12	0.97	0.85	3.93	-2.61	4.40
	S0→S14	0.42	0.87	4.37	-3.33	4.11
water	S0→S1	0.49	0.73	3.81	-0.79	4.55
	S0→S2	0.88	0.79	4.23	-3.06	4.31
	S0→S10	1.56	0.84	3.35	-1.40	4.74
	S0→S13	0.78	0.87	4.09	-2.87	4.27
	Z-2p					
Gas phase	S0→S2	0.61	0.74	3.08	-1.50	4.81
	S0→S6	1.17	0.77	3.10	-0.87	4.63
	S0→S11	3.82	0.53	2.79	1.84	3.72
	S0→S15	1.25	0.75	3.12	-0.84	4.54
water	S0→S2	0.59	0.77	3.21	-1.33	4.64
	S0→S6	1.02	0.75	3.15	-1.04	4.63
	S0→S10	0.87	0.74	3.34	-1.52	4.42
	S0→S12	0.71	0.81	3.22	-0.91	4.57

Under Table 4.4, for E-AVA, the D index was found to be less than one, and t values were also negative for all the excited states. Also, the overlapping extend (Sr) between hole and electron are found to be increasing for S0→S1, S0→S2, S0→S12, and S0→S14 in all the selected excited state revealing the transfer of electron by simple excitation.

For Z-**2p**, besides the S0→S2 transition, the charge transfer lengths of all transitions are greater than one. The charge transfer lengths of S0→S11 are found to be exceptionally high (3.82 Å) among other transitions from the S0 state. For the same, the t index is very much positive (1.84 Å), indicating that the separation of hole and electron is obvious, so it is more reasonable to consider S0→S11 as a CT excitation. The low value of Sr index (0.53 a.u) and H index values support the CT behavior of this transition. The other excitations possess strong coherence between hole and electron revealing these as LE excitations. The coefficients of electron coherence are found to be low for E-**2p** compared to Z-**2p** can effectively correlate with the oscillator strength. The oscillator strength of transitions of E isomer is found to be larger than Z isomer. More the electron-hole coherence, the greater the oscillator strength of the corresponding transition.

The hole-electron Coulomb attractive energy given in Table 4.4 is closely related to the electron excitation characteristics. The larger the D index is, the farther the distance between the main distribution region of hole and electron, and thus the weaker the coulomb attractive energy. From the data, it is indeed found that the Coulomb attraction energy of S0→S11 (the only CT excitation) is the smallest one of that

of all-electron excitations of E & Z isomers. While for the other excitations, since their D indices are very small and very narrow H index, it can easily imagine that the corresponding Coulomb attraction should be very strong.

The change in oscillator strength given by the UV spectrum in an aqueous medium is recreated by the concept of electron-hole coherence analysis. The oscillator strength of the S0→S1 transition increases from 0.52 to 0.80 in an aqueous medium, whereas for S0→S2 oscillator strength decreased from 0.72 to 0.62. From Table 4.4, the D index of S0→S1 changes from 0.66 to 0.49. The decrease in the D value indicates the greater overlap of orbitals in the aqueous medium, hence greater oscillator strength. Similarly for S0→S2, the D value increased from 0.62 to 0.88 Å, decreased the overlapping between orbital, and hence decreased the oscillator strength.

The indices given in Table 4.4 together with the isosurface diagrams (Fig.4.7 & 4.8) can exclusively reveal the transition properties in detail. From Fig.4.7 & 4.8, the picture given on the left is the isosurface representation of electron-hole coherence or isosurface of charge difference density (CDD) and on the right is the TDM. In the isosurface diagram, green represents the electron distribution, blue represents the hole distribution, and the isovalue has been set to be 0.002.

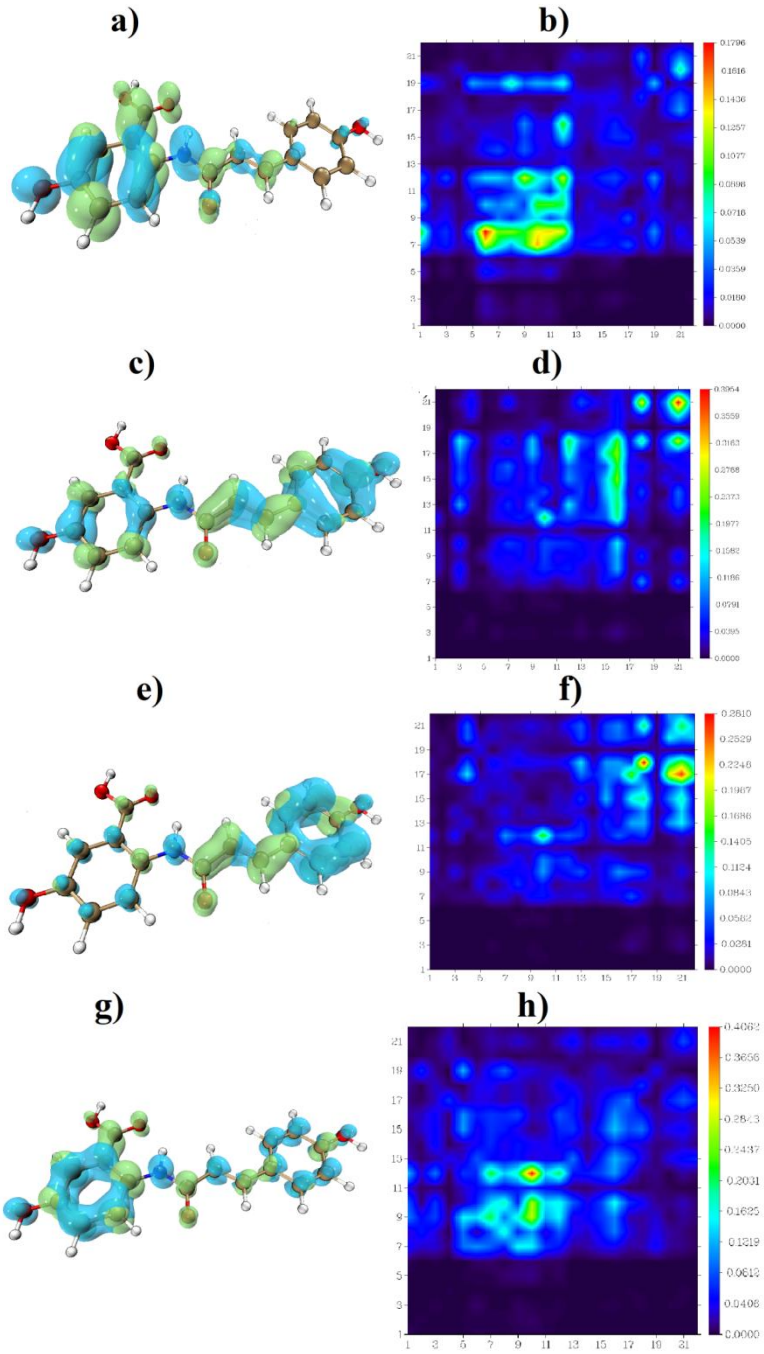

Fig.4.7. The isosurface of CDD (left) and transition density matrix, TDM (right) of excited states S1 (a & b), S2 (c & d), S12 (e & f), and S14 (g & h) of E-**2p**.

For the transition S0→S1, both the CDD and TDM diagram (Fig.4.7.a & b) shows that the excitation concentrated on the A ring. Similarly for S0→S14, the hole and electron share the same region is also on the A-ring (Fig.4.7.g & h). For the transitions S0→S2 & S0→S12, as shown by the CDD and TDM diagram, the region of maximum coherence occurs on the B-ring (Fig.4.7. c & d and Fig.4.7. e & f respectively). In the TDM map of the present instance, the elements represented by green or red color speculate the left side and it can be seen that the transition from S0→S1 and S0→S14 involves localized excitation within the atoms of the A ring. Whereas S0→S2 & S0→S12 localized excitation involves mainly B ring atoms. Hence it can also be said that S0→S1 and S0→S14 transitions are π-π* LE excitation occurring on the A ring whereas S0→S2 & S0→S12 transitions are π-π* LE excitation occurring on the B ring.

The pictorial representation of fragment-based analysis of electron-hole contribution in each excited state of E-**2p** is given in Fig. 4.9. The % of hole and electron are given in Table 4.5. For the S0→S1 transition (Fig.4. 9.b), the contribution of hole and electron emerges from fragment 3, which is the aromatic system of the A ring. The sum of contributions of the hole from carbons 2, 3, 4, 5, 6, and 7 is 55.55% and the sum of electron contribution of 52.62% reveals an overlap of hole and electron in these carbon atoms. The contribution of hole and electron respectively for S0→S2 is 39.19 % and 26.61 % emerge from carbon atoms of B-ring (fragment 6) and also for this transition fragment 3 and fragment 5 have a non-negligible contribution. But the overlapping extend of electron and hole containing orbital predominate

for fragment 6. The heat map given in Fig.4.9.c diagrammatically represents the data given in Table 4.5. For S0→S12 uniquely the B-ring containing carbon atoms contributes with the hole of 68.55% & electron of 45.28 % (Fig.4.9.d). Similarly for S0→S14 excitations, fragment 3 (A-ring carbon atoms) principally donate hole (50.38%) and electron (43.28%) (Fig.4.9.e). The advantage is that what is established in TDM and the isosurface of CDD are quantitatively metamorphosed using fragment analysis.

Fig.4.8 constitutes the isosurface diagram of electron-hole coherence of Z-**2p**. The charge transfer characteristics of S0→S11 excitation are well given in Fig.4.8.c. It is worth noting that the hole density lies on the A-ring as well as the amide moiety whereas the electron density position lies absolutely on the B aromatic ring. Hence the respective transition occurs as the charge transfer excitation is also evident from TDM. This reflects large D index values as well as small Sr and H index values given in Table 4.4. Also, Table 4.6 quantitatively explained the transition as hole density from fragments 3 and 4 (52.4% and 22.81 %) to fragment 6 of electron density of 65.34%. Fig. 4.10.d is the heat map of the S0→S11 excitation. Hence it can be CT excitation of π-π * type from A-ring and the amide moiety to B aromatic ring. In the S0-S15, the electron-hole coherence occurs at A-ring atoms (Fig.4.8. g& h). For the transitions S0→S15 involve B aromatic ring with greater electron-hole coherence and hence these transitions belong to localized excited state involving π-π* of B aromatic ring. Fig. 4.8.b & d represents the corresponding isosurface diagram and Fig. 4.10.c & e communicates it as a heat map.

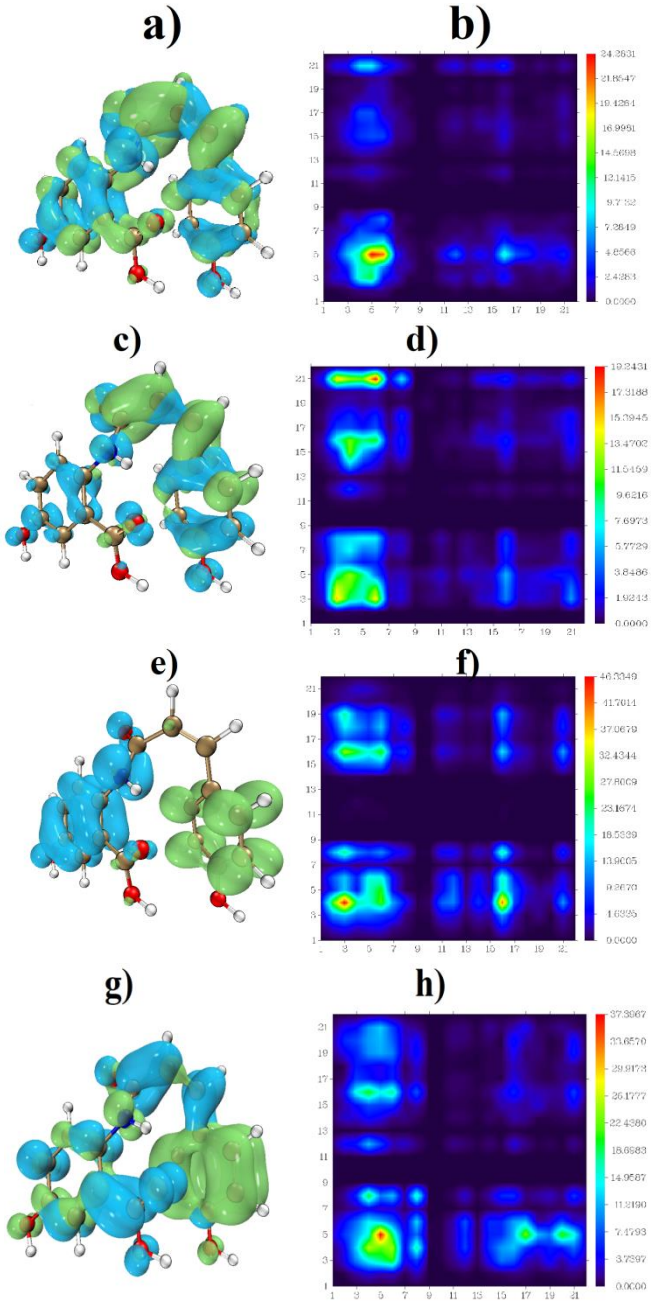

Fig.4.8. The isosurface of CDD (left) and transition density matrix, TDM (right) of excited states S2 (a & b), S6 (c & d), S11 (e & f), and S15 (g & h) of Z-**2p**.

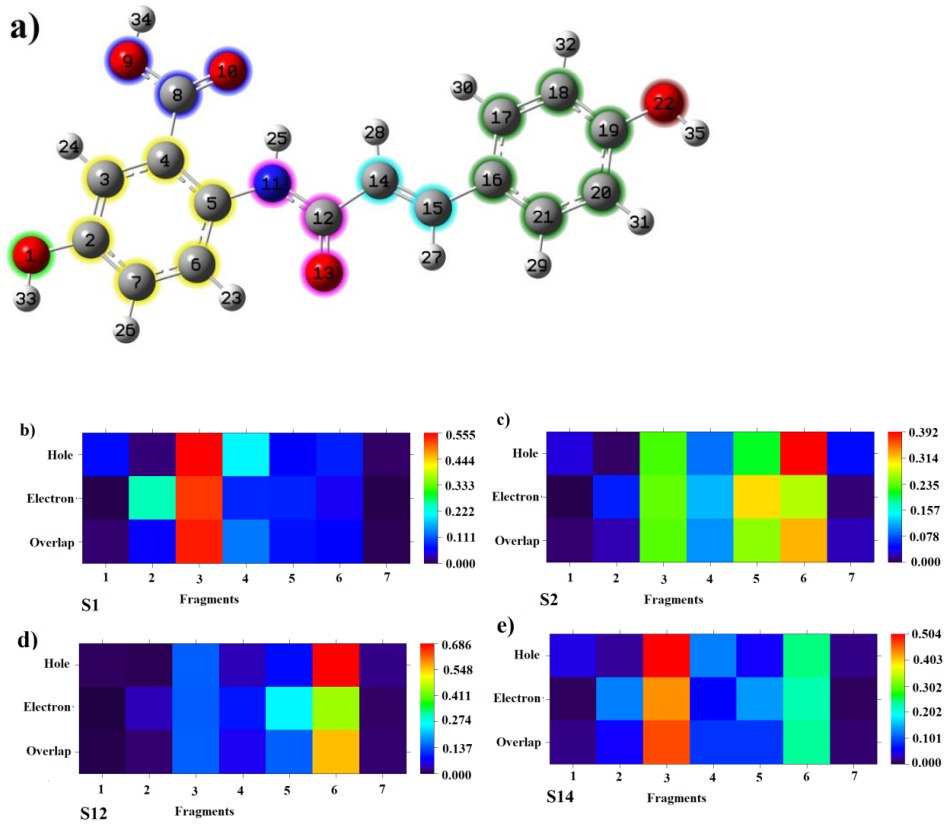

Fig.4.9. Fragment contributions ((a) the selected fragments) of hole-electron coherence in terms of heat map for excited state S1 (b), S2 (c), S12 (d), and S14 (e) of E-**2p**. The numbers in the vertical axis are fragment numbers and each fragment is constituted by the atoms. The seven fragments selected are fragment 1(1), fragment 2 (9, 8, 10), fragment 3 (2, 3, 4, 5, 6, 7), fragment 4 (11, 12, 13), fragment 5 (14, 15), fragment 6 (16, 17, 18, 19, 20, 21), and fragment 7 (22). The numbers in the bracket are atoms number corresponds to each fragments.

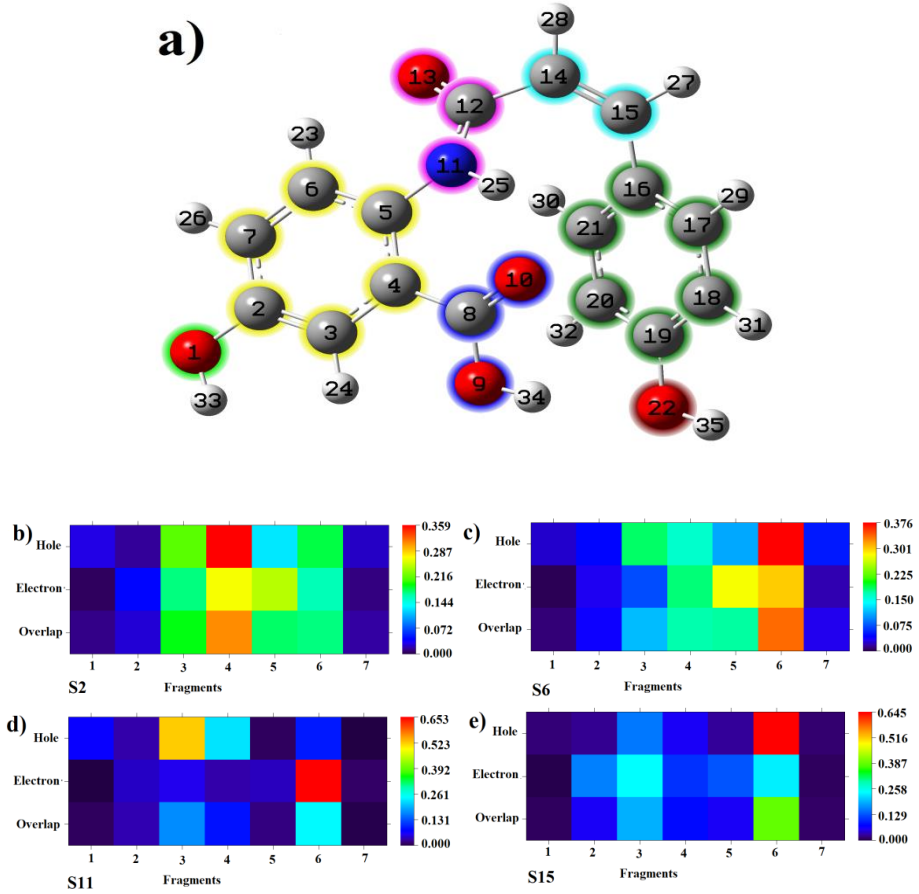

Fig.4.10. Fragment contributions ((a) the selected fragments) of hole-electron coherence in terms of heat map for excited state S2 (b), S6 (c), S11 (d), and S15 (e) of Z-**2p**. The numbers in the vertical axis are fragment numbers and each fragment is constituted by the atoms. The seven fragments selected are fragment 1(1), fragment 2 (9, 8, 10), fragment 3 (2, 3, 4, 5, 6, 7), fragment 4 (11, 12, 13), fragment 5 (14, 15), fragment 6 (16, 17, 18, 19, 20, 21), and fragment 7 (22). The numbers in the bracket are atoms number corresponds to each fragments.

Table 4.5 Contribution of fragments to hole and electron of E-**2p**

E-2p						
	S1 (%)			S2 (%)		
Fragments	Hole	Electron	Overlap	Hole	Electron	Overlap
1	6.94	0.22	1.24	2.98	0.22	0.81
2	1.41	24.71	5.91	0.73	5.64	2.03
3	**55.54**	**52.62**	**54.06**	22.51	23.49	23
4	20.51	8.47	13.18	8.95	11.95	10.34
5	6.55	8.27	7.36	20.61	30.73	25.17
6	7.91	5.23	6.43	**39.19**	**26.61**	32.29
7	0.89	0.25	0.47	4.81	1.03	2.22
	S12 (%)			S14 (%)		
1	0.95	0.24	0.47	3.98	0.73	1.7
2	0.64	4.03	1.61	2.11	12.43	5.13
3	14.81	14.46	14.63	**50.38**	**43.28**	46.7
4	3.96	9.40	6.1	12.33	5.83	8.48
5	8.59	25.12	14.69	5.13	13.82	8.42
6	**68.55**	**45.28**	55.71	24.09	22.82	23.45
7	2.25	1.11	1.58	1.74	0.79	1.17

Table 4.6 Contribution of fragments to hole and electron of Z-**2p**

Z-2p						
	S2 (%)			S6 (%)		
Fragments	Hole	Electron	Overlap	Hole	Electron	Overlap
1	2.94	0.52	1.23	2.65	0.35	0.96
2	1.53	4.3	2.56	4.54	3.4	3.93
3	21.32	17.25	19.18	18.38	7.34	11.61
4	**35.93**	**26.77**	31.02	15.98	18.18	17.04
5	12.59	24.52	17.57	10.84	28.06	17.44
6	18.35	16.11	17.19	**37.56**	**30.04**	**33.59**
7	2.33	1.06	1.57	5.18	1.96	3.18
	S11 (%)			S15 (%)		
1	7.18	0.1	0.83	1.69	0.46	0.89
2	3.1	4.12	3.58	2.32	15.88	6.06
3	**52.4**	5.42	16.85	15.34	24.23	19.28
4	22.81	3.26	8.62	5.87	10.62	7.9
5	0.96	3.98	1.96	2.65	13.02	5.87
6	9.11	**65.34**	24.4	**64.52**	**23.15**	38.65
7	0.17	1.04	0.43	1.5	0.82	1.11

4.3.2.2.ECD

Fig. 4.11 depicts the ECD spectra of both isomers. The E isomer's in gas phase and water medium spectra are depicted respectively in Fig. 4.11. a & b, while the Z isomer's gas phase and water medium spectra are shown in Fig. 4.11. c & d. The main peaks are labelled in their respective position in the spectra. The ECD spectra of the two isomers are different and it is observed that the rotator strength of the E isomer is very low and whereas that of Z isomers is very high. Also, the ECD intensity of the Z isomer is stronger than the E isomer.

The E isomer provides five peaks in the spectral signature (Fig.4.11.a)). The excited states S1 and S12 are characterized by relatively large peaks, strong oscillator strength, and opposite directions. The positive peak at 318 nm is due to the S0 →S1 transition, whereas the negative peak at 216 nm is mainly due to the transition S0 →S12. S17 is the strongest excited state in the maximum absorption peak of 193.9 nm in the absorption spectrum. Hence the excited states S1, S12, and S17 are selected for the detailed analysis. In the aqueous phase (Fig.4.11.b)), the excited states S1, S3, S6, and S12 are the same as the gas phase, and an additional negative peak due to excited state S28 is also formed. The peak at 318.2762 nm and 221.552 nm respectively corresponds to S1 and S12 excited states. Compared to the gas phase the molar absorption coefficients of S1 &S12 excited state were enhanced in a solvent phase whereas the oscillator strength of the transition is very low compared to the gas phase. The absorption of S1 doesn't shift more but is very slightly blue-shifted, whereas the S12 excited state was red-shifted. The direction of absorption peak of

the excited state, S6, changes direction with the medium, gas or water. The absorption peak direction of the S6 excited state is above the coordinate axis in the gas phase whereas below in the aqueous phase.

Fig.4.11. c & d depicts the ECD spectra of the Z isomer. Compare with the E isomer, the ECD signature of the Z isomer are high-intensity peaks with strong rotator strength and opposite directions indicating the conformational flexibility of the Z-isomer. The positive peak at 303.0 nm is due to the S1 excited state. The peak at 247.9 nm in the negative direction characterizes supremely due to the S0 →S3 transition. The positive peak at 197.2 nm is especially contributed by S0 →S19 and S0 →S23 transitions. The fourth peak (negative) at 181.7 nm is due to the S0 →S26 transition. The peak at 210 nm is also a non-negligible peak due to the excited state of S11. The excited states S1, S11, and S26 are the relatively high-intensity peak of strong rotator strength and opposite directions and hence these excited states are analyzed in detail. In the aqueous phase, the molar absorption coefficient of peaks corresponding to S1 and S26 is increased. The absorption corresponding to the S1 excited state is red shifted to 310.9 nm from the gas phase (303.0 nm), whereas blue shifted slightly corresponding to 180.9 nm from 181.7 nm of the gas phase. The common excitation to reveal excited state properties between gas phase and water medium are S1 and S19 excited states. Hence the S1, S11, and S26 excited states were selected for further discussion. Since the strength of ECD spectra can reveal more in the sense of electric-magnetic interactions within the molecule [27–30], when it is excited by light, the electric-magnetic dipole moment density analysis has been carried out in relevant transitions for both isomers.

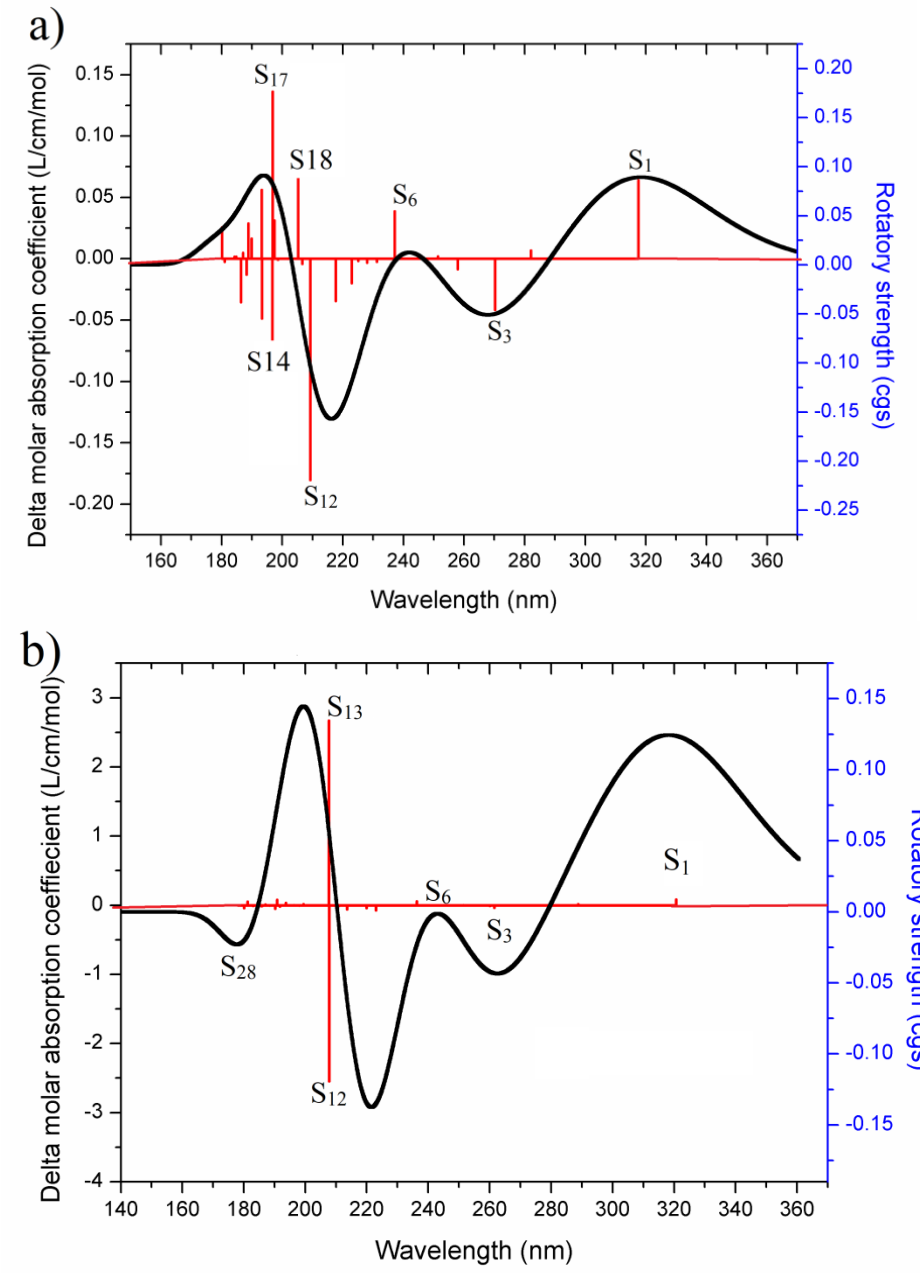
a)
Delta molar absorption coefficient (L/cm/mol)
Rotatory strength (cgs)
Wavelength (nm)
S17
S18
S6
S1
S14
S3
S12
b)
Delta molar absorption coefficient (L/cm/mol)
Rotatory strength (cgs)
Wavelength (nm)
S13
S6
S1
S3
S28
S12

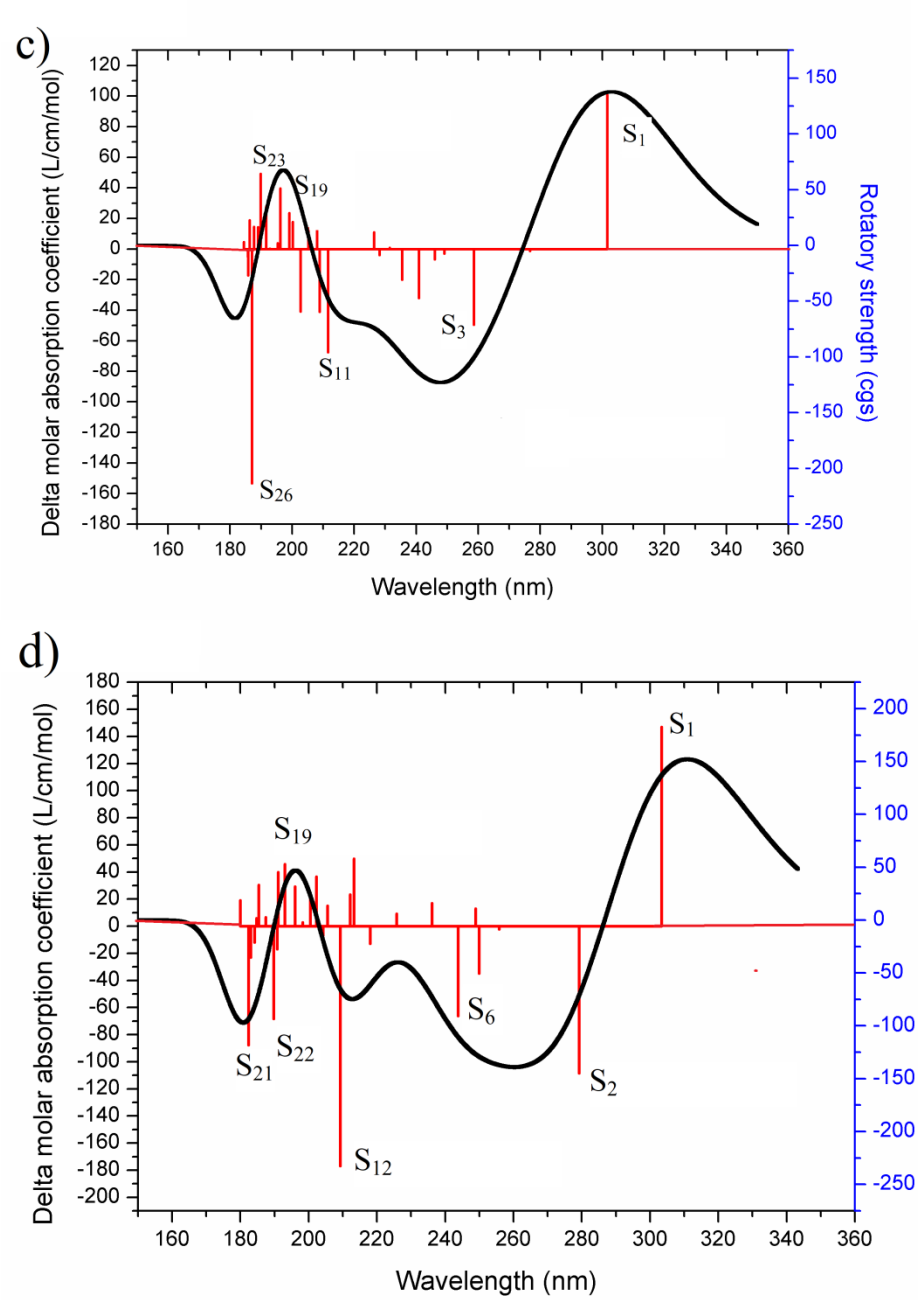

Fig.4.11. The ECD spectra of compounds E-**2p** a) in gas phase b) in aqueous phase, and Z-**2p** c) in gas phase d) aqueous phase.

4.3.2.2.1. The electric-magnetic interaction of E-**2p**

The interactions within molecules alter when they are stimulated by photons of various wavelengths. The excited states of S1, S12, and S17 are chosen to analyze the contribution of electric–magnetic component interaction in the ECD signature. Accordingly, S1 (positive peak) and S12 (negative peak) are the strongest intensity absorption and are characterized by relatively large peaks, strong oscillator strength, and opposite directions. The S17 is the strongest excited state in the maximum absorption spectrum and it corresponds to the positive peak. Since the ECD spectrum, the rotator strength theoretically will be [35, 36]

$$I \propto \left|\left\langle \varphi_j \left| \mu_e \right| \varphi_i \right\rangle E\right|^2 + \left|\left\langle \varphi_j \left| \mu_e \right| \varphi_i \right\rangle \left\langle \varphi_j \left| \mu_m \right| \varphi_i \right\rangle B\right|^2$$

Where μ_e is the transition electric dipole moment and μ_m is the transition magnetic dipole moment. The first term and the second term respectively characterize light absorption and circular dichroism. The physical mechanism of the ECD by the electric and magnetic interactions can be visualized in term $\left\langle \varphi_j \left| \mu_e \right| \varphi_i \right\rangle \left\langle \varphi_j \left| \mu_m \right| \varphi_i \right\rangle$s of, which is the tensor product of electric ($\left\langle \varphi_j \left| \mu_e \right| \varphi_i \right\rangle$) and magnetic components ($\left\langle \varphi_j \left| \mu_m \right| \varphi_i \right\rangle$). The $\left\langle \varphi_j \left| \mu_e \right| \varphi_i \right\rangle$ X $\left\langle \varphi_j \left| \mu_m \right| \varphi_i \right\rangle$ can be calculated with a generalized Kronecker product (also called tensor product) of $\mu_e \otimes \mu_m$ where μ_e is $\left[e_x, e_y, e_z\right]^T$ and μ_m is $\left[m_x, m_y, m_z\right]^T$ in three-dimensional real spaces. The tensor product has nine components, and the matrix composed of these nine components is not symmetric. The square of

the magnitude of the tensor product of the transition electric dipole moment and the transition magnetic dipole moment ($\left|\langle\varphi_j|\mu_e|\varphi_i\rangle\langle\varphi_j|\mu_m|\varphi_i\rangle\right|^2$) let out directly to the peak intensity in the ECD spectrum.

A matrix diagram of the atomic basis function contribution fill of the transition electric dipole moment density and the transition magnetic dipole moment density are given in Fig. 4.12. (a-f). In the isosurface (isovalue 0.01) representation of transition electric dipole moment densities, the positive and negative parts are correspondingly represented by green and mauve colors, while the purple and cyan in the isosurface in the transition magnetic dipole moment densities respectively give the positive and negative parts. Table 4.7 shows the interactions of transition electric and magnetic coupling for Z- AVA in ECD. From the ECD spectra of the E isomer, it could be understandable that its oscillator strength of it is very low compared to the Z isomer and which can be very clearly depicted in Table 4.7 and Table 4.8. The magnitude of the interaction between electric and magnetic components $\left|\langle\varphi_j|\mu_e|\varphi_i\rangle\langle\varphi_j|\mu_m|\varphi_i\rangle\right|^2$ is very low compared with that of the Z isomer. Hence it can be said that the product can explain the ECD spectra of the isomers

Table 4.7 The interactions of transition electric and magnetic coupling for E- **2p** in ECD

Excited-state		$\langle \varphi_j \mid \mu_e \mid \varphi_i \rangle$	$\langle \varphi_j \mid \mu_m \mid \varphi_i \rangle$	$\langle \varphi_j \mid \mu_e \mid \varphi_i \rangle \langle \varphi_j \mid \mu_m \mid \varphi_i \rangle$	$\lvert \langle \varphi_j \mid \mu_e \mid \varphi_i \rangle \times \langle \varphi_j \mid \mu_m \mid \varphi_i \rangle \rvert^2$
Gas phase					
	X	2.231284	-0.000274		
S1	Y	0.717609	-0.000199	0.000660	4.31163×10^{-07}
	Z	-0.000065	-1.491510		
	X	-1.349450	0.000150		
S12	Y	-0.286479	0.000481	-0.776283	0.602616
	Z	-0.000372	-2.710924		
Aqueous phase					
	X	2.825781	0.000016		
S1	Y	0.672036	-0.000574	0.00012	1.5293×10^{-08}
	Z	-0.000139	-1.560225		
	X	0.031318	0.046446		
S12	Y	-0.046076	-0.232296	- 0.012985	0.000169
	Z	0.029005	0.028499		

The peak corresponding to the S1 lies above the coordinate axis in the ECD spectra representing it as a positive peak. Accordingly, to Table 4.7, the major contribution from this transition is owned by the electric components of dipole moment density, $(\mu_e)x$, in the X component. The positive value of which is consistent with the peak. The transition corresponding to the S12 is a negative peak and the major contribution of it comes from the magnetic component in the Z direction, $(\mu_m)z$, and it is the most intense peak in ECD. The peak is also explained by the electric and magnetic interaction with one to one relationship. The strongest excited state is the S12 and the next highest S1 is harmonious with the ECD spectra. The matrix representation given in Fig. 4.12 a & b respectively is the electric and magnetic dipole

moment densities interaction in of S1 excited state in ECD of XYZ component. Fig.4.12 a & b also replicate Table 4.7, where the contribution of the electric component in X direction during the excitation of S1 in ECD is depicted. The major contribution of S1 transition occurs from the A-aromatic system including hydroxyl and carboxylic functional group and a relatively non-negligible contribution is also provided by the B-aromatic ring in ECD spectra. For S12 excitation, the major contribution occurs from the Z-component of transition magnetic moment density and which is contributed by the B-aromatic ring including the hydroxyl group (Fig. 4.12. c & d). Hence Fig.4.12 is the mimeograph of Table 4.7. The positive peak at 193.9 nm is mainly contributed by the S17 excited state and the transition X-component of transition magnetic dipole moment contributes and is influenced by the B- aromatic ring and hydroxyl group.

In the aqueous phase, the transition intensity of S1 and S12 are very low compared to the gas phase. The ECD curve in Fig.4.11.b depicts the low intensity of S1 excitation compared with the gas phase. The intensity of the S12 excited state is higher than S1 as observed in ECD also reveals Table 4.7. For S1 excitation as gas phase excitation, the major contribution of concentrated in the X component of electric dipole moment and the X component of magnetic dipole moment contribution is lower than the same in the gas phase. The Z-component of magnetic dipole moment is greater than the gas phase in the solvent medium. For the case of the S12 excited state, the components are very lower than the gas phase for both electric and magnetic components.

The major contribution obtained in magnetic dipole moment was in Z-component in the gas phase and the Y component in the solvent phase.

The tensor products given in Table 4.7 are in consistent with ECD spectral signature in both the media. According to ECD spectra S1 is a positive peak because it lies above the coordinate axis and the transition corresponding to S12 is a negative peak because it is below the coordinate axis.

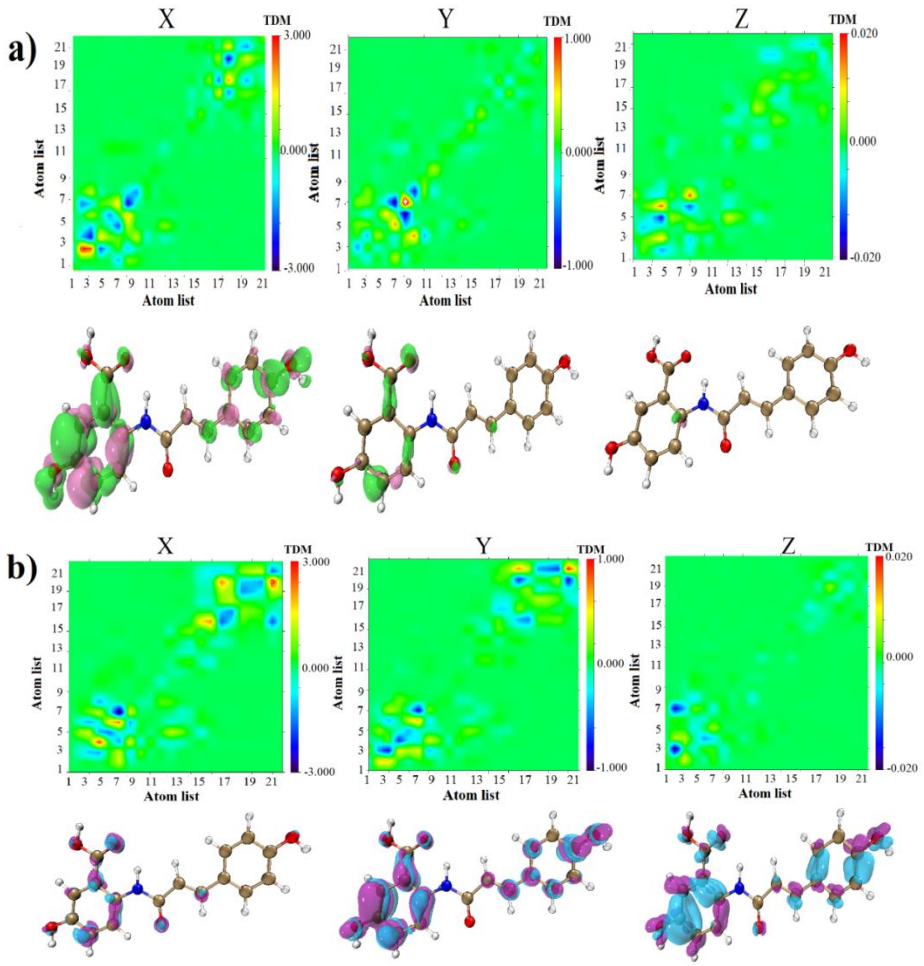

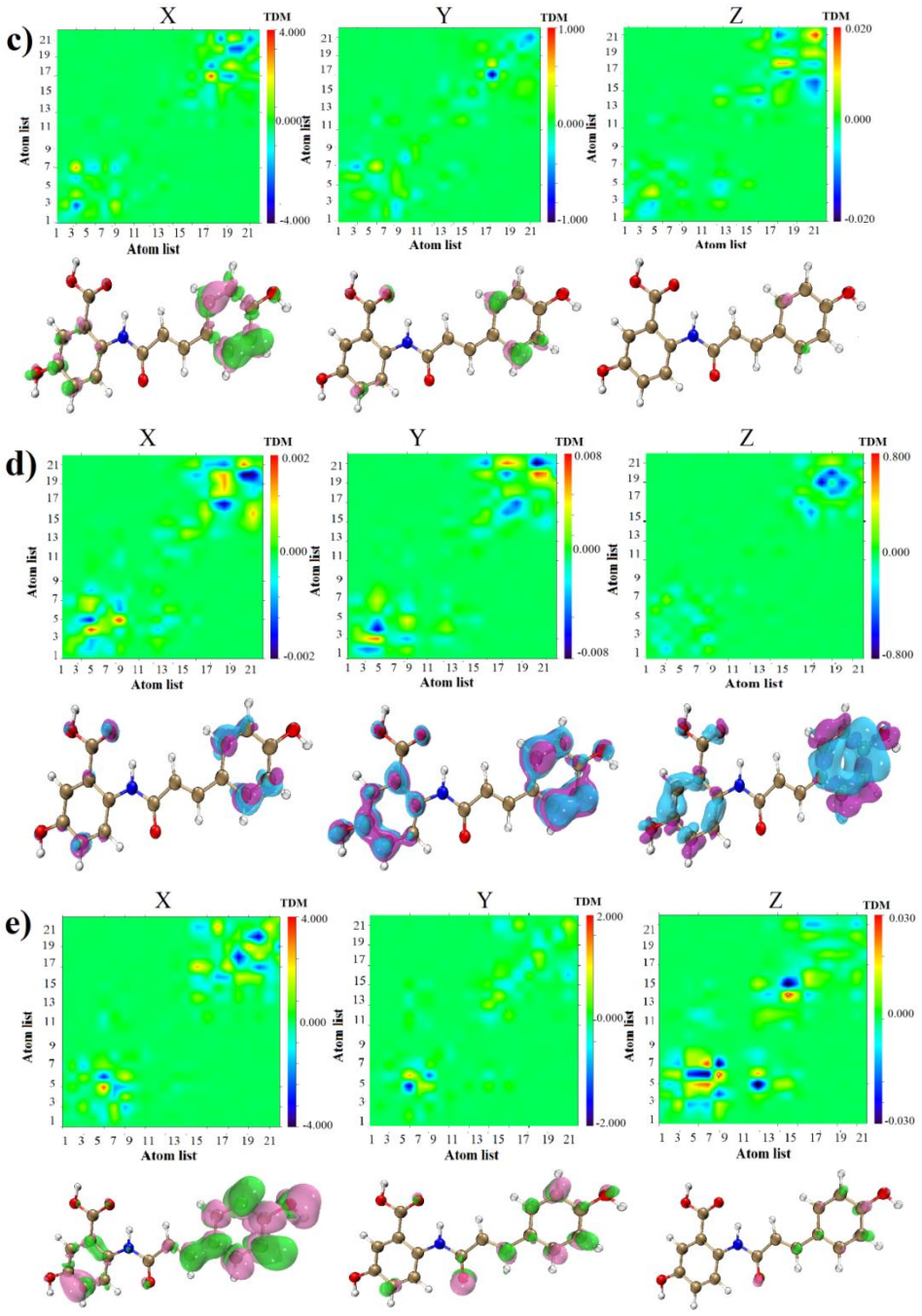
c)
X
Y
Z
TDM
Atom list
d)
e)

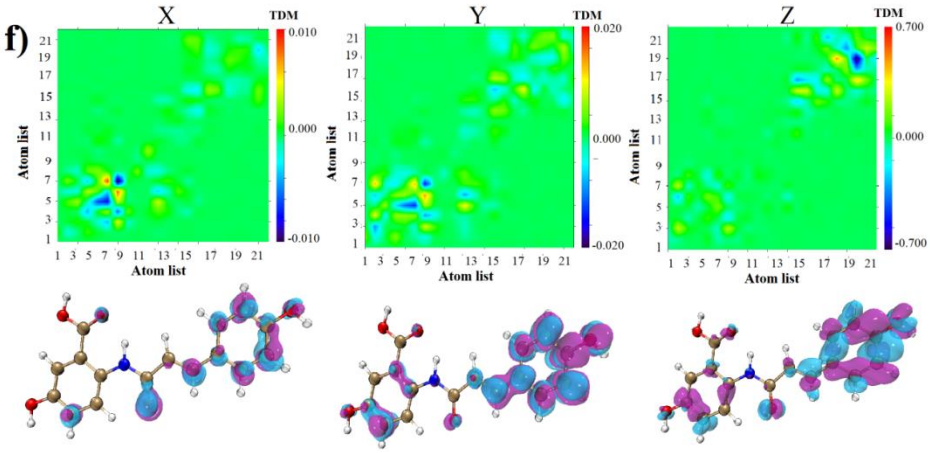

Fig 4.12. Transition electric dipole moment densities and transition magnetic dipole moment densities for excited state of S1 (a & b respectively), S12 (c & d respectively), and S17 (e & f respectively). The electric dipole moment densities are represented by the green and mauve colours (positive and negative respectively) and transition magnetic dipole moment density by the purple and cyan (positive and negative respectively) and isovalues is set to be 0.01.

4.3.2.2.2. The electric-magnetic interaction of Z-**2p**

The transition electric/magnetic dipole moment density diagrams for Z- **2p** in the X, Y, and Z directions in cartesian components by two and three-dimensional diagrams (isovalue 0.02), are provided in Fig.4.13. Table 4.8 lay out the interactions of transition electric and magnetic coupling for Z- **2p** in ECD. In line with the absolute value of the tensor product given in Table 4.5 was found to be consistent with the peak strength of ECD. The higher the magnitude, $\left|\left\langle \varphi_j \left| \mu_e \right| \varphi_i \right\rangle \times \left\langle \varphi_j \left| \mu_m \right| \varphi_i \right\rangle\right|^2$, the greater the peak strength. By comparing the value size $\left|\left\langle \varphi_j \left| \mu_e \right| \varphi_i \right\rangle \times \left\langle \varphi_j \left| \mu_m \right| \varphi_i \right\rangle\right|^2$ given in Table 4.8, we can also get the same conclusion as the ECD spectra. The mentioned quantity

reveals that S26 has greater intensity followed by S1 and S11 are roughly equal to the ECD signature.

It is found that the transition magnetic dipole moment density of excited states S1 and S26 is greater than that of transition electric dipole moment density (Table 4.8) and the magnetic dipole moment density lies in the Z- component of Cartesian coordinates, $(\mu_m)z$. For S11 excited states, the transition electric dipole moment density has a greater contribution towards the X component, $(\mu_e)x$. The maximum peak intensity found for S26 (Table 4.8) was consistent with the ECD spectra and the next highest intense transition occurs in S1 excitation. The ECD corresponds to the S11 excited state as a low-intensity transition and the peak intensity was consistent with the tensor product of transition electric and magnetic components (Table 4.8).

For S1 and S11 excited states, the sign of the component of maximum contribution is in correlation with the direction peak in ECD spectra. For the S1 excite state the maximum contribution was owned by the Z component of the magnetic dipole moment and its positive values were found to be consistent with the positive peak corresponding to the S1 transition. Like that, for S11 transition, the electric component of transition dipole moment in x direction has maximum contribution with negative charge also consistent with the negative peak in ECD. But S26 transition the Z component of transition magnetic dipole moment density has a maximum contribution and its value is positive, but the Y component of both the electric and magnetic dipole moments are competently negative and coupling of these Y components will the reason for the negative

transition corresponding to S26 excited state. To explain the positive and negative values of ECD, the tensor product of transition electric dipole moment and transition magnetic dipole moment is given in Table 4.8 and which gives one–to–one correspondence with the ECD signature. In ECD it can be seen that the S1 excitation occurs in the upper part of the coordinate axis whereas the S11 and S26 in the lower part. The tensor product of S1 is positive and S11 and S26 as negative peaks.

The 2D matrix and 3D density map are given in Fig.4.13 for Z-**2p**. The highest peak intensity owned by S26 has a greater contribution from magnetic dipole moment density, $(\mu_m)z$, itself has a greater contribution towards excitation. The isosurface and the 2D plot given in Fig.4.13 (e&f) disclose the observation. During excitation, for the S26 excited state, the $(\mu_m)z$ components concentrate on the B-aromatic ring including hydroxyl functional group, alkene moiety, and carbonyl oxygen. The Y components of the transition electric and transition magnetic moments, $(\mu_e)y$ and $(\mu_m)y$, has competing benefaction with$(\mu_m)z$ and here the redistribution of electron and hole density ensures enormously from the alkene carbon and the carbonyl oxygen. Likely, for the S1 transition, the $(\mu_m)z$ components concentrate mainly on the A-aromatic ring including the hydroxyl functional group. Hence during excitation and the redistribution of electron and hole density ensures enormously from the A aromatic ring (Fig.4.13. a&b). The electric dipole moment of the X component for the excited state S11 (Fig.4.13. c&d) has a greater contribution during excitation and the A- and B-ring containing aromatic carbon atoms particularly has a great

influence on the redistribution of electron and hole density after light excitation.

Table 4.8 The interactions of transition electric and magnetic coupling for Z- **2p** in ECD

Excited state		$\langle\varphi_j\|\mu_e\|\varphi_i\rangle\times\langle\varphi_j\|\mu_m\|\varphi_i\rangle$		$\langle\varphi_j\|\mu_e\|\varphi_i\rangle\langle\varphi_j\|\mu_m\|\varphi_i\rangle$	$\left\|\langle\varphi_j\|\mu_e\|\varphi_i\rangle\times\langle\varphi_j\|\mu_m\|\varphi_i\rangle\right\|^2$
Gas phase					
	X	0.325550	0.112740		
S1	Y	0.684404	0.055663	0.45151	0.203861
	Z	-0.302266	1.741211		
	X	-0.960964	-0.262869		
S11	Y	0.049463	0.066044	-0.292199	0.085380
	Z	-0.173070	-0.209883		
	X	0.519804	0.4664801		
S26	Y	-0.737272	-0.594030	-0.601753	0.362107
	Z	-0.048821	1.611741		
			Aqueous medium		
	X	0.468291	0.142778		
S1	Y	0.682528	-0.000985	0.56858	0.323288
	Z	-0.334975	1.894988		

The electric and magnetic components of transition dipole moment density in the aqueous phase were given in Table 4.8, where the common transition S1 was analyzed. In this case, in the solvent phase or the polar medium, the transition intensity of the S1 transition was increased as obtained in ECD spectra. As that of the gas phase, the Z component of transition magnetic dipole moment has a greater contribution during the excitation. The X, Y, and Z component of transition electric dipole moment density also provides non-negligible contribution during excitation.

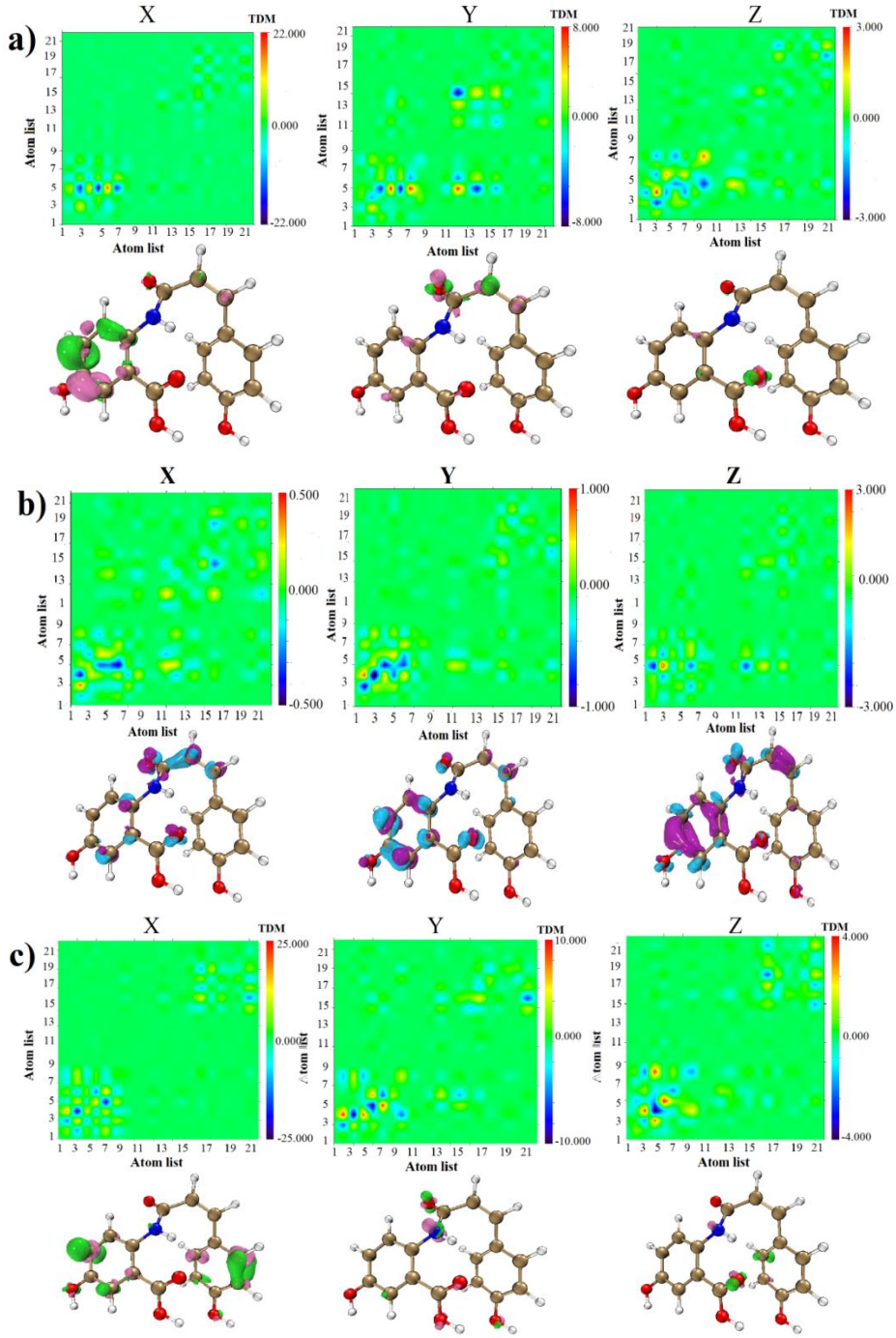
a)
X
Y
Z
TDM
Atom list
b)
X
Y
Z
TDM
Atom list
c)
X
Y
Z
TDM
Atom list

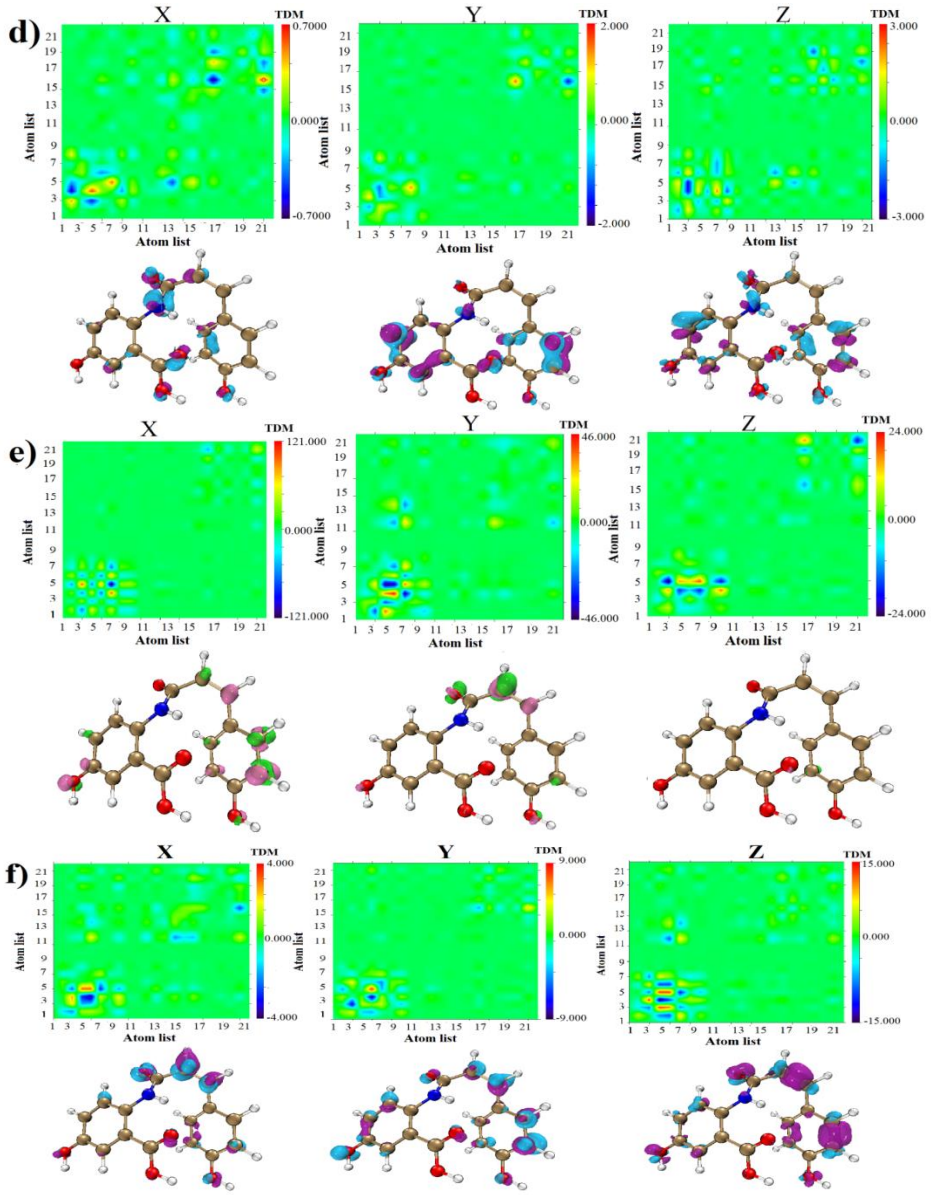

Fig 4.13. Transition electric dipole moment densities and transition magnetic dipole moment densities for excited state S1 (a & b respectively), S11 (c & d respectively), and S26 (e & f respectively). The electric dipole moment densities are represented by the green and mauve colours (positive and negative respectively) and transition magnetic dipole moment density by the purple and cyan (positive and negative respectively) and isovalues is set to be 0.01

4.4. Conclusions

Using 2D and 3D visualization methods, we analyzed the physical mechanism of interaction between light and matter of UV-Vis and ECD processes in two isomers of AVs, E-**2p**, and Z-**2p**. These cinnamoyl anthranilic acid derivatives are secondary metabolites found in oats (Avena Sativa. L). AVs are a good option for skin protection due to their high potential antioxidant activity and absorbance of compounds in the UV region. For a high-quality theoretical approach, the M06-2X /6-31+G (d, p) level of theory was used. The calculations of excited states and UV and ECD were obtained by performing the TD-DFT calculation method by using IEF-PCM as the solvent models. A well-defined UV with high-intensity peaks was obtained for E- **2p** and whereas ECD for Z-**2p**. Also found that E-**2p** can be a good UVB absorber. Since Z-**2p** absorbs only in the UVC region, wide application of these molecules especially in the cosmetic industry as UV filters or UV blockers can be excluded. The transition properties of both the molecules are well characterized with help of the hole electron concept of electron excitation. The entire prominent transitions exhibit localized orbitals except for the S0-S11 of Z-**2p**. The S0-S11 of Z-**2p** possesses charge transfer transition. The TDM and CDD plot exactly communicates the transition type diagrammatically. The increase in the oscillator strength as the increase in the polarity of solvent is also well recreated by the hole electron concept. The hole and electron are decomposed to orbital pair contributions as well as fragment contributions and then quantitatively investigated the electron transfer distances. Moreover, absence of dominant transitions in MO orbitals,

the NTO orbital analysis was also carried out in each transition and made it more explainable. The high-intensity peaks with strong rotator strength and opposite directions of the excited states of Z isomers indicate the conformational flexibility of Z-isomer. Also, the interaction mechanism in ECD is quantitatively revealed by the transition electric dipole moment, transition magnetic dipole moment, and their tensor product. It can be found that these values are in one-to-one correspondence with the ECD spectra.

References

1. Garcia RD, Maltarollo VG, Honório KM, Trossini GHG (2015) Benchmark studies of UV–vis spectra simulation for cinnamates with UV filter profile. J Mol Model 21:150. https://doi.org/10.1007/s00894-015-2689-y
2. Bratt K, Sunnerheim K, Bryngelsson S, et al (2003) Avenanthramides in Oats (Avena sativa L.) and Structure−Antioxidant Activity Relationships. J Agric Food Chem 51:594–600. https://doi.org/10.1021/jf020544f
3. Yang J, Ou B, Wise ML, Chu Y (2014) In vitro total antioxidant capacity and anti-inflammatory activity of three common oat-derived avenanthramides. Food Chem 160:338–345. https://doi.org/https://doi.org/10.1016/j.foodchem.2014.03.059
4. Dimberg LH, Theander O, Lingnert H (1993) Avenanthramides--a group of phenolic antioxidants in oats. Cereal Chem 70:637–641
5. Chu Y-F, Wise ML, Gulvady AA, et al (2013) In vitro antioxidant capacity and anti-inflammatory activity of seven common oats. Food Chem 139:426–431. https://doi.org/https://doi.org/10.1016/j.foodchem.2013.01.104
6. Turrini E, Maffei F, Milelli A, et al (2019) Overview of the Anticancer Profile of Avenanthramides from Oat. Int. J. Mol. Sci. 20
7. Peterson DM, Hahn MJ, Emmons CL (2002) Oat avenanthramides exhibit antioxidant activities in vitro. Food Chem 79:473–478. https://doi.org/https://doi.org/10.1016/S0308-8146(02)00219-4
8. Mierina I, Stikute A, Mishnev A, Jure M (2019) An alternative way to analogues of avenanthramides and their antiradical activity. Monatshefte für Chemie - Chem Mon 150:85–101. https://doi.org/10.1007/s00706-018-2288-6
9. Collins FW (1989) Oat phenolics: avenanthramides, novel substituted N-cinnamoylanthranilate alkaloids from oat groats and hulls. J Agric Food Chem 37:60–66. https://doi.org/10.1021/jf00085a015

10. Collins FW, Mullin WJ (1988) High-performance liquid chromatographic determination of avenanthramides, n-aroylanthranilic acid alkaloids from oats. J Chromatogr A 445:363–370. https://doi.org/https://doi.org/10.1016/S0021-9673(01)84548-9

11. Kakegawa H, Mitsuo N, Matsumoto H, Satoh T, Akagi M TK (1985) Hyaluronidase-inhibitory and anti-allergic activities of the photo-irradiated products of tranilast. Chem Pharm Bull 33:3738–44. https://doi.org/10.1248/cpb.33.3738

12. M. J. Frisch, G. W. Trucks, H. B. Schlegel, G. E. Scuseria, M. A. Robb, J. R. Cheeseman, G. Scalmani, V. Barone, G. A. Petersson, H. Nakatsuji, X. Li, M. Caricato, A. V. Marenich, J. Bloino, B. G. Janesko, R. Gomperts, B. Mennucci, H. P. Hratchian, J. V. and DJF (2016) Gaussian 16, Revision C.01

13. Truhlar YZ and DG (2008) The M06 suite of density functionals for main group thermochemistry, thermochemical kinetics, noncovalent interactions, excited states, and transition elements: two new functionals and systematic testing of four M06-class functionals and 12 other function. Theor Chem Acc 120:215–41. https://doi.org/10.1007/s00214-007-0310-x

14. Miertuš S, Scrocco E, Tomasi J (1981) Electrostatic interaction of a solute with a continuum. A direct utilizaion of AB initio molecular potentials for the prevision of solvent effects. Chem Phys 55:117–129. https://doi.org/https://doi.org/10.1016/0301-0104(81)85090-2

15. Martin RL (2003) Natural transition orbitals. J Chem Phys 118:4775–4777. https://doi.org/10.1063/1.1558471

16. Liu Z, Lu T, Chen Q (2020) An sp-hybridized all-carboatomic ring, cyclo[18]carbon: Electronic structure, electronic spectrum, and optical nonlinearity. Carbon N Y 165:461–467. https://doi.org/https://doi.org/10.1016/j.carbon.2020.05.023

17. Lu T, Chen F (2012) Multiwfn: A multifunctional wavefunction analyzer. J Comput Chem 33:580–592. https://doi.org/10.1002/jcc.22885

18. Humphrey W, Dalke A, Schulten K (1996) VMD: Visual molecular dynamics. J Mol Graph 14:33–38. https://doi.org/https://doi.org/10.1016/0263-7855(96)00018-5

19. Ajmala Shireen P, Abdul Mujeeb VM, Muraleedharan K (2017) Theoretical insights on flavanones as antioxidants and UV filters: A TDDFT and NLMO study. J Photochem Photobiol B Biol 170:286–294. https://doi.org/10.1016/j.jphotobiol.2017.04.021

20. J Clayden, N Greeves, S Warren PW (2001) Organic chemistry, first. university press, Oxford

21. Uv H, Uva A Ultraviolet (UV) Radiation. 1–11

22. B. FR, Prasana JC, Muthu S, Abraham CS (2019) Molecular docking studies, charge transfer excitation and wave function analyses (ESP, ELF, LOL) on valacyclovir : A potential antiviral drug. Comput Biol Chem 78:9–17. https://doi.org/https://doi.org/10.1016/j.compbiolchem.2018.11.014

23. Le Bahers T, Adamo C, Ciofini I (2011) A Qualitative Index of Spatial Extent in Charge-Transfer Excitations. J Chem Theory Comput 7:2498–2506. https://doi.org/10.1021/ct200308m

24. Kraner S, Scholz R, Plasser F, et al (2015) Exciton size and binding energy limitations in one-dimensional organic materials. J Chem Phys 143:244905. https://doi.org/10.1063/1.4938527

25. Kraner S, Prampolini G, Cuniberti G (2017) Exciton Binding Energy in Molecular Triads. J Phys Chem C 121:17088–17095. https://doi.org/10.1021/acs.jpcc.7b03923

26. Li Y, Ullrich CA (2011) Time-dependent transition density matrix. Chem Phys 391:157–163. https://doi.org/https://doi.org/10.1016/j.chemphys.2011.02.001

27. Ma J, Sun M (2020) Photo-physical properties of vinigrol revealed by two-photon absorption, electronic circular dichroism, Raman spectroscopy and Raman optical activity. Chem Phys Lett 755:137798. https://doi.org/https://doi.org/10.1016/j.cplett.2020.137798

28. Mu X, Chen X, Wang J, Sun M (2019) Visualizations of Electric and Magnetic Interactions in Electronic Circular Dichroism and Raman Optical Activity. J Phys Chem A 123:8071–8081. https://doi.org/10.1021/acs.jpca.9b06674

29. Wang X, Yan P, Mu X (2020) Optical properties of S2 and S3

excited states of protonated schiff-base retinal chromophores in TPA, ECD and ROA. Spectrochim Acta Part A Mol Biomol Spectrosc 228:117532. https://doi.org/https://doi.org/10.1016/j.saa.2019.117532

30. Tian C, Zhang Y, Mu X, et al (2020) Optical physics on chiral brominated azapirones: Bromophilone A and B. Spectrochim Acta Part A Mol Biomol Spectrosc 242:118780. https://doi.org/https://doi.org/10.1016/j.saa.2020.118780
31. Lu C, Yu J, Sheng H, et al (2022) Linear and Nonlinear Photon-Induced Cross Bridge/Space Charge Transfer in STC Molecular Crystals. Nanomaterials 12
32. Lu C, Chen P, Sheng H, et al (2022) Physical mechanism on linear spectrum and nonlinear spectrum in double helical carbon nanomolecule–infinitene. Spectrochim Acta Part A Mol Biomol Spectrosc 282:121674. https://doi.org/https://doi.org/10.1016/j.saa.2022.121674
33. Lu C, Li N, Jin Y, et al (2022) Physical Mechanisms of Intermolecular Interactions and Cross-Space Charge Transfer in Two-Photon BDBT-TCNB Co-Crystals. Nanomaterials 12
34. Wikipedia contributors Carbon–carbon bond. In: Wikipedia, Free Encycl.
35. Warnke I, Furche F (2012) Circular dichroism: electronic. WIREs Comput Mol Sci 2:150–166. https://doi.org/https://doi.org/10.1002/wcms.55
36. Bruhn T, Schaumlöffel A, Hemberger Y, Bringmann G (2013) SpecDis: Quantifying the Comparison of Calculated and Experimental Electronic Circular Dichroism Spectra. Chirality 25:243–249. https://doi.org/https://doi.org/10.1002/chir.22138

Appendix 4

A1. Conformational analysis of Z-isomer of 2p

A detailed investigation of the E isomer of 2p is discussed in the chapter 3. The conformational analysis of Z-isomer of **2p** was checked using a dihedral scan at key locations, as this appears to be important in forward search. The dihedral angles in 12 steps of 30° from 0 to 360° was carried out at the B3LYP/3-21G level of theory. The dihedrals Φ (O9', C9', C7, C8), Φ (C6, C5, O5, H5), and Φ (C2', C1', C7, C8) are included in Fig.A.4.1. The Z isomer of the compound first formed from the E isomer and lowest energy conformer of the compound investigated by the mentioned dihedral scanning procees. The lowest energy conformer thus obtained subjected to geometry optimisation using M06-2X/6-31+G (d,p) level of theory.

a)

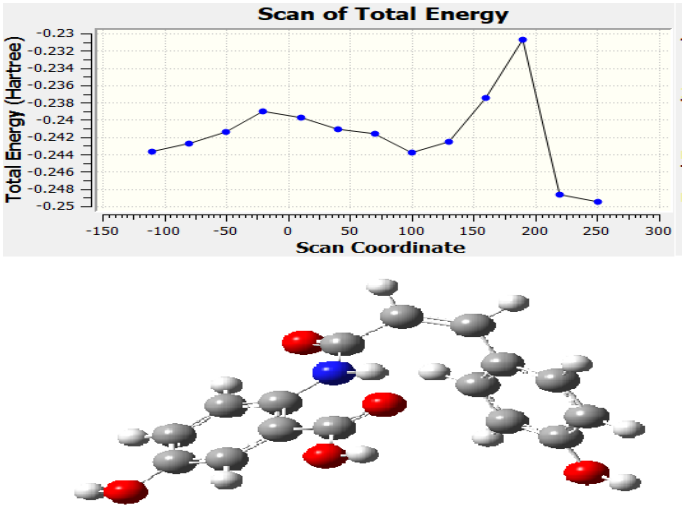

b)

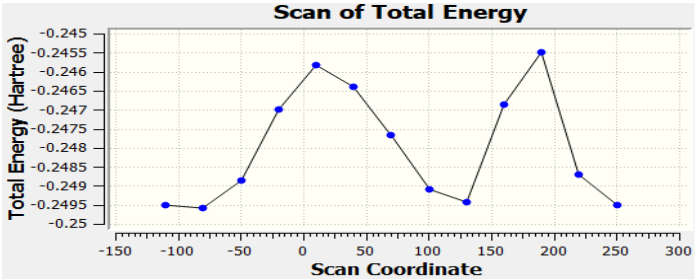

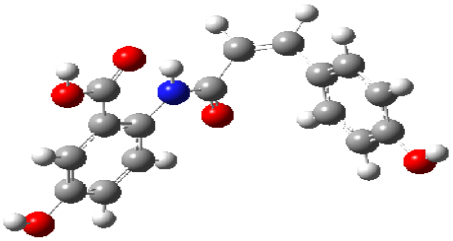

c)

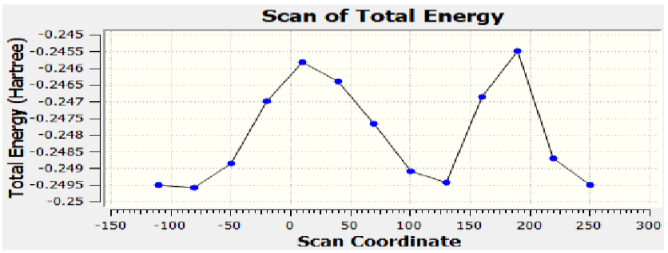

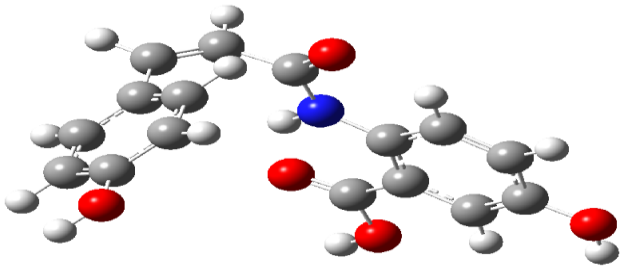

Fig.A.4.1. The PES of Z-**2p** on dihedrals **a)** Φ (O9', C9', C7, C8), Φ **b)** (C6, C5, O5, H5), and **c)** Φ (C2', C1', C7, C8)

Chapter 5

Quantum chemical investigation on Avenanthramides as antioxidants and UV filters

- ✓ *The antioxidant activity of selected Avenanthramides was explored using three primary mechanism-HAT, SET-PT, and SPLET*
- ✓ *The chapter devoted particular attention to how the catechol, guaiacyl, and carboxyl groups affected the activity and the mechanism.*
- ✓ *The UV filtering capacity are discussed as an application of the studied molecules*

5.2.Introduction

Oxidation reactions, which are often begun by radicals, are key processes in biological systems[1]. Radical reactions are thought to be the start of many pathological disorders, and lipid oxidation is one of the main reasons for the deterioration of numerous materials, including food. Any molecule that, when present in small amounts compared to an oxidizable substrate's concentrations, greatly slows down or stops that substrate from oxidizing is referred to as an antioxidant[2]. To scavenge free radicals, phenolic antioxidants work primarily by giving a hydrogen atom to a radical[3]. The effectiveness is determined by the quantity of hydrogen-donating hydroxyl groups present as well as structural factors that stabilise the radical produced, such as resonance and hyperconjugation. This can be attained via an extended double bond system and functional group arrangement, such as the presence of electron-donating groups in the aromatic rings ortho and/or para to the hydroxyl function.

The biological benefits of the AVs are detailed in Chapter 1 and activities of these compounds against various disease conditions are also discussed. Many of these disease conditions are due to the involvement of free radicals. One probable explanation of biological benefits is that AVs protect by acting as antioxidants. The antioxidant activities of oat grains are first suggested independently by Lowen et al (1937), and Peters and Musher (1937) [4]. About 50 years later, Collin identified around 40 AVs (hydroxy or methoxy) derivatives that are responsible for the antioxidant activity of oat grains[5] and the complete structural analyses of the 10 AVs were successfully

identified spectrometrically [5]. Literature mainly focused on AVs, **2p**, **2c**, and **2f** in discussions of the antioxidant activity of oats phenolics. In vitro, antioxidant studies using different assays; NORAC, SORAC, ORAC, SOAC, and HORAC respectively for peroxynitrite, superoxide anion, peroxy radicals, singlet oxygen, and hydroxyl radicals reported that activity **2c** was 1.5 fold than **2p** and **2f** [6–10].

Although earlier studies have greatly increased our knowledge of the anti-oxidant capabilities of AVs, the knowledge about the structure-activity connection and the underlying mechanisms remains limited. Given the success of the density functional theory (DFT) method in elucidating the antioxidant property of phenolic compounds, since both are based on electron density, we set out to conduct a systematic DFT study to clarify the relationship between molecular/electronic structure and free radical scavenging activity, as well as the possible mechanisms of selected molecules. The chapter devoted particular attention to how the catechol, guaiacyl, and carboxyl groups affected the activity and the mechanism.

5.3.Computational method

All calculations described in this work were performed with the Gaussian 16W computational programming package [11]. The geometry optimization of neutral molecules, their radicals, cations, and anions are optimized using M06-2X/6-31+G (d, p) level of theory to obtain the descriptors like BDE (Bond Dissociation Enthalpy), IP (Ionization Potential), PDE (Proton Dissociation Enthalpy), PA (Proton affinity), and ETE (Electron Transfer Enthalpy) needed for

radical scavenging activity in the ground state in the gas phase and solvent media (aqueous and ethanol). Moreover, the spin density computations of AVs have been carried out using Multifunctional Wave function Analyzer, Multiwfn 3.3.8 suite [12] using M06-2X/6–31+G (d, p) level of theory. Solvent effects were included by the integral equation formalism of polarized continuum model (IEF-PCM)[13].

Radical scavenging activity of phenolic antioxidants theoretically expressed primarily by three possible mechanisms, namely, Hydrogen atom transfer (HAT) mechanism(equation 5.1), Single-electron transfer followed by proton transfer (SET-PT) mechanism (equation 5.2.1 & 5.2.2) and Sequential proton loss electron transfer (SPLET) mechanism (equation 5.3.1 & 5.3.2) [14–19] and were calculated under standard conditions of 1 atm. and 298.15 K. A schematic representation of the three primary mechanisms on the **2p** is given in Fig 5.1. The final outputs of all three mechanisms are radicals of antioxidant molecules. Ranking of bond dissociation enthalpy (BDE), adiabatic ionization potential (AIP), proton dissociation enthalpy (PDE), proton affinity (PA), and electron transfer enthalpy (ETE) for the several hydroxyl groups in the polyphenol's structure (to distinguish between HAT, SET, and SPLET processes) offers important knowledge regarding the preferred first step in these compounds' interactions with free radicals.

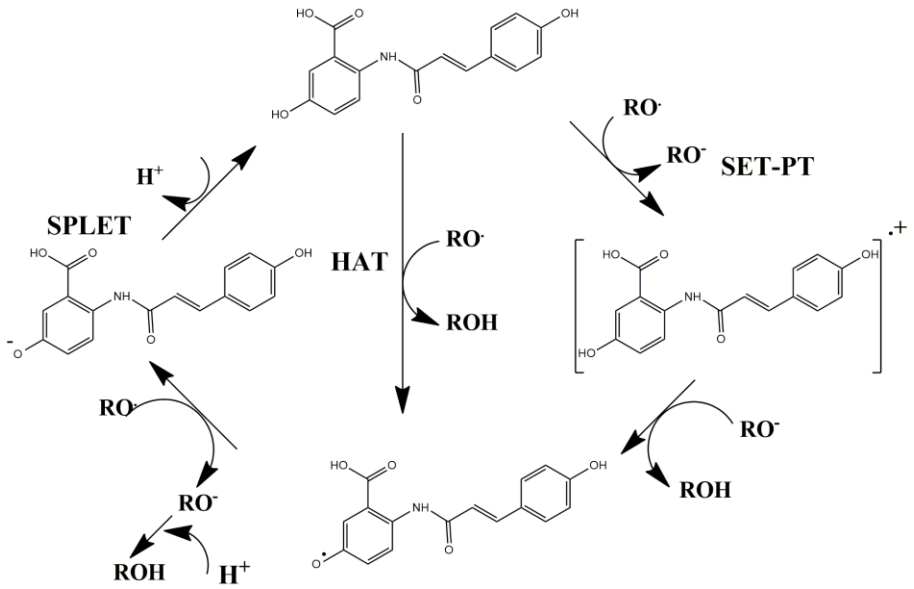

Fig.5.1. Schematic representation of the radical scavenging activity of **2p**

$$AV(OH)_n \rightarrow AV(OH)_{n-1}O^{\cdot} + H^{\cdot} \quad (5.1)$$

$$AV(OH)_n \rightarrow [AV(OH)_n]^{+\cdot} + e^- \quad (5.2.1)$$

$$[AV(OH)_n]^{+\cdot} \rightarrow AV(OH)_{n-1}O^{\cdot} + H^+ \quad (5.2.2)$$

$$AV(OH)_n \rightarrow AV(OH)_{n-1}O^- + H^+ \quad (5.3.1)$$

$$AV(OH)_{n-1}O^- \rightarrow AV(OH)_{n-1}O^{\cdot} + e^- \quad (5.3.2)$$

The H-atom is transferred directly from the antioxidant (AV-H) to the free radical via a homolytic bond breakage in the HAT mechanism. The descriptor BDE determines the capacity of the process (equation 5.4).

$$BDE = H(AV(OH)_{n-1}O^{\cdot}) + H(H^{\cdot}) - H(AV(OH)_n) \quad (5.4)$$

The SET-PT mechanism is a two-step process that involves electron transfer in the first step and deprotonation in the second, which are governed by the parameters IP and PDE, respectively (equation 5.5 & 5.6).

$$IP = H([AV(OH)_n]^{+\cdot}) + H(e^{-}) - H(AV(OH)_n) \quad (5.5)$$

$$PDE = H(AV(OH)_{n-1}O^{\cdot}) + H(H^{+}) - H(AV(OH)_n]^{+\cdot}) \quad (5.6)$$

The SPLET mechanism has two phases as well, although they are performed in a different format compared to that of SET-PT. The first and second steps are respectively controlled by the descriptors PA and ETE (equation 5.7 & 5.8).

$$PA = H(AV(OH)_{n-1}O^{-}) + H(H^{+}) - H(AV(OH)_n) \quad (5.7)$$

$$ETE = H(AV(OH)_{n-1}O^{\cdot}) + H(e^{-}) - H(AV(OH)_{n-1}O^{-}) \quad (5.8)$$

5.4.Results and discussion

5.4.1. Optimized structures of Avenanthramides

The lowest energy structures of the E – Avenanthramides are taken for conducting the detailed radical scavenging activity of the compounds. The carbonyl oxygen of the carboxylic acid and the NH group were found to form an intramolecular hydrogen bond (IHB) in the optimal structure of AVs with a length of ~1.85 Å, which is beneficial for their stability. Therefore, it is predicted that these IHBs

would prefer coplanarity between the A- ring, bridging chain, and the B ring. Furthermore, the IHB may form between the OH group and the adjacent OH or OMe group in the A- or B-ring. Detailed studies of IHB were given in Chapter 3. From the data of dihedral angles discussed in the previous chapter, **2p**, **2c**, **1p**, **1c**, and **1f** are completely planar, and **2f**, **1s**, and **2s** are very slightly deviating from planarity. The radicals ($AV(OH)_{n-1}O^{\cdot}$), cations ($[AVOH]^{\cdot+}$) radicals, and anions ($AV(OH)_{n-1}O^{-}$) have also been optimized using the same method, starting with the optimized structure of neutral AVs by removing hydrogen atoms from successive positions. By comparison, no major geometrical shift was observed when moving from neutral to the corresponding radical, cation radical, and anionic forms except for NH. When radical/anion is formed from the NH group of molecules some degree of distortion from planarity to the ring A has been observed due to the disappearance of IHB between NH and C=O group and other part of ring B has been found to keep its planarity with the O = C- Cα = Cβ bond. In Table 5.1, the dihedral angles Φ (C4, C3, C2, N) and (C3', C2', C1', C7') of the anion and radical of each reactive site are given and support the above observation.

Table 5.1 Dihedral angles of radicals and anions in the optimized structures of AVs in the gas phase

		Dihedral angle Φ (^{0})			Dihedral angle Φ (^{0})	
AVs	Radicals	(C4, C3, C2, N)	(C3', C2', C1', C7')	Anions	(C4, C3, C2, N)	(C3', C2', C1', C7')
2p	N˙	-177.46	-179.73	N˙	-175.55	-179.81
	COO˙	-179.99	179.99	COO˙	179.99	179.99
	4' O˙	179.99	179.99	4' O˙	-180.00	179.99
	5 O˙	-179.99	179.99	5 O˙	-179.99	-179.99
2f	N˙	-177.42	179.94	N˙	-175.89	-179.69
	5 O˙	-179.86	-179.85	5 O˙	179.87	-179.62
	COO˙	-179.94	-179.72	COO˙	-179.91	-179.86
	4' O˙	-179.93	-179.80	4' O˙	-179.92	-179.67
2c	N˙	177.32	179.77	N˙	175.65	179.60
	5O˙	-180.00	-179.99	5O˙	179.99	180.00
	COO˙	-180.00	-179.99	COO˙	-179.99	-180.00
	4' O˙	-180.00	180.00	4' O˙	180.00	180.00
	5'O˙	180.00	180.00	5’ O˙	180.00	180.00
2s	N˙	-177.31	-179.62	N˙	-174.59	179.41
	COO˙	-179.92	-179.81	COO˙	179.97	179.02
	5 O˙	179.97	-179.80	5 O˙	-179.96	179.01
	4' O˙	179.94	179.29	4' O˙	-179.83	179.68
1p	N˙	-173.92	179.82	N˙	175.40	179.95
	COO˙	179.99	179.99	COO˙	179.99	179.99
	4'O˙	179.99	179.99	4'O˙	-179.99	179.99
1f	N˙	-176.84	-179.89	N˙	-175.41	179.99
	COO˙	179.99	-179.76	COO˙	-179.99	-180.00
	4' O˙	179.94	-179.92	4' O˙	179.93	-179.86
1c	N˙	179.99	180.00	N˙	179.99	180.00
	COO˙	179.99	-179.99	COO˙	179.99	179.99
	5' O˙	-180.00	180.00	5' O˙	180.00	180.00
	4' O˙	-180.00	-180.00	4' O˙	180.00	180.00
1s	N˙	-177.04	-179.96	N˙	175.41	-179.12
	COO˙	179.85	179.90	COO˙	179.95	-179.15
	4' O˙	-179.99	-179.35	4' O˙	179.82	-179.70

5.3.2. Radical scavenging mechanism- The First H^+/e^- Reactions (HAT, SET-PT, and SPLET)

5.3.2.1. HAT mechanism

The calculated BDE values of selected AVs in both the gas phase and solvents are given in Table 5.2. The enthalpy of bond dissociation is the best parameter to explain a molecule's radical scavenging activity because hydrogen bond strength dictates the efficacy of hydrogen abstraction. Here, the free radicals are deactivated by the transfer of a hydrogen atom from the molecule. In a compound with more than one phenolic hydroxyl group, the one with the lowest BDE accounts for the radical scavenging action. The optimized structure of radical species and their spin density distributions for each of the AV after radical formation are analyzed (Fig.5.2). The highest BDE for carboxylic-OH functionality (greater than 110) in the gas phase is found in all studied cases of AV, so this is the least reactive site for radical formation reaction. As discussed above, the phenolic NH groups in all AV form intramolecular interaction (IHB) with the adjacent carbonyl oxygen of carboxylic functionality. Hence the abstraction of the H atom from this N-H implies the breaking of IHB. This will cause a higher BDE of the N-H group. The BDE value of NH in all cases is around 104-108 kcal /mol. Since the BDE values of COOH and NH are above 100 kcal/mol and hence, H atom donation reactions may be overlooked for these two functional groups.

The spin density distribution (SD) [20]and delocalization index (DI) [21] given in Table 5.3 and the SD distribution isosurface

diagram in Fig.5.2, also support these observations. When the H abstraction takes place from the COOH functional group and forms the COO radical, the formed electron density at the O radical delocalizes only at the functional group itself not to the ring, hence lowering the stability of these radicals. The greater SD value of 0.153 indicates that the electron density concentrates on that region itself. DI values of a radical quantitatively explain the extent of the delocalization of that radical [21, 22]. The lower the SD, the higher the DI implies that the one-electron formed at a site is more delocalized and hence stable. Hence, the DI of the COO radical is quite higher not mean it is a contradictory result, but it is due to continuous delocalization within the COO radical. The higher SD and lower DI values of nitrogen radical when compared to other radical, except COO radical also supports the lower stability of radical formed. Hence due to two reasons; the IHB and the low delocalization of radical formed; the involvement of these two functional groups can be neglected from radical scavenging activity.

For the compound **2p**, among the two phenolic hydroxyl groups, the lowest BDE value is obtained for 5 OH (84.81 kcal/mol) than the 4' OH (108.11 kcal/mol), hence the activity of **2p** is through 5 OH. The SD and DI values also suggest the stability of radicals formed from the 5 OH. In both the solvents, the same trend in BDE is obtained for 5 OH (85.10 kcal/mol) and 4' OH (87.07 kcal/mol). But the change is lowest for 4' OH may be due to the stabilization of the radical formed by the solvent.

The compound **2f** also contains two hydroxyl groups on both A and B rings and 5 OH (84.75 kcal/mol) of the A ring exhibits lower energy for bond dissociation than the 4' OH (86.23 kcal/mol) of the B ring. However, in a methoxy group in the ortho of donor hydroxy group, considerable enhancement in activity is observed. In **2c**, when ortho of a donor hydroxyl group, 4' OH substituted with another hydroxyl group resulted in an enhanced activity than methoxy substituted molecule with BDE of 77.87 kcal/mol. The other hydroxyl groups present in the B ring and A ring respectively are 89.19 kcal/mol (3'OH) and 84.87 kcal/mol (5 OH). From these two AVs, more than one conclusion can be made according to their bond dissociation enthalpy values. Firstly, the hydroxyl group present on the B- ring is more active than the A-ring, secondly, 4' OH will be the donor hydroxyl group due to extended delocalization of radicals formed through the molecule and is supported by SD and DI values given in Table 5.3, and thirdly hydroxyl group in the ortho position of donor hydroxyl group can enhance the activity by stabilizing the radical formed more than the methoxy group, and finally, the substitution on B-ring doesn't effect on the hydroxyl group of A ring. All these computationally obtained observations are correlating well with previous experimental conclusions [7, 23].

Table 5.2 Calculated BDEs of the Studied AVs in the gas phase and solvents (In kcal/mol)

		BDE(kcal/mol)					BDE(kcal/mol)		
Compound	Position	Gas	Ethanol	Water	Compound	Position	Gas	Ethanol	Water
2p	N-H	104.27	101.13	100.88	**1p**	N-H	108.32	105.78	105.55
	COOH	113.97	95.49	95.15		COOH	113.86	109.25	108.22
	4' OH	108.11	87.07	87.08		4' OH	86.51	87.12	87.13
	5 OH	84.81	85.10	85.11	**1c**	N-H	110.45	105.89	105.77
2f	N-H	104.59	101.01	100.78		COOH	113.85	106.72	106.07
	COOH	113.98	94.93	94.55		4' OH	78.02	79.71	79.77
	4' OH	86.23	83.53	83.37		3' OH	89.27	86.70	86.48
	5 OH	84.75	84.59	84.59	**1f**	N-H	108.42	105.41	105.22
2c	N-H	104.24	101.10	100.87		COOH	113.89	104.37	103.16
	COOH	113.93	95.67	95.34		4' OH	86.34	83.60	83.45
	4' OH	77.87	79.47	79.57	**1s**	N-H	108.26	105.48	105.30
	5 OH	84.87	85.26	85.27		COOH	113.88	105.16	91.62
	3' OH	89.19	85.97	85.99		4' OH	82.29	81.93	81.49
2s	N-H	104.40	100.68	100.77		-	-	-	-
	COOH	114.16	94.82	94.52		-	-	-	-
	4' OH	82.27	81.72	81.61		-	-	-	-
	5 OH	84.78	84.62	84.65			-	-	-

The BDE values of the donor hydroxyl group (4' OH) of **1p**, **1c**, **1f**, **1s**, and **2s** respectively are 86.51 kcal/mol, 78.02 kcal/mol, 86.34 kcal/mol, 82.29 kcal/mol, and 82.27 kcal/mol. Comparing **1c**, **1s**, and **2s**, stabilization of radicals formed in the donor hydroxy group happens more in the presence of a hydroxyl group at the nearest position than a dimethoxy group. However, **2f** changed to **1s** and **2s,** and enhanced activity was observed due to two methoxy groups on either side of the radical formed. The SD and DI values in Table 5.3 and the isosurface plots (Fig.5.2) also support this HAT mechanism in

all studied samples. According to the HAT mechanism, the order of radical scavenging activity among the studied compounds is in the order of **2c > 1c > 2s > 1s > 2f > 2p > 1f > 1p** exactly follows the order caffeic acid>sinapic acid >ferulic acid>p-coumaric acid suggested by the experimental observations [7, 23].

Table 5.3. The spin density values for the O-radical and delocalization index of the C-O bond computed for AVs using M06-2X /6-31+G(d,p) level of theory in the gas phase

AVs	Parameter			Bond		
		$N^{\cdot}$	$COO^{\cdot}$	5-$O^{\cdot}$	4'-$O^{\cdot}$	3'-$O^{\cdot}$
2p	SD	0.120	0.153	**0.087**	0.115	-
	DI	1.532	1.898	1.859	1.676	-
2f	SD	0.121	0.153	0.086	**0.068**	-
	DI	1.532	1.899	1.859	1.913	-
2c	SD	0.120	0.153	0.087	**0.071**	0.084
	DI	1.532	1.896	1.859	1.872	1.872
1p	SD	0.131	0.153	-	**0.076**	-
	DI	1.494	1.892	-	1.899	-
1c	SD	0.107	0.153	-	**0.071**	0.084
	DI	1.512	1.891	-	1.872	1.872
1f	SD	0.138	0.153	-	**0.068**	-
	DI	1.496	1.894	-	1.914	-
1s	SD	0.139	0.153	-	**0.075**	-
	DI	1.496	1.892	-	1.880	-
2s	SD	0.120	0.152	0.087	**0.075**	-
	DI	1.534	1.894	1.859	1.879	-

In the solution phase, not much change in BDE was not observed. It follows the same trend as the gas phase of each molecule under consideration. For **2p** and **2f**, in the aqueous phase, the BDE value of 4'-OH is found to be lower than the gas phase due to greater stabilization of the radical formed. For **2c** and **1c**, in aqueous solution, BDE of the 4'-OH slightly increased. The slight reluctance of the bond

in solution will be due stabilization of radicals formed with hydrogen from the solution, which is less feasible than stabilization through delocalization. For 3'-OH and 5-OH the bond becomes more reactive in the aqueous phase due to their lower BDE than gas phase due to the stabilization of radicals formed through the solvent cage.

The lowest BDE value of the compounds in the c-series is lower or comparable to those of DPPHH estimated (78.24 kcal/mol) at the same level of theory, indicating the viability of the reaction between the compounds and DPPH through the HAT mechanism. Since the lowest BDEs of **2p**, **2f**, **2s**, **1p**, **1f**, and **1s** are a little bit higher than those of DPPHH, the reaction with DPPH• is less likely to occur through the HAT mechanism than it is for the **c**-series.

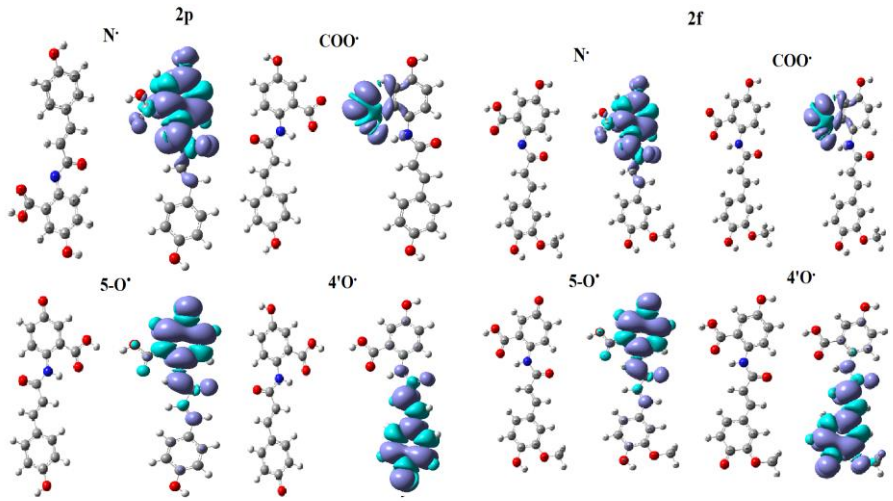

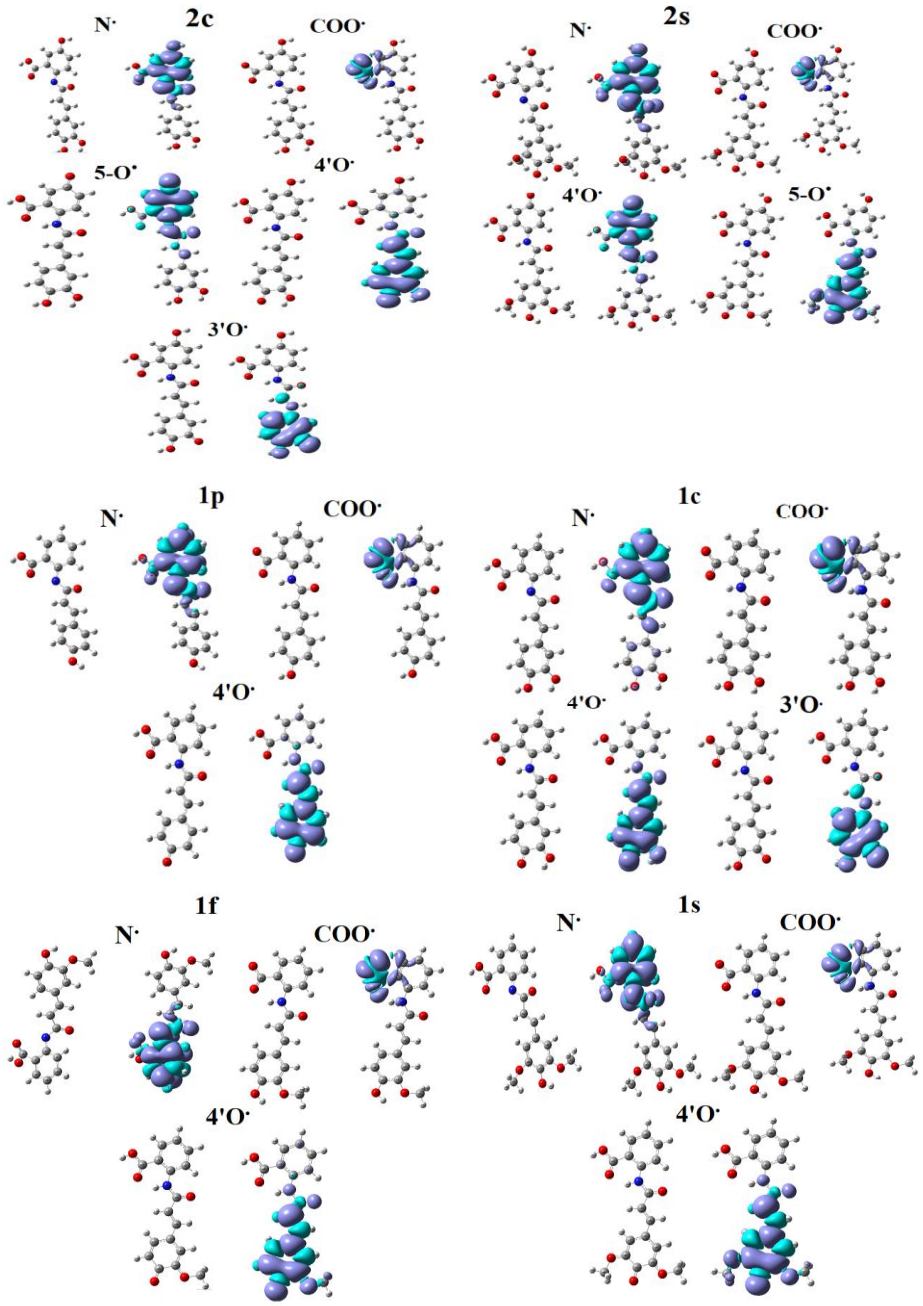

Fig.5.2. Spin density contour diagrams of **2p, 2f, 2c, 2s, 1p, 1c, 1f,** and **1s** showing the distribution of electron density when a radical is formed in respective positions (isovalue = 0.004)

5.3.2.2.Analysis of SET-PT mechanism

In this mechanism, the radical scavenging molecule AV-H upon electron donation in the presence of free radical species results in the formation of a radical cation $AVH^{\bullet+}$, and further subsequent deprotonation from the first intermediate forms the corresponding radical $AV^{\bullet}$. In this two-step mechanism, the associated numerical descriptors respectively are the IP (ionization potential) and PDE (proton dissociation enthalpy). Low IP molecules are more vulnerable to ionization and have strong antioxidant properties.

The calculated IP and PDEs of all compounds in both the gas phase and solvents are summarized in Table 5.4. From Table 5.4, it can be found that the lowest IP is found for **2s** irrespective of media implying that electron donation ability is higher for this molecule. The increasing order of electron donation in terms of IP in the gas phase is **2s < 2p < 2f < 2c < 1s < 1p < 1f < 1c** indicating that abstracting electrons from **2s** is more easy than abstraction from others, while **1c** is the least effective one. This finding demonstrates that the introduction of OH and/ or OCH3 groups facilitates electron abstraction, which can be attributed to the extension of the molecular conjugation due because of the presence of substituents.

Table 5.4 Calculated IPs and PDEs of the Studied AVs in the gas phase and solvents (In kcal/mol)

Compound	Position	IP(kcal/mol)			PDE(kcal/mol)		
		Gas	Ethanol	Water	Gas	Ethanol	Water
2p	N-H				244.50	28.98	34.43
	COOH	172.19	123.82	136.67	254.19	23.34	28.70
	4' OH				248.34	14.92	20.63
	5 OH				225.04	12.95	18.66
2f	N-H				246.34	28.84	29.44
	COOH	170.66	123.84	141.56	255.74	22.76	23.21
	4' OH				227.99	11.37	12.03
	5 OH				226.51	12.42	13.25
2c	N-H				244.30	22.22	27.64
	COOH	172.35	130.56	143.44	253.99	16.79	22.11
	4' OH				217.93	0.59	6.34
	5 OH				224.93	6.38	12.05
	3' OH				229.26	7.09	7.82
2s	N-H				246.24	28.48	34.28
	COOH	170.57	123.88	136.71	256.00	22.61	28.03
	4' OH				224.11	9.51	15.12
	5 OH				226.62	12.42	18.16
1p	N-H				240.84	28.06	34.37
	COOH	179.90	129.39	141.39	246.38	31.53	37.04
	4' OH				219.03	9.40	15.96
1c	N-H				244.02	30.85	32.27
	COOH	178.85	126.71	137.91	247.42	31.69	38.38
	4' OH				211.58	4.67	12.08
	3' OH				222.83	11.66	18.79
1f	N-H				246.59	33.50	39.09
	COOH	174.25	123.58	136.35	252.05	32.46	37.03
	4' OH				224.50	11.69	17.32
1s	N-H				248.05	32.93	38.56
	COOH	172.62	124.22	136.96	253.67	32.61	37.21
	4' OH				222.08	9.38	15.08

The data demonstrate that the solvent has a significant influence on the IP of the AV molecules. In ethanol and water, the IPs decreased by ˜46 kcal/mol and ˜35 kcal/mol, in comparison to those in the gas phase. This means that polar solvents promote electron abstraction from the investigated AVs, and thus solvent polarity is critical in determining the SET-PT mechanism. The order of IPs is different from BDE because the IP value is influenced by the whole molecule structure while the BDE is affected by the local phenomena induced by the substituent.

The second step is the deprotonation from the radical cation formed and its value is lower in solvents when compared to the gas phase. The significant decrease in PDE value in solvents around 200 kcal/mol will be due to the high solvation enthalpy of protons in the solution.

5.3.2.3.Analysis of the SPLET mechanism

In the SPLET mechanism, loss of proton followed by electron transfer from AV is considered. The descriptors associated with the first and second stages of these reactions are represented by PA and ETE respectively. It is an important pathway involved in the antiradical property of polyphenols especially in polar environments. As anticipated, the examined AVs' PAs in the solvents are significantly lower than those in the gas phase. This suggests that deprotonation happens more frequently in solvents, particularly polar solvents. As shown in Table 5.5, the COOH groups in the studied AVs exhibit lower PA values than the phenolic OHs in the polar solvents. However, their corresponding ETEs are very large (>100 kcal/mol), which makes the sum of (PA + ETE) for the COOH significantly larger than that of

the OH groups. The phenolic hydroxyl groups are therefore the top candidates for radical trapping in polar media. This result is consistent with a prior study that the phenoxide anions (ArO-) are responsible for the quick reactions with DPPH for cinnamic acids even while COOH is present. The observed higher value of PA of NH exhibits the reluctance of this group to form an anion by releasing a proton from it. It may be due to the strong IHB interaction with the carbonyl of the carboxylic group.

Considering PA+ETE values, 4'OH is less energy-demanding than the other phenolic hydroxyl bonds for all compounds except **2p**. These are the most likely locations for the SPLET process to occur in polar solvents. According to the lowest (PA + ETE) of the studied AVs, their activity obeys the order **2c** < **1c** < **2s** < **1s** < **2f** < **1f** < **2p** < **1p** which is in good agreement with the experimental results[7]. Considering **2f** and **2c**, the 4'OH of **2c** shown to exhibit lower PA+ETE value revealed increased stabilization of OH functionality than the OCH3 group in the o-position. This could be attributed to the electron-donating nature of the OCH3 group.

Comparing **2p** and **1p**, the change in PA of 4'OH very low (0.04 kcal/mol). This suggests that substitution in ring A only exerts a minor influence on the deprotonation of OHs in ring B. These findings demonstrate that the two rings A and B appear to exercise their proton-donation ability independently, which is comparable to the HAT situation previously mentioned.

To analyze the feasibility of the reaction between the generated phenoxide anions (AV $(OH)_{n-1}O^{-}$) and $DPPH^{\bullet}$, equation 5.9 was utilized.

$$AV(OH)_{n-1}O^{-} + DPPH^{\bullet} \rightarrow AV(OH)_{n-1}O^{\bullet} + DPPH^{-} \qquad (5.9)$$

Table 5.5 Calculated PAs and ETEs of the Studied AVs in the gas phase and solvents (In kcal/mol)

Compound	Position	PA(kcal/mol)			ETE(kcal/mol)			PA+ETE (kcal/mol)		
		Gas	Ethanol	Water	Gas	Ethanol	Water	Gas	Ethanol	Water
2p	N-H	347.80	59.32	62.41	68.879	93.49	108.69	416.68	152.81	171.10
	COOH	324.48	36.28	39.54	101.90	110.89	125.83	426.38	147.17	165.37
	4' OH	330.05	45.91	49.35	90.47	92.84	107.94	420.52	138.75	157.29
	5 OH	337.47	49.04	52.33	59.76	87.74	103.00	397.23	136.78	155.33
2f	N-H	347.68	58.41	62.32	69.33	94.28	108.69	417.01	152.69	171.01
	COOH	324.54	35.61	38.87	101.86	111.00	125.90	426.40	146.61	164.77
	4' OH	335.27	48.32	51.51	63.37	86.89	102.08	398.64	135.21	153.59
	5 OH	337.88	48.99	52.26	59.29	87.27	102.54	397.17	136.26	154.80
2c	N-H	347.56	59.14	62.17	69.10	93.64	108.91	416.66	152.78	171.08
	COOH	324.07	36.32	39.61	102.28	111.02	125.94	426.35	147.34	165.55
	4' OH	323.37	41.52	45.09	66.91	89.62	104.70	390.28	131.14	149.79
	5 OH	337.31	49.00	52.27	59.97	87.94	103.22	397.28	136.94	155.49
	3' OH	343.73	51.38	49.64	57.88	86.26	87.85	401.61	137.64	137.49
2s	N-H	347.49	57.96	61.01	69.32	94.39	109.97	416.81	152.35	170.98
	COOH	323.21	35.26	38.13	103.36	111.23	126.61	426.57	146.49	164.74
	4' OH	332.46	46.77	50.00	62.22	86.62	101.82	394.68	133.39	151.82
	5 OH	337.98	46.66	52.15	59.22	89.63	102.72	397.2	136.29	154.87
1p	N-H	347.21	58.89	62.36	73.53	98.56	113.41	420.74	157.45	175.77
	COOH	324.42	36.07	39.39	101.86	124.85	139.04	426.28	160.92	178.43
	4' OH	329.38	45.57	49.03	69.55	93.22	108.32	398.93	138.79	157.35
1c	N-H	346.86	57.87	61.27	76.00	97.70	114.82	422.86	155.57	176.09
	COOH	324.42	36.72	40.02	101.84	121.68	136.27	426.26	158.40	176.29
	4' OH	322.90	41.51	45.05	67.53	89.88	104.94	390.43	131.39	149.99
	3' OH	343.41	51.46	54.45	58.27	86.91	102.25	401.68	138.37	156.70
1f	N-H	347.22	57.91	60.91	73.62	99.17	114.53	420.84	157.08	175.44
	COOH	324.80	36.08	39.37	101.50	119.96	134.00	426.3	156.04	173.37
	4' OH	334.63	47.93	51.15	64.13	87.35	102.53	398.76	135.28	153.68
1s	N-H	347.04	57.75	60.78	73.64	99.41	114.74	420.68	157.16	175.52
	COOH	324.93	36.06	27.02	101.36	120.78	134.82	426.29	156.84	161.84
	4' OH	332.12	46.64	37.56	62.58	86.97	102.15	394.70	133.61	139.71

In ethanol and water, respectively, the electron affinity (EA) of DPPH• was calculated to be 90.3 and 86.3 kcal/mol. It can be deduced that the electron transfer between the $AV(OH)_{n-1}O^-$ and DPPH• is thermodynamically favored due to the negative value of (ETE + EA) when compared to the ETE values of the $AV(OH)_{n-1}O^-$ (hardly in between 86-93 and 87-104 kcal/mol in ethanol and water, respectively). This suggests that the examined AVs can trap DPPH• radicals by the SPLET mechanism in polar solvents.

5.3.2.4.Thermodynamically preferred pathway

In conclusion, as discussed above the preferred descriptors corresponding to HAT, SET-PT, and SPLET are BDE, IP, and PA respectively. These descriptors are therefore used to determine the thermodynamically preferred mechanism for the radical scavenging activity of the compounds studied. Because of the lowest value of BDE relative to other descriptors, it could be found from the above discussions that HAT would be the optimal pathway for these molecules in the gas phase or vacuum. So in the gas phase, free radicals deactivates by the transfer of hydrogen atom from the compound. But when the medium turns to ethanol, the PA pathway overtakes the HAT and SET-PT mechanisms. SPLET would, therefore, be the preferred mechanism to explain radical scavenging activity in the polar medium.

5.3.2.5.Reliability of result obtained

The antioxidant activities of eight AVs are discussed in the work by three possible mechanisms. The health-promoting benefits of AVs are observed to be mainly due to due to the potent antioxidant

activity as presented in previous pieces of literature. It was found that 2c dispenses comparable antioxidant activity to the standard synthetic antioxidant BHT in the β-carotene test and is more active than Trolox in the DPPH assay[24]. According to the laboratory investigation of antioxidant activity, the activity order is likewise claimed to be **c** ≥ **s** ≥ **f** ≥ **p**, and **2** ≥ **1**[7, 23, 25, 26]**.** Interestingly, the results obtained were correlating with the experimental findings and **2c** and **1c** followed by **2s** and**1s** are highly reactive among the studied compound.

5.3.3. Electronic spectrum: UV-Vis spectrum and electronic excited state

Using the TD-DFT approach, the UV-visible spectra of the AVs that were addressed in the current work are examined in the gas phase and polar solutions ethanol. The IEF-PCM model of solvent was employed for the current study. The reported actual spectra in methanol were used to simulate the experimental environment and found a good agreement in the level of theory selected for the study (see Chapter 4). Here, we adopted the first 30 excited states to calculate excitation energy and oscillator strength, and the resulting data were used to simulate the UV-Vis absorption spectrum of the molecules, as depicted in Table 5.6. In Table 5.6, detailed transition characteristics of the compounds **2p**, **2f**, **2c**, **2s**, **1p**, **1f**, **1c**, and **1s** are provided.

In the gas phase, the spectra as given in Fig.5.3 contain two peaks (major and minor) that correspond to four major transitions as represented in Table 5.6. The HOMO to LUMO as well as HOMO to LUMO+1 transition are the responsible transition corresponding to the major peak in Fig.5.3 for **2p**, **2f**, **2c**, and **2s**. In the absorption spectrum which are observed at 321.87 (f=0.50) & 285.71 (f=0.73) nm for **2p**,

324.15 (f=0.59) & 293.37 (f=0.54) nm for **2f**, 322.21 (f=0.59) & 288.30 (f=0.59) nm for **2c**, and 324.38 (f=0.60) & 292.56 (f=0.56) nm. Here the first absorption corresponds to HOMO to LUMO and the second corresponds to HOMO to LUMO+1 for each compound. The absorptions are red-shifted as with the change in the substitution on the B ring. The shift was observed to be higher in **2s** and **2f** revealing the influence of the OCH3 substituent in the transition. The absorptions corresponding to the second peaks are observed at 211.55 (f=0.29) & 207.47 nm (f=0.34) for **2p**, 221.72 (f=0.44) & 208.98 nm (f=0.32) for **2f**, 223.64 (f=0.38) & 207.77 nm (f=0.39) for **2c**, and 222.64 (f=0.26) & 210.86 nm (f=0.27) nm for **2s**. The absorption spectrum of **1f**, **1c**, and **1s** as observed in Fig.5.3 possess three peaks except for **1p**. For **1p** major peaks are due to the transition HOMO to LUMO and HOMO-1 to LUMO leads to absorption peaks at 303.86 (f=0.88) and 277.37 (f=0.26) nm the minor peak are obtained due to the contribution of transition from HOMO-2 to LUMO and HOMO to LUMO+8 with intensities 211.54 (f=0.24) and 196.47 (f=0.15) nm. For **2f** the major absorption at 309.99 (f=0.94) is in response of HOMO to LUMO transition. The absorption peaks at 224.01 (f=0.34) & 221.53 (f=0.27) nm form the second intense peak (HOMO-3 to LUMO & HOMO-2 to LUMO) and the third peaks at 196.03 (f=0.17) due to transition HOMO-3 to LUMO+1. For **1c**, major peaks are observed at 304.71 (f=0.83), and the second peak is due to transition corresponding to 225.22 (0.48) & 204.77 (f=0.24) nm and a short peak at 196.47 (f=0.15) nm due to transition HOMO-3 to LUMO+1. As obtained for the 2 series compounds the methoxy (-OCH3) substitution on the B ring (**1f** and **1s**) leads to a significant red shift in the spectra. In solvent ethanol, the absorption maxima are red-shifted. The shift was more pronounced in 1 series of compounds than in 2 series compounds.

Table 5.6 Calculated UV–visible maximum absorption wavelength (λmax), excitation energy, oscillator strength (f), and dominant MO contributions for the electronic transitions of the studied compounds

	Gas				Ethanol			
	λ_{max} (nm)	ΔE (eV)	f	MO involved (%)*	λ_{max} (nm)	ΔE (eV)	f	MO involved (%)*
2p								
	321.87	3.85	0.50	H -> L (77.31%)	325.04	3.81	0.77	H-> L (81.16%)
	285.71	4.34	0.73	H -> L+1 (53.20%)	292.65	4.24	0.66	H -> L+1 (54.14%)
	211.55	5.86	0.29	H-2 -> L (38.12%)	210.15	5.90	0.38	H -> L+8 (48.95%)
	207.47	5.98	0.34	H -> L+8 (40.18%)	183.12	6.77	0.37	H-2-> L+4 (50.44%)
2f								
	324.15	3.82	0.59	H -> L (69.06%)	328.48	3.77	0.87	H-> L (77.35%)
	293.37	4.22	0.54	H -> L+1 (49.16%)	299.17	4.14	0.41	H -> L+1 (45.56%)
	221.72	5.59	0.44	H-2 -> L (42.08)	227.13	5.46	0.43	H-2 -> L (26.10%)
	208.98	5.93	0.32	H -> L+9 (43.95%)	211.15	5.87	0.34	H -> L+10 (46.57%)
2c								
	322.21	3.85	0.49	H -> L (73.28 %)	325.85	3.80	0.77	H-> L (77.44%)
	288.30	4.30	0.59	H -> L+1 (49.42%)	295.87	4.19	0.49	H -> L+1 (47.98%)
	223.64	5.54	0.38	H-2 -> L (34.20%)	227.65	5.45	0.46	H-2 -> L (27.67%)
	207.77	5.97	0.39	H-> L+9 (44.64%)	210.30	5.90	0.37	H -> L+8 (47.22%)
2s								
	324.38	3.82	0.60	H-> L (69.63%)	320.17	3.87	0.62	H-> L (70.16%)
	292.56	4.24	0.56	H -> L+1 (46.86%)	288.83	4.29	0.54	H -> L+1 (45.21%)
	222.64	5.57	0.26	H-2 -> L (26.36%)	224.72	5.52	0.11	H-3-> L (43.43%)
	210.86	5.88	0.27	H -> L+8 (16.66%)				
1p								
	303.86	4.08	0.88	H -> L (76.92%)	311.79	3.98	1.15	H-> L (83.23%)
	277.37	4.47	0.26	H-1 -> L (39.32%)	216.10	5.74	0.24	H-2-> L (48.36%)
	211.54	5.86	0.24	H-2 -> L (52.72%)	197.60	6.27	0.20	H-3 -> L+1 (58.84%)
	204.56	6.06	0.22	H -> L+8 (51.48%)	184.38	6.72	0.34	H-2-> L+4 (44.50%)
1c								
	304.71	4.07	0.83	H-> L (72.60%)	314.07	3.95	1.05	H-> L (80.32%)
	225.22	5.50	0.48	H -> L+6 (27.59%)	228.35	5.43	0.47	H -> L+6 (37.21%)
	204.77	6.05	0.24	H-> L+8 (38.54%)	191.83	6.46	0.20	H-2 -> L+6 (31.19%)
	196.47	6.31	0.15	H-3 -> L+1(57.99%)				
1f								
	309.99	4.00	0.94	H -> L (76.69%)	319.07	3.89	1.10	H -> L (82.03%)
	224.01	5.53	0.34	H-3 -> L (35.56%)	283.40	4.37	0.13	H-1 -> L (51.21%)
	221.53	5.60	0.27	H-2 -> L (33.12%)	227.84	5.44	0.46	H-> L+8 (35.74%)
	196.03	6.32	0.17	H-3 -> L+1(54.05%)				
1s								
	309.50	4.01	0.95	H -> L (76.87%)	318.23	3.90	1.12	H -> L (82.73%)
	223.81	5.54	0.25	H-3 -> L (36.51%)	282.96	4.38	0.14	H-2 -> L (49.92%)
	222.14	5.58	0.21	H-2 -> L (20.63%)	226.28	5.48	0.37	H-3 -> L (28.43%)
	191.55	6.47	0.23	H-1 -> L+7 (15.61%)	223.60	5.55	0.24	H-1-> L+1 (16.96%)

* H and L denote the HOMO and LUMO, respectively

It is commonly recognized that the solar electromagnetic spectrum contains a wide range of wavelengths, including UV radiation that can be damaging[27, 28]. This radiation can be classified into three: UVA (320–400 nm), UVB (290–320 nm), and UVC (200–280 nm)[27, 29]. Exposure of skin to UVA and UVB can cause serious damage to the skin including erythema (sunburn), photo aging of skin, and increased risk of skin cancer UVC is highly damaging but is fully absorbed by the earth's atmosphere[30–32].

Sunscreen is routinely used to protect the skin from these harmful effects. Organic UV filters, which may absorb these damaging radiations, are one of the major constituents in topical sunscreens. The absorption maxima of these molecules are located in the UVA region (around 324 nm) and UVB region (around 280 nm) in both media. Most of the compounds span the absorption with appreciable oscillatory strength in the UVA region except for 2p and 2c which UVB region. Thus these molecules can effectively screen UV radiations. The good antioxidant potential and UV filtering potential of the selected compound revealed the skin application of the compounds.

The results obtained point the fingers to the personal care purpose of oats since antiquity. Wild oats (*Avena sativa. L*) were utilized in skin care in Egypt and the Arabian peninsula as early as 2000 BC and Oat baths were commonly used to cure sleeplessness, anxiety, and skin problems such as dermatitis and burns[33]. The colloidal oatmeal was officially approved as a skin protectant by the US Food and Drug Administration (FDA)[33, 34]. AVs, an oat ingredient, is known to decrease histamine release at extremely low

levels, assisting in plumping up the skin, reducing wrinkles, and restoring the skin's natural barrier[34]. Numerous studies have consistently shown their advantages in treating eczema and other inflammatory skin disorders[35]. Oat AVs's antigenotoxic action, which can shield epidermal cells' DNA from environmental damages like UV radiation, is another advantage for health and antiaging[36]. Together, the proven benefits of AVs in skin protection and the treatment of dermatological diseases and their potential to prevent and treat chronic oxidative stress and inflammation linked to the onset, progression, and severity of aging-related diseases, such as metabolic, cardiovascular, cerebrovascular, and neurodegenerative diseases, point to these compounds as a promising new elixir of youth with both cosmetic and pharmaceutical benefits.

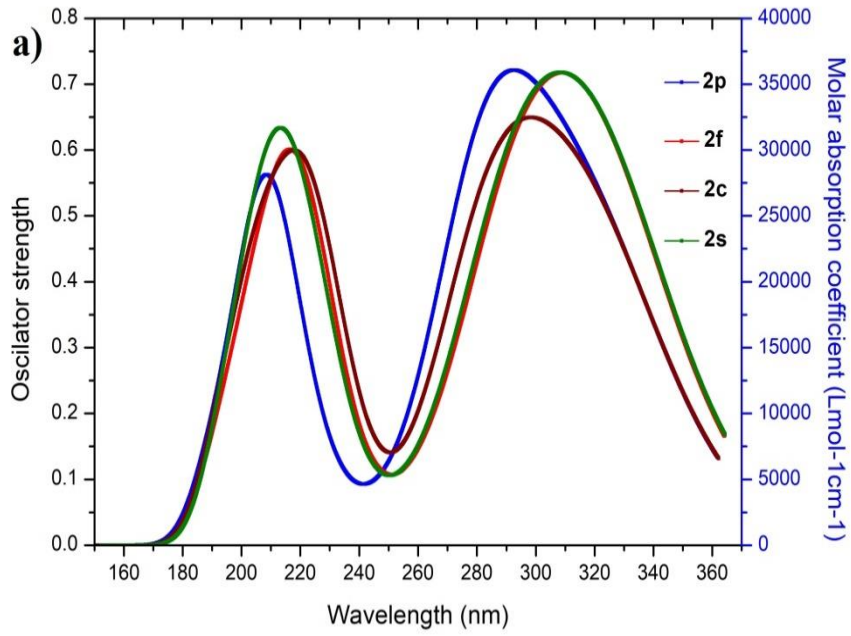

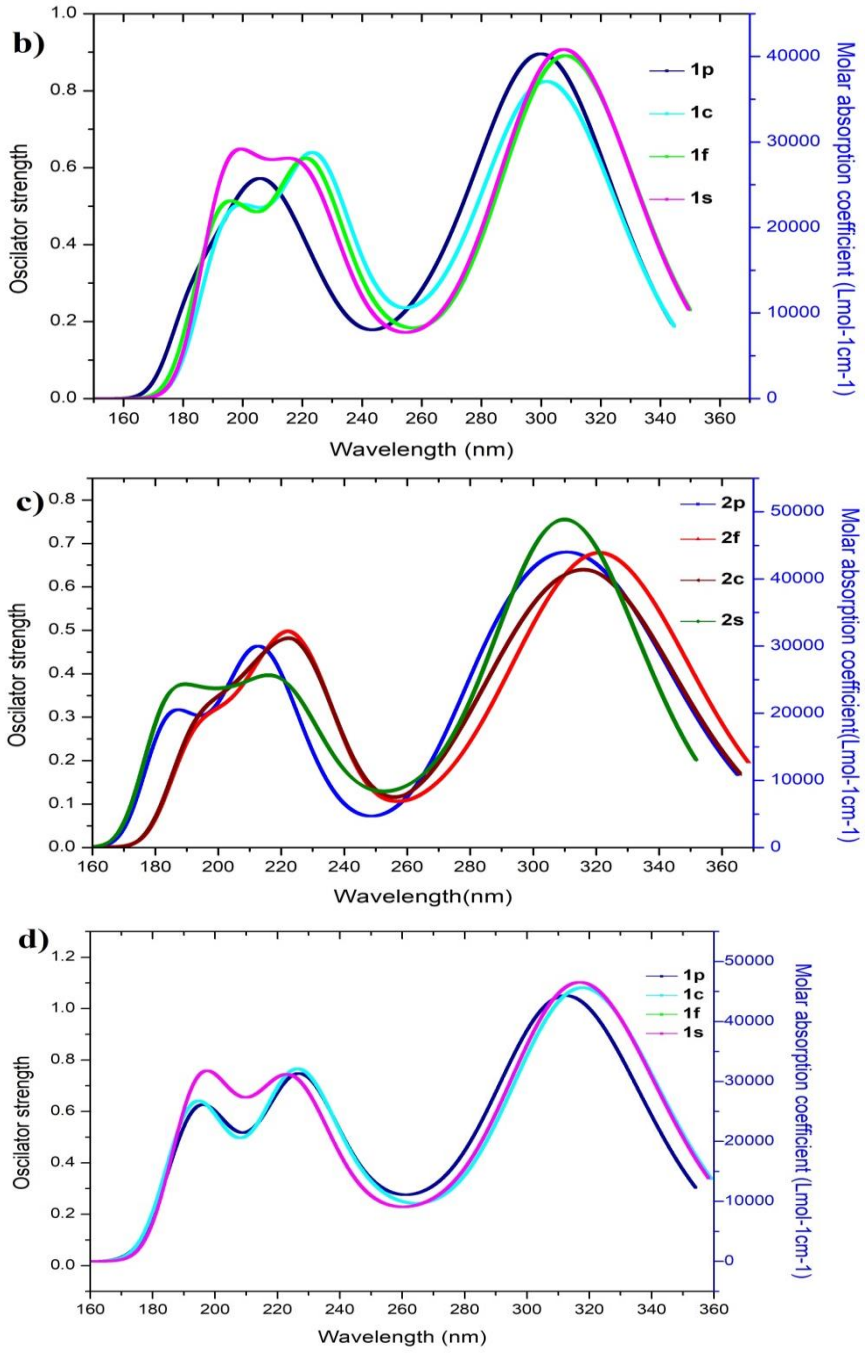

Fig.5.3. UV spectra of the compound studied a) and b) in gas phase, and c) and d) in ethanol medium

5.4. Conclusions

In this chapter, the radical scavenging activity of mainly eight Avenanthramides **(2p, 2f, 2c, 1p, 1c, 1f, 1s,** and **2s)** derived from oats phenolics are computationally explored using DFT/M06-2X/6-31+G(d, p) level of theory in the gas phase, ethanol and water solvents. Among the three mechanisms, the thermodynamically favorable mechanism in the gas phase is HAT whereas SPLET in ethanol and water. The BDE values are found to be the best correlating with SD and DI values. Also, the trends in BDE are found to be exactly correlating with corresponding experimental results of evidence of radical scavenging activity. The hydroxyl group present on the B- ring is more active than the A-ring and the hydroxyl group in the ortho position of the donor hydroxyl group can enhance the activity by stabilizing the radical formed more than the methoxy group. The substitution on the B-ring doesn't affect the hydroxyl group of A ring. The studied compounds are found to be effectively screening only UVA radiations. The good antioxidant potential and UV filtering potential of the selected compound revealed the skin application of the compounds. Together, the proven benefits of Avenanthramides in skin protection and the treatment of dermatological diseases and their potential to prevent and treat chronic oxidative stress and inflammation linked to the onset, progression, and severity of aging-related diseases, such as metabolic, cardiovascular, cerebrovascular, and neurodegenerative diseases, point to these compounds as a promising new elixir of youth with both cosmetic and pharmaceutical benefits.

References

1. Pizzino G, Irrera N, Cucinotta M, et al (2017) Oxidative Stress: Harms and Benefits for Human Health. Oxid Med Cell Longev 2017:8416763. https://doi.org/10.1155/2017/8416763

2. Valko M, Leibfritz D, Moncol J, et al (2007) Free radicals and antioxidants in normal physiological functions and human disease. Int J Biochem Cell Biol 39:44–84. https://doi.org/https://doi.org/10.1016/j.biocel.2006.07.001

3. Larson R (1988) Larson RA. The antioxidants of higher plants. Phytochemistry 27: 969-978. Phytochemistry 27:969–978. https://doi.org/10.1016/0031-9422(88)80254-1

4. Peterson DM (2001) Oat Antioxidants. J Cereal Sci 33:115–129. https://doi.org/https://doi.org/10.1006/jcrs.2000.0349

5. Collins FW (1989) Oat phenolics: avenanthramides, novel substituted N-cinnamoylanthranilate alkaloids from oat groats and hulls. J Agric Food Chem 37:60–66. https://doi.org/10.1021/jf00085a015

6. Yang J, Ou B, Wise ML, Chu Y (2014) In vitro total antioxidant capacity and anti-inflammatory activity of three common oat-derived avenanthramides. Food Chem 160:338–345. https://doi.org/https://doi.org/10.1016/j.foodchem.2014.03.059

7. Fagerlund A, Sunnerheim K, Dimberg LH (2009) Radical-scavenging and antioxidant activity of avenanthramides. Food Chem 113:550–556. https://doi.org/https://doi.org/10.1016/j.foodchem.2008.07.101

8. Chu Y-F, Wise ML, Gulvady AA, et al (2013) In vitro antioxidant capacity and anti-inflammatory activity of seven common oats. Food Chem 139:426–431. https://doi.org/https://doi.org/10.1016/j.foodchem.2013.01.104

9. de Bruijn WJC, van Dinteren S, Gruppen H, Vincken J-P (2019) Mass spectrometric characterisation of avenanthramides and enhancing their production by germination of oat (Avena sativa). Food Chem 277:682–690. https://doi.org/https://doi.org/10.1016/j.foodchem.2018.11.013

10. Soycan G, Schar MY, Kristek A, et al (2020) Composition and content of phenolic acids and avenanthramides in commercial oat products: Are oats an important polyphenol source for consumers?

TI2 - Food Chemistry: X

11. M. J. Frisch, G. W. Trucks, H. B. Schlegel, G. E. Scuseria, M. A. Robb, J. R. Cheeseman, G. Scalmani, V. Barone, G. A. Petersson, H. Nakatsuji, X. Li, M. Caricato, A. V. Marenich, J. Bloino, B. G. Janesko, R. Gomperts, B. Mennucci, H. P. Hratchian, J. V. and DJF (2016) Gaussian 16, Revision C.01

12. Lu T, Chen F (2012) Multiwfn: A multifunctional wavefunction analyzer. J Comput Chem 33:580–592. https://doi.org/10.1002/jcc.22885

13. Tomasi J, Mennucci B, Cammi R (2005) Quantum Mechanical Continuum Solvation Models. Chem Rev 105:2999–3094. https://doi.org/10.1021/cr9904009

14. Leopoldini M, Marino T, Russo N, Toscano M (2004) Antioxidant Properties of Phenolic Compounds: H-Atom versus Electron Transfer Mechanism. J Phys Chem A 108:4916–4922. https://doi.org/10.1021/jp037247d

15. Leopoldini M, Russo N, Toscano M (2011) The molecular basis of working mechanism of natural polyphenolic antioxidants. Food Chem 125:288–306. https://doi.org/10.1016/j.foodchem.2010.08.012

16. Litwinienko G, Ingold KU (2007) Solvent Effects on the Rates and Mechanisms of Reaction of Phenols with Free Radicals. Acc Chem Res 40:222–230. https://doi.org/10.1021/ar0682029

17. Litwinienko G, Ingold KU (2004) Abnormal Solvent Effects on Hydrogen Atom Abstraction. 2. Resolution of the Curcumin Antioxidant Controversy. The Role of Sequential Proton Loss Electron Transfer. J Org Chem 69:5888–5896. https://doi.org/10.1021/jo049254j

18. Musialik M, Litwinienko G (2005) Scavenging of dpph• Radicals by Vitamin E Is Accelerated by Its Partial Ionization: the Role of Sequential Proton Loss Electron Transfer. Org Lett 7:4951–4954. https://doi.org/10.1021/ol051962j

19. Nakanishi I, Kawashima T, Ohkubo K, et al (2005) Electron-transfer mechanism in radical-scavenging reactions by a vitamin E model in a protic medium. Org Biomol Chem 3:626–629. https://doi.org/10.1039/b416572a

20. Bruno GM, , Leonardo Lo Presti CG (2020) Spin Density Topology.

Molecules 25:3537

21. Matito E, Poater J, Solà M, et al (2005) Comparison of the AIM Delocalization Index and the Mayer and Fuzzy Atom Bond Orders. J Phys Chem A 109:9904–9910. https://doi.org/10.1021/jp0538464

22. Shameera Ahamed TK, Rajan VK, Sabira K, Muraleedharan K (2019) DFT and QTAIM based investigation on the structure and antioxidant behavior of lichen substances Atranorin, Evernic acid and Diffractaic acid. Comput Biol Chem 80:66–78. https://doi.org/https://doi.org/10.1016/j.compbiolchem.2019.03.009

23. Bratt K, Sunnerheim K, Bryngelsson S, et al (2003) Avenanthramides in Oats (Avena sativa L.) and Structure−Antioxidant Activity Relationships. J Agric Food Chem 51:594–600. https://doi.org/10.1021/jf020544f

24. Peterson DM, Hahn MJ, Emmons CL (2002) Oat avenanthramides exhibit antioxidant activities in vitro. Food Chem 79:473–478. https://doi.org/https://doi.org/10.1016/S0308-8146(02)00219-4

25. Zhang T, Shao J, Gao Y, et al (2017) Absorption and Elimination of Oat Avenanthramides in Humans after Acute Consumption of Oat Cookies. Oxid Med Cell Longev 2017:2056705. https://doi.org/10.1155/2017/2056705

26. Dimberg LH, Theander O, Lingnert H (1993) Avenanthramides--a group of phenolic antioxidants in oats. Cereal Chem 70:637–641

27. Shama G (2014) Ultraviolet Light. In: Batt CA, Tortorello MLBT-E of FM (Second E (eds). Academic Press, Oxford, pp 665–671

28. D'Orazio J, Jarrett S, Amaro-Ortiz A, Scott T (2013) UV radiation and the skin. Int J Mol Sci 14:12222–12248. https://doi.org/10.3390/ijms140612222

29. Ajmala Shireen P, Abdul Mujeeb VM, Muraleedharan K (2017) Theoretical insights on flavanones as antioxidants and UV filters: A TDDFT and NLMO study. J Photochem Photobiol B Biol 170:286–294. https://doi.org/https://doi.org/10.1016/j.jphotobiol.2017.04.021

30. Colls J (2010) Ozone depletion and ultraviolet radiation. Air Pollut 163:472–510. https://doi.org/10.4324/9780203476024_chapter_12

31. Uv H, Uva A Ultraviolet (UV) Radiation. 1–11

32. Finkel T, Holbrook NJ (2000) NATURE - Finkel 2000 - Oxidative stress and biology of ageing. 408:239–247. https://doi.org/10.1038/35041687

33. Baumann LS (2007) Less-known botanical cosmeceuticals. Dermatol Ther 20:330–342. https://doi.org/https://doi.org/10.1111/j.1529-8019.2007.00147.x

34. Perrelli A, Goitre L, Salzano AM, et al (2018) Biological Activities, Health Benefits, and Therapeutic Properties of Avenanthramides: From Skin Protection to Prevention and Treatment of Cerebrovascular Diseases. Oxid Med Cell Longev 2018:6015351. https://doi.org/10.1155/2018/6015351

35. Sur R, Nigam A, Grote D, et al (2008) Avenanthramides, polyphenols from oats, exhibit anti-inflammatory and anti-itch activity. Arch Dermatol Res 300:569–574. https://doi.org/10.1007/s00403-008-0858-x

36. Chen C-YO, Milbury PE, Collins FW, Blumberg JB (2007) Avenanthramides Are Bioavailable and Have Antioxidant Activity in Humans after Acute Consumption of an Enriched Mixture from Oats12. J Nutr 137:1375–1382. https://doi.org/https://doi.org/10.1093/jn/137.6.1375

Chapter 6

Extended double proton and electron transferability of Avenanthramides, feasibility of formation of benzodioxole /o-quinone, and scavenging of ROS/RNS

- ✓ *The possibility of dHAT, SPLHAT, and StPLdET mechanism in the compounds were explored other than HAT, SET-PT and SPLET mechanism.*
- ✓ *The study also extended to the quenching of different reactive oxygen and nitrogen species by the selected compounds.*
- ✓ *The radical deactivation is studied by utilizing parameters, redox potential and equilibrium constant in a thermodynamic cycle.*

7.4. Introduction

In Chapter 5, the pathways of radical scavenging activity of selected AVs are discussed by three possible mechanisms. The reaction pathways both in the solvent and gas phase are discussed. Herein, the extended reaction mechanisms of radical action by the compounds are involved. The phenoxyl radicals generated in the first H^+ /e^- reaction may proceed in a second H^+ /e^- reaction to trap free radicals as the molecule contains more than one hydroxyl group[1]. So in this regard, the thermodynamic feasibility of double HAT (dHAT) is further explored. Furthermore, the mono-deprotonated form of AVs (carboxylates) may further exhibit free radical scavenging activity. The mechanism may further extend to sequential proton loss hydrogen atom transfer (SPLHAT) and sequential triple proton loss double electron transfer (StPLdET) (Fig.6.1).

Moreover, the study also extended to the quenching of different reactive species by the selected compounds. Reactive oxygen species (ROS) are produced as a result of regular metabolic processes or in reaction to outside influences like UV radiation. Although reactive species play an important role in regulating the physiological function of living systems, their overproduction causes oxidative stress, which leads to cell death and tissue damage. Even though reactive species play an important role in regulating the physiological function of living systems, their overproduction causes oxidative stress, which leads to cell death and tissue damage, which causes neurodegenerative diseases, cancer, diabetes, and cardiovascular disease[2–4].

In this regard, five reactive oxygen and nitrogen species (RONs) that are known to harm biological systems have been taken

into consideration. Superoxide radical anions, hydroxyl and hydroperoxyl radicals, and nitrogen monoxide and nitrogen dioxide radicals make up the ROS and RNS, respectively. The most oxidizing ROS is the hydroxyl radical, which is responsible for DNA oxidative damage. The hydroperoxyl radical's lengthy half-life permits it to reach distant cellular sites. Even though the reactivity of the nitric oxide radical is minimal, excessive synthesis may cause damage to cells. It may react with the superoxide radical anion to form peroxynitrite, a potent oxidizing, and nitrating agent capable of causing protein, lipid, and DNA damage[5].

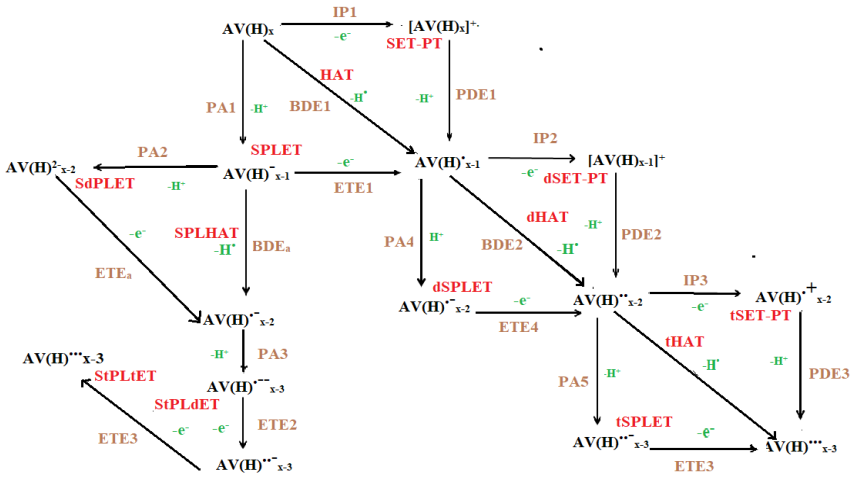

Fig. 6.1. A schematic representation of all the antioxidant mechanisms along with the associated enthalpy change for an AVs molecule (AV(H)x).

Moreover, the equilibrium constant and redox potential of electron transfer were calculated to determine the feasibility of scavenging the RONs under study in an aqueous solution by the proposed AVs. These were compared with the hydrogen atom affinity results to ascertain the relative reactivity of the considered RONs.

7.5. Computational details

The calculations were performed and the geometries of all the structures were fully optimized with M06-2X/6-31+G (d, p) level of theory using the Gaussian 16W suite [6]. At the same level of theory, the reactive species were optimized using the unrestricted open-shell technique. The integral equation formalism of polarised continuum model (IEF-PCM) was used to account for solvent effects [7]. The solvent water (ε=78.35) was selected to model the aqueous environment.

7.6. Results and discussion

The optimized structures are given in Fig.3.4. A detailed description of conformational search and geometry optimization is given in Chapter 3. Scavenging of a reactive oxygen or nitrogen species (RONs) by an antioxidant molecule can take several forms, including hydrogen atom abstraction by the reactive species from the neutral form (HAT, SET-PT, and SPLET), mono-deprotonated form (SPLHAT and StPLdET), and single electron transfer (SET) from and to the antioxidant molecule. The antioxidant activities of the eight molecules selected are communicated by its three antioxidant mechanisms (HAT, SET-PT, and SPLET) in the gas phase and two solution media earlier. Here the extended reactivity studies of the molecules are included.

7.6.2. dHAT Mechanism: The second hydrogen atom transfer

Since the compound contains more than one hydroxyl group, the chance of a second hydrogen atom transfer from the first phenoxyl radical formed is indispensable. The radical formed in the first process may react further by providing second hydrogen to radical species. The

corresponding enthalpy differences are given as BDE_d. As mentioned above, the lower the value of BDE_d higher the radical quenching ability. The second possibility of each compound toward hydrogen atom transfer was included in Table 6.1. The Table 6.1, clearly depicts the uneasiness of the hydrogen atom transfer from both rings, *i.e.* the bond dissociation enthalpy for the hydrogen atom transfer from (5,4')-OH (The numbers in the bracket of position are represented in order of first radical and second radical formed respectively) or vice versa spans in the range of 100 kcal/mol. Hence these processes are high energy demanding and less favourable.

For **2c** and **1c** compounds, the second chance will be energetically favorable for the hydrogen atom donation from the 3'OH. The BDE_d of 3'OH is found to be lower than the 4'OH in the first HAT (74.91 (72.31) kcal/mol for **2c** and 74.98 (73.02) kcal/mol for **1c** (values in bracket represents the corresponding in aqueous phase)) and it also found that which is also lower than in aqueous solution. For compound **2c**, the transfer of a second hydrogen atom (3'OH of 4'O$^{\cdot}$radical) is more feasible than the first HAT by the difference of 3 and 7 kcal/mol respectively in the gas phase and water medium. This shows that the produced phenoxyl radicals have strong antioxidant activity and that the second HAT process from 3′- OH is feasible when trapping radicals via the formation of a highly stabilized o-quinone intermediate. The spin density distribution given in Fig. 6.2 also supports the second radical formation from the 3'OH group. The radicals formed from the 4'OH group are highly delocalized with a spin density value of 0.071 in 4'O$^{\cdot}$ species. In the mono-radical species

of the compound, the oxygen of 3'OH possesses some radical nature by a spin density value of 0.023. Hence, the feasibility of the diradical formation and o-quinone intermediate are confirmed. In addition, the BDE_d values of (5,4')-OH or (4',5)-OH are significantly higher than the first HAT both in the gas phase and water medium which denies the possibility of a second H-abstraction from the 5- OH or 4'-OH position.

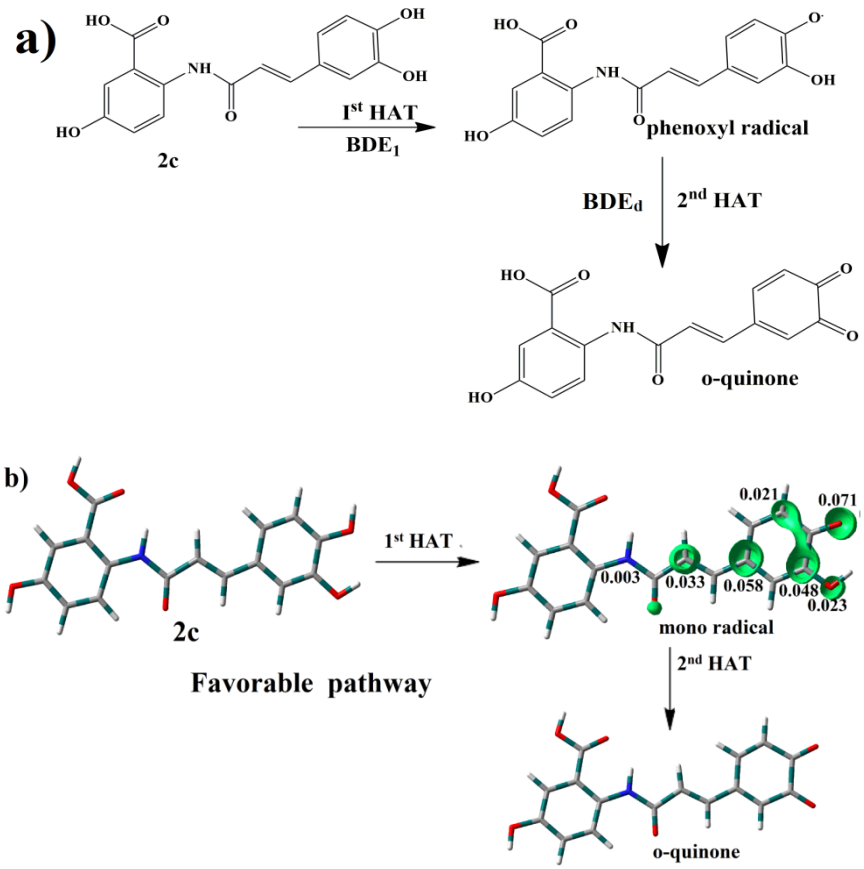

Fig. 6.2. Double HAT mechanism of **2c** a) probable route b) the optimized structures of each compound and spin density distribution of mono radical formed (isovalue 0.004).

According to calculations, for **2s** after the first hydrogen transfer from 4'OH, the chances of a second hydrogen transfer were analyzed. The possibility of a second process is highly unfavorable for 5OH in 4'O· due to a very high BDE value of 104 kcal/mol. Hence considering the higher reactivity of the **s** series compound in the radical quenching process, the pathway of second hydrogen atom transfer via the OCH3 group will have to be checked. The schematic representation of the dHAT of **2s** is given in Fig. 6.3. For **2s**, the ortho-OCH3 group from the 5' position was considered. The second OCH_2 radical was formed which upon cyclization led to the formation of 1, 3-benzodioxole of **2s**. The formation of cyclic intermediate in ortho-OCH3 group are already reported by various literature [8–15]. The ortho-OCH3 group from 3'OH is excluded because cyclic formation for 1, 3- benzodioxole formation occurs by the reorientation of OCH3, and choosing this step takes additional energy need than 5'OCH3. The production of benzodioxole (singlet state) rather than phenoxyl diradical (triple state) after the double HAT reaction accounts for the high activity of the phenoxyl radicals of **2s**. In our results, the more stable benzodioxole formation takes place with BDE of 43.32 and 44.50 kcal/mol, respectively in the gas phase, and aqueous phase. Spin distribution analysis reveals that the radical stabilization of the 4'O radical (0.075) is lower than **2c** (0.071). Moreover, as observed in **2c** (3'OH), the **2s** compounds lack the radical spin localization at the OCH3 group. Additionally, the bond energy of C-H is high compared to the phenolic O-H group. Hence the process is likely to be less feasible compared to **2c** and o-quinone formation.

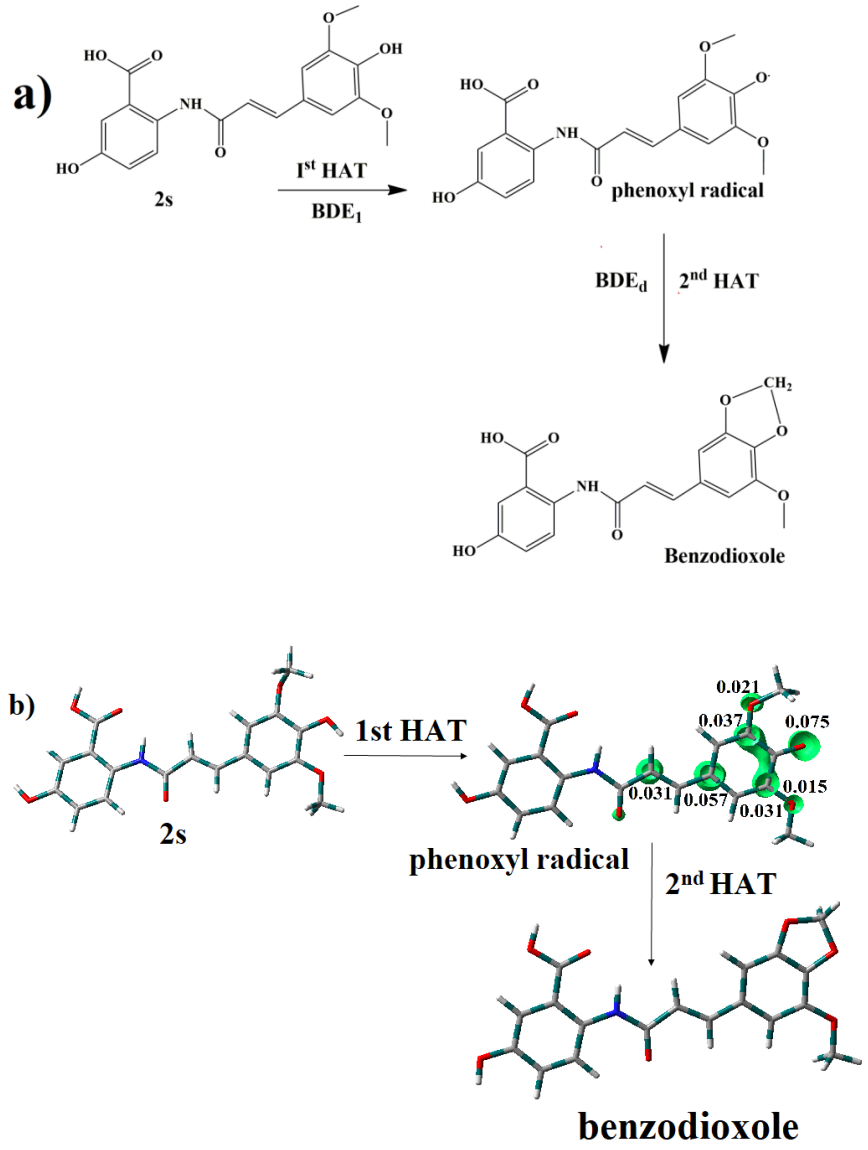

Fig. 6.3. Double HAT mechanism in **2s** a) probable route b) the optimized structures of each compound and spin density distribution of mono radical formed (isovalue 0.004).

For **2p** and **2f**, the second HAT is found to be unfavorable due to larger BDEd for the 4′-OH in 5-O• radicals in comparison with the first hydrogen transfer reactions. The observed higher reactivity of **c**

series and **s** series displays the experimental findings [16] compared to other compounds.

Table 6.1 The calculated BDE_d values of AVs in the gas phase and water medium. The numbers in the bracket of position (column 2) are represented in order of first radical and second radical formed respectively.

Compound	position	BDE_d (kcal/mol)	
		Gas	Water
2p	(5,4')-OH	103.58	99.85
2f	(5,4')-OH	104.61	99.45
2c	(4',5)-OH	103.99	100.99
	(4',3')-OH	74.91	72.31
2s	(4',5)-OH	104.29	101.34
	(4'-OH, 3'-OCH3)	43.32	44.50
1c	(4',3')-OH	74.98	73.02
1f	(4'-OH, 3'-OCH3)	40.58	44.28
1s	(4'-OH, 3'-OCH3)	43.24	44.18

7.6.3. SPLHAT Mechanism: proton affinities and bond dissociation enthalpies

The HAT and SPLET pathways in the mono-deprotonated form of AVs are respectively known as SPLHAT and StPLdET mechanisms.

$$AV(OH)_{n-1}O^- \rightarrow [AV(OH)_{n-2}OO]^{\bullet -} + H^{\bullet} \quad (6.1)$$

The first step of SPLHAT is like SPLET, a proton is lost from the molecule, and the second step is HAT. The initial step of both these mechanisms is deprotonation of the parent compound to give the monoanion. The BDE_s (BDE of anionic forms of the molecule) are

given in Table 6.2. As can be seen from Table 6.2, the calculated BDEs are lower than the ETE of the corresponding position in each solvent. Hence it can be concluded that the feasibility of radical activity through SPLHAT in polar media. Also, the BDE of deprotonated AVs is lower than the BDE in the HAT process revealing the easiness of electron donation of the OH group from the mono-deprotonated form of the molecule (carboxylate anions). That means deprotonation favors hydrogen abstraction from phenolic hydroxyl groups[17].

Table 6.2 The calculated BDEs in the SPLHAT process of the studied AVs in polar solvents (In kcal/mol).

	BDE_s(kcal/mol)				
Compound	Position	Water	Compound	Position	Water
2p- COO^-	4' OH	86.26	**1p-** COO-	4' OH	85.76
	5 OH	82.87	**1c-** COO^-	4' OH	79.73
2f- COO^-	4' OH	82.64		3' OH	86.13
	5 OH	81.00	**1f-** COO^-	4' OH	82.83
2c- COO^-	4' OH	78.95	**1s-** COO^-	4' OH	81.19
	5 OH	81.01		-	-
	3' OH	85.44		-	-
2s- COO^-	4' OH	81.08		-	-
	5 OH	81.25		-	-

7.6.4. StPLdET Mechanism: proton affinities and electron transfer enthalpies

In solution phase calculations, depending upon the pH, AVs containing carboxylic functionalities can be partially or fully dissociated according to the polarity of the media. Apart from the SPLHAT mechanism the molecule may further lose a proton from the molecule and radical action may occur through sequential double proton loss electron transfer (SdPLET) or sequential triple proton loss double electron transfer (StPLdET) mechanism.

In the StPLdET mechanism, the first proton loss or proton transfer (PT) occurs in the carboxylic group due to a low PA_1 value which leads to the formation of ($AV(OH)_{n-1}O^-$) (Equation 6.2). The second proton transfer (Equation 6.3) takes place followed by electron transfer (Equation 6.4) generates dianions ($[AV(OH)_{n-2}OO]^{2-}$) and radical anions ($[AV(OH)_{n-2}OO]^{\bullet -}$, respectively. The lower PA_2 values than ETE_1 (electron transfer from the carboxylate anion) values of the molecule are evidenced by the feasibility of second proton transfer from the monoanionic form of the compound. The third proton transfer (Equation 6.5) and sequential electron loss (Equation 6.6) may result in the formation of a radical dianion ($[AV(OH)_{n-3}OOO]^{\bullet 2-}$), followed by a quinone or benzodioxole ($[AV(OH)_{n-3}OOO]^{\bullet\bullet -}$) (Equation 6.6). The values of parameters of the StPLdET mechanism are tabulated in Table A6.1. The enthalpy differences corresponding to the Equations 6.3, 6.4, 6.5, and 6.6 respectively are PA_2, ETE_2, PA_3, and ETE_3. The

complete steps for the StPLdET mechanism in AVs are given as Equations 6.2-6.6.

$$AV(OH)_n \xrightarrow{I^{st}PT} AV(OH)_{n-1}O^- \tag{6.2}$$

$$AV(OH)_{n-1}O^- \xrightarrow{2^{nd}PT} \left[AV(OH)_{n-2}OO\right]^{2-} \tag{6.3}$$

$$\left[AV(OH)_{n-2}OO\right]^{2-} \xrightarrow{I^{st}ET} \left[AV(OH)_{n-2}OO\right]^{\bullet-} \tag{6.4}$$

$$\left[AV(OH)_{n-3}OO\right]^{\bullet-} \xrightarrow{3^{rd}PT} \left[AV(OH)_{n-3}OOO\right]^{\bullet 2-} \tag{6.5}$$

$$\left[AV(OH)_{n-3}OOO\right]^{\bullet 2-} \xrightarrow{2^{rd}ET} \left[AV(OH)_{n-3}OOO\right]^{\bullet\bullet-} \tag{6.6}$$

In the case of **2c**, the compound readily forms its carboxylates by a PA value of 39.61 kcal/mol (PA1). The complete schematic diagram for **2c** is given in Fig. 6.4. Then the carboxylate can either transfer an electron or release a proton. Due to the higher ETE (ETE1 = 125.94 kcal/mol) value for the electron transfer from the carboxylates, the compound preferably goes for ionization from the 4'OH group (PA2 = 46.61 kcal/mol). The dianion formed releases electrons from the 4'O^- and forms 4'$O^{\cdot}$ (ETE2 = 102.55 kcal/mol). The formed radical dianion upon successive proton and electron transfer (PA3 = 42.56 & ETE3 = 99.66 kcal/mol) from the 3'OH group leads to the formation of the o-quinone derivative of **2c**. The o-quinone is also favored for **1c** (Fig. 6.4). The spin density distributions of radical intermediates formed are represented in Fig. 6.5. Similar to dHAT, the electron transfer from both rings are unfavorable. For compound **2s**, carboxylate formation and the third proton transfer and electron

transfer will be favored through the formation of 1, 3- benzodioxole. By the way, the third proton transfer was taken up by the methoxy group (PA3 = 67.31 kcal/mol) and successive electron transfer (ETE3 = 47.71 kcal/mol) (Fig. 6.4).

In the case of the **2p**, after the formation of the carboxylate anion, the next proton transfer takes place from the 4'OH position due lower value of PA_2(= 50.85 kcal/mol). The formed dianion after the electron transfer leads to the formation of its radical anion. The third proton transfer is found to be more feasible (PA_3 = 44.49 kcal/mol) than PA_2 by its 5OH. The ETE3 (= 108.65 kcal/mol) of the corresponding step revealed less electron transfer capability of the compound. Hence the StPLdET mechanism will be less favourable for **2p**. Similarly, for **2f** the second proton abstraction and electron transfer occur in the 4'OH bond, and a radical anion of it is formed. The chance of third proton transfer may take place from the 5 OH position or the methoxy group. The formation of OCH^{2-} and electron transfer is lower energy demanding by its PA_3+ETE_3 values (115.22 kcal/mol) than from 5OH (159.93 kcal/mol).

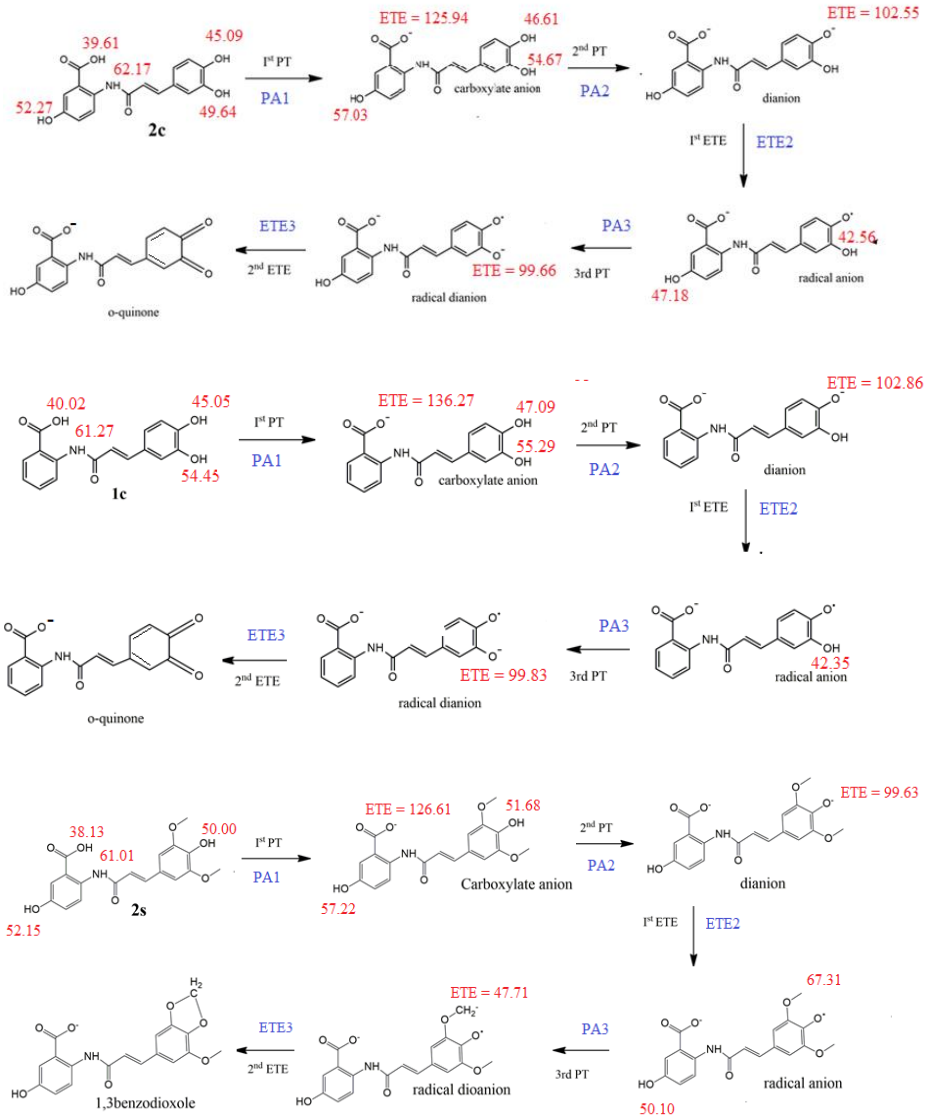

Fig. 6.4. The complete route of StPLdET mechanism in polar medium. PA1 is taken from PA values given in Chapter 5 (in kcal/mol).

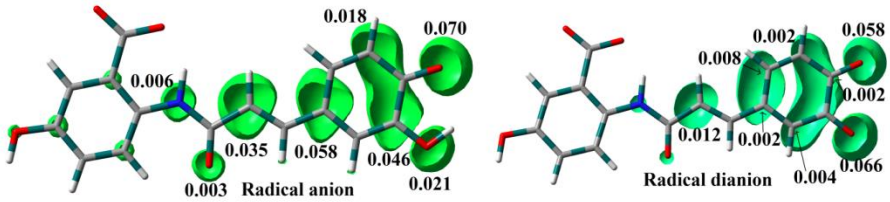

Fig. 6.5. StPLdET mechanism in **2c** spin density distribution of intermediates (isovalue = 0.004)

On comparing the PA_1+ETE_1 and PA_2+ETE_2 values of each molecule the mono-deprotonated form of AVs is found to be less energy demanding than neutral form. A plot of the feasibility of mono-deprotonated and non-deprotonated forms of the molecules is given in Fig.6.6. It indicates the feasibility of the StPLdET mechanism at physiological pH over the SPLET mechanism. At physiological pH, the AVs with carboxyl group can be partially or fully dissociated and form carboxylates of each. The involvement of anionic form of molecule in radical scavenging action is StPLdET mechanisms. The lower PA2 values than ETE1 values, the formation of double deprotonated species would be favorable. Hence StPLdET mechanisms would be favorable in a water medium (polar solvent) provided the pH of the solution is very high.

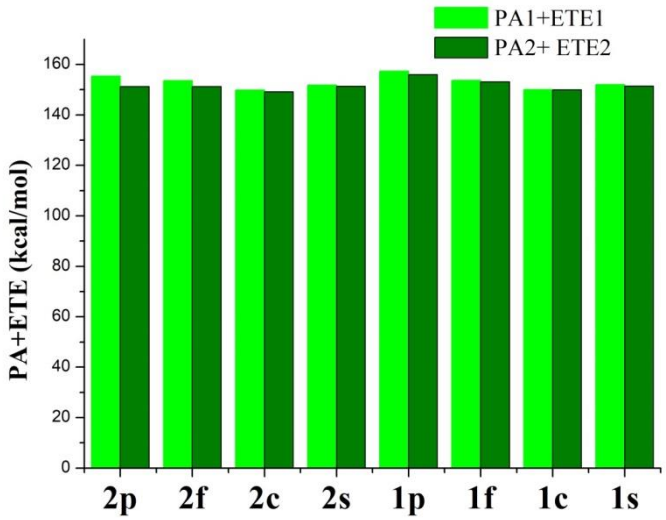

Fig. 6.6. The feasibility of the StPLdET mechanism in mono-deprotonated and non-deprotonated forms of AVs in polar solvents (in kcal/mol).

Aside from dealing with various mechanisms, it is also necessary to emphasize the participation of various targets in radical scavenging action. So for this purpose, the understanding of the features of reactive species has to be considered. Herein the thermodynamic feasibility of the radical reaction between the selected radical species and AVs is involved.

7.6.5. Quenching of reactive oxygen species and nitrogen species **(**RONs)

Reactive oxygen and nitrogen species (RONs) are vital in cell signaling, immunity, and tissue homeostasis and are required for proper physiological activities[18, 19]. Excess radical species, on the other hand, are implicated in the development and accelerated

pathogenesis of a variety of disorders[18]. The common radical species ROS include oxygen-based free radicals, such as the superoxide radical anion ($O_2^{\bullet -}$), hydroxyl ($HO^{\bullet}$), alkoxyl ($RO^{\bullet}$), organic peroxyl ($ROO^{\bullet}$), and hydroperoxyl (HOO•) radicals. RNS comprises peroxynitrite ($ONOO^-$), nitric oxide ($NO^{\bullet}$), and nitrogen dioxide ($NO_2^{\bullet}$)[20]. We considered five ROS/RNS that are significant for biological systems among several RONs. The hydroxyl, hydroperoxyl radicals, and superoxide radical anions are selected under ROS and nitric oxide and nitrogen dioxide radicals among RNS.

7.6.5.1.Hydrogen atom affinity (HAA) and electron affinity (EA)

The energy needs of AVs and selected radical species are essential in predicting probable radical scavenging processes. The optimized images of the radical species considered are given in Table 6.3. So for this purpose, the hydrogen atom affinity (HAA) and electron affinity (EA) of each radical species were calculated both in the gas phase and solvent medium with the help of Equations 6.7 & 6.8 respectively for HAA and EA.

$$R^{\cdot} + H^{\cdot} \rightarrow RH \tag{6.7}$$

$$R^{\cdot} + e^{-} \rightarrow R^{-} \tag{6.8}$$

Where $R^{\bullet}$ represents the radical species and R^- is the radical after one electron acceptance and RH is the protonated radical species. The triplet state of NO^- was considered for calculating the EA. The values of $H^{\bullet}$ and e^- were calculated using the method. The frequently recognized value of 0.001200 Hartree (3.146 kJ/mol) for the electron

enthalpy can be used to calculate the standard values of electron enthalpies in the gas phase[21]. The enthalpies of the hydrogen radical in the gas phase were calculated using Gaussian 16 software with the selected DFT methods and basis set combinations. The enthalpies of hydrogen radicals and electrons in the water phase are also estimated using the Gaussian 16 program package with selected DFT methods and basis set combinations based on the methodology proposed by Markovi et al [22]. The enthalpy values for the hydrogen atom respectively for the gas phase and water phase are taken as -0.494305 Hartree and -0.494314 Hartree. The value of electron enthalpy in water obtained using the above-mentioned method is -0.00299 Hartree.

The computed HAA and EA values are tabulated in Table 6.3. The highest HAA value of hydroxyl radical among all radicals in the gas phase and aqueous phase describes the highly destructive nature of the OH radical. The $O_2^{\bullet -}$ and $^{\bullet}NO$ radicals are in the lower range, suggesting that they are fruitless at accepting a hydrogen atom either in the gas phase or in an aqueous solution. Further, the HAA of the majority of the species under examination increases upon solvation.

The tendency of electron acceptance and formation of its anion is higher for $^{\bullet}NO_2$ followed by $^{\bullet}OH$ and $^{\bullet}OOH$ in the gas phase. The electron acceptance and formation of corresponding anion O_2^{2-} is found to be quite energetically unfavorable in the gas phase due to its positive electron affinity but favorable upon solvation. The negative value of $^{\bullet}NO$ radical in the gas phase is also meant for the lower reactivity. However, the EA values of each reactive species are found to be much higher in the solution phase as compared to the gas phase.

In conclusion, according to HAA and EA values, hydrogen atom acceptance and detoxification through the HAT (hydrogen atom transfer) mechanism will be highly favorable for the radicals, hydroxyl, hydroperoxyl, and nitrogen dioxide radicals among selected RNS in the gas phase and aqueous phase. The SET or SET-PT mechanism, which includes the transfer of a single electron (connected with EA value in Table 6.3) is unfavorable for superoxide radical anions and nitric oxide in the gas phase and it is higher for radicals $^{\bullet}OH$, $^{\bullet}OOH$, and $^{\bullet}NO_2$ in both solutions. In the SPLET mechanism, the second step is electron acceptance (by radical species from antioxidant species) also favorable for $^{\bullet}OH$, $^{\bullet}OOH$, and $^{\bullet}NO_2$ radicals due to their feasible EA values.

Table 6.3 Computed HAA and EA of the considered ROS/RNS (in kcal mol^{-1}) in the gas phase and aqueous solution.

RONS		HAA		EA	
		Gas	Aqueous	Gas	Aqueous
$^{\bullet}OH$		-116.37	-118.28	-36.55	-114.22
$^{\bullet}OOH$		-84.98	-85.56	-21.50	-92.30
$O_2^{\bullet-}$		-59.99	-65.57	165.71	-38.55
$^{\bullet}NO$		-47.02	-49.50	-5.66	-72.40
$^{\bullet}NO_2$	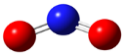	-80.27	-83.36	-55.95	-117.71

7.6.5.2.Electron Affinity (EA) versus Ionization Energy (IE) Map

To assess the electron transfer power between the radical and the selected molecules vertical Ionization Energy (IE) and vertical Electron Affinity (EA) were employed. It has previously been

observed that antioxidant species could either give or take up an electron to scavenge free radicals[23, 24]. This demonstrates that the electron transfer reaction is governed by the ionization energy and the electron affinity of the antioxidant and the free radical. Low ionization energy indicates that the molecule will donate an electron at a low energetic cost, but high electron affinity indicates that the molecule will readily take an extra electron. Here, the single electron transfer tendencies of the compounds are considered.

For this purpose created the IE versus EA map including selected free radicals, selected AVs, and their mono-deprotonated forms (carboxylates) (Fig.6.7 &Table A6.2). The electron flow will occur from molecules in the bottom left area of the map to molecules in the top right section of the map. Hence a radical scavenging action will take place. All the AVs and their mono-deprotonated forms lie in the bottom left area of the map and are better electron donors and worse electron acceptors than the $^{\bullet}OH$, $^{\bullet}OOH$, and $^{\bullet}NO_2$ radicals. Hence they are predicted to act as electron donors to deactivate these free radicals.

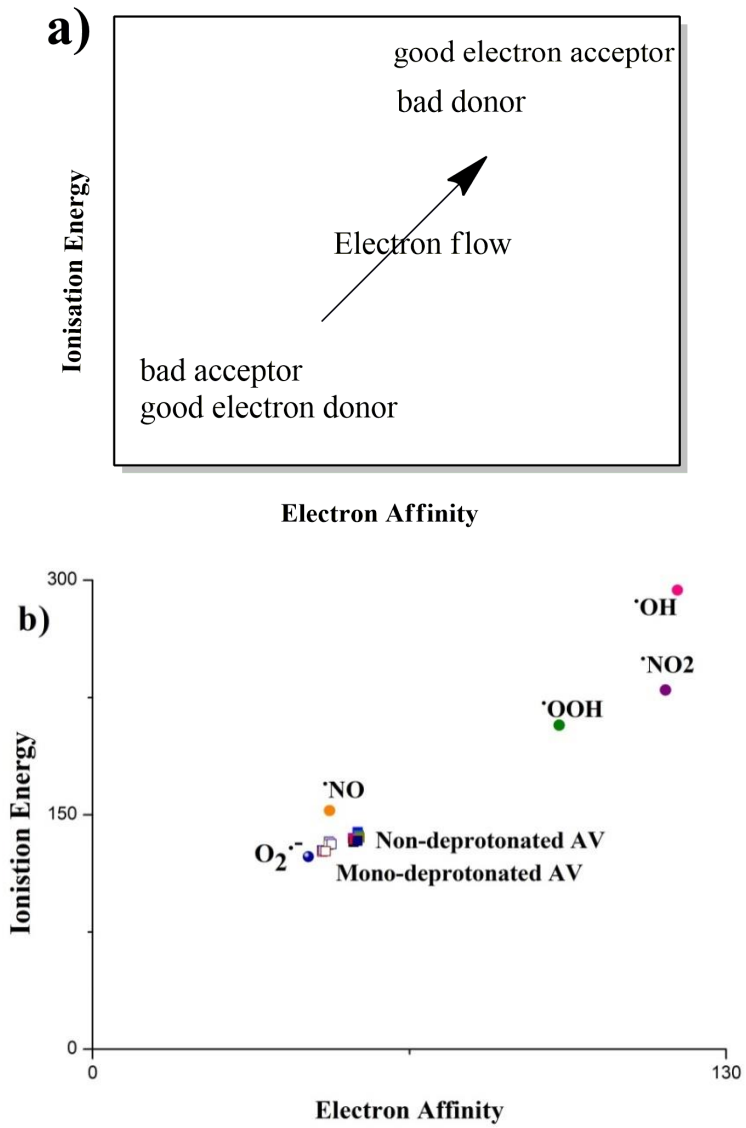

Fig. 6.7. The Map allows a straightforward comparison of the electron donor-acceptor capability of AVs (squares), Mono-deprotonated AVs (squares with filled colors), and radicals •OH (circle-pink), $^{\bullet}$OOH (circle-light green), $O_2^{\bullet-}$ (circle-royal blue), $^{\bullet}$NO (circle-orange), and $^{\bullet}NO_2$ (circle-purple) in water (values are given in kcal/mol).

Selected AVs and their mono-deprotonated equivalents, as well as the free radicals $O_2^{\bullet -}$ and $^{\bullet}NO$, are localized more or less at the same position in the map. As a result, no electron transfer between AVs or mono-deprotonated forms and the radicals $O_2^{\bullet -}$ and $^{\bullet}NO$ is expected. As can be seen from Table A6.2 and Fig.6.7, deprotonated forms are better electron donors than the neutral form of the molecule. The electron affinities are lower in mono-deprotonated molecules than the neutral molecules. According to these results, deprotonated AVs will be better scavengers for radicals $^{\bullet}OH$, $^{\bullet}OOH$, and $^{\bullet}NO_2$ than AVs.

7.6.5.3.Redox potentials and equilibrium constant calculation

To conclude the viability of the reaction of AVs with different reactive oxygen species occurring in an aqueous solution at the physiological pH, the redox potential of the overall reaction, and the corresponding equilibrium constant are carried out [25]. As concluded from the above calculations, the compounds favor the SPLET mechanism in aqueous medium. The previous reports also suggest that the compounds containing carboxylic functional groups exist in their monoanionic forms at physiological pH [17].

Let's now explore if neutral and mono-deprotonated versions of compounds in an aqueous solution could effectively scavenge various RONs. The overall redox reaction of neutral and mono-deprotonated AVs with RONs can be represented by Equations 6.9 & 6.10 respectively. The details of the overall reaction for the calculation of ΔG^0_{rxn} of mono-deprotonated (carboxylates) are discussed here.

Similar is for neutral molecules and adding one H with COO^- is sufficient to understand the cycle.

$$AV(OH)_nCOOH + R^\bullet \xrightarrow{\Delta G^0_{rxn}} AV(OH)_{n-1}O^\bullet COOH + RH \quad (6.9)$$

$$AV(OH)_nCOO^- + R^\bullet \xrightarrow{\Delta G^0_{rxn}} AV(OH)_{n-1}O^\bullet COO^- + RH \quad (6.10)$$

Using the three thermodynamic cycles given in Fig.6.8 the redox potential was calculated. The first step of the SPLET mechanism, i.e. loss of a proton (Equation 6.11), and the second step, scavenging of the free radical species (Equation 6.12) are shown as

$$AV(OH)_nCOO^- \xrightarrow{\Delta G^0(I)} AV(OH)_{n-1}O^-COO^- + H^+ \quad (6.11)$$

$$AV(OH)_{n-1}O^-COO^- + R^\bullet + H^+ \xrightarrow{\Delta G^0(II)} AV(OH)_{n-1}O^\bullet COO^- + RH \quad (6.12)$$

This reaction 6.12 may split up into two half-cell reactions represented as (Equations 6.13 & 6.14)

$$\boldsymbol{R^\bullet + H^+ + e^- \xrightarrow{\Delta G^0(i)} RH} \quad (6.13)$$

$$AV(OH)_{n-1}O^-COO^- \xrightarrow{\Delta G^0(ii)} AV(OH)_{n-1}O^\bullet COO^- + e^- \quad (6.14)$$

The standard Gibbs free energy change for the redox reaction (ΔG^0rxn) can be calculated using Equation 6.15

$$\Delta G^0_{rxn} = \Delta G^0(I) + \Delta G^0(II) \quad (6.15)$$

Then, the corresponding redox potentials and the equilibrium constants were calculated using Equations 6.16 & 6.17 respectively with different radical species. Here, F represents the Faraday constant (23.06 kcal mol^{-1} V^{-1}).

$$E_{rxn} = \frac{-\Delta G^0_{rxn}}{F} \tag{6.16}$$

$$\log K = \frac{FE_{rxn}}{2.303RT} \tag{6.17}$$

Where ΔG^0 (I) is the Gibbs energy change for the step of deprotonation (first step) and ΔG^0 (II) for the second step.

$$\Delta G^0(I) = \Delta G^0_{gas}(I) + \Delta G^0_{solv}(AV(OH)_{n-1}O^-COO^-) + \Delta G^0_{solv}(H^+) - \Delta G^0_{solv}(AV(OH)_nCOO^-) \tag{6.18}$$

$$\Delta G^0(II) = \Delta G^0(i) + \Delta G^0(ii) \tag{6.19}$$

$$\Delta G^0(i) = \Delta G^0_{(g)}(i) + \Delta G^0_{solv}(RH) - \Delta G^0_{solv}(R^\bullet) - \Delta G^0_{solv}(H^+) \tag{6.20}$$

$$\Delta G^0(ii) = \Delta G^0_{(g)}(ii) + \Delta G^0_{solv}(AV(OH)_{n-1}O^\bullet COO^-) - \Delta G^0_{solv}(AV(OH)_{n-1}O^-COO^-) \tag{6.21}$$

The equilibrium constant and redox potential for the radical reaction are tabulated in Table 6.4. From Table 6.4, it is observed that, among the considered reactive species, the hydroxyl group has the highest value of equilibrium constant and redox potential values for both neutral and mono-deprotonated forms of all compounds. Therefore, we can say that the scavenging of hydroxyl radicals by Avenanthramides

at the physiological pH is highly advantageous and spontaneous. The Gibbs free energies corresponding to the scavenging process via the SPLET mechanism are also found to be highly negative for hydroxyl radicals in all cases (both non-deprotonated and deprotonated forms) indicating the feasibility of radical deactivation aqueous solution (Table A6.3).

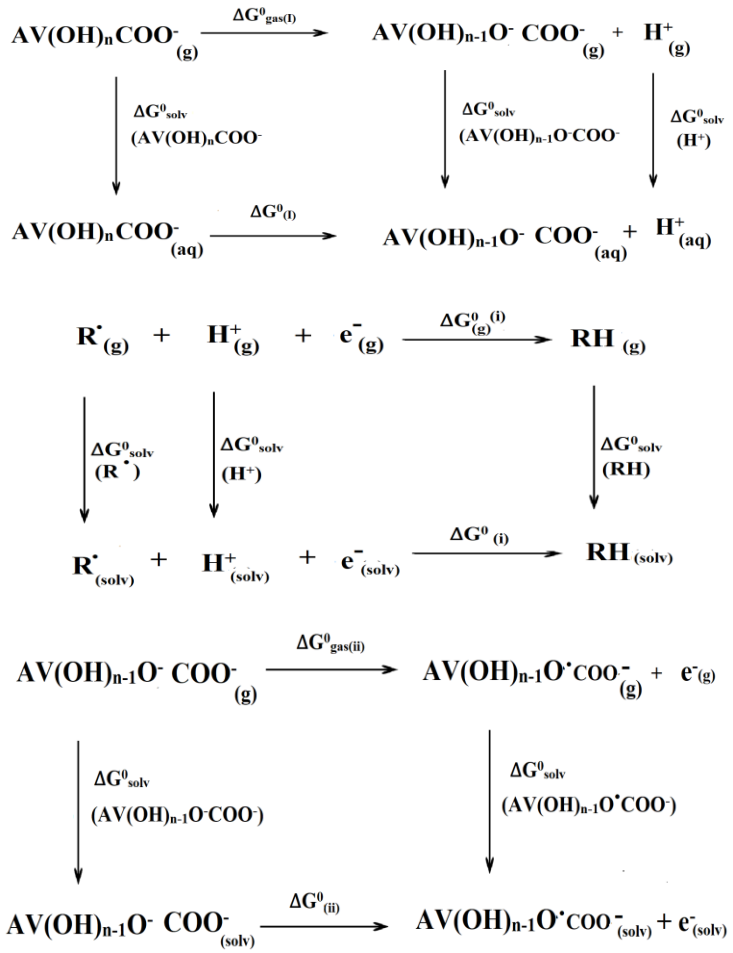

Fig. 6.8. Thermodynamic cycles to compute the standard Gibbs energy change for different reactions in aqueous solution.

Among the species, **2c** has a higher equilibrium constant than other compounds for all reactive species and **1c** in the mono-deprotonated form of the compounds. The order of reactivity follows caffeic acid >sinapic acid>ferulic acid>p-coumaric acid. These results are in line with the previously reported studies on radical scavenging activity[16, 26]. The higher reactivity of **the c** series and **s** series of compounds was due to the presence of stabilizing hydroxyl and methoxy groups. The equilibrium constant and redox potential of all the compounds including both forms are negative for $O_2^{\cdot-}$ and $^{\cdot}NO$ radicals. Hence these radicals are not scavenged by the Avenanthramides. The $^{\cdot}OOH$ radicals are scavenged by all the compounds except **1p**. Likewise, NO2 also exhibits a positive equilibrium constant in most of the cases (**2f** neutral state and **1p** in both forms are exceptions) and shows that it also can scavenge the selected compounds.

The higher values of the equilibrium constants in the case of the mono-deprotonated forms of the Avenathramides indicate their greater potential for scavenging the reactive species. The ease of scavenging of the considered RONS by both the neutral and mono-deprotonated forms of compounds follows the order: $^{\bullet}OH$ > $^{\bullet}OOH$ > $^{\bullet}NO_2$ > $O_2^{\bullet-}$ >$^{\bullet}NO$, which is consistent with the order of the hydrogen atom affinity (HAA) in aqueous solution.

Table 6.4 Computed redox potential (in V) and equilibrium constants with the considered RONs

RONs	Redox potential (E_{rxn})							
	2p	**2f**	**2c**	**2s**	**1p**	**1f**	**1c**	**1s**
$^{\bullet}OH$	1.58 (1.50)	1.51 (1.55)	1.70 (1.71)	1.63 (1.66)	1.47 (1.42)	1.54 (1.55)	1.67 (1.77)	1.63 (1.64)
$^{\bullet}OOH$	0.13 (0.05)	0.06 (0.10)	0.25 (0.26)	0.17 (0.21)	0.02 (-0.03)	0.09 (0.10)	0.22 (0.32)	0.18 (0.18)
$O_2^{\bullet-}$	-0.67 (-0.75)	-0.74 (-0.70)	-0.55 (-0.54)	-0.62 (-0.59)	-0.78 (-0.83)	-0.71 (-0.70)	-0.58 (-0.48)	-0.62 (-0.61)
$^{\bullet}NO$	-1.39 (-1.47)	-1.46 (-1.42)	-1.27 (-1.26)	-1.34 (-1.31)	-1.50 (-1.55)	-1.43 (-1.42)	-1.30 (-1.19)	-1.34 (-1.33)
$^{\bullet}NO_2$	0.05 (-0.03)	-0.02 (0.02)	0.17 (0.19)	0.10 (0.13)	-0.06 (-0.1)	0.02 (-0.02)	0.14 (0.25)	0.10 (0.11)
	Equilibrium constant (K)							
$^{\bullet}OH$	6.27×10^{26} (2.77×10^{25})	3.90×10^{25} (1.82×10^{26})	6.10×10^{28} (1.05×10^{29})	3.79×10^{27} (1.33×10^{28})	7.68×10^{24} (1.24×10^{24})	1.35×10^{26} (1.95×10^{26})	2.06×10^{28} (1.21×10^{30})	4.31×10^{27} (5.70×10^{27})
$^{\bullet}OOH$	1.48×10^{2} (6.55)	9.22 (4.32×10^{1})	1.45×10^{4} (2.48×10^{4})	8.97×10^{2} (3.16×10^{6})	1.82 (2.93×10^{-1})	3.19×10^{1} (4.61×10^{1})	4.88×10^{3} (2.87×10^{5})	1.02×10^{3} (1.35×10^{3})
$O_2^{\bullet-}$	4.16×10^{-12} (1.83×10^{-13})	2.58×10^{-13} (1.21×10^{-12})	4.05×10^{-10} (6.96×10^{-10})	2.51×10^{-11} (8.85×10^{-11})	5.09×10^{-14} (8.22×10^{-15})	8.95×10^{-13} (1.29×10^{-12})	1.37×10^{-10} (8.04×10^{-9})	2.86×10^{-11} (3.78×10^{-11})
$^{\bullet}NO$	2.85×10^{-24} (1.26×10^{-25})	1.77×10^{-25} (8.28×10^{-25})	2.77×10^{-22} (4.77×10^{-22})	1.72×10^{-23} (6.06×10^{-23})	3.49×10^{-26} (5.63×10^{-27})	6.13×10^{-25} (8.84×10^{-25})	9.35×10^{-23} (5.51×10^{-21})	1.96×10^{-23} (2.59×10^{-23})
$^{\bullet}NO_2$	8.41 (0.37)	5.22×10^{-1} (2.44)	8.19×10^{2} (1.41×10^{3})	5.08×10^{1} (1.79×10^{2})	1.03×10^{-1} (1.66×10^{-2})	1.81 (2.61)	2.76×10^{2} (1.63×10^{4})	5.78×10^{1} (7.65×10^{1})

Yang and *et.al* [27] determined the antioxidant activity of three Avenanthramides-**2p**, **2f**, and **2c** against peroxyl radicals, hydroxyl radicals, superoxide anion, singlet oxygen, and peroxynitrite were

determined by using ORAC, HORAC, SORAC, SOAC, and NORAC assays, respectively. The study also included the ability to inhibit NF-kB activation by the three compounds. The report finalized the 1.5-fold total antioxidant activity of **2c** than those of **2f** and **2p**. The EC_{50} values for inhibiting TNF-α-induced NF-kB activation were 64.3 (**2c**), 29.3 (**2f**), and 9.10 lM (**2p**), respectively. Also, it was found that **2c** dispenses comparable antioxidant activity to the standard synthetic antioxidant BHT in the β-carotene test and is more active than Trolox in the DPPH assay[28]. According to the laboratory investigation of antioxidant activity, the activity order is likewise claimed to be **c** ≥ **s** ≥ **f** ≥ **p** [16, 29–31].

7.7. Conclusions

In this work, the extended radical scavenging activities of eight Avenanthramides (**1p**, **1c**, **1f**, **1s**, **2p**, **2f**, **2c**, and **2s**) were evaluated using M06-2X/6-31+G (d, p) level of theory in the gas phase and aqueous solution. The results of this investigation show that all the substances under examination have a strong antioxidant capacity to remove different RONs. The double HAT (dHAT) is more favorable for **s**-series and **c**-series compounds due to the possibility of forming benzodixole and o-quinone, respectively. Moreover, the BDE of SPLHAT is somewhat lower than the BDE of HAT. Hence SPLHAT can also be an alternative pathway in polar medium. The viability of the StPLdET pathway increases with higher pH. Among different radical species selected, the hydroxyl radical displays the highest affinity for the hydrogen atom and electron. Moreover, the higher values of the redox potential and equilibrium constant corresponding to

hydroxyl radical suggest its highly favorable and spontaneous scavenging by the Avenanthramide at the physiological pH. We may also conclude that the neutral and mono-deprotonated forms of the Avenanthramides are effective at scavenging the hydroxyl and hydroperoxyl radicals as well as the nitrogen dioxide radical based on the computed equilibrium constant values. The superoxide radical anion and nitrogen monoxide radical are shown to be ineffective by the selected compounds. Among AVs, the reactivity of caffeic acid derivatives is found to be more reactive followed by sinapic acid derivatives. The lower reactivity with these radicals is exhibited by the p-coumaric acid derivatives. The results obtained coincide with reported experimental antioxidant activity. Moreover, the results also indirectly conclude the independent importance of both aromatic rings towards antioxidant activity.

Given the complexity of antioxidant action, it should be noted that the chosen pathway is influenced not only by the intrinsic reactivity of antioxidant species but also by the characteristics of the targeted radicals. To improve the inferences made from the thermodynamic calculations, it is beneficial to comprehend the kinetics of the processes involved in the radical-trapping process.

References

1. Biela M, Rimarčík J, Senajová E, et al (2020) Antioxidant action of deprotonated flavonoids: Thermodynamics of sequential proton-loss electron-transfer. Phytochemistry 180:112528. https://doi.org/https://doi.org/10.1016/j.phytochem.2020.112528

2. Pizzino G, Irrera N, Cucinotta M, et al (2017) Oxidative Stress: Harms and Benefits for Human Health. Oxid Med Cell Longev 2017:8416763. https://doi.org/10.1155/2017/8416763

3. Sharifi-Rad M, Anil Kumar N V, Zucca P, et al (2020) Lifestyle, Oxidative Stress, and Antioxidants: Back and Forth in the Pathophysiology of Chronic Diseases . Front. Physiol. 11

4. Mellon I (2004) Transcription-Coupled DNA Repair, Overview. In: Lennarz WJ, Lane MDBT-E of BC (eds). Elsevier, New York, pp 204–208

5. Islam BU, Habib S, Ahmad P, et al (2015) Pathophysiological Role of Peroxynitrite Induced DNA Damage in Human Diseases: A Special Focus on Poly(ADP-ribose) Polymerase (PARP). Indian J Clin Biochem 30:368–385. https://doi.org/10.1007/s12291-014-0475-8

6. M. J. Frisch, G. W. Trucks, H. B. Schlegel, G. E. Scuseria, M. A. Robb, J. R. Cheeseman, G. Scalmani, V. Barone, G. A. Petersson, H. Nakatsuji, X. Li, M. Caricato, A. V. Marenich, J. Bloino, B. G. Janesko, R. Gomperts, B. Mennucci, H. P. Hratchian, J. V. and DJF (2016) Gaussian 16, Revision C.01

7. Tomasi J, Mennucci B, Cammi R (2005) Quantum Mechanical Continuum Solvation Models. Chem Rev 105:2999–3094. https://doi.org/10.1021/cr9904009

8. Kozlowski D, Trouillas P, Calliste C, et al (2007) Density functional theory study of the conformational, electronic, and antioxidant properties of natural chalcones. J Phys Chem A 111:1138–1145. https://doi.org/10.1021/jp066496+

9. Brand-Williams, W., Cuvelier, M.E. and Berset C (1995) Use of a Free Radical Method to Evaluate Antioxidant Activity. LWT-Food Sci Technol 28:. https://doi.org/http://dx.doi.org/10.1016/S0023-6438(95)80008-5

10. Zheng Y-Z, Zhou Y, Guo R, et al (2020) Structure-antioxidant activity relationship of ferulic acid derivatives. Eff ester groups end carbon side Chain 120:. https://doi.org/10.1016/j.lwt.2019.108932

11. Lu X-Q, Qin S, Li J (2023) Radical Scavenging Capability and Mechanism of Three Isoflavonoids Extracted from Radix Astragali: A Theoretical Study. Molecules 28

12. Anouar E, Calliste CA, Košinová P, et al (2009) Free Radical Scavenging Properties of Guaiacol Oligomers: A Combined Experimental and Quantum Study of the Guaiacyl-Moiety Role. J Phys Chem A 113:13881–13891. https://doi.org/10.1021/jp906285b

13. Amić A, Marković Z, Klein E, et al (2018) Theoretical study of the thermodynamics of the mechanisms underlying antiradical activity of cinnamic acid derivatives. Food Chem 246:481–489. https://doi.org/https://doi.org/10.1016/j.foodchem.2017.11.100

14. Nenadis N, Sigalas MP (2008) A DFT Study on the Radical Scavenging Activity of Maritimetin and Related Aurones. J Phys Chem A 112:12196–12202. https://doi.org/10.1021/jp8058905

15. Zheng Y-Z, Zhou Y, Guo R, et al (2020) Structure-antioxidant activity relationship of ferulic acid derivatives: Effect of ester groups at the end of the carbon side chain. LWT 120:108932. https://doi.org/https://doi.org/10.1016/j.lwt.2019.108932

16. Fagerlund A, Sunnerheim K, Dimberg LH (2009) Radical-scavenging and antioxidant activity of avenanthramides. Food Chem 113:550–556. https://doi.org/https://doi.org/10.1016/j.foodchem.2008.07.101

17. Mittal A, Vashistha VK, Das DK (2023) Free radical scavenging activity of gallic acid toward various reactive oxygen, nitrogen, and sulfur species: a DFT approach. Free Radic Res 1–10. https://doi.org/10.1080/10715762.2023.2197556

18. Ferreira CA, Ni D, Rosenkrans ZT, Cai W (2018) Scavenging of reactive oxygen and nitrogen species with nanomaterials. Nano Res 11:4955–4984. https://doi.org/10.1007/s12274-018-2092-y

19. Alfadda AA, Sallam RM (2012) Reactive Oxygen Species in Health and Disease. J Biomed Biotechnol 2012:936486. https://doi.org/10.1155/2012/936486

20. Galano A (2015) Free Radicals Induced Oxidative Stress at a Molecular Level: The Current Status, Challenges and Perspectives of Computational Chemistry Based Protocols

21. Bartmess JE (1994) Thermodynamics of the Electron and the Proton. J Phys Chem 98:6420–6424. https://doi.org/10.1021/j100076a029

22. Marković Z, Tošović J, Milenković D, Marković S (2016) Revisiting the solvation enthalpies and free energies of the proton and electron in various solvents. Comput Theor Chem 1077:11–17. https://doi.org/10.1016/j.comptc.2015.09.007

23. Najafi H (2013) Theoretical study of the substituent effects on the reaction enthalpies of the antioxidant mechanisms of stobadine derivatives in the gas-phase and water. J Theor Comput Chem 12:

24. Martínez A, Hernández-Marin E, Galano A (2012) Xanthones as antioxidants: A theoretical study on the thermodynamics and kinetics of the single electron transfer mechanism. Food Funct 3:442–450. https://doi.org/10.1039/C2FO10229C

25. Mittal A, Kakkar R (2020) The effect of solvent polarity on the antioxidant potential of echinatin, a retrochalcone, towards various ROS: a DFT thermodynamic study. Free Radic Res 54:777–786. https://doi.org/10.1080/10715762.2020.1849670

26. Xue Y, Teng Y, Chen M, et al (2021) Antioxidant Activity and Mechanism of Avenanthramides: Double H+/e– Processes and Role of the Catechol, Guaiacyl, and Carboxyl Groups. J Agric Food Chem 69:7178–7189. https://doi.org/10.1021/acs.jafc.1c01591

27. Yang J, Ou B, Wise ML, Chu Y (2014) In vitro total antioxidant capacity and anti-inflammatory activity of three common oat-derived avenanthramides. Food Chem 160:338–345. https://doi.org/https://doi.org/10.1016/j.foodchem.2014.03.059

28. Peterson DM, Hahn MJ, Emmons CL (2002) Oat avenanthramides exhibit antioxidant activities in vitro. Food Chem 79:473–478. https://doi.org/https://doi.org/10.1016/S0308-8146(02)00219-4

29. Bratt K, Sunnerheim K, Bryngelsson S, et al (2003) Avenanthramides in Oats (Avena sativa L.) and Structure−Antioxidant Activity Relationships. J Agric Food Chem 51:594–600. https://doi.org/10.1021/jf020544f

30. Zhang T, Shao J, Gao Y, et al (2017) Absorption and Elimination of Oat Avenanthramides in Humans after Acute Consumption of Oat Cookies. Oxid Med Cell Longev 2017:2056705. https://doi.org/10.1155/2017/2056705

31. Dimberg LH, Theander O, Lingnert H (1993) Avenanthramides--a group of phenolic antioxidants in oats. Cereal Chem 70:637–641

Appendix 6

Table A6.1 The calculated parameters of the StPLdET mechanism in the polar solvent of all AVs (in kcal/mol)

	Compound		PA_2	ETE_2
2^{nd} PT + I^{st} ETE	**2p**	$[4'O,COO]^{2-}$	50.85	105.63
		$[5O, COO]^{2-}$	57.00	94.18
	2f	$[4'O, COO]^{2-}$	52.28	100.58
		$[5O, COO]^{2-}$	57.03	94.19
	2c	$[3' O, COO]^{2-}$	54.67	100.99
		$[4' O, COO]^{2-}$	46.61	102.55
		$[5 O, COO]^{2-}$	57.03	94.20
	2s	$[4' O, COO]^{2-}$	51.68	99.63
		$[5 O, COO]^{2-}$	57.22	94.24
	1p	$[4'O, COO]^{2-}$	50.62	105.36
	1f	$[4'O, COO]^{2-}$	52.75	100.30
	1c	$[3' O, COO]^{2-}$	55.29	101.06
		$[4' O, COO]^{2-}$	47.09	102.86
	1s	$[4'O, COO]^{2-}$	51.50	99.91
			PA_3	ETE_3
3^{nd} PT + 2^{nd} ETE	**2p**	$[4'O^{\cdot},5O, COO]^{2-}$	44.49	108.65
	2f	$[4'O^{\cdot},5O, COO]^{2-}$	49.42	110.50
		$[4'O^{\cdot},3OCH_2, COO]^{2-}$	66.76	48.46
	2c	$[4'O^{\cdot},3'O,COO]^{2-}$	42.56	99.66
		$[4'O^{\cdot},5O,COO]^{2-}$	47.18	108.94
	2s	$[4'O^{\cdot},3OCH_2, COO]^{2-}$	67.31	47.71
		[4'O.,5O, COO]2	50.10	111.25
	1c	$[4'O^{\cdot},3'O,COO]^{2-}$	42.35	99.83

Table A6.2 Ionisation energy and electron affinity value of selected compound, mono-deprotonated species and radicals (In kcal/mol)

	Species	Vertical ionization energy	Vertical electron affinity
Radicals	**•OH**	286.26	116.26
	•OOH	203.36	93.67
	O2•⁻	116.97	39.87
	•NO	146.52	73.47
	•NO2	230.92	119.06
Non-deprotonated Avenanthramides	**2p**	135.09	53.41
	2f	132.60	53.52
	2c	134.20	53.70
	2s	133.35	54.31
	1p	138.95	54.36
	1f	134.66	54.37
	1c	136.84	54.58
	1s	135.44	54.80
Mono-deprotonated Avenanthramides	**2p**	127.22	47.07
	2f	126.39	47.15
	2c	127.20	47.36
	2s	126.72	47.82
	1p	132.97	48.45
	1f	130.72	48.40
	1c	132.35	48.64
	1s	131.30	49.01

Table A6.3 The Gibbs free energies of the reaction between neutral and mono-deprotonated form of compounds in aqueous solvents (kcal/mol)

	ΔG0 (rxn)									
	Mono deprotonated form of avenanthramide					Neutral from of avenanthramide				
	$^{\bullet}OH$	$^{\bullet}OOH$	$O_2^{\bullet-}$	$^{\bullet}NO$	$^{\bullet}NO_2$	$^{\bullet}OH$	$^{\bullet}OOH$	$O_2^{\bullet-}$	$^{\bullet}NO$	$^{\bullet}NO_2$
2p	-34.58	-1.11	17.31	33.85	0.59	-36.43	-2.95	15.47	32.01	-1.26
2f	-35.70	-2.22	16.20	32.74	-0.53	-34.79	-1.31	17.11	33.65	0.38
2c	-39.45	-5.97	12.45	28.98	-4.28	-39.13	-5.66	12.77	29.30	-3.96
2s	-38.23	-4.76	13.67	30.21	-3.06	-37.49	-4.01	14.41	30.94	-2.32
1p	-32.75	0.72	19.15	35.68	2.42	-33.83	-0.35	18.07	34.61	1.34
1f	-35.74	-2.26	16.16	32.70	-0.57	-35.52	-2.05	16.38	32.91	-0.35
1c	-40.89	-7.42	11.00	27.54	-5.72	-38.49	-5.01	13.41	29.94	-3.32
1s	-37.73	-4.26	14.17	30.70	-2.56	-37.56	-4.09	14.33	30.87	-2.40

Chapter 7

Kinetic investigation of quenching of hydroperoxyl radical by the selected Avenanthramides

- ✓ *The kinetic and thermodynamic feasibility of quenching of hydroperoxyl radical with the selected Avenanthramides by two mechanisms FHAT and RAF mechanism in the gas phase are involved.*

7.1. Introduction

As part of the body's defense mechanism, free radicals are helpful to humans in low to moderate concentrations. We can experience oxidative stress in our bodies when there is an excessive amount of free radical generation due to extracellular stress, exposure to toxins, etc[1–4]. One of the intriguing biological functions of AVs that has drawn significant interest is its antioxidant capacity, which is linked to a wealth of health benefits for people, most notably the reduction of harmful cellular effects brought on by Reactive Oxygen Species (ROS)[3, 5, 6]. The ROS are known to play a role in normal cellular processes (such as acting as signal mediators), but their overproduction frequently results in detrimental outcomes like functional loss of cellular membranes, protein modification that results in the deactivation of enzymes, damage to nucleic acids, and other things that are collectively known as oxidative stress. Numerous disorders, including cancer, cardiovascular conditions, Alzheimer's, and Parkinson's diseases, are attributed to the pathophysiology of oxidative stress, which is brought on by an imbalance between the production and scavenging of ROS[7, 8]. Lipid peroxidation is the fundamental mechanism causing both reversible and irreversible cell and tissue damage. Lipid peroxide radical is continually created as a result of polyunsaturated fatty acid-free radical chain oxidation events. It is well known that several dietary polyphenols can efficiently scavenge hydroperoxyl (•OOH) radicals to reduce the negative consequences of lipid peroxidation. Additionally, as worries about the carcinogenic consequences of synthetic antioxidants that are employed

to counteract oxidative stress and oxidative degradation of foods containing lipids have grown, interest in natural phenolic antioxidants has surged. The method of •OOH detoxification by AVs, the phenolic antioxidant found only in oats, acquires enormous significance in such a situation.

Density functional theory (DFT) has been used as a reliable and powerful tool for the study of the oxidation kinetics, by-product formation, and mechanisms at the molecular level of the radical deactivation kinetics. Herein, we use the DFT method to investigate the thermodynamic and kinetic behavior of the selected AVs. Previous studies reported detailed investigations on the different possible mechanisms and different bond cleavage possibilities along with the structure-activity relationship of the compound. In the present case specifically, the kinetics of radical quenching of hydroperoxyl radicals are incorporated.

7.2.Computational Methodology

All calculations were performed using the Gaussian 16W suite of quantum chemical programs[9]. The geometries of the reactants, radicals, transition states, and products were optimized using the Density functional theory (DFT) method employing the Becke, three-parameter[10], Lee-Yang-Parr (B3LYP) [11] and 6-31+G(d,p) basis set in the gas phase and aqueous phase. Both the B3LYP and M06 functionals were tried for the molecules and the thermodynamic parameters calculated using both these functionals showed only slight difference and was similar in trend. So considering computational cost

and time we opted to continue with B3LYP functional. The solvent effects were included by the self-consistent reaction field-polarizable continuum model (SCRF-PCM) method.

For radicals, the unrestricted open-shell method was used, and all outputs were checked for spin contamination errors. The value of a doublet radical (i.e., = 0.75) in all cases denoted the absence of spin contamination. Calculations of vibrational frequencies were made at the same level to verify that each stationary point was minima (zero imaginary frequency) or a transition state (one imaginary frequency). Calculations using the intrinsic reaction coordinate (IRC) were also done to support the idea that the transition state is connected to the proper minima. After the transition states were confirmed, the rate coefficients (kTST(T)) were calculated using Transition State Theory using the KiSThelP program[12], which had previously been used to predict the rate constants involved in free radicals[13]. Through the thermodynamic formulation of the Transition State Theory (TST), the rate constants (k) were calculated with the following equation:

$$k^{TST}(T) = \sigma \frac{k_B T}{h} \left(\frac{RT}{P^0}\right)^{\Delta n} e^{-} \frac{\Delta G^{\neq}(T)}{k_B T}$$

where σ and k_B are respectively the reaction path degeneracy and Boltzmann's constant, h is Planck's constant, and T and P^0 refer to the temperature (298.15 K) and pressure (1 atm) respectively. $\Delta G^{\neq}(T)$ represents the standard Gibbs free energy of activation for the considered reaction and Δn = 1 or 0 for bimolecular or unimolecular reactions, respectively.

7.3.Results and discussion

7.3.1. Reaction mechanism

The two most typical methods employed to activate various reactive species are formal hydrogen atom transfer (FHAT) and radical adduct formation (RAF) are detailed [14–16]. Because single electron transfer (SET) has a substantially greater activation barrier than FHAT and RAF, the process of single electron transfer is not taken into account in this study[14, 16, 17]. The highest positive potential at the phenolic OH group in the molecular electrostatic map given in Chapter 3 (Fig.3.9) indicates that •OOH is inclined to react with the aromatic OH group of AVs. Moreover, the Fukui functions[18], as displayed in Fig. 3.10, showed that the most prominent regions of f^0 are localized in α,β unsaturated carbons, and phenolic carbon and oxygen, which further indicates that these sites are susceptible to radical attacks. The thermal properties of the reactive sites with free radicals will help us understand the initial reaction mechanisms of AVs selected in the radicals system. Therefore, the •OOH attacks through FHAT and RAF mechanisms were calculated in each reactive site. The transition states corresponding to FHAT and RAF reactions were computed and named TS^n and $TS_R{}^n$ in the gas respectively, where n indicates the pathway numbers (see Fig.7.1 for FHAT and Fig.7.A2 for RAF). The optimized structures of transition states are depicted in Fig 7.A1 and 7.A3).

7.3.2. Hydrogen abstraction reactions (HAT)

The complete schematic representations of hydrogen abstraction pathways of each compound initiated by •OOH radicals are

given in Fig.7.1. The hydroxyl groups in the compounds are considered and the carboxylic and nitrogen-containing hydrogen are excluded because of these groups are ineffective for radical reaction as discussed in Chapter 5. In the hydrogen abstraction reaction mechanism between the selected compounds and $^{\bullet}$OOH, the H atom of the phenyl hydroxyl groups of the compounds is transferred to $^{\bullet}$OOH leading to the formation of H_2O_2 along with an unreactive (stabilized) radical (ArO$^{\bullet}$) intermediate (IM). So considering the hydroxyl groups in each compound, two pathways; pathway 1 and pathway 2 are considered and for **2c** an additional pathway; pathway 3 also included. Pathway 1 in each compound stands for the hydrogen abstraction from the 5th hydroxyl group (numbering of the compound is included in chapter 3) and pathway 2 for the hydrogen atom abstraction from 4'OH. The additional pathway for compound **2c** will be due to the hydrogen abstraction from 3'OH by the hydroperoxyl radical. As observed from Fig.7.1, the hydrogen abstraction reactions from the hydroxyl group of selected AVs with •OOH was thermodynamically favorable with negative Gibbs free energy ($\Delta G^0 < 0$) and exothermic with negative reaction enthalpy change ($\Delta H^0 < 0$) except for 3'OH of **1c** and **2c**.

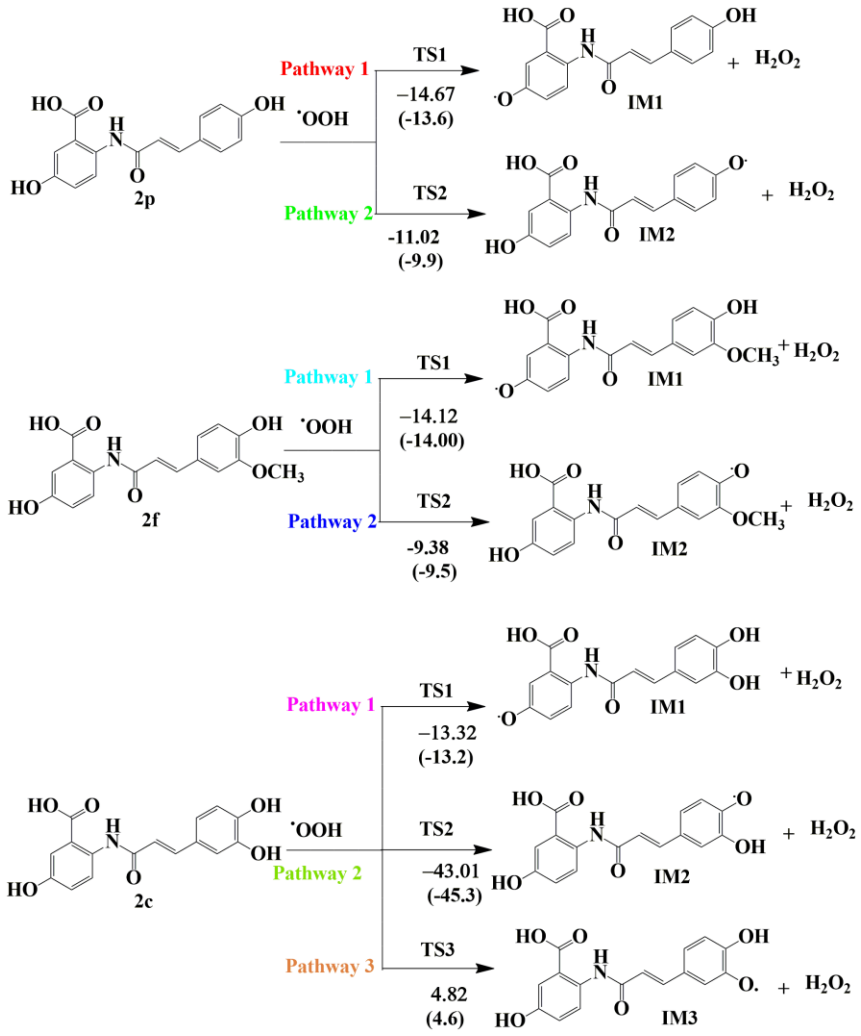
2p
·OOH
Pathway 1
TS1
−14.67
(-13.6)
IM1
+ H2O2
Pathway 2
TS2
-11.02
(-9.9)
IM2
+ H2O2
2f
·OOH
Pathway 1
TS1
−14.12
(-14.00)
IM1
OCH3
+ H2O2
Pathway 2
TS2
-9.38
(-9.5)
IM2
OCH3
+ H2O2
2c
·OOH
Pathway 1
TS1
−13.32
(-13.2)
IM1
+ H2O2
Pathway 2
TS2
−43.01
(-45.3)
IM2
+ H2O2
Pathway 3
TS3
4.82
(4.6)
IM3
+ H2O2

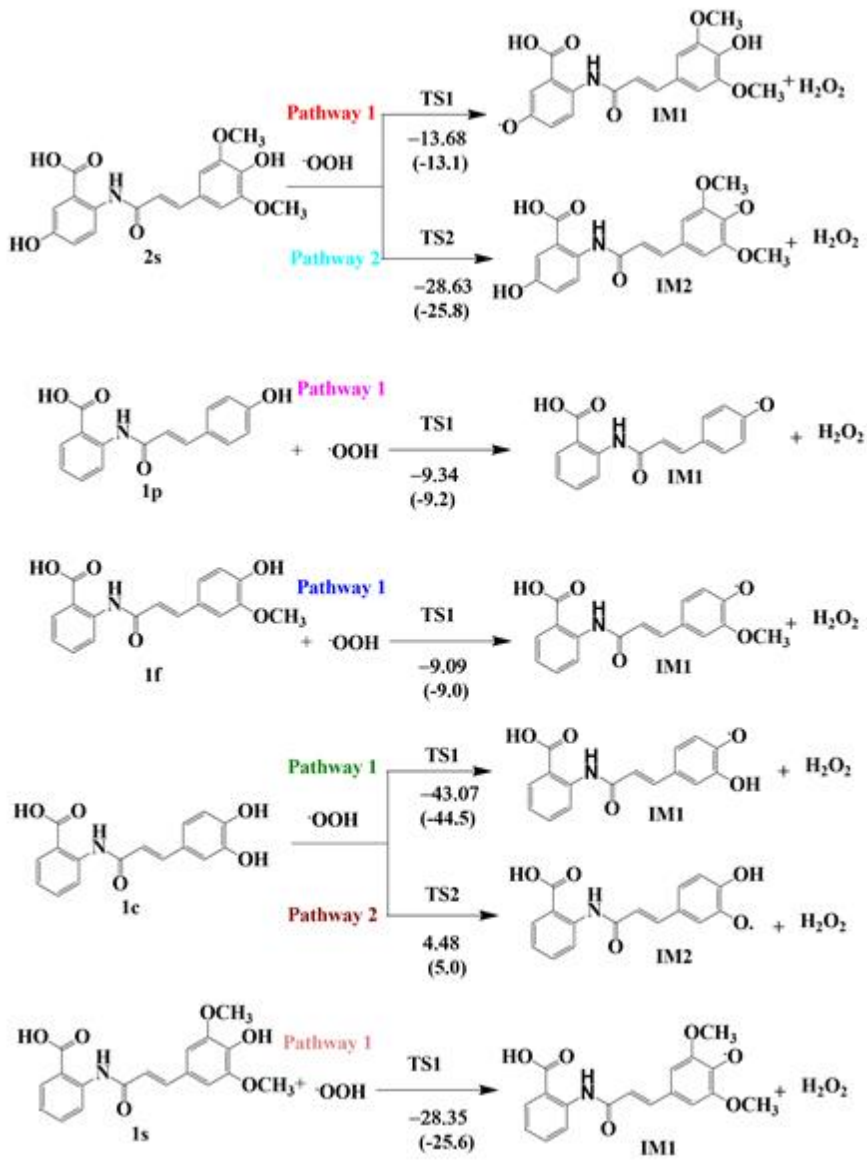

Fig.7.1. The thermodynamics of hydrogen abstraction reactions initiated by •OOH in gas phase ΔG^0 (ΔH^0)of all compounds. The values are given in Unit of kJ mol^{-1}.

The free energy profile of hydrogen abstraction of each compound by their hydroxyl groups is given in Fig.7.2. For 2 series compounds, **2p** and **2f**, the radical reaction will be highly favored from the 5^{th} hydroxyl group (pathway 1). It is evident from the lowest energy barrier and the lowest energy radical intermediate formed from the corresponding positions. For **2c** and **2s**, pathway 2 will be favored by their lowest energy barrier for the radical formation from the 4'hydroxyl group. For 1 series compounds except **1c**, a single pathway (pathway 1) is included and the energy profile diagram of the reaction is given in Fig.7.2. Considering all the compounds, the higher reactivity will be observed for **2c** and **1c** compounds as evidenced from radical mechanism investigations (Fig.7.3). The result is also consistent with experimental observations. The more negative ΔG^0 of formation of product (for **2c**, -43.01 kJ/mol and for **1c**, -43.07 kJ/mol) and low energy barrier (for **2c**, 24.42 kJ/mol and for **1c**, 24.6 kJ/mol). It was worth noting that the H atom connected to 4'OH of **2c** and **1c** was easier to release with the lower Gibbs free energy of activation ($\Delta G^{\neq}$).

The optimized structures of transition states along with the most relevant geometrical features were depicted in Fig.7.A1. The most relevant geometrical parameters of each transition state are the distances of the bonds that are being broken (H1-O1) and that are being formed (H1-O2), and their bond angle (O1-H1-O2). The bond length of H1-O1 and H1-O2 respectively, is in the range of 1.10-1.17 Å and 1.22-1.30 Å, depicting it as an early transition state[19]. The bond angle of these transition states occurs between 163 - 173^0,

implying the closeness of linear relationship in hydrogen atom transfer[20].

The spin density distribution of radical intermediates formed for each compound is discussed in Chapter 5 and it is consistent with the results obtained in the hydrogen atom transfer process. The spin distributions of the transition state structure are given in Table 7.1. From spin density values, **c** series compounds upon radical formation from 4'OH will delocalise better than any compound.

Table 7.1 Spin density values on the transition state structures of each compound (O1 is the oxygen of the bond being broken and O2 is the oxygen of the bond being formed (hydroperoxyl radical oxygen)).

Compound	Transition state	O1	O2
2p	5OH….OOH	0.026	0.046
	4'OH…OOH	0.027	0.052
2f	5OH….OOH	0.022	0.052
	4'OH…OOH	0.023	0.058
2c	5OH….OOH	0.022	0.049
	4'OH…OOH	0.016	0.056
	3'OH…OOH	0.017	0.046
2s	5OH….OOH	0.025	0.047
	4'OH…OOH	0.022	0.06
1p	4'OH…OOH	0.025	0.052
1f	4'OH…OOH	0.023	0.058
1c	4'OH…OOH	0.018	0.056
	3'OH…OOH	0.028	0.057
1s	4'OH…OOH	0.022	0.060

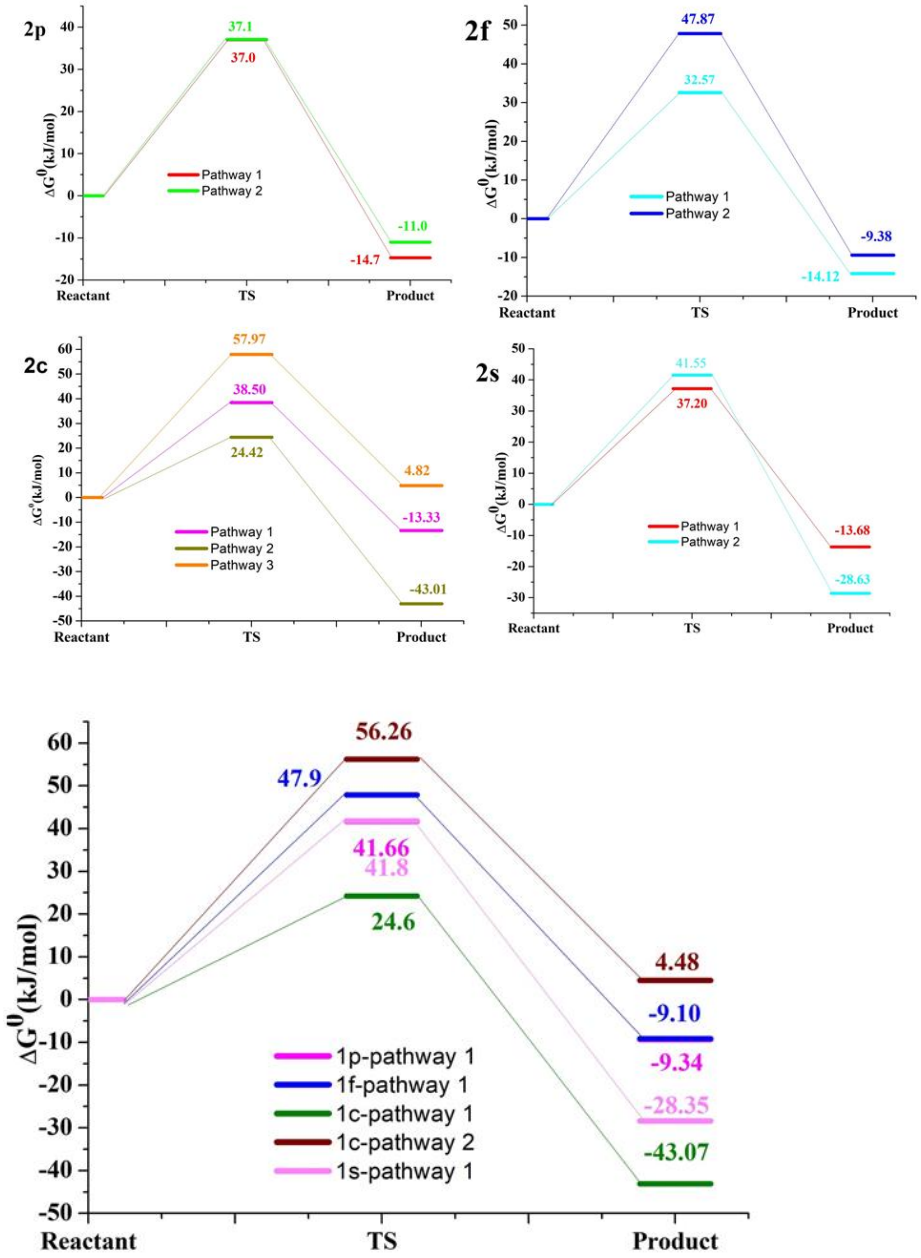

Fig.7.2. Free-energy profiles for reactions of the abstraction of the hydrogen atom by •OOH radical in the gas phase. Unit of ΔG^0 are kJ mol^{-1}

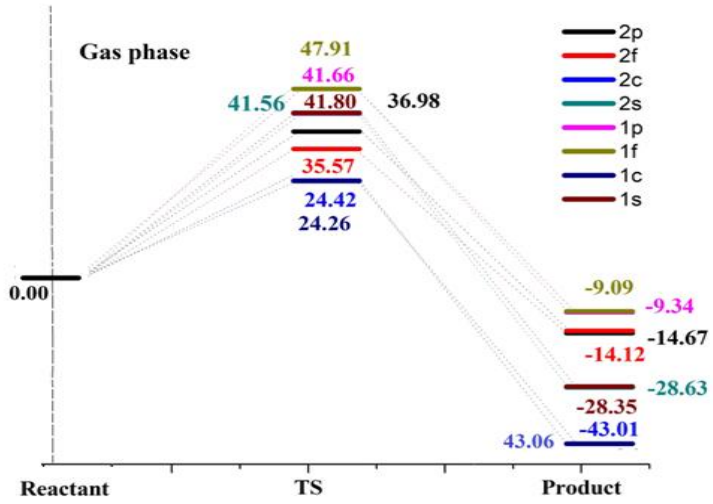

Fig.7.3. A comparative analysis of free-energy profiles for the radical reaction of each compound with •OOH.

7.3.3. Radical adduct formation reaction (RAF)

The direct addition of radical species to the unsaturated moiety is led by the radical adduct formation reactions (Fig.7.A2). It is another prominent pathway other than hydrogen atom abstraction reactions. Herein, the radical species can undergo radical adduct formation reaction at the double bond at either α or β positions as shown in Fig 7.4 & Fig.7.A2. Two pathways; pathway 1 and pathway 2 corresponding to β addition and α addition are created for each compound. The radical adduct RAF 1 is formed through pathway 1 and RAF 2 by pathway 2. RAF 1 and RAF 2 are formed through the transition states of TS_R1 and TS_R2 upon the reaction of •OOH with the selected AVs (Fig.7.A2).

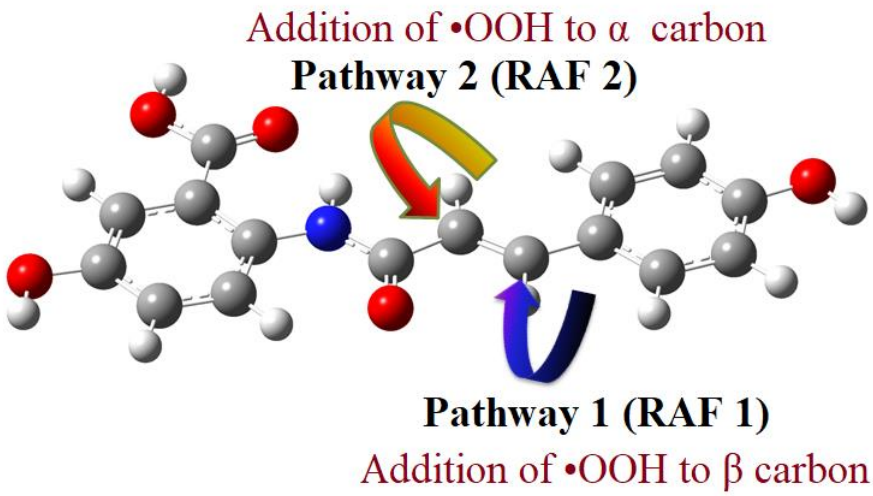

Fig.7.4. The possible RAF mechanism in AVs (here 2p molecule are used for representation)

The thermodynamics of radical adduct formation were analyzed and observed that both RAF 1 and RAF 2 are thermodynamically unfavorable due to the positive value of ΔG^0 (Fig.7.5). The radical adduct formed in RAF 2 is found to be lower in energy than RAF 1, but still unfavorable. The low-lying energy of the adduct formed in RAF 2 compared to RAF 1 will be due to the stabilization of spin developed on the β carbon by the extended delocalization to the aromatic ring.

On comparing the thermodynamics of hydrogen atom transfer over radical adduct formation reaction, the preference of hydrogen atom transfer over the RAF mechanism can be seen by comparing the energy barriers of RAF and HAT. Thus RAF will be a less probable pathway in comparison to hydrogen atom transfer reactions. The

comparative investigations of FHAT of the highly reactive hydroxyl group versus RAF 2 are provided in Fig.7.6.

The optimized geometries of the transition state structures of RAF pathways are given in Fig.7.A3. The optimized geometries indicate the perpendicular approach of the •OOH radical to the Cα = Cβ bond (in optimized structures represented as C1=C2) of the side chain. Herein, the bonds that are being broken are elongated (C1=C2 conversion to C1-C2 during radical addition) as well and those bonds that are being formed (C1–O1 or C2-O1 bond) have distances within the range 1.39–1.40 and 1.87–2.62 Å, respectively. Spin density analysis as well as visual inspection of the distributed atomic density of radicals of each radical adduct are given respectively in Table 7.2 and Fig.7.A4, enables us to understand the extent and nature of the spin delocalization, which in turn helps assess the radical stability. From the data, it is observed that RAF 2 products are much more stabilized by the stabilization of radical species with the aromatic ring. When radical adduct (RA) is formed at α (RAF 2) position, it could noticed that a delocalized spin density values 0.070-0.075 in β carbon position whereas the radical addition at β carbon (RAF 1), a localised spin density of 0.087 on α carbon position. Comparatively higher value of spin density on RAF 1 and RAF 2 products compared to HAT products the relative instability of radical adduct formation further validated. The above observation further justifies the comparatively lower energy of the adduct RAF 2 in comparison to that of RAF 1. Further, from the inspection of spin density isosurface distribution, it can also be seen that the radical spin is less distributed in TSs of RAF

compared to HAT, which in turn further indicates the instability and lower probability of radical adduct formation reactions during radical scavenging mechanism. Thus, in general, spin density analysis further corroborates the predicted energy trends of reactivity in the radical scavenging mechanism of AVs.

Table 7.2 Spin density values of the intermediate structures of each compound in RAF mechanism.

Compound	RAF 1	RAF 2
2p	0.087	0.073
2f	0.085	0.071
2c	0.086	0.070
2s	0.086	0.073
1p	0.088	0.074
1f	0.087	0.075
1c	0.091	0.071
1s	0.092	0.073

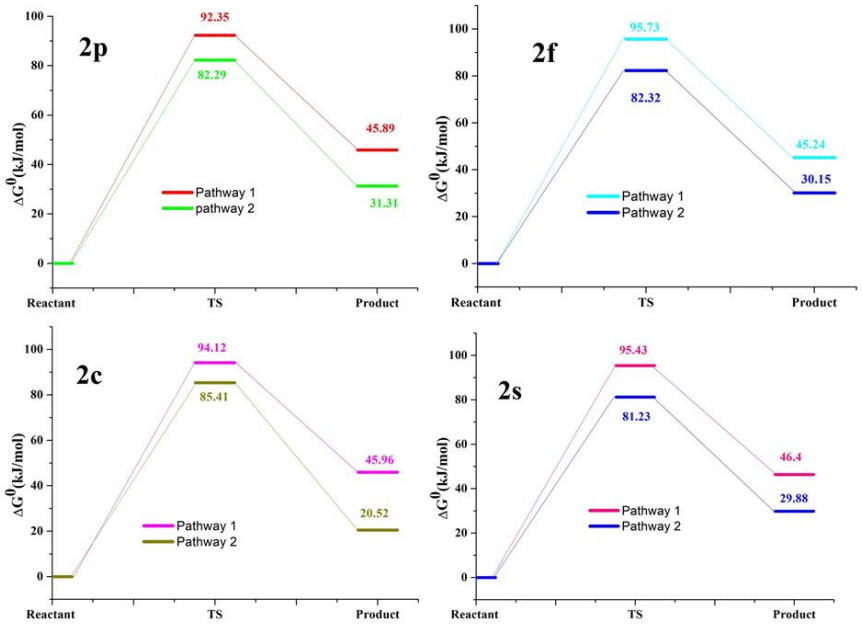

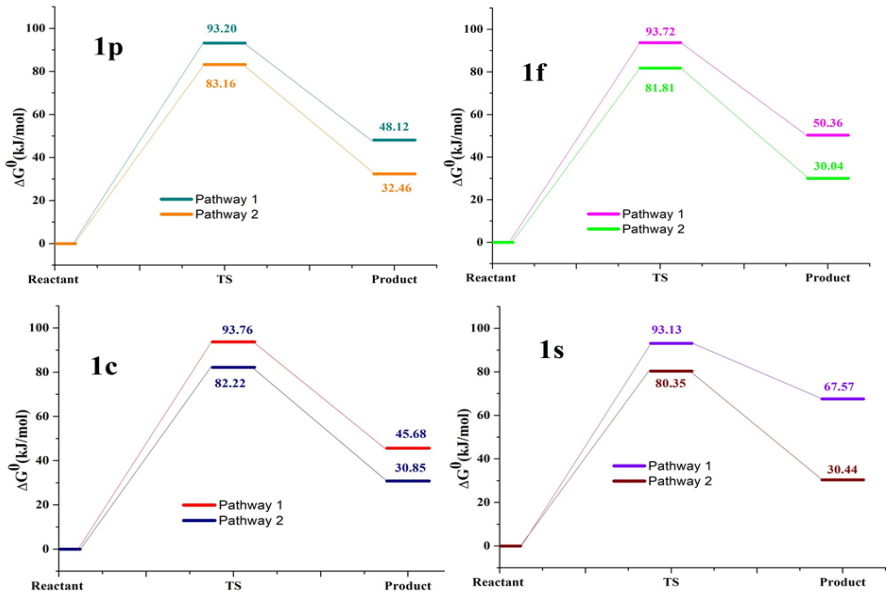

Fig.7.5. Free-energy profiles for reactions of the radical adduct formation upon addition of •OOH radical in the gas phase. Unit of ΔG^0 are kJ $mol^{-1.}$

7.3.4. Reaction kinetics calculations

The rate constant of a radical-induced reaction is the most valuable and intuitive information for evaluating the radical deactivation process and such data are useful for Predicting the reaction locations, and reaction processes. Nevertheless, because of the quick reaction rates and the dearth of experimental analytical techniques, the rate constants of the radical-initiated reactions are typically unpredictable. This shortcoming could be filled by using theoretical computation, which offers a quick, practical, and economical method of determining radical degradation rates. Hence the rate constant of the reaction initiated by •OOH attacking the different reactive sites of the AVs was calculated at 298.15 K and 1 atm in the gas phase, which was shown in Table 7.3. The rate constants

induced by •OOH in FHAT pathways are much higher than those involved in RAF pathways which is well agreed with their energy barriers. In the case of hydrogen abstraction reactions, the hydrogen abstraction from the 4' hydroxyl position of c-series compounds (8.00 x 10^9 L $mol^{-1}s^{-1}$ for **2c** and 8.54 x 10^9 L $mol^{-1}s^{-1}$ for **1c**) was found to be the most important channel with the largest rate constant. These results revealed that 4'OH of c- series compounds was the preferred position for •OOH attack which was in accordance with the thermodynamic data. For **2p** and **2f** the rate constant are correlating with the thermodynamic data discussed earlier. The 5 OH groups in each are important channels for radical deactivation. However, for compound 2s, the rate constant of radical deactivation by the 5^{th} hydroxyl group (4.62x 10^7 L $mol^{-1}s^{-1}$) was higher than the 4' hydroxyl group (8.00x10^6 L $mol^{-1}s^{-1}$). The observation was contrary to the thermodynamic data, hence it can concluded that the kinetic preference of 5OH over 4'OH towards hydroperoxyl deactivation and thermodynamically the opposite one. The steric crowd of 4'OH will be the reason for the low kinetic feasibility of the radical deactivation.

Table 7.3. Rate constants (L $mol^{-1}s^{-1}$) of $^{\bullet}OOH$ with different sites of AVs in the gas phase.

Reaction mode	Compound	Position	Species	Imaginary frequency (cm^{-1})	Rate constant (k) L $mol^{-1}s^{-1}$
H-abstraction	**2p**	5	TS-1	-1551	5.05×10^{7}
		4'	TS-2	-1594	4.86×10^{7}
	2f	5	TS-1	-1508	2.98×10^{7}
		4'	TS-2	-1608	6.24×10^{5}
	2c	5	TS-1	-1559	2.74×10^{7}
		4'	TS-2	-1187	8.00×10^{9}
		3'	TS-3	-1474	1.06×10^{4}
	2s	5	TS-1	-1518	4.62×10^{7}
		4'	TS-2	-1442	8.00×10^{6}
	1p	4'	TS-1	-1653	7.63×10^{6}
	1f	4'	TS-2	-1619	6.12×10^{5}
	1c	4'	TS-1	-1219	8.54×10^{9}
		3'	TS-2	-1751	2.10×10^{4}
	1s	4'	TS-1	-1454	7.20×10^{6}
Radical adduct formation reaction	**2p**	RAF-1	TS_R1	-530	9.94×10^{-3}
		RAF-2	TS_R2	-467	5.77×10^{-1}
	2f	RAF-1	TS_R1	-477	2.55×10^{-3}
		RAF-2	TS_R2	-470	5.71×10^{-1}
	2c	RAF-1	TS_R1	-491	4.88×10^{-3}
		RAF-2	TS_R2	-498	1.64×10^{-1}
	2s	RAF-1	TS_R1	-479	2.87×10^{-3}
		RAF-2	TS_R2	-471	8.87×10^{-1}
	1p	RAF-1	TS_R1	-526	7.07×10^{-3}
		RAF-2	TS_R2	-468	4.14×10^{-1}
	1f	RAF-1	TS_R1	-529	5.72×10^{-3}
		RAF-2	TS_R2	-471	7.01×10^{-1}
	1c	RAF-1	TS_R1	-492	5.62×10^{-3}
		RAF-2	TS_R2	-480	5.93×10^{-1}
	1s	RAF-1	TS_R1	-531	7.26×10^{-3}
		RAF-2	TS_R2	-467	1.26×10^{0}

7.3.5. Solvent effect on reactions

Water is selected as the solvent for studying the effect on the free radical initiated reactions of selected AVs with •OOH by the HAT and RAF patways. The free-energy profiles for the reactions of selected AVs with •OOH through FHAT and RAF mechanism in water phase are given in Fig.A5 & A7. Table 7.A.1 represents the reaction enthalpies(ΔH^0) and free energies (ΔG^0) of the radical deactivation reaction by •OOH radical in water medium (kJ/mol). Hydrogen abstraction pathways are found to be thermodynamically favourable and exothermic in water medium. Compared to gas phase (Fig.A6). The reaction has to pass slightly higher energy barrier in water phase. The rate constant calculated in water medium are given in Table are also consistent with less feasibility of hydrogen atom transfer mechanism in water phase comaperd to gas phase. The result is compared with the thermodynamic results in which the compounds favours SPLET mechanism in water phase as discussed in the previous chapters. Moreover, the very high energy reaction barrier and the positive ΔG^0 reveals the absence RAF mechanism in water mediam too. The results are also consistent with the low rate constant of RAF mechamism in water medium.

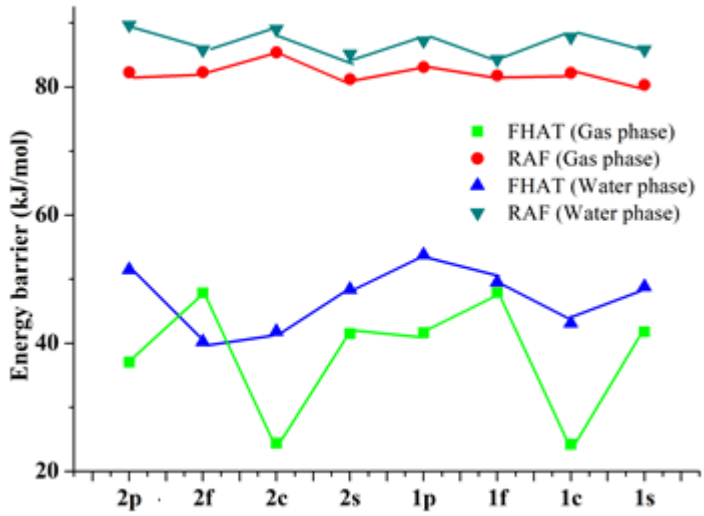

Fig.7.6. Energy barriers for FHAT and RAF reactions initiated by •OOH gas phase and aqueous phase

Table 7.4. Rate constant (L mol^{-1} s^{-1}) of •OOH with different sites of AVs in the water mudium.

Reaction mode	Compound	Position	Species	Imaginary frequency (cm^{-1})	Rate constant (k) L $mol^{-1}s^{-1}$
H-abstraction	**2p**	5	TS-1'	-1636	$1.44x10^{5}$
		4'	TS-2 '	-1903	$6.04x10^{4}$
	2f	5	TS-1 '	-1686	$1.35x10^{6}$
		4'	TS-2 '	-1714	$4.01x10^{5}$
	2c	5	TS-1 '	-1655	$5.39x10^{5}$
		4'	TS-2 '	-1580	$7.10x10^{6}$
		3'	TS-3 '	-1157	$6.04x10^{3}$
	2s	5	TS-1 '	-1619	$4.68x10^{5}$
		4'	TS-2 '	-1706	$5.00x10^{5}$
	1p	4'	TS-1 '	-1927	$5.63x10^{4}$
	1f	4'	TS-2 '	-1739	$3.15x10^{5}$
	1c	4'	TS-1 '	-1616	$4.15x10^{6}$
		3'	TS-2 '	-1156	$2.48x10^{3}$
	1s	4'	TS-1 '	-1174	$4.23x10^{5}$

Radical adduct formation reaction	**2p**	RAF-1	TS_R1'	-473	$4.18x10^{-4}$
		RAF-2	TS_R2'	-416	$2.92x10^{-2}$
	2f	RAF-1	TS_R1'	-469	$3.87x10^{-2}$
		RAF-2	TS_R2'	-405	$2.33x10^{0}$
	2c	RAF-1	TS_R1'	-473	$2.53x10^{-3}$
		RAF-2	TS_R2'	-446	$3.82x10^{-2}$
	2s	RAF-1	TS_R1'	-474	$1.21x10^{-3}$
		RAF-2	TS_R2'	-410	$1.81x10^{-1}$
	1p	RAF-1	TS_R1'	-476	$9.85x10^{-4}$
		RAF-2	TS_R2'	-418	$7.81x10^{-2}$
	1f	RAF-1	TS_R1'	-474	$4.98x10^{-4}$
		RAF-2	TS_R2'	-408	$2.56x10^{-1}$
	1c	RAF-1	TS_R1'	-476	$6.01x10^{-4}$
		RAF-2	TS_R2'	-419	$6.26x10^{-2}$
	1s	RAF-1	TS_R1'	-476	$7.45x10^{-4}$
		RAF-2	TS_R2'	-412	$1.39x10^{-1}$

7.4. **Conclusions**

The feasibility of FHAT and RAF mechanism with ·OOH in gas phase was calculated for all the selected compounds. FHAT mechanism is favored for 4'OH sites in each compound except for 2p and 2f as obtained in earlier studies. The RAF 2 is more favorable than RAF 1 for each compound studied. Kinetic data of radical scavenging activity are exactly matching with the obtained thermodynamic results in each cases.The results showed that FHAT mechanism overtake RAF mechanism in radical scavenging mechanism. The kinetic as well as thermodynamic data provides the higher quenching ability of hydroperoxyl radical by the c-series compound. The role is mainly taken by the 4'OH in the compound. The higher potential reactivity of the c series compounds are expected to be due to the increased stabilisation of intermediate 4'O radical by the nearest 3'OH through

intramolecular hydrogen bonding interaction and the increased stabilisation through aromatic ring by the resonance.

References

1. Pizzino G, Irrera N, Cucinotta M, et al (2017) Oxidative Stress: Harms and Benefits for Human Health. Oxid Med Cell Longev 2017:8416763. https://doi.org/10.1155/2017/8416763
2. Sharifi-Rad M, Anil Kumar N V, Zucca P, et al (2020) Lifestyle, Oxidative Stress, and Antioxidants: Back and Forth in the Pathophysiology of Chronic Diseases . Front. Physiol. 11
3. Galano A, Raúl Alvarez-Idaboy J (2019) Computational strategies for predicting free radical scavengers' protection against oxidative stress: Where are we and what might follow? Int J Quantum Chem 119:e25665. https://doi.org/https://doi.org/10.1002/qua.25665
4. Galano A (2015) Free Radicals Induced Oxidative Stress at a Molecular Level: The Current Status, Challenges and Perspectives of Computational Chemistry Based Protocols
5. Çalişkan B, Çalişkan AC (2021) Antioxidant and Oxidative Stress. In: Waisundara V (ed). IntechOpen, Rijeka, p Ch. 6
6. Finkel T, Holbrook NJ (2000) Oxidants, oxidative stress and the biology of ageing. Nature 408:239–247. https://doi.org/10.1038/35041687
7. Wang C, Eskiw CH (2019) Cytoprotective effects of Avenathramide C against oxidative and inflammatory stress in normal human dermal fibroblasts. Sci Rep 9:2932. https://doi.org/10.1038/s41598-019-39244-9
8. Azmanova M, Pitto-Barry A (2022) Oxidative Stress in Cancer Therapy: Friend or Enemy? ChemBioChem 23:e202100641. https://doi.org/https://doi.org/10.1002/cbic.202100641
9. M. J. Frisch, G. W. Trucks, H. B. Schlegel, G. E. Scuseria, M. A. Robb, J. R. Cheeseman, G. Scalmani, V. Barone, G. A. Petersson, H. Nakatsuji, X. Li, M. Caricato, A. V. Marenich, J. Bloino, B. G. Janesko, R. Gomperts, B. Mennucci, H. P. Hratchian, J. V. and DJF (2016) Gaussian 16, Revision C.01
10. Becke AD (1993) Density-functional thermochemistry. III. The role of exact exchange. J Chem Phys 98:5648–5652.

https://doi.org/10.1063/1.464913

11. Lee, Yang, Parr (1988) Development of the Colle-Salvetti correlation-energy formula into a functional of the electron density. Phys Rev B Condens Matter 37:785–789. https://doi.org/10.1103/physrevb.37.785

12. S. Canneaux, F. Bohr and EH (2014) KiSThelP: a program to predict thermodynamic properties and rate constants from quantum chemistry results. J Comp Chem 35:82–93. https://doi.org/http://dx.doi.org/10.1002/jcc.23470.

13. Thion S, Zaras AM, Szőri M, Dagaut P (2015) Theoretical kinetic study for methyl levulinate: oxidation by OH and CH3 radicals and further unimolecular decomposition pathways. Phys Chem Chem Phys 17:23384–23391. https://doi.org/10.1039/C5CP04194E

14. Vo Q V, Tam NM, Bay M Van, Mechler A (2020) The radical scavenging activity of natural ramalin: A mechanistic and kinetic study. Chem Phys Lett 739:137004. https://doi.org/https://doi.org/10.1016/j.cplett.2019.137004

15. Li H, Zhang Y, Wan J, et al (2018) Theoretical investigation on the oxidation mechanism of dibutyl phthalate by hydroxyl and sulfate radicals in the gas and aqueous phase. Chem Eng J 339:381–392. https://doi.org/https://doi.org/10.1016/j.cej.2017.12.153

16. Lu Y, Wang A, Shi P, Zhang H (2017) A Theoretical Study on the Antioxidant Activity of Piceatannol and Isorhapontigenin Scavenging Nitric Oxide and Nitrogen Dioxide Radicals. PLoS One 12:e0169773

17. Sumayya PC, Babu G, Muraleedharan K (2021) Quantum chemical investigation of the antiradical property of avenanthramides, oat phenolics. Heliyon 7:e06125. https://doi.org/10.1016/j.heliyon.2021.e06125

18. Analyzer AMW, Lu T (2019) Multiwfn. 7:

19. Shang Y, Zhou H, Li X, et al (2019) Theoretical studies on the antioxidant activity of viniferifuran. New J Chem 43:15736–15742. https://doi.org/10.1039/C9NJ02735A

20. Vo Q V, Nam PC, Thong NM, et al (2019) Antioxidant Motifs in Flavonoids: O–H versus C–H Bond Dissociation. ACS Omega 4:8935–8942. https://doi.org/10.1021/acsomega.9b00677

Appendix 7

Table 7.A.1 The reaction enthalpies and free energies of the radical deactivation reaction by $^{\bullet}$OOH radical in water medium. Unit kJ mol^{-1}.

Mechanism	Compound	Pathway	ΔH^0(reaction)	ΔG^0(reaction)
Hydrogen abstraction	**2p**	Pathway 1	-20.78	-9.96
		Pathway 2	-13.69	-11.58
	2f	Pathway 1	-18.49	-17.94
		Pathway 2	-22.80	-32.03
	2c	Pathway 1	-18.43	-19.88
		Pathway 2	-41.77	-39.91
		Pathway 3	-12.59	-15.19
	2s	Pathway 1	-18.28	-18.57
		Pathway 2	-33.22	-33.37
	1p	Pathway 1	-13.06	-12.12
	1f	Pathway 1	-24.57	-24.678
	1c	Pathway 1	-40.61	-38.03
		Pathway 2	-12.16	-10.28
	1s	Pathway 1	-32.35	-32.78
Radical adduct formation reaction	**2p**	Pathway 1	7.15	58.95
		Pathway 2	-8.43	45.03
	2f	Pathway 1	8.06	47.91
		Pathway 2	-9.02	32.54
	2c	Pathway 1	6.64	54.11
		Pathway 2	-15.61	37.70
	2s	Pathway 1	6.74	52.76
		Pathway 2	-12.26	37.66
	1p	Pathway 1	-8.56	42.91
		Pathway 2	-8.39	43.36
	1f	Pathway 1	8.66	63.29
		Pathway 2	-11.45	39.19
	1c	Pathway 1	7.89	56.09
		Pathway 2	-10.38	43.00
	1s	Pathway 1	17.06	65.03

	Pathway 2	-11.3579	35.98773

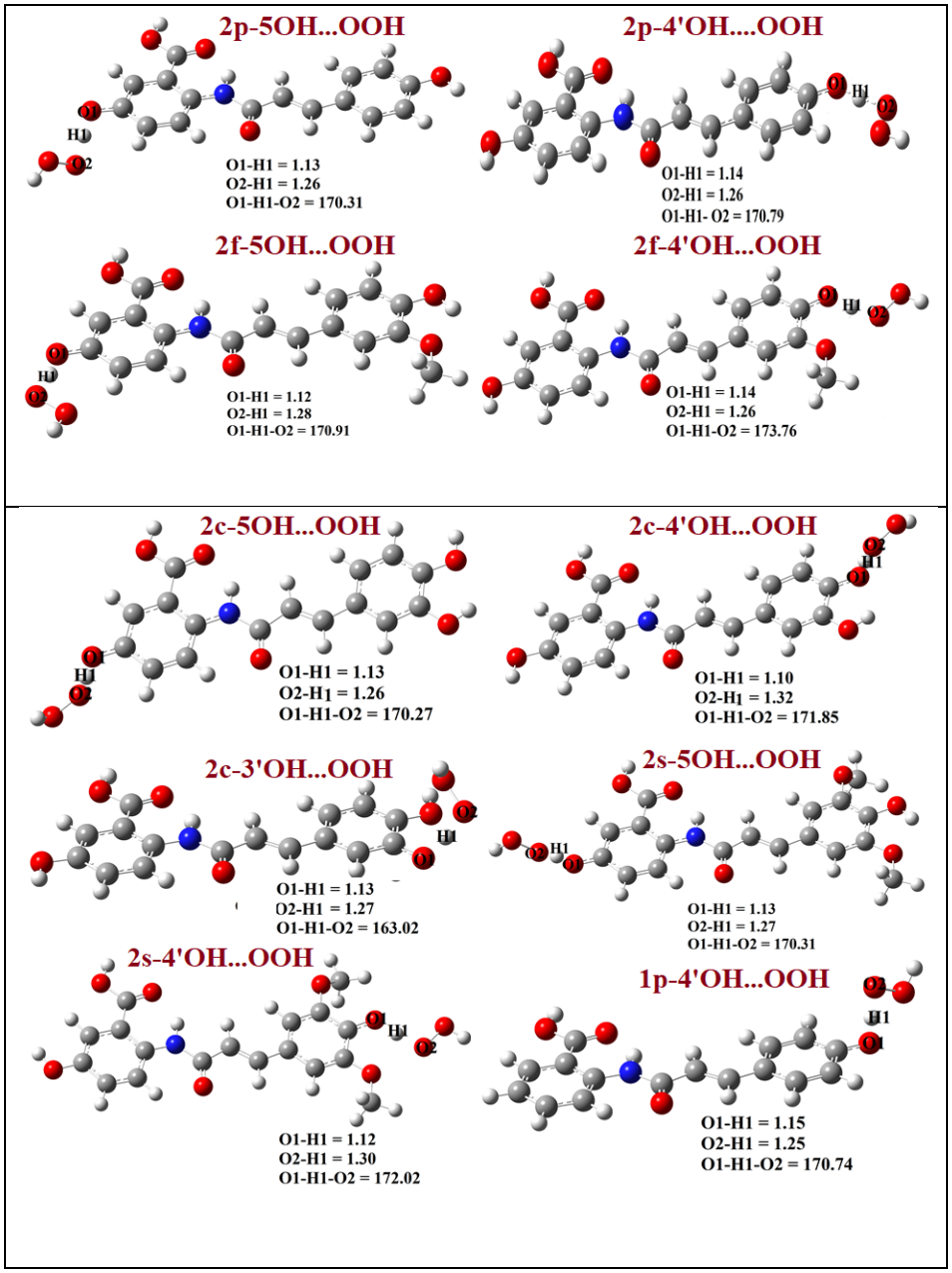

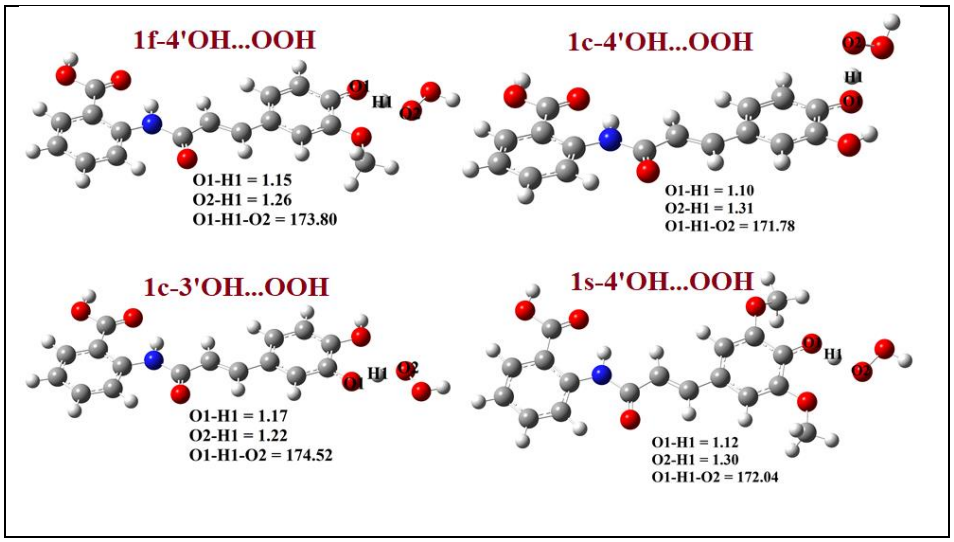

Fig.7.A1. The optimized geometries for transition states (TSs) of the reaction of AVs (selected sites) with •OOH through FHAT mechanism (distances in Å, and angles in ^{o})

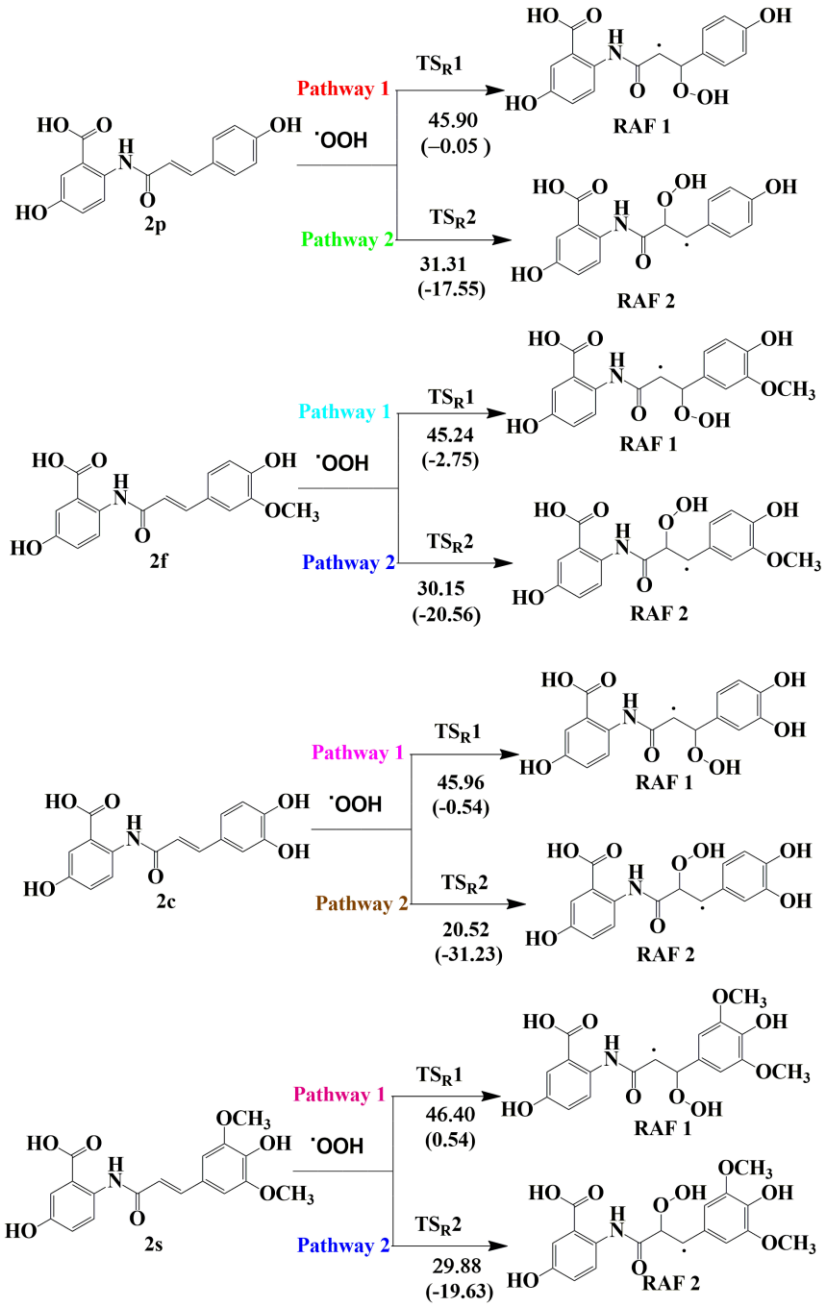
2p
·OOH
Pathway 1
TS$_R$1
45.90
(–0.05)
RAF 1
Pathway 2
TS$_R$2
31.31
(-17.55)
RAF 2
2f
·OOH
Pathway 1
TS$_R$1
45.24
(-2.75)
RAF 1
Pathway 2
TS$_R$2
30.15
(-20.56)
RAF 2
2c
·OOH
Pathway 1
TS$_R$1
45.96
(-0.54)
RAF 1
Pathway 2
TS$_R$2
20.52
(-31.23)
RAF 2
2s
·OOH
Pathway 1
TS$_R$1
46.40
(0.54)
RAF 1
Pathway 2
TS$_R$2
29.88
(-19.63)
RAF 2

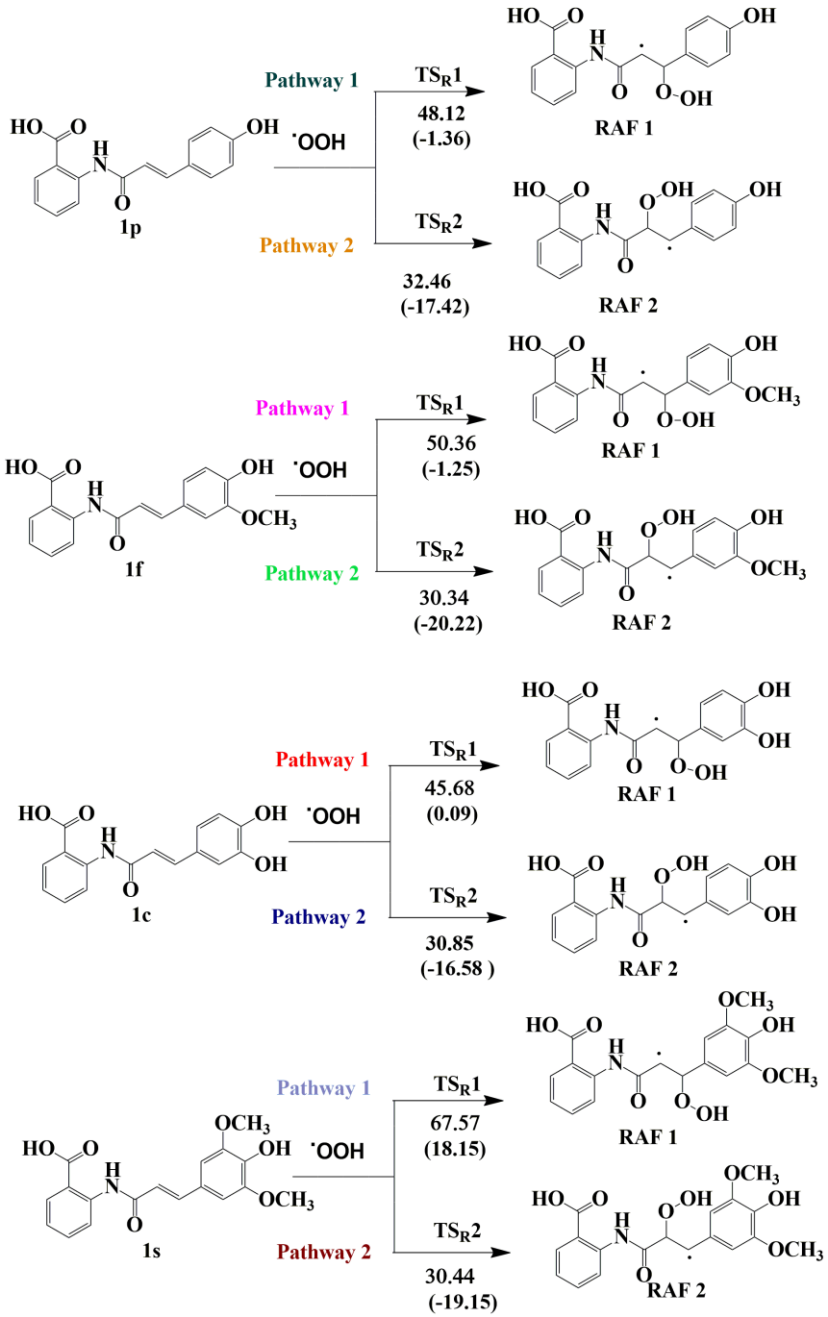

Fig.7.A2. The pathway of radical adduct formation reactions initiated by •OOH in gas phase ΔG^0 (ΔH^0) of each compounds under study. The values are given in Unit of kJ mol^{-1}.

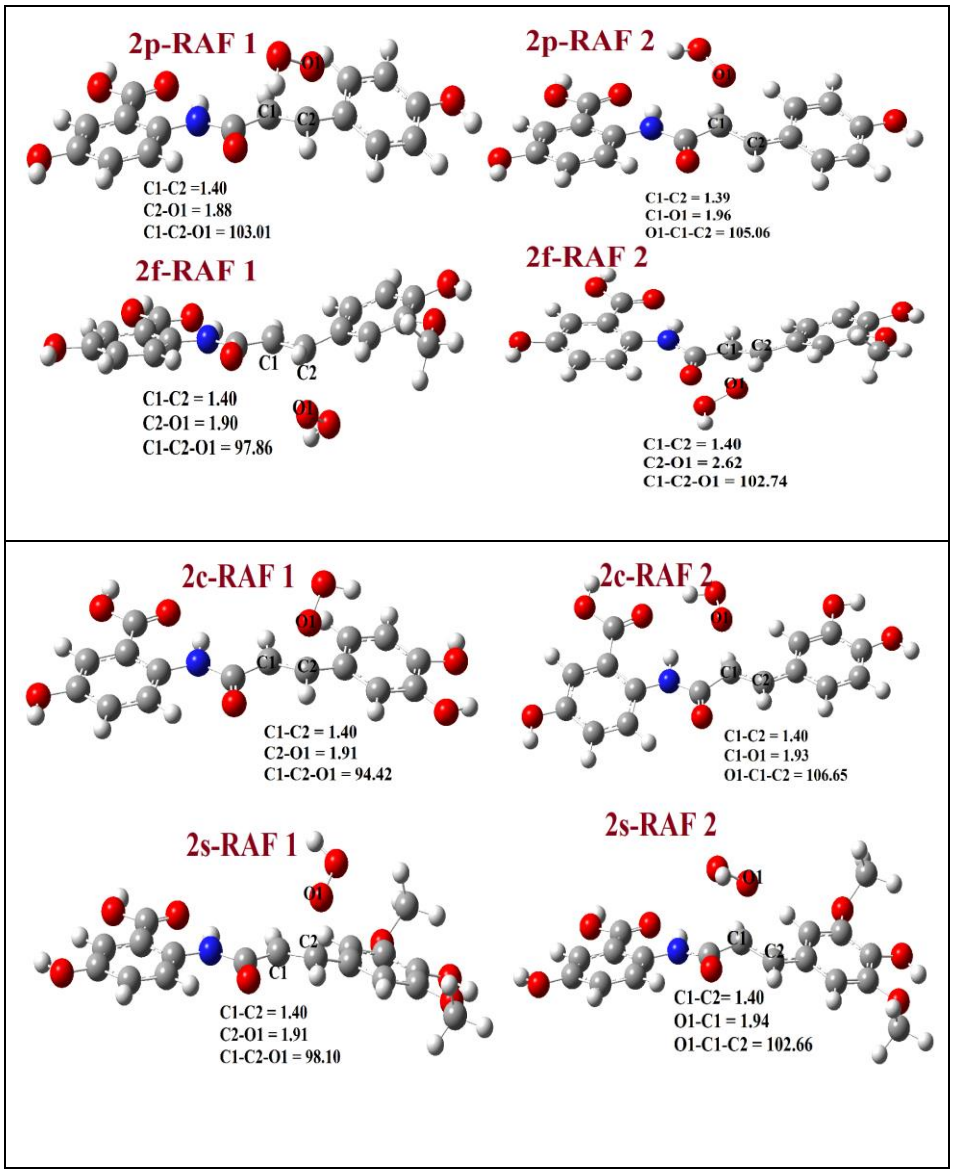
2p-RAF 1
C1-C2 =1.40
C2-O1 = 1.88
C1-C2-O1 = 103.01
2p-RAF 2
C1-C2 = 1.39
C1-O1 = 1.96
O1-C1-C2 = 105.06
2f-RAF 1
C1-C2 = 1.40
C2-O1 = 1.90
C1-C2-O1 = 97.86
2f-RAF 2
C1-C2 = 1.40
C2-O1 = 2.62
C1-C2-O1 = 102.74
2c-RAF 1
C1-C2 = 1.40
C2-O1 = 1.91
C1-C2-O1 = 94.42
2c-RAF 2
C1-C2 = 1.40
C1-O1 = 1.93
O1-C1-C2 = 106.65
2s-RAF 1
C1-C2 = 1.40
C2-O1 = 1.91
C1-C2-O1 = 98.10
2s-RAF 2
C1-C2= 1.40
O1-C1 = 1.94
O1-C1-C2 = 102.66

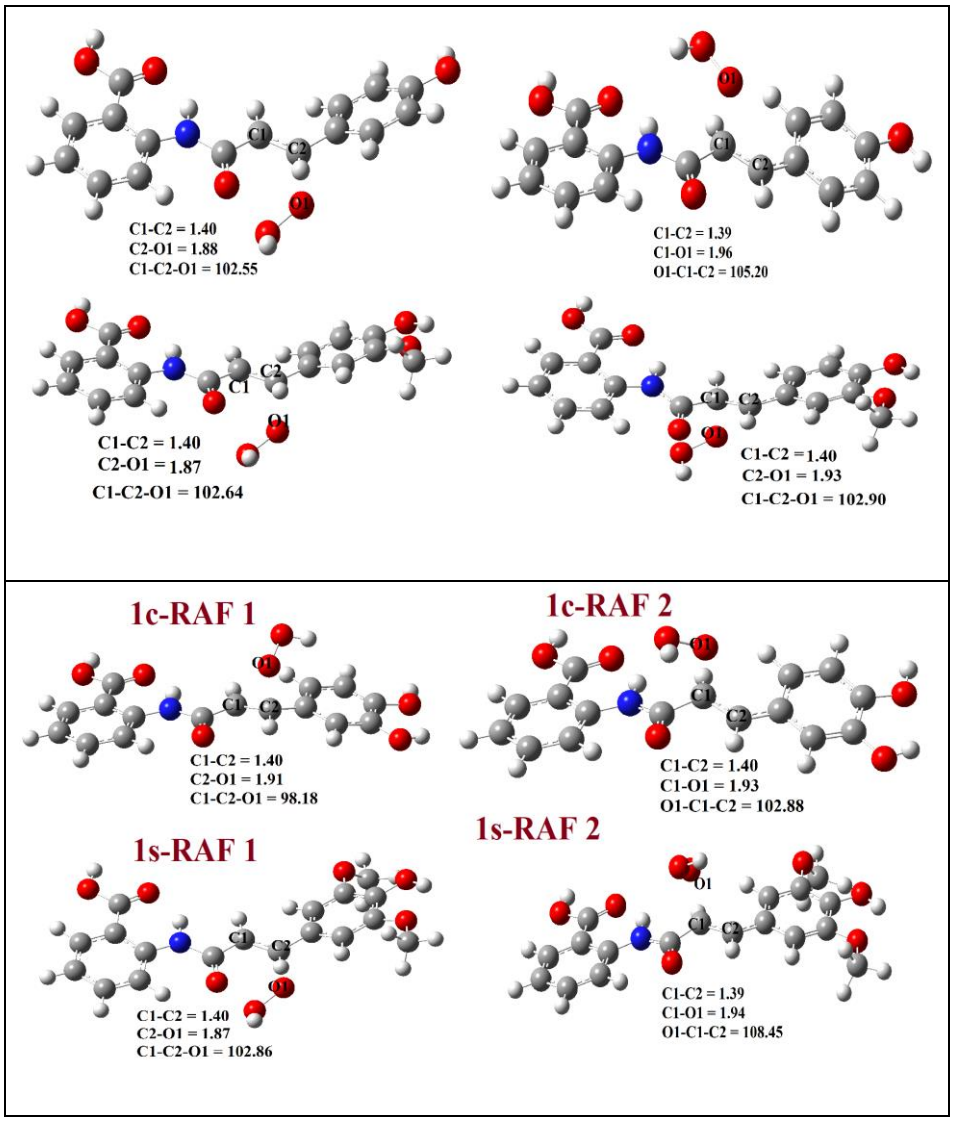

Fig.7.A3. The optimized geometries for transition states (TSs) of the reaction of AVs (selected sites) with •OOH through RAF mechanism (distances in Å, and angles in ^{o})

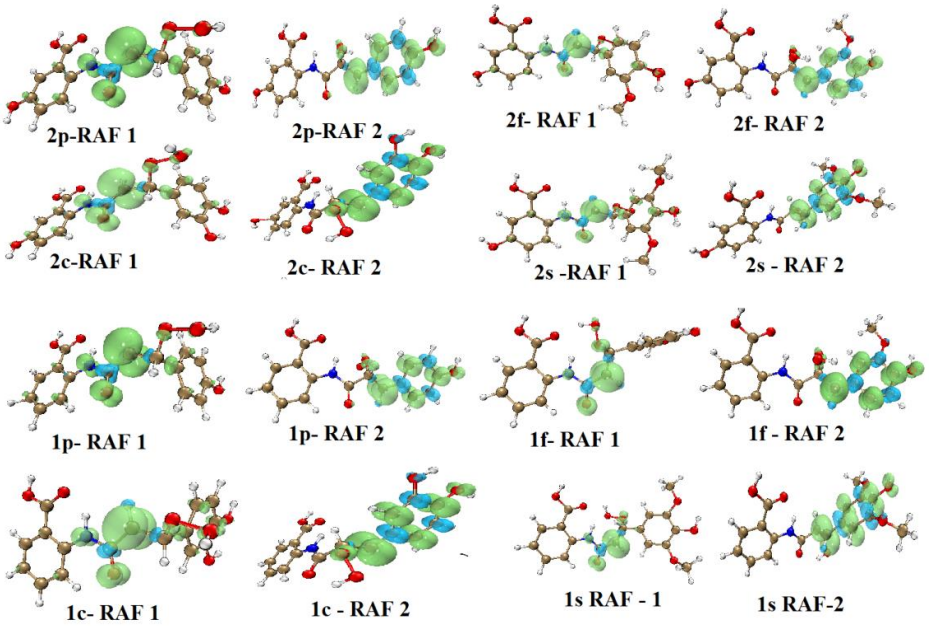

Fig.7.A4. Spin density distributions of radical adduct formed in each compounds upon addition of •OOH radical (Isovalue 0.003). For RAF 2 intermediates greater delocalisation of radical was observed.

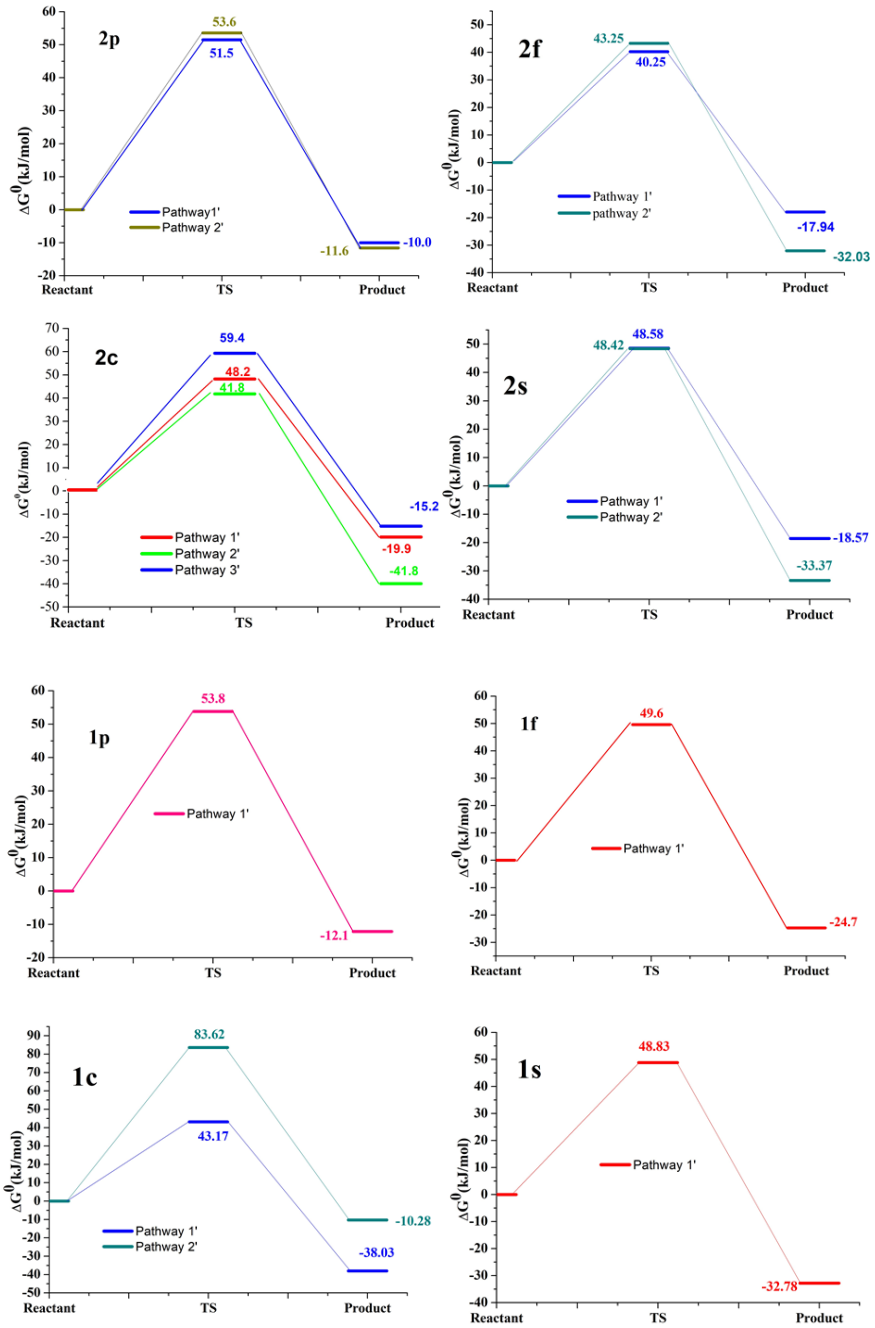

Fig.7.A5. Free-energy profiles for reactions of the abstraction of the hydrogen atom by •OOH radical in the water medium. Unit of ΔG^0 are kJ mol^{-1}.

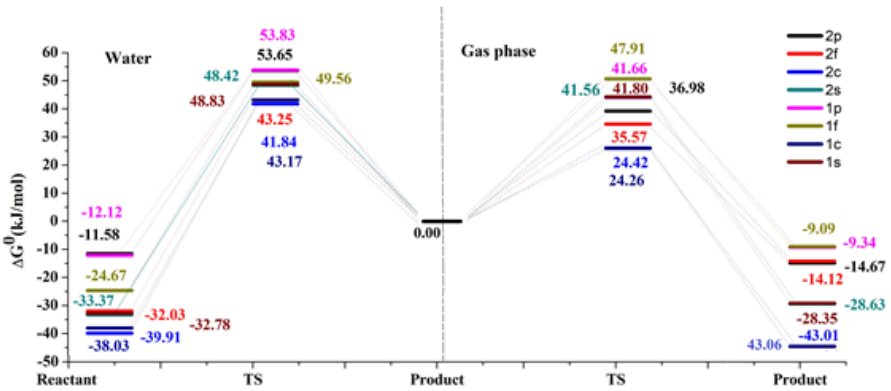

Fig.7.A6. Comparative investigation of gas phase and water medium on hydrogen atom transfer mechanism.

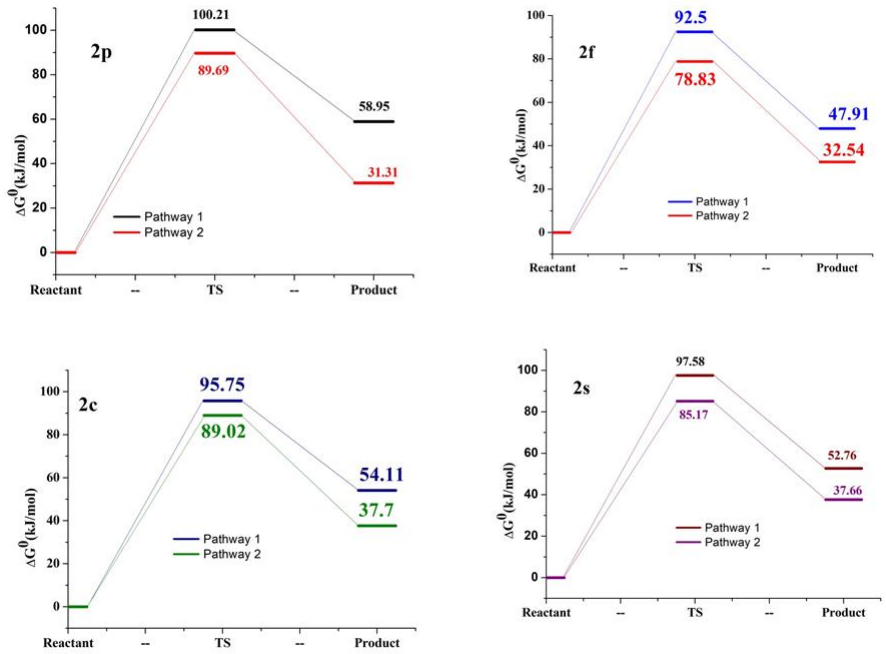

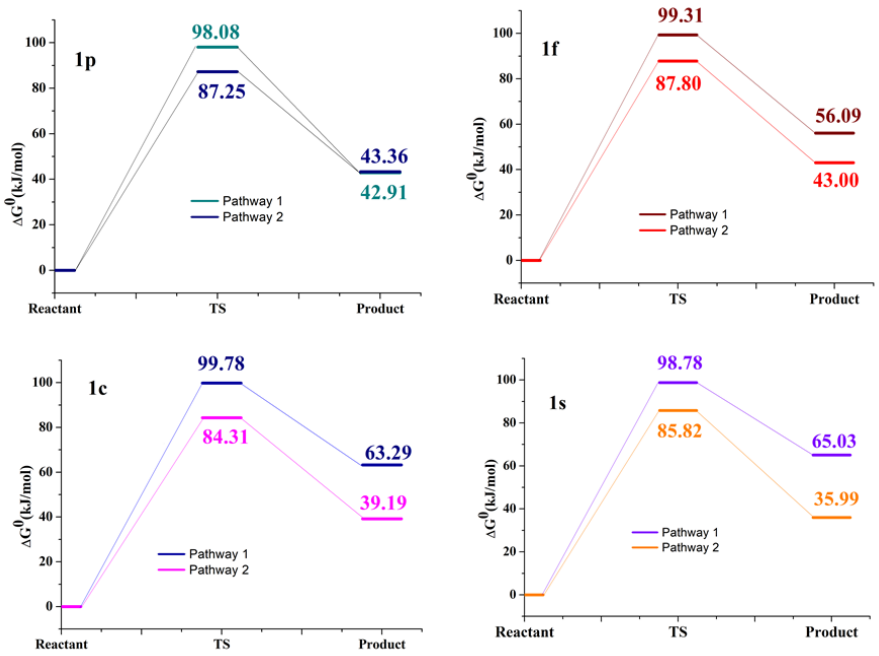

Fig.7.A7. Free-energy profiles for reactions of the radical adduct formation upon addition of •OOH radical in the water medium. Unit of ΔG^0 are kJ mol^{-1}.

Chapter 8

Predicting the affinity of various reactive species towards N-(3', 4' -dihydroxy-(E)-cinnamoyl)-5- hydroxyanthranilic acid (2c) by quantum chemical calculations

- ✓ *The compound 2c was screened through a pool of free radicals-including reactive oxygen species, reactive sulfur species, reactive nitrogen species, and reactive carbon species*
- ✓ *The methanol-induced oxidative degradation pathway of 2c was also studied*

8.1. Introduction

In the previous chapters, a detailed investigation of the radical scavenging activity of the eight AVs was discussed. The compound **2c**/**1c** is found to exhibit good antioxidant activity by the above methods. The 4' phenolic hydroxyl group is obtained to be the main contributor to the radical scavenging mechanism. The higher reactivity of the **c**-series compound is expected to be due to the increased stabilization through the delocalization of the radical formed after electron donation as well as the stabilization by the nearest hydroxyl group. Moreover, the **c**-series compounds are found to exist in their mono-anionic form at physiological pH (Chapter 3). Hence, considering the excellent reactivity and natural abundance of **2c**, the compound is screened through a pool of free radicals (Fig.8.1). By selecting the radicals from various sources, the radical pool gets created. A detailed description of free radicals, sources, classification, etc. is discussed in Chapter 1. The redox potential and equilibrium constant are used to fetch the affinity of the compound with radical species.

In the study, we have considered forty-four reactive species from various sources (Fig.8.2) other than the radical discussed in Chapter 6. The radicals include various reactive oxygen species, reactive sulfur species, and reactive carbon species. The quenching of reactive nitrogen species is included in Chapter 6. Here in the selected species are methoxyl radical (**FR1**), allyloxyl radical (**FR2**), allyl peroxyl radical (**FR3**), methyl peroxyl radical (**FR4**), vinyl peroxyl radical (**FR5**), chloromethyl peroxyl radical (**FR6**), dichloromethyl

peroxyl radical (**FR7**), trichloro methyl peroxyl radical (**FR8**), peroxy chloroformyl radical (**FR9**) (both cis and trans isomers are considered), t-butoxyl radical (**FR10**), formyloxyl radical (**FR11**), acetate radical (**FR12**), peroxy acetyl radical (**FR13**), methyl sulfonyloxyl radical (**FR14**), methyl thiyl peroxyl radical (**FR15**), methylsulfinyl peroxyl radical (**FR16**), methyl sulfonyl peroxyl radical (**FR17**), carbonates radical anion (**FR18**), phenoxyl radical (**FR19**), o-hydroxy phenoxyl radical (**FR20**), meta-hydroxy phenoxyl radical (**FR21**), p-hydroxy phenoxyl radical (**FR22**), 1,2-dihydroxy-2-phenoxyl radical (**FR23**), benzyloxyl radical (**FR24**), 1,2-dihydroxy-3-phenoxyl radical (**FR25**), 1,4-dihydroxy-2-phenoxyl radical (**FR26**), 1,2-dihydroxy-4-phenoxyl radical (**FR27**), 1,3-dihydroxy-5-phenoxyl radical (**FR28**), ortho-methyl phenoxyl radical (**FR29**), meta-methyl phenoxyl radical (**FR30**), para-methyl phenoxyl radical (**FR31**), phenyl peroxyl radical (**FR32**), hydroxymethyl radical (**FR33**), sulphate radical anion (**FR34**), sulphur pentoxide radical anion (**FR35**), thiocyanato radical (**FR36**), hydrosulfide radical (**FR37**), methyl thiyl radical (**FR38**), methyl perthiyl radical (**FR39**), methyl sulfinyl radical (**FR40**), methyl sulfonyl radical (**FR41**), dimethyl aminothiyl radical (**FR42**), dimethyl sulphide radical cation (**FR43**), sulphur trioxide radical anion (**FR44**).

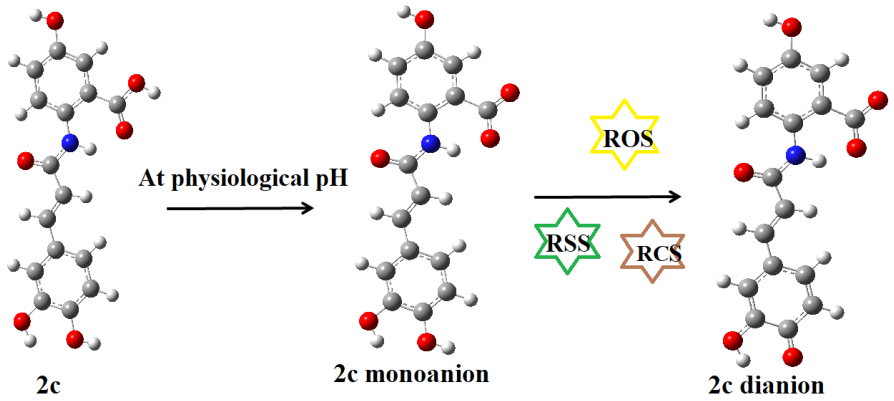

Fig.8.1 Schematic diagram of the overall mechanism of radical scavenging activity of **2c**.

The reactive oxygen species, ROS (**FR1**-**FR32**, **FR34**-**FR35**), reactive carbon species, RCS (**R33**), and reactive sulfur species, RSS (**R36**-**R44**) are included in the present study. In ROS, **FR3**, **FR4**, **FR5**, **FR6**, **FR7**, **FR8**, **FR9**, **FR13**, **FR15**, **FR16**, and **FR17** are considered peroxyl radicals and others are alkoxyl radicals. Moreover, RSS includes sulfur-centered free radicals (**FR36**-**FR44**). The alkoxyl and peroxyl radicals can cause protein oxidation, which results in the oxidation of some amino acids, the creation of protein-protein crosslinks, and ultimately the loss of protein activity[1, 2]. The importance of carboxyl radicals (RCOO) in synthetic organic chemistry is considerable[3, 4]. The first member of the carboxyl radical family is the formyloxyl radical ($^{\cdot}$OOCH). Environmental toxins like CCl_4 lead to the production of the exogenous trichloromethyl peroxyl radical ($Cl_3COO^{\cdot}$)[4]. Additionally, due to its redox potential, sulfate-radical anion has been described as a highly reactive oxidizing species.

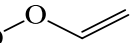

FR1

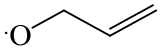

FR2

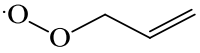

FR3

FR4

FR5

FR6

FR7

FR8

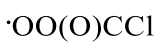

FR9

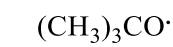

FR10

FR11

FR12

FR13

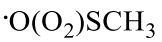

FR14

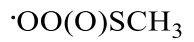

FR15

FR16

FR17

FR18

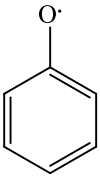

FR19

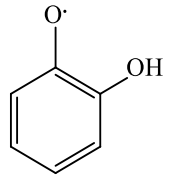

FR20

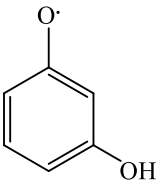

FR21

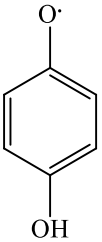

FR22

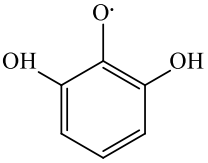

FR23

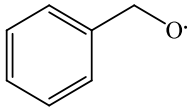

FR24

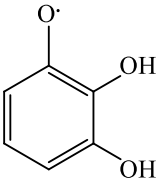

FR25

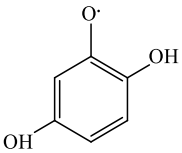

FR26

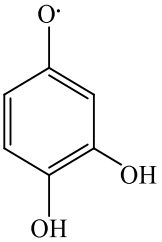

FR27

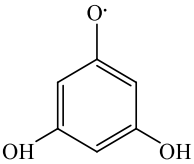

FR28

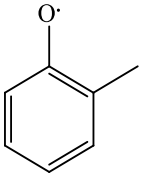

FR29

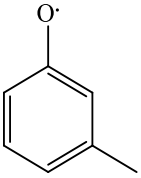

FR30

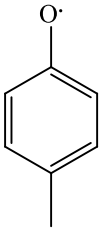

FR31

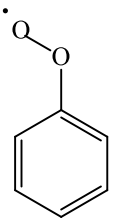

FR32

$^{\bullet}CH_2OH$	$SO_4^{\bullet -}$	$SO_5^{\bullet -}$	$^{\bullet}SCN$
FR33	**FR34**	**FR35**	**FR36**
$^{\bullet}SH$	$^{\bullet}SCH_3$	$^{\bullet}SSCH_3$	$CH_3S^{\bullet}O$
FR37	**FR38**	**FR39**	**FR40**
$CH_3S^{\bullet}(O_2)$	$^{\bullet}SN(CH3)_2$	$(CH_3SCH_3)^{\bullet +}$	$SO_3^{\bullet -}$
FR41	**FR42**	**FR43**	**FR44**

Fig. 8.2. Various reactive species considered for study (FR-free radical)

8.2. Computational details

The structures of N-(3', 4' -dihydroxy-(E)- cinnamoyl)-5-hydroxyanthranilic acid (**2c**) and the free radical considered are optimized with M06-2X/6-31+G(d,p) level of theory using Gaussian 16W suite[5]. The unrestricted open-shell approach was used to optimize the reactive species. The solvent model IEF-PCM was used to include an aqueous environment. The calculations of vibrational frequencies were made at the same level to verify that each stationary point was minima (zero imaginary frequency) or a transition state (one imaginary frequency). The intrinsic reaction coordinate (IRC) calculations were also carried out to further verify the relation of the right minima by the transition state. After the transition states were confirmed, the rate coefficients (kTST(T)) were calculated using Transition State Theory using the KiSThelP program[6], which had previously been used to predict the rate constants involved in free radicals[7]. Through the thermodynamic formulation of the Transition State Theory (TST), the rate constants (k) were calculated as the

method mentioned in Chapter 7 at a temperature of 298.15 K and pressure of 1 atm.

8.3. Results and Discussion

8.3.1. Optimized geometries of the reactive species

The optimized geometries of all the reactive species (**FR1-FR44**) in the gas phase are shown in Fig.8.4 and optimized images of N-(3', 4' -dihydroxy-(E)- cinnamoyl)-5- hydroxyanthranilic acid, its monoanion and dianion are given in Fig.8.3. The structures of **FR21**, **FR23**, **FR25**, **FR26**, **FR27**, and **FR28** can exist in more than one conformations and the lowest energy conformer of each reactive species are considered for the analysis. Moreover, the cis and trans conformers of **FR9** are possible and considered as **FR9** (cis) and **FR9** (trans).

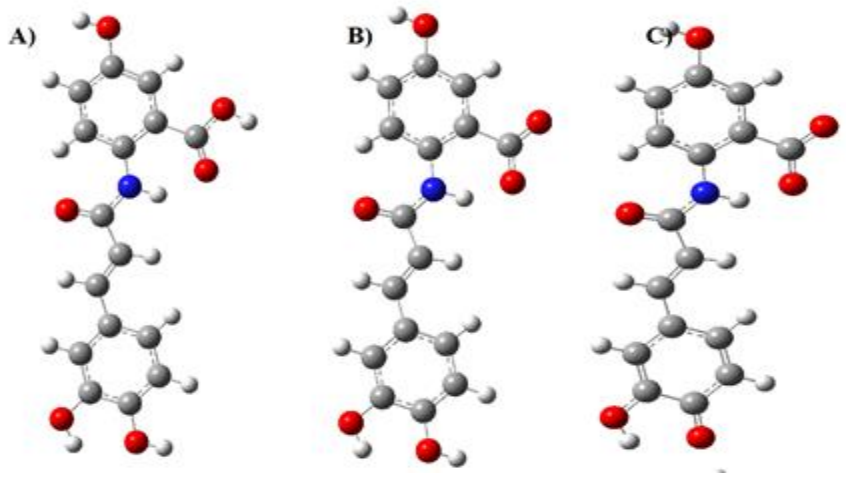

Fig. 8.3. Optimized geometries of (a) neutral (b) monoanionic and (c) dianionic form of N-(3', 4' -dihydroxy-(E)- cinnamoyl)-5-hydroxyanthranilic acid in the gas phase.

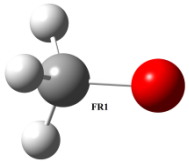

FR1

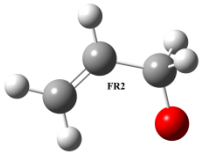

FR2

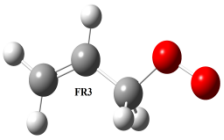

FR3

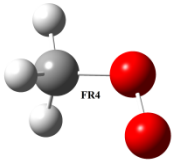

FR4

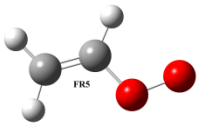

FR5

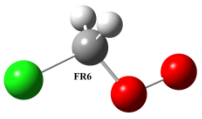

FR6

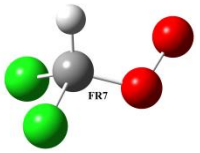

FR7

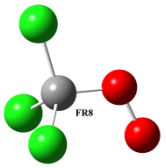

FR8

FR9_CIS

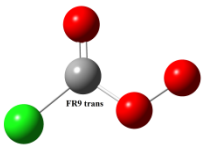

FR9_TRANS

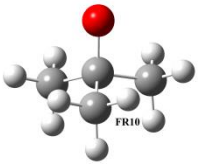

FR10

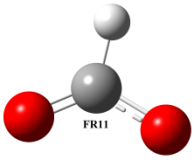

FR11

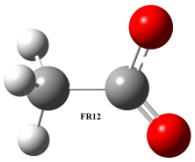

FR12

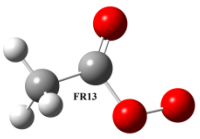

FR13

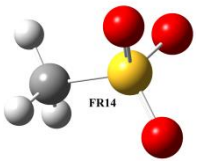

FR14

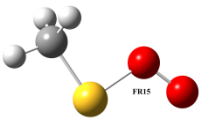

FR15

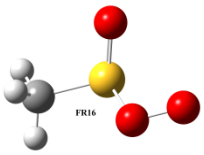

FR16

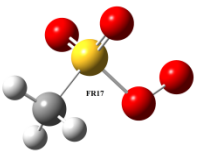

FR17

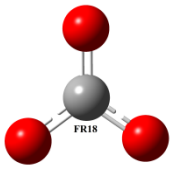

FR18

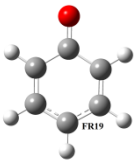

FR19

FR20

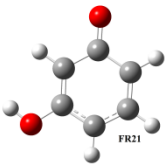

FR21

FR22

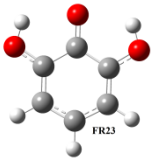

FR23

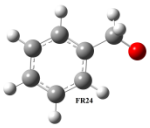

FR24

FR25

FR26

FR27

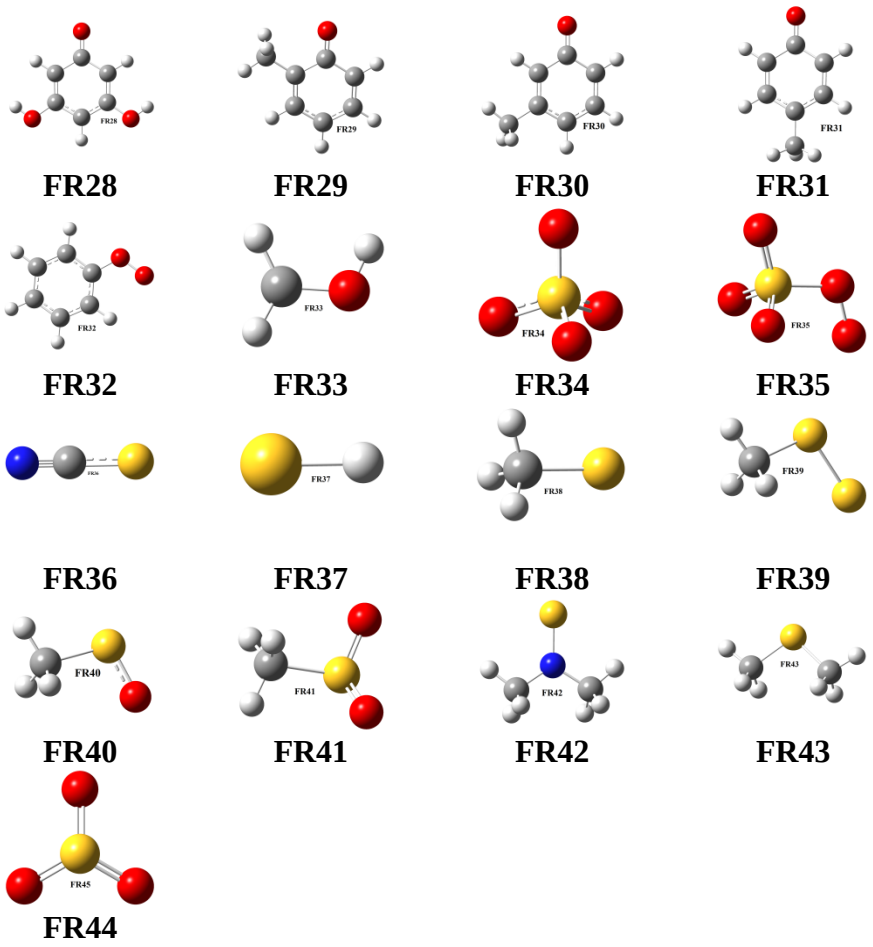

Fig.8.4. The optimized geometries of all the reactive species (**FR1-FR44**) in the gas phase

8.3.2. Reactivity of free radical species

8.3.2.1. Hydrogen atom affinity and electron affinity

The hydrogen atom affinity (HAA) and electron affinity (EA) were investigated to comprehend the energetics of the radical species, as these are significant aspects responsible for antioxidant compounds'

free radical scavenging capacity. Equations 6.7 & 6.8 and the method are utilized to calculate the values. The computed HAA and EA (in kcal/ mol) of all the reactive species in the gas phase and aqueous solution are tabulated in Table 8.1. In Chapter 6, the HAA and EA values of five reactive species are already studied among them it has been observed that the hydroxyl group possesses the highest HAA value (116 kcal/mol). Herein, the highest HAA are observed for radical species; methoxyl (**FR1**), allyloxyl (**FR2**), t-butoxyl (**FR10**), formyloxyl (**FR11**), acetate (**FR12**), methyl sulfonyloxyl (**FR14**), benzyloxyl (**FR24**), and sulphate (**FR34**). Among these **FR11**, **FR12**, and **FR14** (HAA values respectively -114.12, -112.39, and -111.35 kcal/mol) are highly destructive. The HAA values are found to be rising in the majority of radical species. Moreover, the radicals with the aromatic system or radical stabilizing group are less destructive and they might be thought to be ineffective in accepting a hydrogen atom in either the gas phase or an aqueous solution. Compared to oxygen-centered free radicals the destructive nature of sulphur-containing species is obtained to be less. This might be confirmed by estimating the redox potential and equilibrium constant values for each reactive species scavenged by the monoanionic form of N-(3', 4' -dihydroxy-(E) -cinnamoyl)-5- hydroxyanthranilic acid at physiological pH using SPLET mechanism.

Compared to the gas phase the electron affinity tendencies of the radical species are found to be higher in polar solvent than in gas phase. Hence the radical quenching by the single electron transfer will be highest for the radicals **FR11**, **FR14**, **FR17**, **FR34**, and **FR43**. The

formyloxyl (**FR11**), methyl sulfonyloxyl (**FR14**), and sulfate (**FR34**) have high HAA and EA values and are hence expected to be highly reactive.

Table 8.1 The computed hydrogen atom affinity (HAA) and electron affinity (EA) of the studied reactive species (in kcal/mol) in the gas phase and aqueous solution.

Radical species	HAA		EA	
	Gas	Aqueous	Gas	Aqueous
FR1	-101.68	-102.75	-32.31	-98.94
FR2	-102.98	-104.00	-42.53	-102.97
FR3	-83.85	-84.45	-28.77	-92.52
FR4	-83.44	-84.36	-24.11	-91.13
FR5	-84.65	-84.92	-38.74	-98.66
FR6	-85.34	-86.24	-43.19	-100.95
FR7	-89.94	-91.49	-57.59	-111.73
FR8	-89.74	-92.41	-64.10	-117.48
FR9_CIS	-91.86	-94.82	-67.84	-121.60
FR9_trans	-94.64	-95.53	-68.58	-122.93
FR10	-104.42	-105.34	-41.36	-100.53
FR11	-114.12	-115.13	-84.04	-143.50
FR12	-112.39	-112.92	-78.55	-137.47
FR13	-94.94	-94.76	-48.91	-111.18
FR14	-111.35	-114.47	-105.39	-159.70
FR15	-87.84	-88.62	-30.37	-94.609
FR16	-88.39	-88.18	-47.05	-105.59
FR17	-90.26	-91.78	-57.20	-115.23
FR18	-96.41	-101.62	75.25	-102.05
FR19	-86.27	-85.49	-53.40	-103.40
FR20	-79.83	-80.83	-53.59	-101.00
FR21	-88.65	-88.16	-55.64	-104.42
FR22	-83.21	-81.79	-46.48	-95.08
FR23	-74.63	-76.51	-54.07	-99.66
FR24	-102.69	-103.39	-47.28	-103.52
FR25	-81.38	-82.39	-56.69	-102.88
FR26	-76.67	-78.39	-53.46	-99.66
FR27	-82.07	-80.98	-46.70	-95.12
FR28	-88.50	-88.88	-58.19	-106.077

FR29	-86.31	-85.81	-51.92	-100.77
FR30	-88.34	-87.55	-52.57	-102.26
FR31	-86.67	-85.53	-50.09	-99.50
FR32	-84.44	-84.75	-44.09	-95.02
FR33	-96.13	-96.26	5.34	-56.33
FR34	-104.11	-109.81	29.38	-134.58
FR35	-84.28	-87.58	58.34	-98.57
FR36	-80.88	-83.24	-83.92	-135.53
FR37	-88.63	-89.37	-54.04	-117.18
FR38	-83.33	-83.83	-42.38	-103.92
FR39	-65.16	-65.31	-43.25	-99.47
FR40	-72.34	-72.18	-24.95	-84.86
FR41	-66.18	-69.15	-61.63	-116.16
FR42	-64.66	-63.33	-29.46	-86.18
FR43	-56.91	-55.65	-201.33	-143.98
FR44	-79.86	-83.49	74.87	-92.94

8.3.2.2. Global reactivity descriptors

An examination of the relative reactivity of the free radicals was carried out using the following equations. The calculated global chemical hardness (η), global chemical potential (μ), electronegativity (χ), and global electrophilicity (ω) are tabulated in Table 8.2 (Equations 8.1-8.5). Here, the E^{α}_{HOMO} and E^{β}_{LUMO} are the highest occupied molecular orbital (HOMO) and lowest unoccupied molecular orbital (LUMO) energies of the α and β spin states of reactive species, respectively. Global chemical descriptors provide information on these compounds' chemical reactivity and sensitivity to external perturbations. Electronegativity is the tendency to draw electrons towards it, whereas chemical potential is the tendency of electrons to flow from higher potential areas to lower potential areas until uniformity is achieved. The resistance of the molecule to use

electrons is represented by hardness, while its opposite is represented by softness. The charge density is identified as hardness, which is the ability to maintain electronic charge once it has been obtained whereas the electrophilicity index is a measure of affinity of electrons.

$$\eta = \frac{1}{2}(E^{\beta}_{LUMO} - E^{\alpha}_{HOMO}) \tag{8.1}$$

$$\mu = \frac{1}{2}(E^{\beta}_{LUMO} + E^{\alpha}_{HOMO}) \tag{8.2}$$

$$\chi = -\mu \tag{8.3}$$

$$\omega = \frac{\mu^2}{2\eta} \tag{8.4}$$

$$S = \frac{1}{2\eta} \tag{8.5}$$

Among the considered reactive species, the dimethyl sulfide (**FR43**) radical cation is shown to exhibit the highest electronegativity in both the gas phase and aqueous phase, and hence the highest chemical potential value, because of the presence of positive charge and an unpaired electron. The chemical hardness will be higher for **FR6** in both media. Moreover, the lowest electrophilicity values are exhibited by radical anion species; carbonates radical anion (**FR18**), sulfate (**FR34**), sulfur pentoxide (**FR35**), and dimethyl disulphide (**FR44)** in the gas phase and increased significantly in the aqueous phase. The highest electrophilicity value was exhibited by the radical. These variations in the reactivity parameters of the reactive species

under discussion prompted us to investigate the feasibility of scavenging these species in an aqueous solution with the title molecule.

Table 8.2 Global reactivity descriptors (eV) of the considered reactive species (**FR1**-**FR44**) in the gas phase and aqueous solution

	Gas phase					Aqueous phase				
	χ	η	μ	S	ω	χ	η	μ	S	ω
FR1	6.18	3.97	-6.18	0.13	4.82	6.30	3.92	-6.30	0.13	5.07
FR2	5.64	3.23	-5.64	0.15	4.92	5.71	3.14	-5.71	0.16	5.21
FR3	5.50	3.72	-5.50	0.13	4.08	5.52	3.50	-5.52	0.14	4.36
FR4	5.82	4.09	-5.82	0.12	4.14	6.00	4.05	-6.00	0.12	4.45
FR5	5.57	3.36	-5.58	0.15	4.63	5.65	3.24	-5.65	0.15	4.92
FR6	6.36	4.08	-6.36	0.12	4.96	6.35	4.02	-6.34	0.12	5.01
FR7	6.76	4.04	-6.76	0.12	5.67	6.74	3.99	-6.74	0.13	5.70
FR8	6.87	3.91	-6.87	0.13	6.02	6.86	3.84	-6.86	0.13	6.12
FR9_cis	7.21	3.83	-7.21	0.13	6.78	7.11	3.83	-7.11	0.13	6.60
FR9_trans	7.37	3.99	-7.37	0.13	6.81	7.31	3.97	-7.31	0.13	6.72
FR10	5.88	3.77	-5.88	0.13	4.59	6.07	3.69	-6.07	0.14	4.98
FR11	7.50	3.26	-7.50	0.15	8.63	7.44	3.34	-7.44	0.15	8.28
FR12	7.08	3.32	-7.08	0.15	7.55	7.20	3.38	-7.20	0.15	7.67
FR13	6.47	3.87	-6.47	0.13	5.41	6.62	3.81	-6.62	0.13	5.73
FR14	8.23	3.31	-8.23	0.15	10.23	8.19	3.36	-8.19	0.15	9.96
FR15	5.08	3.27	-5.08	0.15	3.94	5.25	3.13	-5.25	0.16	4.40
FR16	5.81	3.64	-5.81	0.14	4.64	5.85	3.62	-5.85	0.14	4.73
FR17	6.60	4.02	-6.59	0.12	5.40	6.69	3.98	-6.69	0.13	5.62
FR18	0.71	3.26	-0.71	0.15	0.08	5.93	3.29	-5.93	0.15	5.35
FR19	5.44	2.32	-5.44	0.22	6.37	5.52	2.30	-5.52	0.22	6.61
FR20	5.20	2.20	-5.20	0.23	6.13	5.24	2.20	-5.24	0.23	6.24
FR21	5.48	2.31	-5.48	0.22	6.49	5.54	2.29	-5.54	0.22	6.69
FR22	4.90	2.23	-4.90	0.22	5.40	4.98	2.19	-4.98	0.23	5.67
FR23	5.20	2.22	-5.20	0.23	6.09	5.20	2.22	-5.20	0.23	6.10
FR24	5.37	2.92	-5.37	0.17	4.95	5.46	2.87	-5.46	0.17	5.19
FR25	5.35	2.22	-5.35	0.22	6.43	5.35	2.21	-5.35	0.23	6.47
FR26	5.06	2.18	-5.06	0.23	5.89	5.11	2.17	-5.11	0.23	6.00
FR27	4.85	2.20	-4.86	0.23	5.35	4.95	2.18	-4.95	0.23	5.63
FR28	5.55	2.28	-5.55	0.22	6.75	5.62	2.27	-5.62	0.22	6.94
FR29	5.25	2.26	-5.25	0.22	6.09	5.35	2.24	-5.35	0.22	6.38
FR30	5.34	2.31	-5.34	0.22	6.17	5.45	2.29	-5.45	0.22	6.49
FR31	5.16	2.26	-5.16	0.22	5.88	5.27	2.23	-5.27	0.22	6.22
FR32	5.32	3.03	-5.32	0.17	4.67	5.46	2.91	-5.46	0.17	5.13
FR33	3.26	3.21	-3.26	0.16	1.66	3.31	3.19	-3.31	0.16	1.72

FR34	1.90	2.90	-1.90	0.17	0.63	6.03	6.32	-6.03	0.08	2.88
FR35	1.23	3.79	-1.23	0.13	0.20	5.80	3.87	-5.80	0.13	4.35
FR36	7.31	2.41	-7.31	0.21	11.09	7.08	2.48	-7.08	0.20	10.10
FR37	6.38	2.73	-6.38	0.18	7.46	6.34	2.80	-6.34	0.18	7.19
FR38	5.62	2.66	-5.62	0.19	5.94	5.71	2.70	-5.71	0.19	6.05
FR39	5.33	2.44	-5.33	0.21	5.83	5.41	2.41	-5.41	0.21	6.07
FR40	5.09	2.99	-5.09	0.17	4.34	5.16	2.95	-5.16	0.17	4.52
FR41	6.07	2.73	-6.07	0.18	6.75	6.06	2.73	-6.06	0.18	6.71
FR42	4.28	2.60	-4.28	0.19	3.52	4.49	2.60	-4.49	0.19	3.89
FR43	12.93	3.04	-12.93	0.16	27.48	7.97	3.06	-7.97	0.16	10.38
FR44	0.11	2.62	-0.11	0.19	0.00	4.79	2.72	-4.79	0.18	4.22

8.3.3. Redox potential and equilibrium constant calculations

From the previous work, it is observed that in the aqueous phase, the compound follows the SPLET mechanism for the radical quenching process. Moreover, the work regarding pka calculation revealed the existence of a monoanionic form in physiological pH. Hence feasibility of the above radical species is screened by the compound **2c** through the SPLET mechanism at physiological pH. The redox potential and equilibrium constant are calculated by utilizing the thermodynamic cycle mentioned in Chapter 6.

According to the calculated redox potentials and equilibrium constant values of the compound with reactive species (Table 8.3), it is observed that seven reactive species are not to be quenched by the dianionic form of the compound at physiological pH in aqueous solution since the positive value of free energy change of the overall reaction (ΔG^0 (rxn)). The equilibrium constants (K) of these reactive species are also found to be less than one. The radical species include 1, 2-dihydroxy-2-phenyl (**FR23**), 1,4-dihydroxy-2-phenoxyl (**FR26**), methy perthiyl (**FR39**), methyl sufinyl (**FR40**), methyl sulfonyl (**FR41**), dimethyl amino thiyl (**FR42**), and dimethyl sulphide radical cation (**FR43**). The radical; methoxyl (**FR1**), allyloxyl (**FR2**), t-

butoxyl (**FR10**), formyloxyl (**FR11**), acetate (**FR12**), methyl sulfonyl oxyl (**FR14**), benzyloxyl (**FR24**) and sulphate radical anion (**FR34**) are highly reactive and spontaneous with the compound in the radical quenching reactions. The obtained results are consistent with the HAA results. Among aromatic reactive oxygen species **FR23** and **FR26** are less reactive will be due to increased stabilisation of the radical with nearby hydroxyl group.

Table 8.3 Calculated Gibbs energy change in the gas phase (in kcal/mol), redox potential (in V), and the equilibrium constant for the scavenging of each reactive species by the dianionic form of **2c** via SPLET mechanism

	ΔG^0 (rxn)	E_{rxn}	K		ΔG^0 (rxn)	E_{rxn}	K
FR1	-23.34	1.01	$1.47x10^{17}$	FR23	2.61	-0.11	$1.21x10^{-2}$
FR2	-23.98	1.04	$4.35x10^{17}$	FR24	-24.29	1.05	$7.34x10^{17}$
FR3	-4.31	0.19	$1.49x10^{3}$	FR25	-3.05	0.13	$1.76x10^{2}$
FR4	-4.17	0.18	$1.16\ x10^{3}$	FR26	0.56	-0.02	$3.87x10^{-1}$
FR5	-6.80	0.29	$1.01x10^{5}$	FR27	-1.61	0.07	$1.54x10^{1}$
FR6	-6.14	0.27	$3.28x10^{4}$	FR28	-9.20	0.40	$5.83x10^{6}$
FR7	-11.83	0.51	$5.02x10^{8}$	FR29	-5.88	0.26	$2.12x10^{4}$
FR8	-12.32	0.53	$1.16x10^{9}$	FR30	-8.06	0.35	$8.50x10^{5}$
FR9 Cis	-14.78	0.64	$7.50x10^{10}$	FR31	-5.56	0.24	$1.23x10^{4}$
FR9 Trans	-16.31	0.71	$9.94x10^{11}$	FR32	-4.25	0.18	$1.33x10^{3}$
FR10	-25.56	1.11	$6.39x10^{18}$	FR33	-16.58	0.72	$1.56x10^{12}$
FR11	-35.18	1.53	$7.60x10^{25}$	FR34	-30.37	1.32	$2.19x10^{22}$
FR12	-34.09	1.48	$1.20x10^{25}$	FR35	-7.79	0.34	$5.35x10^{5}$
FR13	-15.47	0.67	$2.40x10^{11}$	FR36	-4.90	0.21	$4.02x10^{3}$
FR14	-35.19	1.53	$7.68x10^{25}$	FR37	-10.76	0.47	$8.22x10^{7}$
FR15	-8.59	0.37	$2.08x10^{6}$	FR38	-5.04	0.22	$5.14x10^{3}$
FR16	-8.35	0.36	$1.38x10^{6}$	FR39	13.49	-0.58	$1.20x10^{-10}$
FR17	-11.84	0.51	$5.16x10^{8}$	FR40	7.76	-0.34	$1.95x10^{-6}$
FR18	-21.71	0.94	$9.37x10^{15}$	FR41	10.90	-0.47	$9.62x10^{-9}$
FR19	-5.35	0.23	$8.58x10^{3}$	FR42	17.37	-0.75	$1.68x10^{-13}$
FR20	-1.34	0.06	9.67	FR43	21.317	-0.92	$2.10x10^{-16}$
FR21	-8.31	0.36	$1.30x10^{6}$	FR44	-3.78	0.16	$6.06x10^{2}$
FR22	-1.81	0.08	$2.16x10^{1}$				

8.3.4. Methanol-induced oxidative degradation pathway of 2c

Radicals centered on carbon, like hydroxymethyl radical ($^{\cdot}CH_2OH$) as well as its extremely reactive isomeric form methoxy radical ($CH_3O^{\cdot}$) are produced as a result of lipid peroxidation and ethanol intoxication procedures taking place within the body[8–10]. Such radicals can be effectively detoxified, which greatly aids in controlling the oxidative stress caused by methanol. An example of this is a work by Anouar et al. that used computational and experimental methods to examine the antioxidant activity of ferulic acid and its degradation products in the radiolytic solution of methanol[9]. According to the report, In the presence of these radicals, the phenolic antioxidants, ferulic acid are expected to undergo oxidative degradation, resulting in the formation of new stable metabolites after passing through a cascade of reactions including radical adduct formation, neutralization and cyclization in addition to the direct radical scavenging activity. Likewise, different cascades of reactions by the interconversion between $CH_3O^{\cdot}$ and $^{\cdot}CH_2OH$ radicals in the radiolytic methanol medium, are discussed based on the corresponding calculated energetic schemes.

An in-depth analysis of Avenanthramide-2c's oxidative breakdown process in the presence of the extremely unstable alkoxy radical $CH_3O^{\cdot}$ and its more stable isomeric counterpart, the hydroxymethyl radical $^{\cdot}CH_2OH$ is explained. The energetics of conversion between $CH_3O^{\cdot}$ and $^{\cdot}CH_2OH$ are shown in Fig.8.5. From the analysis, it is clear that the direct isomerization between $CH_3O^{\cdot}$ and $^{\cdot}CH_2OH$ was reported to be energetically less favorable, Instead, the

isomer, $^{\cdot}CH_2OH$ is expected to be generated by the reaction of $CH_3O^{\cdot}$ with methanol as given below in Fig 8.5(as per the Equation given on the Right side of the figure). The Reaction energy profiles and optimized TS geometries of self-isomerization reaction as well as the reaction of $CH_3O^{\cdot}$ with $^{\cdot}CH_2OH$ computed using the same level of theory is also given in Fig.8.5. It was found that the activation energy barrier is lesser for the reaction of $CH_3O^{\cdot}$ with methanol (14.69 kcal/mol) compared to direct hydrogen atom transfer between the radicals (31.73 kcal/mol) and the results were found to correlate with the previous results[9]. This could be because the intramolecular reaction involves a restricted three-membered TS. In light of previous studies, the cascade of reaction in the radiolytic solution of methanol during the oxidative degradation mechanism was explored.

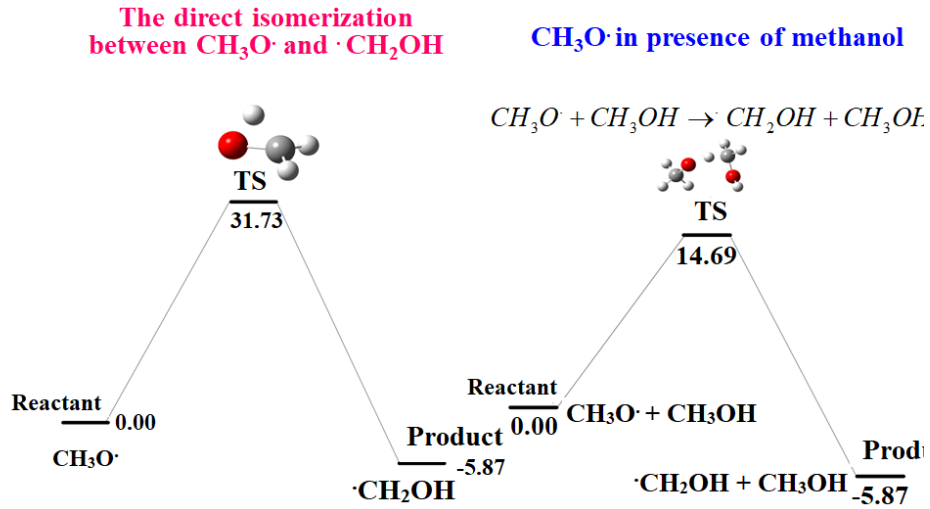

Fig. 8.5. The energetics of conversion between $CH_3O^{\cdot}$ and $^{\cdot}CH_2OH$ 1) The direct isomerization between $CH_3O^{\cdot}$ and $^{\cdot}CH_2OH$ (left) and 2) by the reaction between $CH_3O^{\cdot}$ and methanol (right).

8.3.4.1. First stage of radiolytic degradation - direct radical scavenging mechanisms

The first stage degradation pathway has been evaluated using two mechanisms; HAT and RAF as discussed in earlier Chapters. A graphical representation of the HAT and RAF pathways of **2c** is provided in Fig.8.6. The free energies changes of products and transition states formation of HAT and RAF with $CH_3O^{\cdot}$ and $^{\cdot}CH_2OH$ are given in Table 8.4. The reaction channels for the scavenging of $CH_3O^{\cdot}$ proceeded with comparatively lower energy barriers (4.8 kcal/mol) for position 4'OH, owing to their high reactivity. From Gibb's free energy calculations of transition states, it is clear that the lowest energy barrier is exhibited by the 4'OH position since the radical formed after HAT at this position is strongly stabilized via H-bonding with the vicinal hydroxyl group, 4-OH as obtained from previous analyses and also the extended delocalization of the radical species through the aromatic ring stabilizes the radical species as evident from the previous analysis.

Table 8.4 also summarises the radical adduct (RA) formation possibility of the **2c** as reported in the cases of various polyphenols. Here, out of the two isomeric radicals, the carbon-centered radical $^{\cdot}CH_2OH$ can undergo radical adduct formation at the double bond of **2c** through the addition of α carbon and β carbon, respectively, RA-2' and RA-1'.

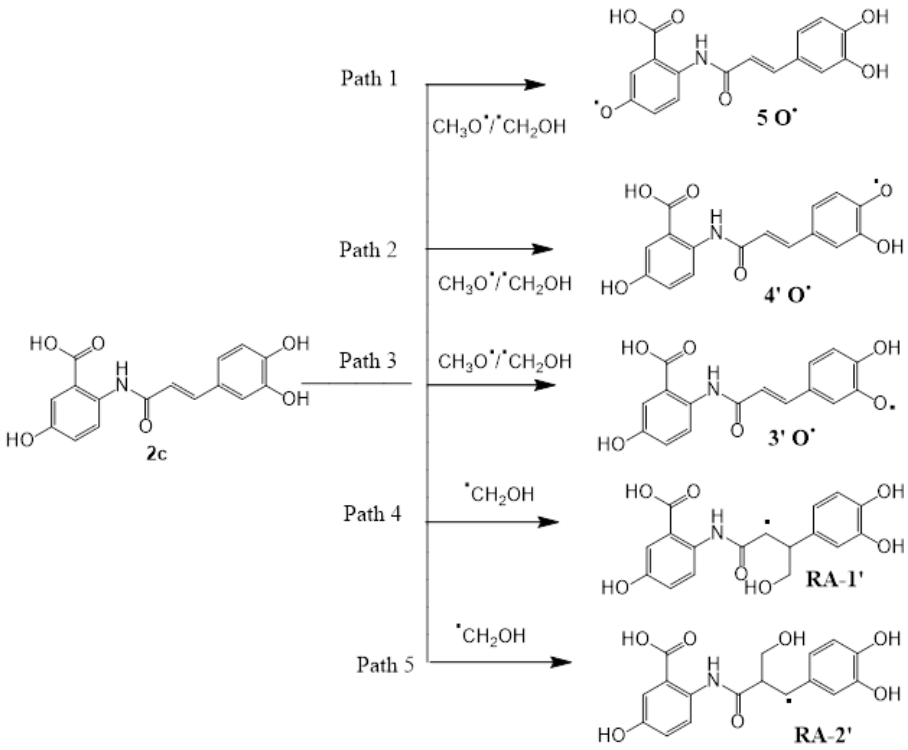

Fig.8.6. Schematic diagram of the first stage of the oxidative degradation mechanism of **2c**: direct free radical scavenging by HAT and RAF mechanisms.

The RAF mechanism is found to be favorable for RA-2' by the lowest energy barrier compared to RA-1' and the adduct formed from RA-2' is found to be more stabilized due to its lower energy. For both HAT and RAF mechanisms the rate constant is inconsistent with the thermodynamic calculations (Table 8.4). The quenching of radical species, $CH_3O^{\cdot}$ by the 4'OH group of **2c** is found to occur with a high reaction rate. Compared to hydrogen abstraction reactions radical adduct formation reactions are less feasible. Moreover, compared to the radical adduct formation by the addition of hydroperoxyl radical

species (Chapter 7), the adduct formed by the methoxy radical/hydroxymethyl radical is found to be more feasible.

Table 8.4 The free energy of reaction and transition states in each reactive site of HAT (phenolic hydroxyl group) and RAF (α,β-unsaturated carbon). Free energy changes are given in kcal/mol and rate constant in L $mol^{-1}s^{-1}$

Path	$\Delta G_{Reaction}$	ΔG_{TS}	Rate constant (k)
5 OH with $CH_3O^{\cdot}$	-18.20	7.19	8.19×10^{8}
4'OH with $CH_3O^{\cdot}$	-24.81	4.8	46.32×10^{9}
3'OH with $CH_3O^{\cdot}$	-13.97	10.58	26.86×10^{5}
5 OH with $^{\cdot}CH_2OH$	-12.33	12.75	6.87×10^{4}
4'OH with $^{\cdot}CH_2OH$	-18.94	11.25	$8.76\ 32 \times 10^{5}$
3'OH with $^{\cdot}CH_2OH$	-8.10	13.28	$4.25\ 32 \times 10^{6}$
$^{\cdot}CH_2OH$ addition on α carbon (RA-2')	-16.24	9.50	16.72×10^{6}
$^{\cdot}CH_2OH$ addition on β carbon (RA-1')	-10.10	11.25	18.32×10^{5}

8.3.4.2. Second stage of oxidative degradation of **2c**

The phenolic antioxidants are anticipated to suffer oxidative degradation in the presence of these radicals, leading to the creation of new stable metabolites after passing through a series of processes such as radical adduct formation, neutralization, and cyclization. The efficient detoxification of such radicals significantly aids in controlling the oxidative stress caused by methanol.

In light of the previous study, herein, we proposed the methanol-induced oxidative degradation pathway of **2c** in its neutral form[9] (Fig.8.7). The cyclic metabolites formation is initiated by the

H atom abstraction from the RA-1' (neutral) by $^{\cdot}CH_2OH$ which produces radical intermediate IN-1. The formed radical intermediate IN-1 undergoes intramolecular radical rearrangement with the nearest carbonyl compound, to yield a cyclized product IN-2. The intermediate IN-2 has a radical center on the oxygen atom, then gets neutralized by abstracting a hydrogen atom from CH_3OH. Accordingly, a stable and neutral cyclized product (P) is formed by the release of $^{\cdot}CH_2OH$ radical. The proposed schematic diagram for the cyclization process in the second stage of radiolytic degradation of **2c** about the degradation pathway proposed by Anouar et al. for ferulic acid[9].

To assess the feasibility of the reaction mechanism, we analyzed the gas phase energies of the transition state and the intermediates. The energy profile diagram of the reaction is given in Fig.8.8. The cyclized neutral product formed from the IN-2 through the transition state TS-3 and product is found to be more stable than all other intermediate formed. The TS-1 corresponds to hydrogen abstraction from the reactant molecule possesses an energy barrier of 17.03 kcal/mol is the lowest barrier among the steps. The process leads to a comparatively stable intermediate IN-1 with an energy of 6.70 kcal/mol from the reactant coordinates. The next, formed IN-1 intermediate undergoes cyclization with an energy barrier of 20.02 kcal/mol, and intermediate IN-2 is formed. The formed intermediate is only slightly lower in energy (16.41 kcal/mol) than the other intermediates from their corresponding transition state and it is unstable compared to the reactant. The transition state TS-3 is the radical neutralization step in which the radical gets neutralized with

methanol in the medium with a reaction barrier of 23.22 kcal/mol. The final product is the most negative and stable low-lying product. To obtain further insights into the reaction pathway, the kinetic aspects of the reactions were analysed. The rate constants (k) are calculated at the same level of theory at 298.15 K and are tabulated in Table 8.5. The kinetic data are found to be consistent with the thermodynamic results.

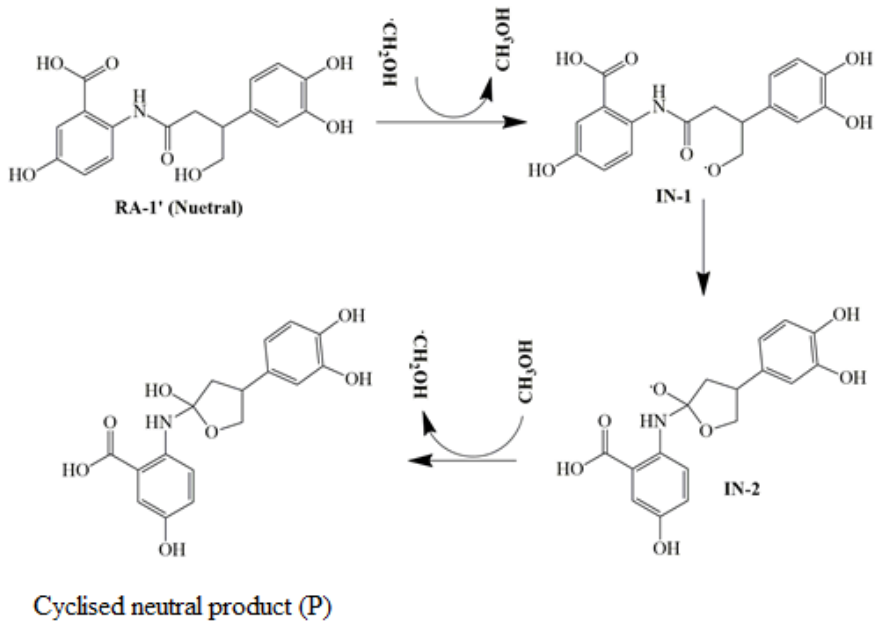

Fig.8.7. Proposed schematic diagram for the cyclization process in the second stage of radiolytic degradation of **2c** about the degradation pathway proposed by Anouar et al. for ferulic acid[9].

The optimized geometries of selected stationary points (TSs) associated with each step in the formation of cyclic metabolite are depicted in Fig.8.9. The most relevant geometrical parameters of transition states are the distances of the bonds that are being broken and that being formed. Analyzing the bond parameters, the initial

hydrogen abstraction step TS-1 is characterized by an O1-H1-C1 bond angle of 168.51°, closer to being linear around the transferred hydrogen, which is also essentially a characteristic of the hydrogen atom transfer mechanism. The O1-H1 and C1-H1 bond lengths of 1.39Å and 1.20Å indicate an early transition state involved with the hydrogen atom transfer reaction. In TS-2, the O1-C2 bond distance of about 1.60Å and C1-O1-C2 bond angle of 109.9° correspond to the new bond formation to form a 5-membered ring. The O1-H1-C1 bond angle of TS-3 for the neutralization of oxygen-centered radical of cyclic intermediate via hydrogen abstraction from the C atom of CH3OH is 171.2°, which agrees with the possibility of hydrogen abstraction by the radical oxygen.

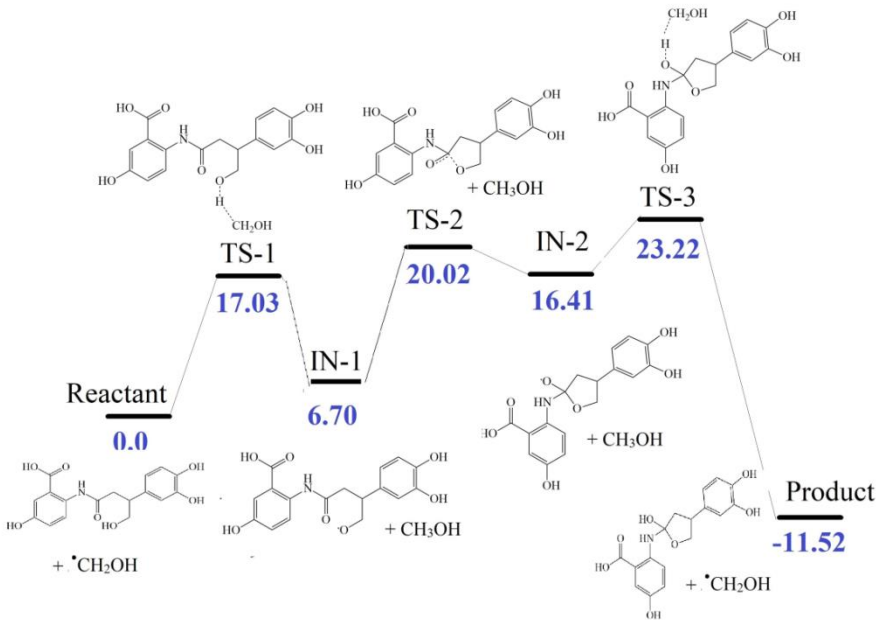

Fig.8.8. TS energy profile of the cyclic metabolite formation in the oxidative degradation mechanism

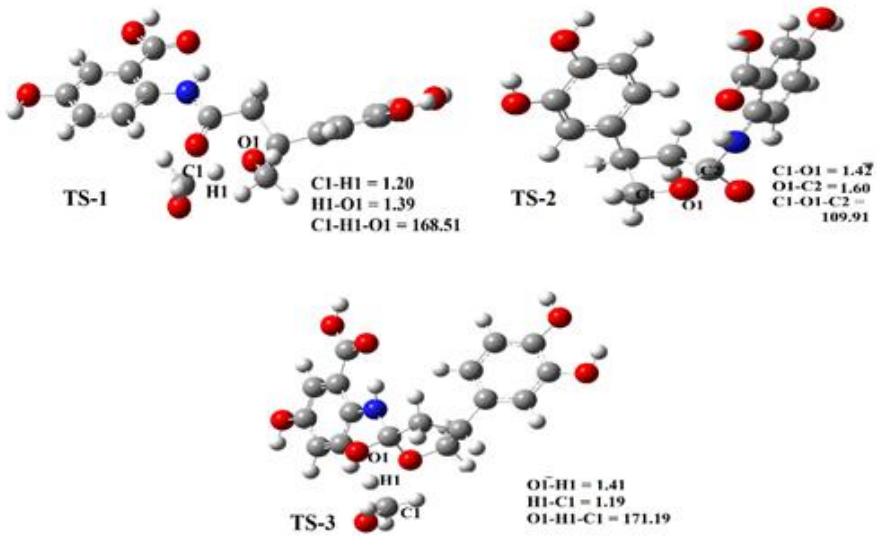

Fig.8.9. Optimised geometries of selected stationary points (TSs) associated with each step in the cyclic metabolite formation in the oxidative degradation mechanism. (Angles in ^{0} and bond lengths in Å).

Table 8.5 Rate constants (L $mol^{-1}s^{-1}$) of different transition states involved in the second stage degradation pathway.

Transition state	Frequency (cm^{-})	Rate constant (k)
TS-1	-998.72	$5.023x10^{1}$
TS-3	-876.66	$1.05x10^{-6}$

8.5. Conclusions

The present work concluded that the dianion of Avenathramides-2c scavenges a variety of free radicals. It is already proved that Avenathramides dianions exist at physiological pH and it favors the SPLET mechanism in solution phase, especially in highly polar solvents like water. So, the forty-four radical species including reactive oxygen, sulfur, and carbon species are selected and screened

for the radical scavenging activity with the 2c dianion through the SPLET pathway. Based on the computed redox potential and equilibrium constant values, it has been found that among all the selected reactive species, seven reactive species are not to be quenched by the dianionic form of the compound at physiological pH in an aqueous solution through the SPLET pathway. The radical species includes 1, 2-dihydroxy-2-phenyl (FR23), 1, 4-dihydroxy-2-phenoxyl (FR26), methy perthiyl (FR39), methyl sufinyl (FR40), methyl sulfonyl (FR41), dimethyl amino thiyl (FR42), and dimethyl sulphide radical cation (FR43). The radical; methoxyl (FR1), allyloxyl (FR2), t-butoxyl (FR10), formyloxyl (FR11), acetate (FR12), methyl sulfonyl oxyl (FR14), benzyloxyl (FR24) and sulphate radical anion (FR34) are highly reactive and spontaneous with the compound in the radical quenching reactions. Majorly, ROS have been scavenged by the compound with higher redox potential, and this has also been verified with the hydrogen atom affinity values. The methanol-induced oxidative degradation pathway of **2c** and cyclic metabolites formation are also analyzed.

References

1. Galano A, Mazzone G, Marino T, et al (2016) Food Antioxidants : Chemical Insights at the Molecular Level. Annu Rev Food Sci Technol 7:335–352. https://doi.org/10.1146/annurev-food-041715-033206

2. Ferreira CA, Ni D, Rosenkrans ZT, Cai W (2018) Scavenging of reactive oxygen and nitrogen species with nanomaterials. Nano Res 11:4955–4984. https://doi.org/10.1007/s12274-018-2092-y

3. Mittal A, Vashistha VK, Das DK (2022) Recent advances in the antioxidant activity and mechanisms of chalcone derivatives: a computational review. Free Radic Res 1–20. https://doi.org/10.1080/10715762.2022.2120396

4. Duan X, Niu X, Gao J et al (2022) Comparison of sulfate radical with other reactive species. Curr Opin Chem Eng 38:100867

5. M. J. Frisch, G. W. Trucks, H. B. Schlegel, G. E. Scuseria, M. A. Robb, J. R. Cheeseman, G. Scalmani, V. Barone, G. A. Petersson, H. Nakatsuji, X. Li, M. Caricato, A. V. Marenich, J. Bloino, B. G. Janesko, R. Gomperts, B. Mennucci, H. P. Hratchian, J. V. and DJF (2016) Gaussian 16, Revision C.01

6. S. Canneaux, F. Bohr and EH (2014) KiSThelP: a program to predict thermodynamic properties and rate constants from quantum chemistry results. J Comp Chem 35:82–93. https://doi.org/http://dx.doi.org/10.1002/jcc.23470.

7. Thion S, Zaras AM, Szőri M, Dagaut P (2015) Theoretical kinetic study for methyl levulinate: oxidation by OH and CH3 radicals and further unimolecular decomposition pathways. Phys Chem Chem Phys 17:23384–23391. https://doi.org/10.1039/C5CP04194E

8. Kozlowski D, Marsal P, Steel M, et al (2007) Theoretical Investigation of the Formation of a New Series of Antioxidant Depsides from the Radiolysis of Flavonoid Compounds. Radiat Res 168:243–252

9. Anouar E, Košinová P, Kozlowski D, et al (2009) New aspects of the antioxidant properties of phenolic acids: a combined theoretical and experimental approach. Phys Chem Chem Phys 11:7659–7668. https://doi.org/10.1039/B904402G

10. Burgers P, Ruttink P (2005) The acid-catalyzed rearrangement CH3O --> CH2OH and its involvement in the dissociation of the methanol dimer radical cation: A Quid pro Quo reaction. Int J Mass Spectrom - INT J MASS SPECTROM 242:49–56. https://doi.org/10.1016/j.ijms.2004.11.006

Chapter 9
Summary and Future Outlook

Natural polyphenols, a broad class of phytochemicals, are becoming more and more recognized as possible therapeutic agents for oxidative stress-related illnesses. Based on their basic structure, these polyphenols are divided into numerous subgroups. Of the different polyphenolic categories, the current work focuses on the compound named Avenanthramides. These are the phenolic amides exclusively found in Oats. Initially, the role of the compound was identified to be in plant protection, adaptation to environmental stressors, to protecting plants from infections, diseases, and herbivore attacks by acting as an antimicrobial agent or chemical barrier.

In recent years, there has been considerable interest in the influence of these phenolic amides in different bioactivities including antioxidant properties and potential therapeutic benefits including anti-inflammatory, antiproliferative, and antigenotoxic effects. Apart from the bioactivity studies the structure-activity relationship, the role of different functionalities in the compound, the underlying mechanism, etc. are still lacking. Interestingly, the compound "Tranilast", a synthetic analog that possesses structural similarity with the studied compound is nowadays used to treat bronchial asthma, atopic dermatitis, keloids and hypertrophic scars, allergic conjunctivitis, allergic rhinitis, and other allergic disorders in Japan and South Korea under Rizaban, Kissei Pharmaceutical Co. with very low adverse effects and good toleration by patients.

Structurally these compounds contain two aromatic rings of an anthranlic acid derivative and cinnamic acid derivative and both these rings are connected through an α,β-unsaturated amide linkage. Around

forty compounds of these types are isolated and among them, eight compounds of interest are included here namely; **2p**, **2f**, **2c**, **2s**, **1p**, **1f**, **1c**, and **1s.**

The development of density functional theory has led to significant applications in the explanation of molecular-level experimental research as well as the prediction of potential uses and mechanisms in certain situations. We have attempted an analysis of the chosen molecule in this circumstance using density functional theory.

To begin with, the structures of these compounds are carefully optimized and their geometrical parameters were compared to the experimentally available crystal structure data for validation of the theoretical model. To ascertain whether molecules of interest serve as efficient barriers against free radicals, their electronic, conformational, and geometric characteristics are examined. Also, the local and global descriptor analysis, surface analysis, and pKa calculations derived important information regarding radical scavenging potential, reactive functional group, and different ionization states of the studied compounds.

We evaluated the antioxidant potential within the mechanism proposed in the literature which was explored by calculating quantum chemical descriptors and then various mechanisms of antioxidant action were investigated from the thermodynamic point of view. It was found that, the presence of multiple bonds in the compound, planarity, and presence of phenolic OH groups are important characteristics of antioxidant molecules. The planarity in the molecule allows the

extended delocalization of electrons. The results strongly revealed that the presence of ortho-dihydroxy group stabilized by strong intramolecular H bonding and it can be identified as the common property of potent phenolic antioxidants. Also, ortho-methoxy substituents possess radical stabilization by the formation of benzodioxozole intermediates. We have considered different molecular descriptors such as reaction enthalpy-related electronic properties, spin densities, and frontier molecular orbitals for predicting antioxidant activity and it was obtained that the dissociation energy of the O-H bond (in gas phase- hydrogen atom transfer mechanism) and proton affinity (in polar phase-sequential proton loss electron transfer mechanism) are the most important thermochemical parameters to determine their antioxidant potential. Other than the SPLET mechanism the compound can exhibit antioxidant activity through the StPLdET pathway increases with higher pH.

Apart from the intrinsic reactivity of antioxidant species, from thermochemical data, utilizing the redox potential and equilibrium constant it was found that the compounds can scavenge •OH more effectively. The reactivity of **c**-series compounds is found to be higher among others followed by **s**-series compounds. The trend in antioxidant activity of the compound obtained was consistent with the experimental results. We may also conclude that the neutral and mono-deprotonated forms of the Avenanthramides are effective at scavenging the hydroxyl and hydroperoxyl radicals as well as the nitrogen dioxide radical based on the computed equilibrium constant

values. The superoxide radical anion and nitrogen monoxide radical are shown to be ineffective by the selected compounds.

UV absorption characteristics of the molecules were studied using TDDFT, which showed that these molecules could be potential UV filters. These compounds' capacity to absorb UV rays and exhibit photoprotective properties may make them useful in the sunscreen industry. The E isomers of the Avenanthramides only show UV filtering activity and Z isomers are UV absorbs only in the UVC region, wide application of these molecules especially in the cosmetic industry as UV filters or UV blockers can be excluded.

The kinetic investigation of hydroperoxyl radical also revealed the higher reactivity of **the c**-series compound. A comparative investigation of hydrogen atom abstraction from the phenolic hydroxyl group and radical adduct formation reaction on the unsaturated compound by the hydroperoxyl radical provides that the FHAT mechanism overtakes the RAF mechanism in the radical scavenging mechanism. Hence the major role in the radical quenching activity by the compounds is taken by OH groups in the molecule.

Concerning the higher antioxidant potential of **c**-series compounds, the **2c** was explored through a pool of different radicals including reactive oxygen, nitrogen, carbon, and sulfur species in aqueous media at physiological pH. The radical species includes 1, 2-dihydroxy-2-phenyl, 1, 4-dihydroxy-2-phenoxyl, methyl perthiyl, methyl sulfinyl, methyl sulfonyl, dimethyl amino thiyl, and dimethyl sulfide radical cation are not to be quenched by the compound in

reaction condition and the radical; methoxyl, allyloxyl, t-butoxyl, formyloxyl, acetate, methyl sulfonyl oxyl, benzyloxyl, and sulfate radical anion are highly reactive and spontaneous with compound in the radical quenching reactions. Theoretical elucidation of Avenanthramides's radiolytic breakdown mechanism illuminates novel facets of its antioxidant activity involving the two radicals $CH_3O•$ and $•CH_2OH$.

The results of quantum chemical calculations are found to correlate with the experimental finding of the antioxidant potential of the molecule, hence, quantum chemistry has evolved as a very effective tool to bring into evidence and confirm the structure-activity relationship of different antioxidants.

Thus the molecules selected for the present study find application in various fields. The molecular framework with modifications could be of great importance in the industry. Several extensions of the current work may be possible in the future like

- ❖ Exploring the activity of more structures of similar kinds of natural, synthetic, and recombinant (YAvn) Avenanthramides and Avenalumic acid isomers. Then compare the reactivity of these structurally similar compounds
- ❖ Kinetics of antioxidant mechanism with several radicals could be carried out.
- ❖ Evaluating the metal chelating capacity and the related metal-catalyzed peroxidations via the Fenton mechanism

- ❖ Studying the corrosion-inhibiting capacity of Avenanthramide towards several metals
- ❖ Molecular docking investigation with different targets has to be studied
- ❖ Developing best QSAR/QSPR models based on virtual screening, machine learning, etc.

DETAILS OF PUBLICATIONS

Journal Publications:

Details of published papers				
In International journals				
No.	Details of paper	Journal	Impact factor	ISSN/ ISBN
1.	Quantum chemical investigation of the antiradical property of avenanthramudes,oat phenolics P.C Sumayya,Godsa Merin Babu, K.Muraleedharan, Heliyon 7 (2021)e06125	Heliyon-Elsevier	4.00	24058440
2.	Structure and non-covalent interactions of (E,Z) 3-benzoyl-1,5-bis(4-ethoxyphenyl)formazan:A crystallographic and DFT/TD-DFT study Rajeena CK, Sumayya PC, Shalina Begum T, Muraleedharan K, Journal of Molecular Structure, Volume 1266, 15 October 2022, 133501,	Journal of Molecular Structure-Elsevier	3.841	0022-2860
3.	Visualization of UV and ECD spectra of E&Z isomers of N-(4'-Hydroxycinnamoyl)-5-hydroxyanthanilic acid P.C.Sumayya, V.K.Jalala, T.K.Shameera Ahammed, K.Muraleedharan, Computational Biology and Chemistry, Volume 101, December 2022,	Computational Biology and Chemistry-Elsevier	3.1	1476-9271

	107777			
4.	Radical scavenging capacity, UV activity, and molecular docking studies of 2', 5', 3, 4-Tetrahydroxychalcone: An insight into the photoprotection P.C.Sumayya, V.M. Abdul Mujeeb, K.Muraleedharan, Chemical Physics Impact, Volume 5, December 2022, 100126	Chemical Physics Impact-Elsevier	2.2	2667-0224
5.	Theoretical investigation on the structural properties, scavenging mechanism and toxicological profile of Nymphaeol C, a flavanone in Macaranga Tanarius G.S. Gopika Krishnan , P.C. Sumayya, K. Muraleedharan, Computational and Theoretical Chemistry 1228 (2023) 114281,	Computational and Theoretical Chemistry--Elsevier	2.8	2210-2728
6.	Free radical scavenging activity of Avenanthramides and its carboxylates toward various reactive oxygen and nitrogen species: a DFT approach P.C. Sumayya, K. Muraleedharan	Theoretical Chemistry Accounts-Springer	2.15	1432-2234

Book chapters

No	Chapter	Book	Publication	ISSN/ISBN
1.	DFT Study of Structure and Radical Scavenging Activity of Natural Pigment Delphinidin and Derivatives Sumayya Pottachola, Arifa Kaniyantavida and Muraleedharan Karuvanthodiyil; Book Chapter, Density Functional Theory - Recent Advances, New Perspectives and Applications; IntechOpen; http://dx.doi.org/10.5772/intechopen.98647	Density Functional Theory - Recent Advances, New Perspectives and Applications	IntechOpen	978-1-83969-846-0
2.	Evaluation of anticancer and antioxidant properties of tranilast-a theoretical approach; Sumayya p.c., Muraleedharan k.* *department of chemistry, university of calicut, malappuram, 673635, India*	Diseases A to Z: From Molecular Mechanisms to Drug Targets and Current Clinical Treatment	BETHAM publishers	In communication

Seminar proceedings

1. A theoretical insight on the influence of structural factors towards antioxidant activity of 2',5', 3,4-Tetrahydroxy chalcone Author: Sumayya PC and K Muraleedharan , Seminar proceedings: National seminar on recent trends in material science(NSRTMS-2019), ISBN 978-93- 5391-561-2

Seminar presentations

International	
1.	International conference Farook college on Frontier in chemical sciences at 2019 and orally presented a paper in "A computational exploration into the structure, antioxidant capacity, and toxicity studies of anthocyanidin "delphinidin" and its derivatives"
2.	Virtual international conference on surface chemistry (SUCH-2022) organized by Department of Chemistry, Annamalai University and presented a paper in " A theoretical study on the UV filtering and radical scavenging activity of Avenanthramides"
National	
1.	National seminar on current trends in organic and computational chemistry organized by Morning Star Home Science College and presented a paper orally in topic "Theoretical study on the structural and antioxidant property of selected chalcone in gas phase
2.	National conference on frontiers in chemical sciences FCS- 2019 at University of Calicut, and presented a paper on Avenanthramides in oats (*Avena sativa L.*): A theoretical investigation of structure antioxidant activity relationship
3.	National conference on recent trends in materials science NSRTMS2019at chittor government college on topic "A theoretical insight on the influence of structural factors towards antioxidant activity of 2', 5', 3, 4 - Tetrahydroxy chalcone"
4.	National seminar Computational Chemistry Summit (CCS-2023) " Unleashing the Power of Virtual Chemistry" and presented a paper in topic "Theoretical Studies on the free radical scavenging mechanism and photoprotective potential of Avenanthramides"

Computational Training Programs Attended

1. Two day hands on training programmes provided by Zamorin's Guruvayurappan College, Calicut in different tools of molecular docking

2. Two day hands on training program of Schrodinger software, provided by Schrodinger software team